Molecular Engineering of N-heteroacenes and Macrocyclic Arenes: Design, Synthesis and Properties

HE, Zikai

A Thesis Submitted in Partial Fulfillment

of the Requirements for the Degree of

Doctor of Philosophy

in

Chemistry

The Chinese University of Hong Kong

August 2013

Thesis/Assessment Committee

Professor Zuowei Xie (Chair)

Professor Qian Miao (Thesis Supervisor)

Professor Dennis Kee Pui Ng (Committee Member)

Professor John Dayton Tovar (External Examiner)

To My Parents and My Wife

Molecular Engineering of N-heteroacenes and Macrocyclic Arenes: Design, Synthesis and Properties

Zikai HE

Department of Chemistry, the Chinese University of Hong Kong

Abstract

Detailed in this thesis is molecular engineering of N-heteroacenes and macrocyclic arenes including design, synthesis and investigations on their organic semiconductor properties. Chapter 1 reviews the advances in the area of the large N-heteroacenes, which have four or more linearly fused six-membered rings, in terms of structure, synthesis, molecular packing and their applications as electronic materials.

Chapter 2 presents three new members of N-heteropentacenes that have adjacent pyrazine and dihydropyrazine rings at one end of the pentacene backbone. Interesting findings from this study include self-complementary N-H•••N H-bonds in the solid state, solvent-dependent UV-vis absorptions caused by H-bonding and new p-type organic semiconductors with field effect mobility up to 0.7 $cm^2V^{-1}s^{-1}$.

Chapter 3 introduces novel silylethynylated N-heteropentacenes that have three adjacent pyrazine rings at the center of a pentacene backbone. These hexaazapentacenes exhibit a record low energy level of lowest unoccupied molecular orbital (LUMO) for N-heteropentacenes and thus able to oxidize dihydroanthracene to anthracene. Their synthetic precursors are the corresponding dihydrohexaaza-

pentacenes, which also exhibit interesting H-bonding.

Chapter 4 presents a novel electron-deficient thiadiazolophenazine, which was found to function as an air-stable n-type organic semiconductor in solution-processed thin film transistors with field effect mobility up to 0.7 $cm^2V^{-1}s^{-1}$. We demonstrate that S-N dipole-dipole interactions enforce self-complementary head-to-head packing while bulky triisopropylsilyl groups in this compound lead to a one dimensional π-π stacking of the aromatic cores.

Chapter 5 reports novel conjugated macrocycles based on phenanthrene, which are connected with varied linkers leading to planar and tubular structures. We have conducted a comparative study on flat or nearly flat conjugated macrocycles with focus on self-assembly behavior and solution-processed organic semiconductor property which is dependent on their ability of self-aggregation in solution. Lewis acid-catalyzed [4+2] benzannulation on the flat macrocycle **5.2** leads to the coronal macrocycle, whose π-backbone is a new segment of [6,6]-carbon nanotube. This suggests a new strategy to synthesize π-extended nanorings from flat conjugated macrocycles that are more easily accessed.

氮雜並苯和共軛芳烴大環的分子工程: 設計，合成和性質研究

何自開

香港中文大學化學系

摘要

此論文討論了氮雜並苯和共軛芳烴大環的分子工程，包括分子設計、合成以及他們的有機半導體性質的研究。第一章綜述了在氮雜並苯領域最近的研究進展，主要討論了並四苯及其以上的分子合成， 結構，晶體排列和在電子材料方面的應用。

第二章介紹了三個全新的氮雜並五苯分子，其中相鄰的吡嗪和二氫吡嗪環位於並五苯骨架的一側末端。通過這種設計，無論是固相中自身互配的 NH•••N 氫鍵還是溶液中由於氫鍵引起的溶劑變色和紫外-可見光吸收得以發現和解釋。並且開發出新的一種 p 型有機半導體， 其場效應遷移率最高可達到 0.7 $cm^2V^{-1}s^{-1}$。

在第三章中，三個相鄰的吡嗪環被放在並五苯骨架的中間從而設計出全新結構的氮雜並五苯。通過這種設計，這類氮雜並五苯呈現出超低 LUMO 分子軌道並且具有了氧化二氫蒽到蒽的能力。相應的還原態前體，二氫氮雜並五苯則同樣表現出了有趣的形成氫鍵的能力。

第四章則主要闡述了另外一類並苯噻二唑分子。研究發現，通過引入合適的

取代基，他們可以成為空氣下穩定的 n 型有機半導體，其溶液法加工的薄膜晶体管最大電子遷移率可以達到 0.7 $cm^2V^{-1}s^{-1}$。噻二唑結構之間產生的 S−N 偶極−偶極相互作用促使分子以頭−對−頭的方式排列，而 TIPS 基團則使得這些分子芳香核平面之間以一維 **π-π** 重疊方式堆積。

第五章介紹了基於菲為芳香單元合成的一系列共軛大環分子，由不同的連接基團而得到平面的和管狀的分子構型：。我們系統地研究平面的和近似平面的大環的自組裝行為及其溶液法加工的有機半導體性質，發現其半導體性質很大程度上決定於其在溶液中自組裝的能力。此外，通過路易士酸催化的[4+2]成苯環反應，從平面分子 **5.2** 我們可以合成全新冠狀大環 **5.4**，其 π 骨架則是[6, 6]-碳納米管的一個新片斷。這種方法開創了一個合成 **π**-延伸納米環全新策略，即以更易合成的平面共軛大環為原料一步轉化。

Acknowledgements

When I was a high school student, my chemistry teacher told me that chemistry is the central science and I was attracted by the miracle chemical reactions. After graduated from university four year ago, I decided to become a doctor in chemistry and joined in this department at the Chinese University of Hong Kong. At the beginning, I found it was really a tough and challenge journey for me. As I'm reaching the end of my graduate student life, I would like to give my sincere appreciations to all people who helped, supported and encouraged me during my four years Ph.D. study. Without their help, this journey would not have been possible.

First of all, I am grateful to my supervisor, Professor Miao Qian, for his kind instruction, guidance, patience, encouragement and support on my research work. During the four years in his group, I have learned lots of professional knowledge including basic experimental techniques, fundamental principles of organic chemistry and organic electronics and presentation skills. His passion in chemistry, diligence in work and kindness and patience in daily life all set a good example to me. I enjoy the research environment in his lab so much and it is a great honor to be his student.

I have many happy memories shared with my colleagues in this group. Many of my colleagues who were present at the beginning of my Ph.D. are now gone and others have arrived since then. To all of them, Mr. Wei Zhao, Dr. Qin Tang, Dr. Zhixiong Liang, Prof. Zhefeng Li, Prof. Minghua Xie, Dr. Shuaijun Yang, Mr. Xing Zheng, Mr. Jiye Luo, Mr. Hai Xia, Mr. Renxin Mao, Ms. Danqing Liu, Mr. Liang Shan, Ms. Xiaomin Xu, Mr. Xiao Gu and Mr. Kwanyin Cheung, I wish to express my

thanks. They are wonderful coworkers and I appreciate their help and discussion. Without their support and cooperation, I can not conduct my research in the lab.

When I came to CUHK and joined this group at 2009, my colleague, Xing Zheng, help me solve lots of troubles in campus life and my research. I really appreciate his help for the instruction of basic organic synthetic methods. My colleague Dr. Qin Tang, Danqing Liu and Xiaomin Xu also gave me a lot of support in OFET device fabrication and characterization. Special thanks are given to Mr. Renxin Mao for his help in the density functional theory calculations. Thanks are also given to Ms. Hoi-Shan Chan and for single-crystal crystallography and Ms. Hau-Yan Ng in CUHK and David Chik in HKBU for mass spectra measurement.

My research was financially supported by the Research Grant Council of Hong Kong (project number: GRF402508 and CUHK2/CRF/08), Chinese University of Hong Kong (Direct Grant for Research, project No.: 2060370) and the University Grants Committee of the Hong Kong Special Administrative Region, China (Project No.: AoE/P-03/08).

Throughout these years from childhood, the love of my family, particularly, my parents have been of great comfort to me. Finally, I want to give my warm-hearted thanks to all my family members for their selfless love, care, understanding, and support. At the final year of my Ph.D. study, I got married with my eight years lover, Yujie. Ever since high school to the present days, I am very grateful to my wife for her continuous understanding, support and her constant love. Any of my achievement in any aspects will dedicate to my family, to whom I owe everything.

Table of Contents

Chapter 1 Introduction

Acenes, a kind of polycyclic aromatic hydrocarbons (PAHs) with linearly fused benzene rings as shown in Figure 1.1, have been known since 1929. [1] As a representative, pentacene was widely investigated in the last two decades as a leading organic semiconductor for applications in organic field effect transistors (OFETs), and is still a benchmark for newly developed small-molecule p-type organic semiconductors. [2] However, the poor solubility and instability limit the development of pentacene and other large acenes for organic semiconductors. Various substituting groups have been introduced to large acenes (e.g. pentacene, hexacene and heptacene) leading to soluble, stable and well-characterized derivatives of large acenes.[3] Among these substituting groups, triisopropylsilylethynyl (TIPS) groups are the most successful in terms of enhancing solubility, stability and π-π stacking. [4]

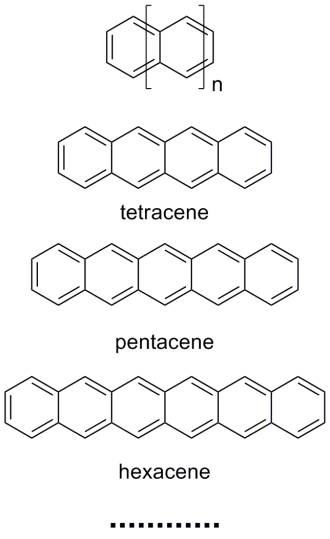

Figure 1.1 Structures of large acenes: tetracene, pentacene, hexacene and so on. (n>2)

Replacing carbon atoms with heteroatoms (i.e., nitrogen) in the backbone of acenes leads to heteroacenes with variable structures, which brings unique opportunity for studying structure-property relationships. When the heteroatom is nitrogen, a combination of varied number, position and valence state of N atoms in N-heteroacenes yields a large number of structurally-related π-backbones with tunable electronic structure, stability, solubility and molecular packing.[5] The following sections review the advances in the area of the large N-heteroacenes, which have four or more linearly fused six-membered rings, in terms of structure, synthesis, molecular packing and their applications as electronic materials.

1.1 Molecular Structures and Syntheses of N-heteroacenes and Their Derivatives

By the strictest definition, N-heteroacenes have only six-member aromatic N-heterocycles (most commonly pyridine and pyrazine rings) fusing with benzene rings. In many cases, strictly defined N-heteroacenes are less stable than their N-hydrogenated derivatives. In extreme cases, some N-heteroacenes have not been synthesized although their dihydro derivatives have been known for decades. In view of this, we consider both strictly defined N-heteroacenes and their N-hydrogenated derivatives as parent N-heteroacenes in this thesis. Unlike acenes, N-heteroacenes can be functionalized by attaching a group either on N atoms or C atoms. In this section, N-heteroacenes and their derivatives are classified in four groups, namely, parent N-heteroacenes, N-substituted N-heteroacene derivatives and C-substituted N-heteroacene derivatives as well as N-heteroquinones. Each group of N-heteroacenes is briefly reviewed in terms of molecular structures and syntheses.

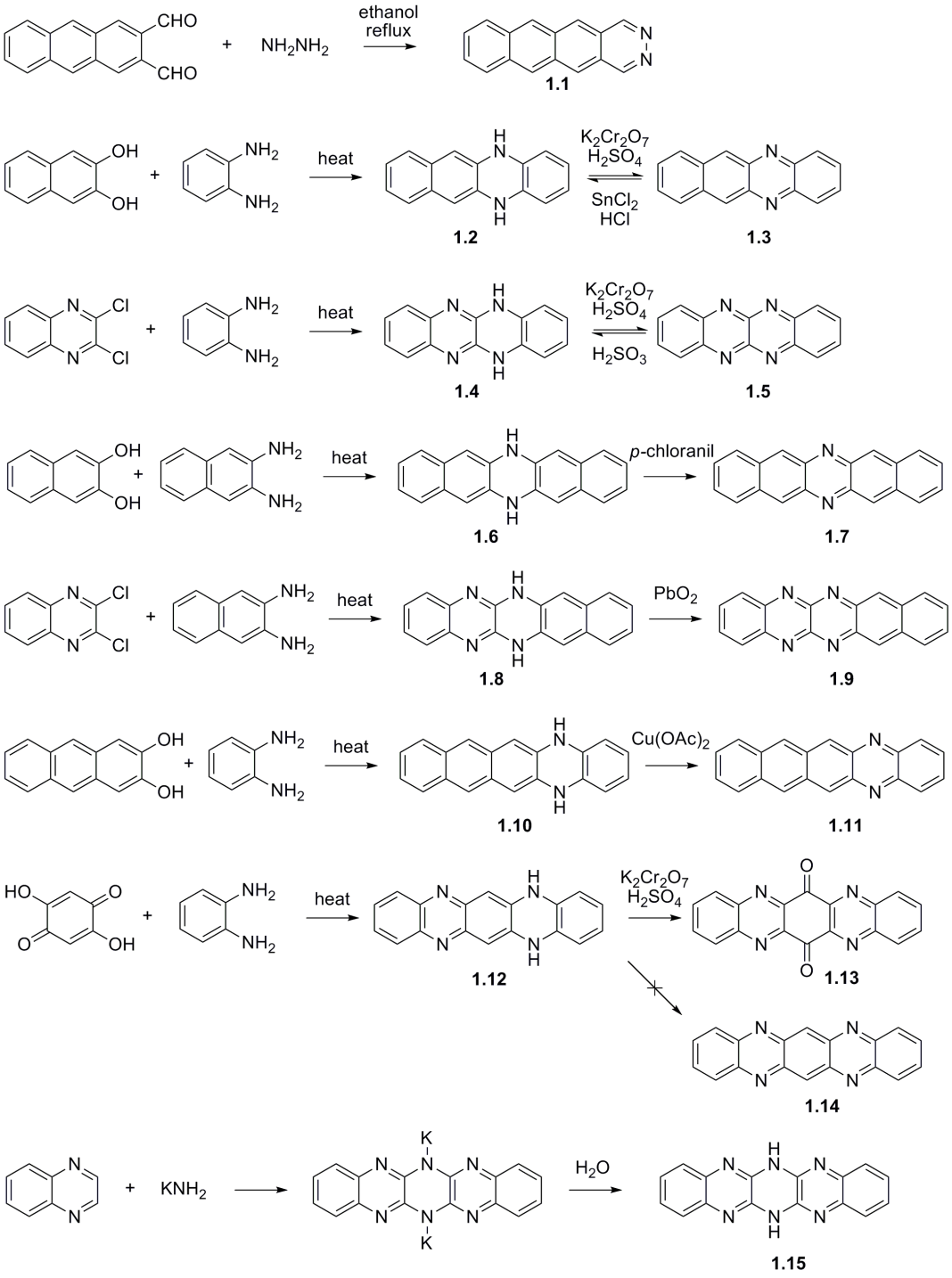

Scheme 1.1 Synthesis of N-heterotetracenes **1.1-1.5** and N-heteropentacenes **1.6-1.15**.

1.1.1 Parent N-heteroacenes

The first group of N-heteroacenes is pyrazinoacenes and their dihydro derivatives, [6] which have pyrazine and dihydropyrazine rings, respectively. In 1901, Hinsberg firstly reported the synthesis of the parent N-heteroacenes **1.2**, **1.4**, **1.6** and **1.8** by simply melting *ortho*-dihydroxynaphthalene or dichloroquinoxaline with *ortho*-phenylenediamine or 2,3-diaminonaphthalene as shown in Scheme 1.1. [7] **1.2** and **1.4** were oxidized by acidic dichromate smoothly, but attempts to oxidize **1.6** and **1.8** by the same method failed to yield **1.7** and **1.9**, respectively. As an isomer of **1.3**, **1.1** was synthesized simply by condensation of *ortho*-dialdehyde-anthracene with hydrazine. [8] In 1967, Kummer and Zimmermann reported azapentacenes **1.7** and **1.9** via oxidation of **1.6** by *p*-chloranil and **1.8** by lead (IV) dioxide, respectively. [9] Interestingly, the dihydrodiazaacenes **(1.2**, **1.4**, **1.6** and **1.8**) exhibit strong green-yellow fluorescence, while the diazaacenes (**1.3**, **1.5**, **1.7** and **1.9**) are almost not fluorescent. In 1951, Badger reported that oxidation of fluorindine **1.12** yielded not the corresponding **1.14** but the quinone **1.13**. [10] In 1966, Leete et al. reported the synthesis of compound **1.10**, an isomer of **1.6**, which was oxidized by copper acetate leading to **1.11**. [11] After 6,13-dihydrohexaazapentacene (**1.15**) was firstly reported and named as fluorubine by Hinsberg in 1903 [12], several patents claimed its derivatives and applications as dyes. [13, 14] In 1931, Ogg reported their synthesis for **1.15** by treating quinoxaline in liquid ammonia followed by carefully hydrolysis. The yellow powder of **1.15** exhibit green fluorescence in a basic solution and red fluorescence in an acid solution. [15]

In 1984, Quast and Schön reported an approach toward 5,7-diazapentacene, an isomer of **1.7** with two pyridine rings,[16] The base-promoted condensation *ortho*-aldehyde-amine with an excess of cyclohexanone resulted in **1.16** in a yield of 73 %, which was dehydrogenated with Pd

on charcoal in a sealed tube at 250 ℃ leading to **1.17.** However, **1.17** was resistant to further dehydrogenation. (Scheme 1.2)

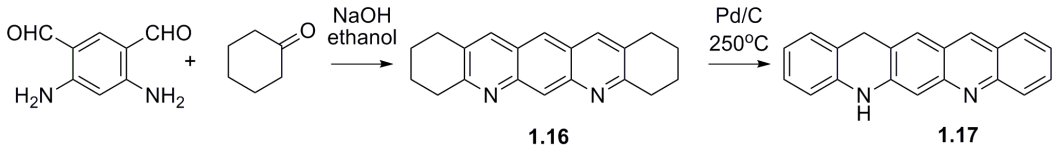

Scheme 1.2 Synthesis of dihydrodiazapentacene **1.17** by Quast and Schön.

1.1.2 Isomerism of N-heteroacenes and N-substituted N-heteroacene Derivatives

Isomerism, an interesting and important phenomenon of N-heteroacenes arises from varying the position of N atoms in the π-backbone and the position of H atoms bonded to N atoms. Specially, the latter type of isomerism is also known as tautomerism involving proton-coupled reactions. For example, fluorindine **1.12,** has three possible isomeric structures, namely, benzenoid (**1.12**), quinonoid (**1.12'**) and zwitterionic (**1.12"**) structures as shown in Figure 1.2.

The quinonoid structure of **1.12** was first proposed in 1951 based on a belief that the absorption near 600 nm is not compatible with the benzenoid structure, [9] which has two nitrogen atoms connecting a phenazine ring and a benzene ring. The true structure of **1.12** is benzenoid structure as first determined in 1987 based on 1H NMR spectroscopy, particularly the AA'XX' patterns for hydrogen on the terminal benzene rings.[17] Unfortunately, **1.12** was often shown as the erroneous quinonoid structure in literatures even until recently.[18] In connection with the debating structures of **1.12**, Miao's group recently found that methylation of **1.12** yielded both benzenoid and quinonoid N-methyl N-heteropentacenes (**1.18** and **1.19**) as shown in Figure 1.2. [19] The complete characterization of **1.18** and **1.19** clearly supported the benzenoid structure of **1.12**.

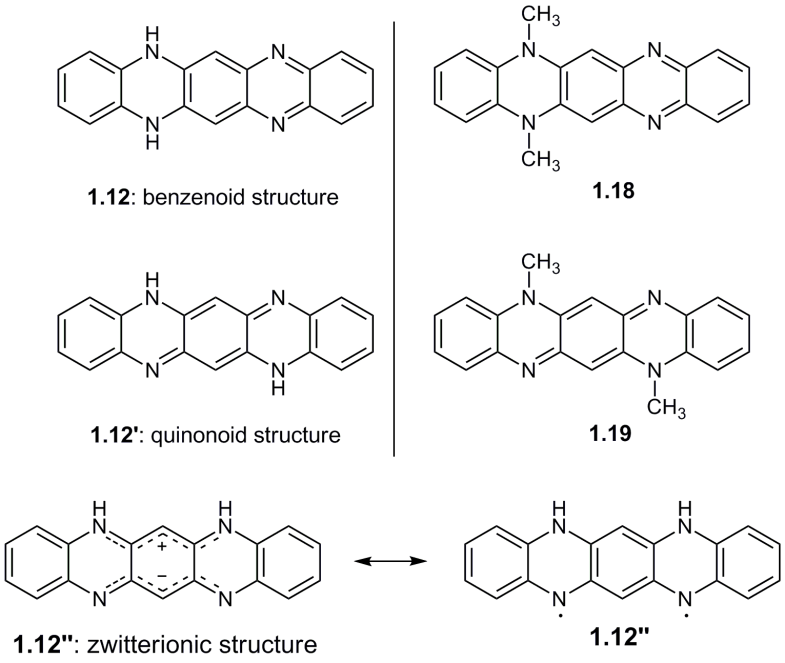

Figure 1.2 Isomeric structures of dihydro-5,7,12,14-tetraazapentacene **1.12** and its methylated derivatives.

In 1999, Wudl et al. prepared zwitterionic isofluorindine **1.20a**, investigating its optical properties as well as protonated species.[20a] The zwitterionic derivative **1.20a** (R = Ph) displays a maximum absorption λ_{max} of 744 nm in ethanol. Upon protonation the maximum absorption λ_{max} is blue-shifted to 660 nm (monoprotonated) and 639 nm (diprotonated). Upon attachment of long alkyl chains, **1.20b** (R=alkyl chain) becomes liquid crystalline.[20b] The optical and liquid crystalline properties allow derivatives of **1.20** to have potential applications in the solid state.

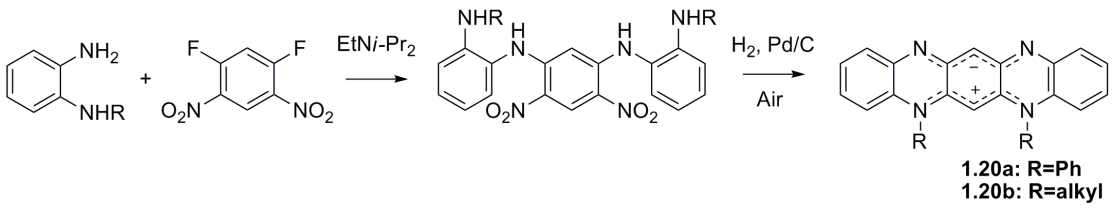

Scheme 1.3 Zwitterionic structures of dihydro-5, 7, 12, 14-tetraazapentacene derivatives.

Recently, Beckert and co-workers developed novel synthesis routes towards fluorubine derivatives. In 2009, they found cationic derivatives of fluorubine (**1.21a-b**) were yielded as a byproduct from reactions of 1,2-diazetines in very poor yield about 1%. A more efficient synthesis route was explored to synthesize the derivatives **1.21c-d** in a high yield. **1.21a-d** are stable crystalline compounds and featured by a strong orange/red fluorescence between 500-600 nm with high fluorescence quantum yield. [21] In 2012, starting from tetrachloropyrazine, Beckert and co-workers synthesized two novel fluorubine derivatives **1.22** and **1.23** in a yield of 3% and 20%, respectively, which had high fluorescence quantum yield and exhibited solvatochromic and acidochromic behaviors. [22]

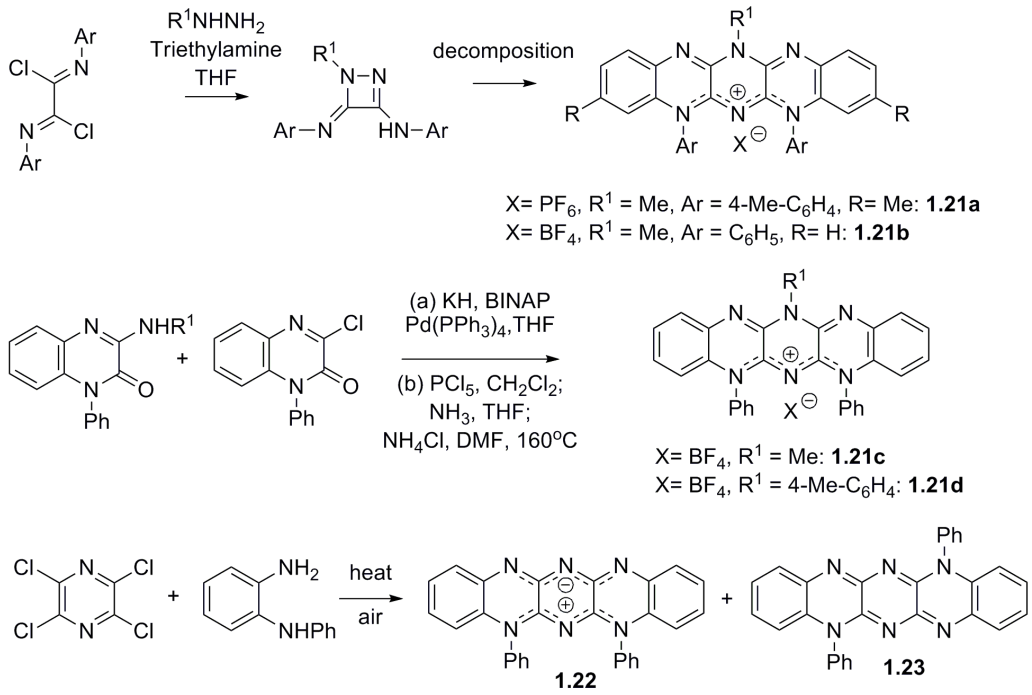

Scheme 1.4 Synthesis of fluorubine derivatives by Beckert.

1.1.3 C-substituted N-heteroacene derivatives

In 2008, Siri et al. synthesized several derivatives of **1.24** by two subsequently condensations.[23] Here, substituents include halides, methyl groups, or carboxylic acids (Scheme 1.5). Tautomerization was observed during synthesis of the carboxylic acid substituted unsymmetrical derivatives. The maximium absorption λ_{max} of **1.24** were relatively broad in a range of 550–600 nm. The cyclic voltammetry of **1.24** exhibited oxidation peaks between –0.14 and 0.01 V vs. ferrocenium/ferrocene.

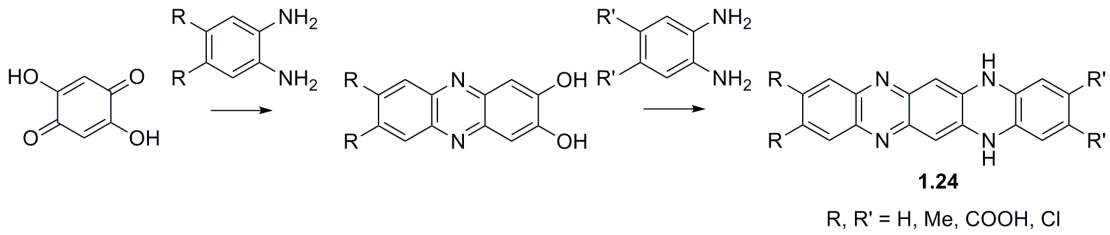

Scheme 1.5 Synthesis derivatives of **1.24** by Siri et al.

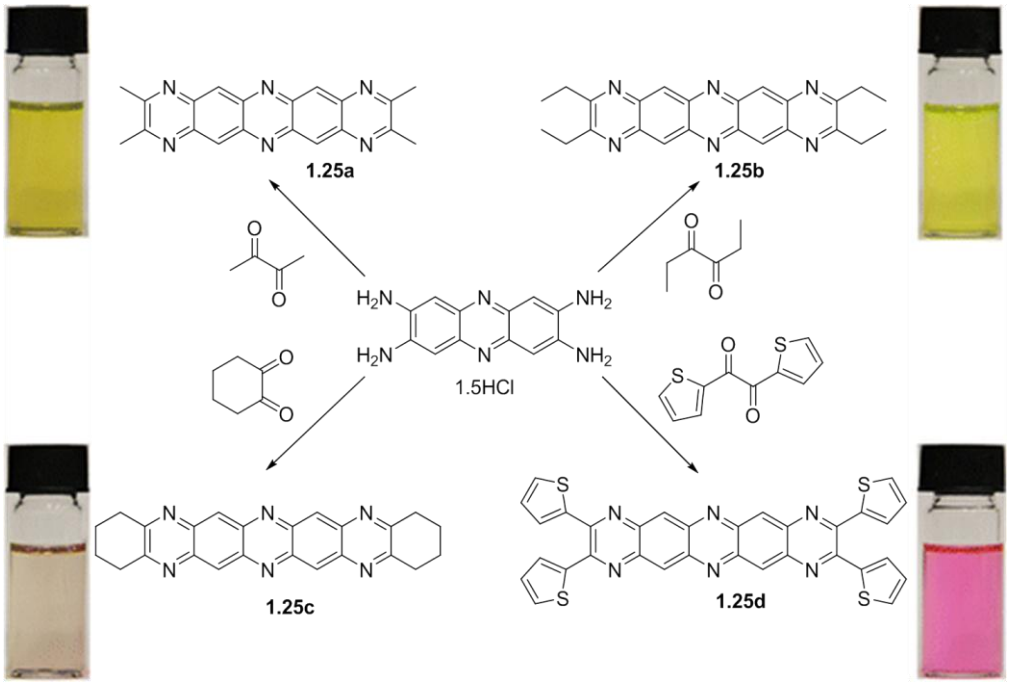

Figure 1.3 Synthesis of hexaazapentacenes and their solutions. (Reprinted from ref. 24 with small modification)

Recently, Zhang et al. completed synthesis of four novel hexazapentacene derivatives (**1.25a-d**) in one step from commercially available starting materials through a condensation reaction between tetraamine and 1, 2-diketones. [24] The observed optical band gaps for **1.25a** to **1.25d** are 2.55, 2.55, 2.45, and 2.25 eV, respectively, in accompany with different color in solutions. (Figure 1.3) The cyclic voltammetry of **1.25a-d** exhibits one revisable reduction wave. The density function theory (DFT) calculated band gaps of **1.25a-d** are 2.41, 2.41, 2.34, and 2.15 eV, respectively, which are close to the experimental results.

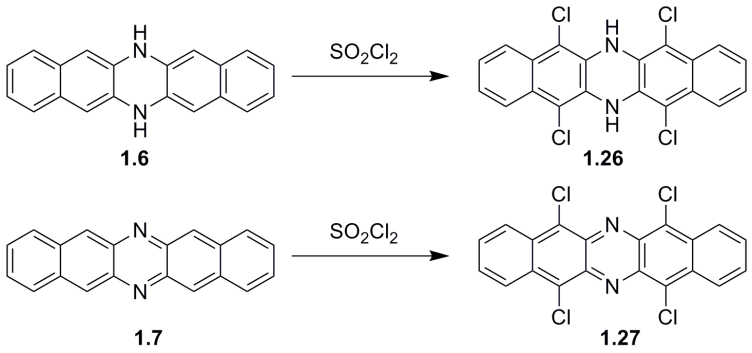

Scheme 1.6 Chlorination of **1.6** and **1.7** by sulfuryl chloride.

In order to fine tune LUMO energy level and molecular packing with chlorine substituent, [25] **1.6** and **1.7** were chlorinated by SO_2Cl_2 to give the tetrachlorinated species **1.26** and **1.27**, respectively (Scheme 1.6). [26] This is a rare example for direct halogen-substituting reaction on N-heteroacenes backbone. Although there are some other halogenated N-heteroacenes, most of halogen atoms were introduced through halogen-containing starting materials.

Following the successful synthesis of trialkylsilylethynylated pentacenes, [27] hexacenes [28] and heptacenes,[29] trialkylsilylethynyl groups were also introduced to N-heteroacenes in 2006 by Bunz. The silylethynyl substituents are found useful in enhancing solubility and stability as well as tuning molecular packing. As a representative, bis(triisopropylsilylethynyl)-

tetraazapentacene (TIPS-TAP) **1.28** was firstly synthesized in 2009 by Bunz's group and modified recently by Miao's group. [30] The reaction condition was found of crucial importance to the reduction of diol precursors in terms of the yield and purity of products. Using NaH_2PO_2-KI-CF_3COOH-CH_3COOH as the reducing condition, Bunz et al. synthesized **1.28** in a low yield of 13% from **1.13**. (Scheme 1.7) Moreover, it was later found that the compound **1.28** as prepared exactly following Bunz's procedure exhibited lower field effect mobility (about 0.1 $cm^2\ V^{-1}s^{-1}$) possibly because of its lower purity. Instead of lithium reagent, Grignard reagent was used for nucleophilic addition followed reduction by $SnCl_2$-HCl and yield was increased to about 40%. Now TIPS-TAP can be synthesized in gram scale, with good purity for application in organic thin film transistors. Together with these works, significant progresses in the synthesis and semiconductor property evaluation of silylethynylated N-heteroacenes have been made since 2009.[5] Synthetic methods for silylethynylated N-heteroacenes have been systematically studied and are detailed in Section 1.2.

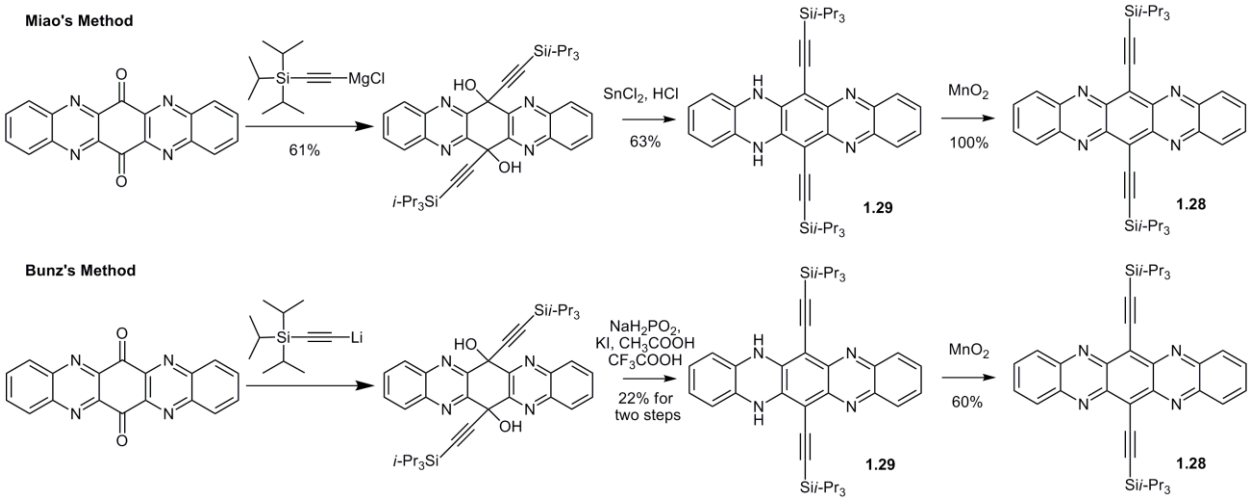

Scheme 1.7 Synthesis of the tetraazapentacene derivatives **1.28** and **1.29** by Miao and Bunz.

1.1.4 N-heteroacenequinones

N-heteroacenequinones are oxidation products of N-heteroacenes. Shown in Scheme 1.8 is the synthesis of N-heteropentacenequinones in two ways. The synthesis of **1.30** and **1.31** was achieved by using Diels-Alder reaction, in which the dienophile was the corresponding quinone and the diene was generated in situ from α, α, α', α'-tetrabromo-*ortho*-dimethylpyrazine at Cava's condition,[31] followed by elimination of HBr. **1.32** and **1.13** were prepared by oxidizing the corresponding dihydro-N-heteropentacenes with dichromate in acidic condition. The low yield of **1.32** was mainly attributed to the lost during separation from its isomer, 7,12-diaza-5,14-pentacenequinone. Most of the quinones are yellow crystalline powders, which appear stable to ambient air and light and do not decompose even heating up to 300 ℃.[32] With electron-withdrawing moieties of both quinone and pyrazine, N-heteroacenequinones have low LUMO energy levels and are found as n-type organic semiconductors in thin film transistors.[32]

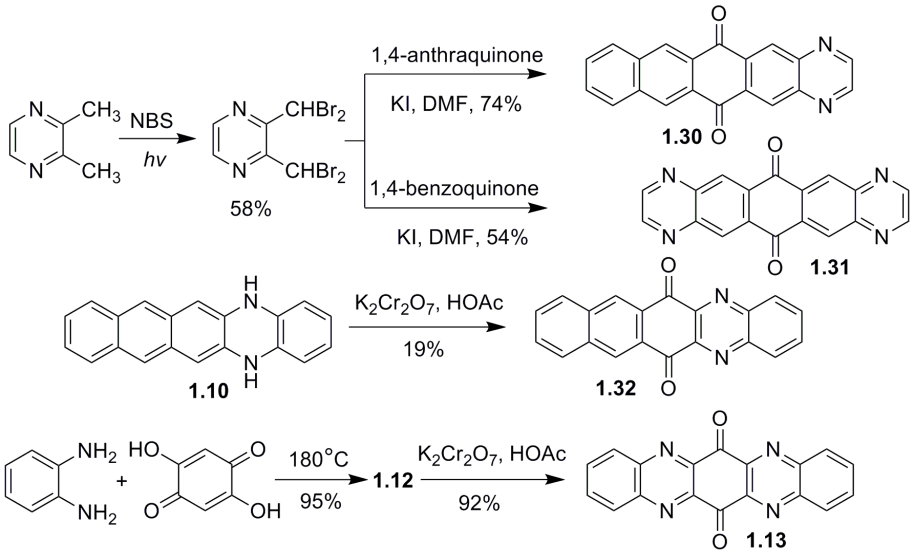

Scheme 1.8 Synthesis of N-heteropentacenequinones.

1.1.5 N-heteroarenes that were reported as N-heteroacenes

Besides substitution on N atoms and C atoms, the backbone of an N-heteroacene can be expanded by fusing with benzene rings. Some of these examples are shown in Figure 1.4. Although these compounds were usually reported as N-heteroacenes, they by a strict definition are not N-heteroacenes in view of Clar's aromatic sextet and electronic structures. For example, Hill and Mateo-Alonso studied pyrene-fused and phenanthrene-fused N-heteroacenes. [33] By combining N-alkylation and ring fusing, Hill and coworkers accomplished N-heteroacene derivatives that self-assembled into nanotubes as well as other nano-structures. These molecules should be more precisely named as N-heteroarenes, and thus are not further discussed them in this thesis. [34]

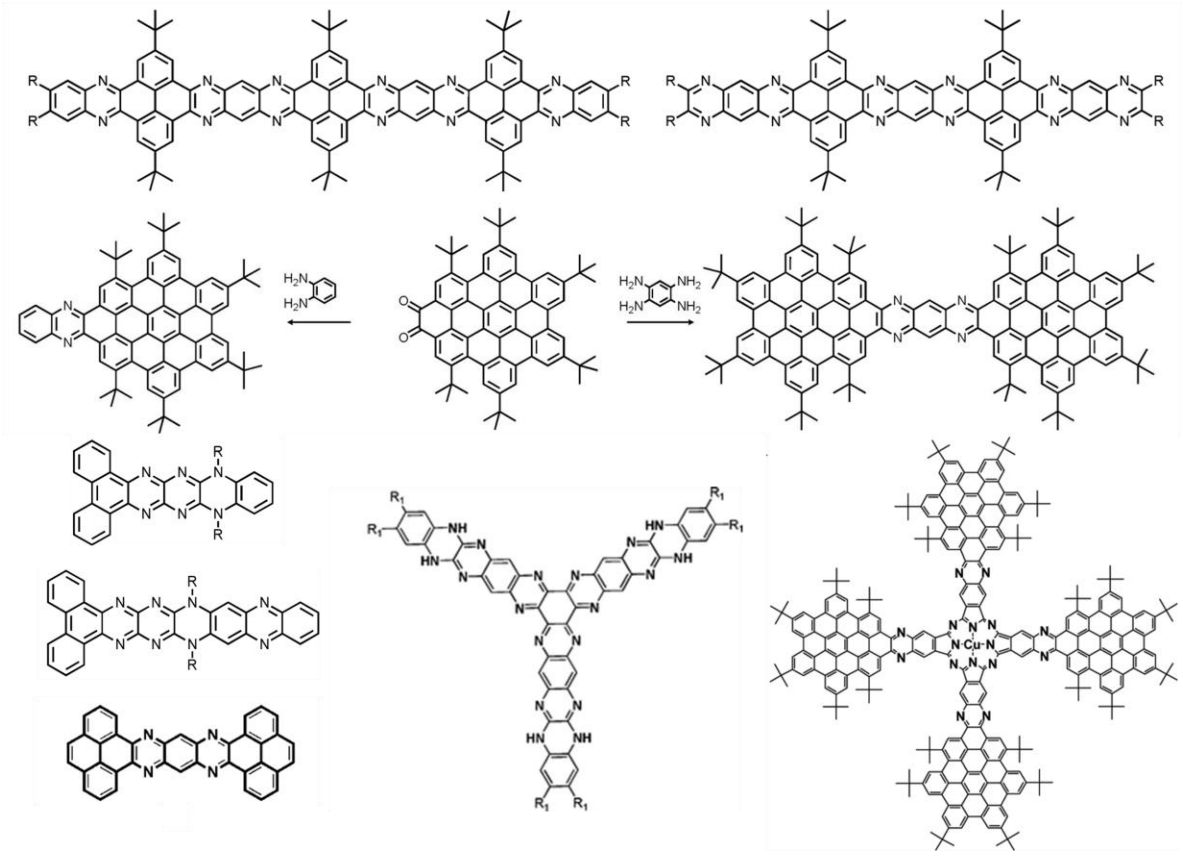

Figure 1.4 Examples N-heteroarenes.

1.2 General Synthetic Methods for Silylethynylated N-heteroacenes

Silylethynylated N-heteroacenes, which are the most successful subgroup of N-heteroacene derivatives for applications in organic electronic devices, have been synthesized with different methods as discussed below.

1.2.1 Direct Condensation

The oldest route to synthesize pyrazine-containing N-heteroacenes is the condensation of *ortho*-quinones or *ortho*-dihydroxyarenes with *ortho*-diamines. Although this method led to several silylethynylated N-heteroacenes, such as **1.33a-c**, **1.34a-c** and **1.35,** the yield became lower when the substituent got larger and π-backbone got more electron-deficient. [35]

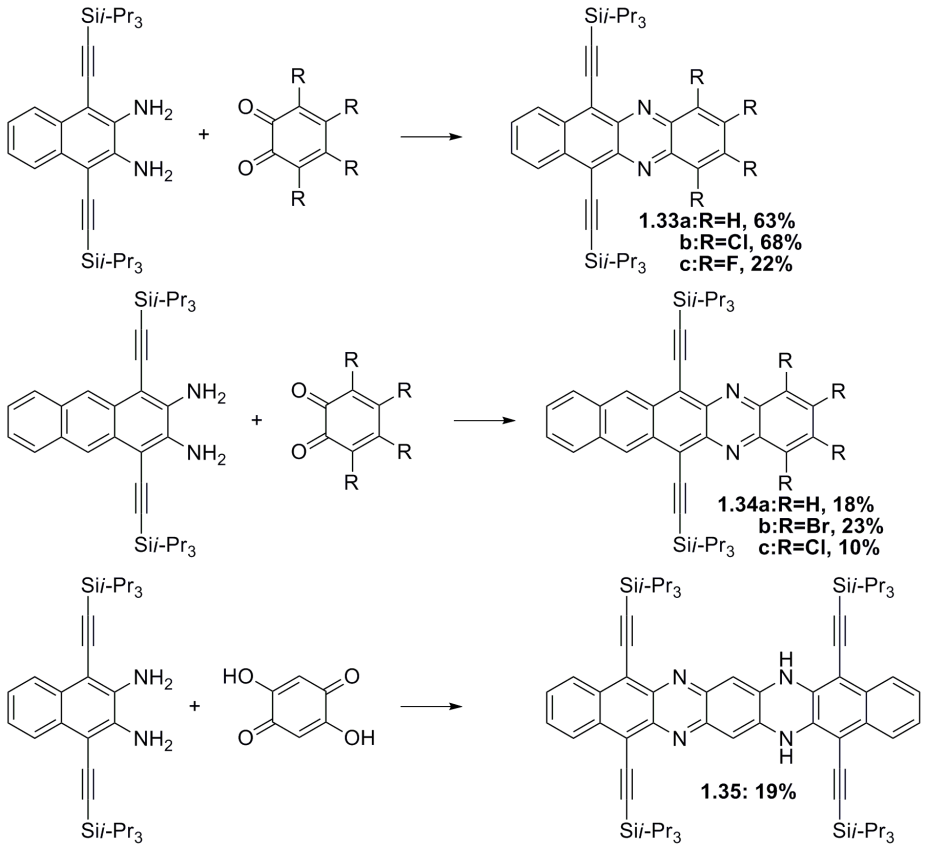

Scheme 1.9 Examples of N-heteroacenes synthesized by direct condensation method.

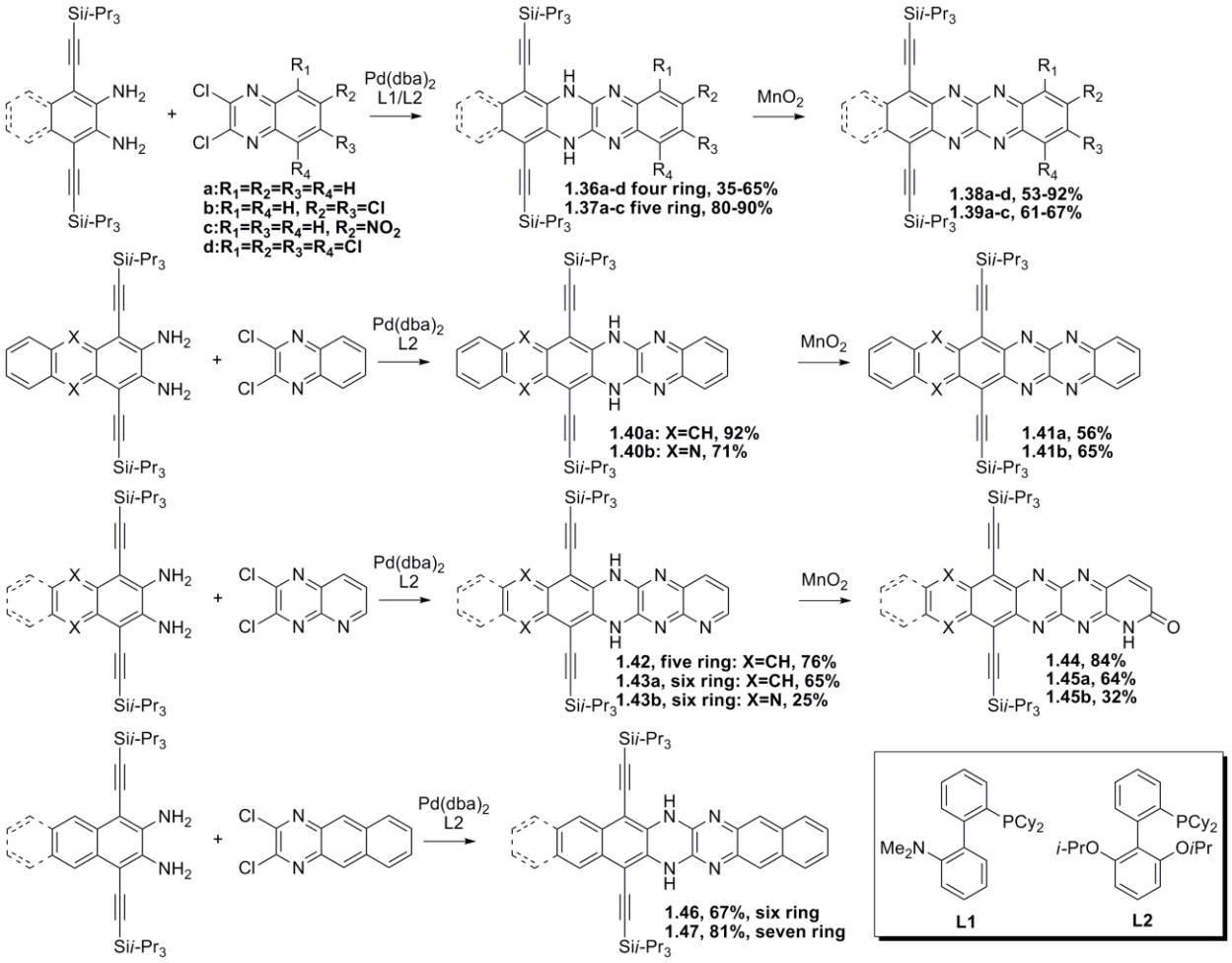

Scheme 1.10 Examples for synthesis of N-heteroacenes with Pd-catalyzed coupling reactions.

1.2.2 Pd-Catalyzed Coupling

Benefiting from palladium catalyzed methods for C-N bond formation developed by Buchwald and Hartwig (**Buchwald–Hartwig Amination**),[36] derivatives of large N-heteroacenes with four to six N atoms in the aromatic backbone can be synthesized by Pd-catalyzed coupling. In 2011, by choosing the suitable catalyst ($Pd(dba)_2$), ligand (L1 and L2) and base (Hünig base), Bunz successfully synthesized **1.37a–c** from *ortho*-amines and the reactive dichloroquinoxalines, in good to excellent yields (Scheme 1.10).[37] This novel protocol was quickly found as a powerful method to synthesize silylethynylated dihydro-N-heteroacenes, leading to numbers of N-

heteroacenes such as tetraazatetracenes **1.38a-d**, [35] tetraazapentacenes **1.39a-c**, [37] tetraazahexacene **1.41a**, [38] hexaazahexacene **1.41b**, [38] dihydropentaazapentacene **1.42** [39] dihydro-pentaazahexacene **1.43a**, [39] dihydro-heptaazapentacene **1.43b**, [39] dihydro-tetraazahexacene **1.46**, [40] dihydro-tetraazaheptacene **1.47**. [40] With these compounds available, new reactions such as oxidation to pyridines, [39] spontaneous reduction [38] and addition of oxalic dichloride [40] were found for silylethynylated N-heteroacenes.

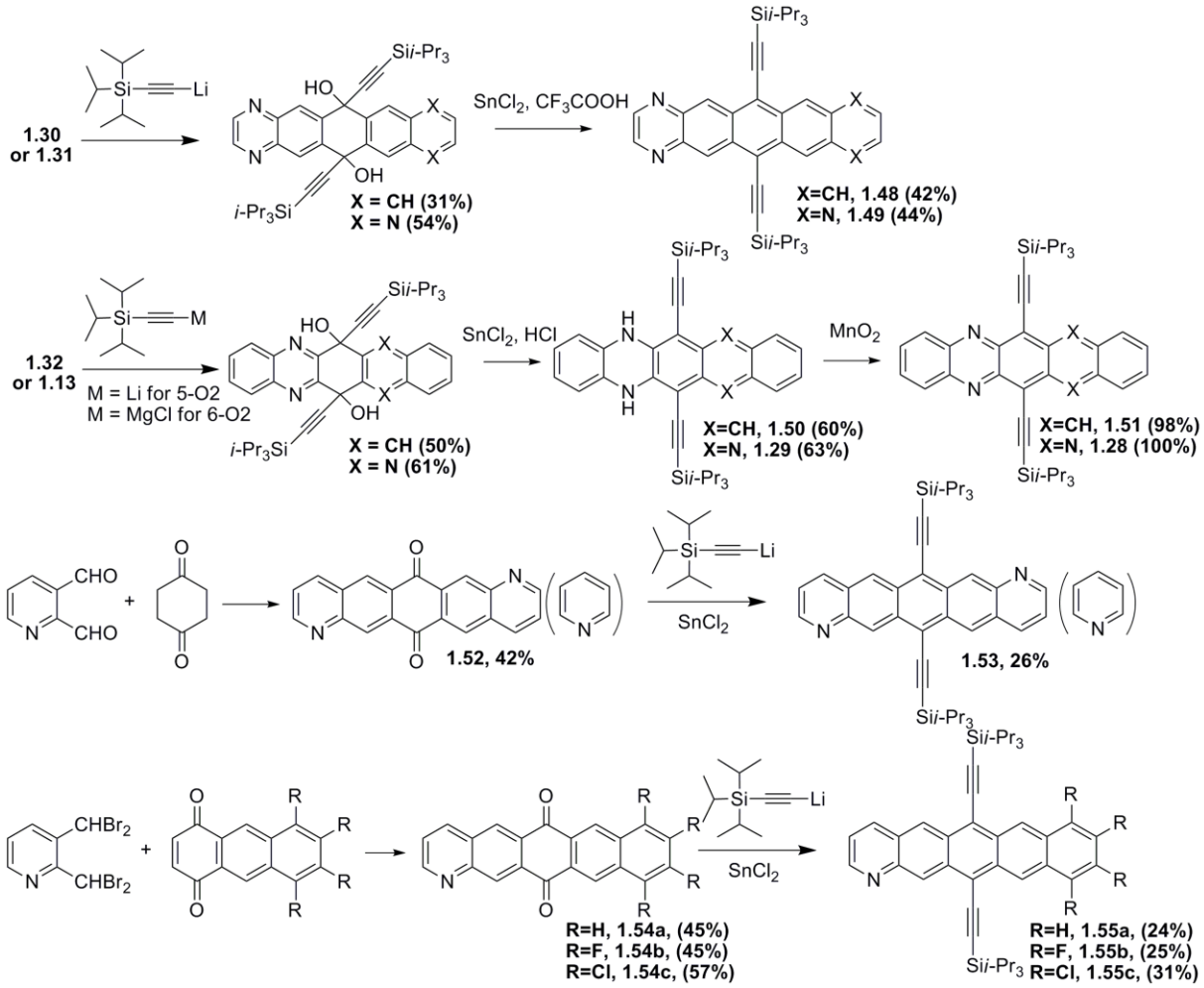

Scheme 1.11 Examples of N-heteroacenes synthesized from N-heteroacenequinones.

1.2.3 Synthesis from N-heteroacenequinones

Another useful and general approach to silylethynylated N-heteroacenes is adapted from Anthony's synthesis of silylethynylated pentacenes. [41] In this method, N-heteroacenequinones are first reacted with silylethynyllithium or silylethynylmagnesium reagents, and resulting diols (isolated or not isolated) are reduced with $SnCl_2$ or KI/Na_2HPO_2 in acid yielding the corresponding silylethynylated N-heteroacenes. With this method, dihydro-tetraazapentacene **1.29**, [30] tetraazapentacene **1.28**, [30] diazapentacene **1.48**, [42] tetraazapentacene **1.49**, [42] dihydro-diazapentacene **1.50**, [43] diazapentacene **1.51**, [43] diazapentacene **1.53** [44] and azapentacene **1.55a-c** [44] were synthesized in moderate to poor yields.

1.3 Molecular Packing of N-heteroacenes

1.3.1 Parent N-Heteroacenes

Very few single crystal structures were got for parent N-heteroacenes possibly because of the poor solubility of these compounds.

Red single crystals of **1.3** qualified for single crystal X-ray crystallography were obtained from solution in DMSO under ambient conditions. Initial attempts to crystallize **1.2** at the same conditions gave red single crystals identical to that of **1.3**. Finally, when crystallized from DMF in a dry box under absence of air, **1.2** was found to produce yellow platelet single crystals. [45] Both **1.2** and **1.3** are nearly planar as shown in Figure 1.5a. As the CH and NH groups are of similar size, the molecules of **1.2** pack as if they possess an inversion center (Figure 1.5a). As shown in Figure 1.5b, **1.3** displays a herringbone packing. In contrast, **1.2** exhibits a face-to-edge arrangement, in which the face to face (cofacial) π-π stacking is absent (as shown in Figure 1.5c).

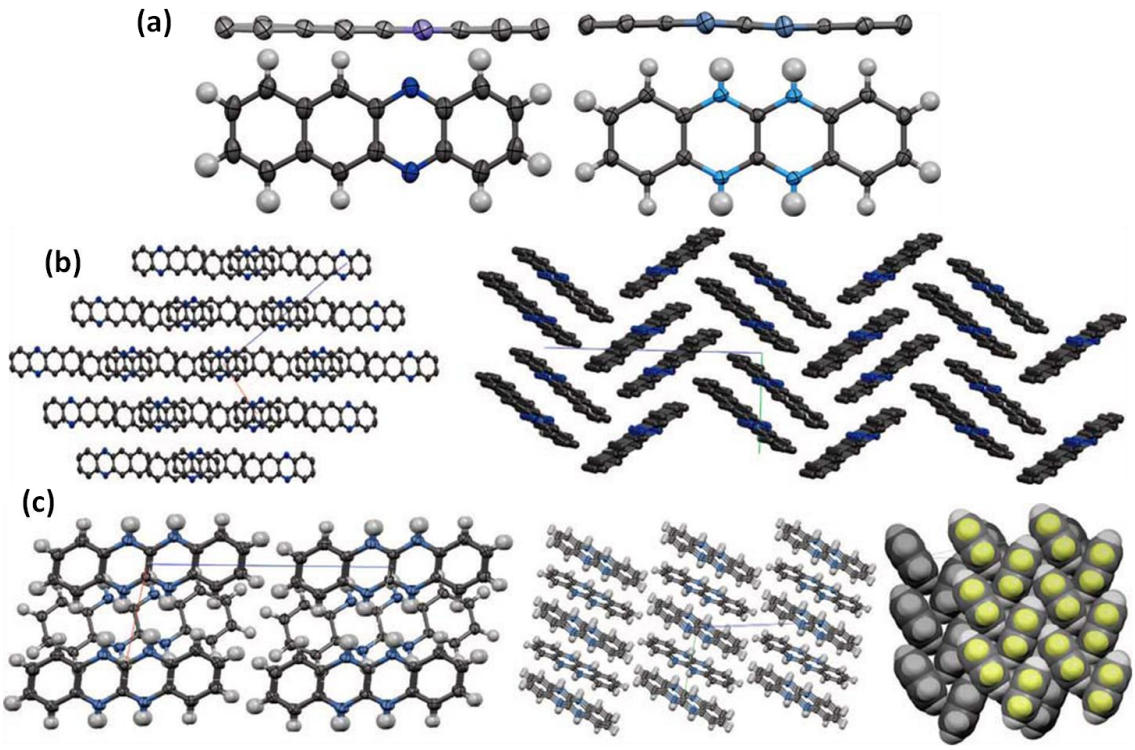

Figure 1.5 (a) Molecular structures of **1.3** (left) and of **1.2** (right). The top view displays the planarity of both **1.2** and **1.3**. The four powder blue colored positions in **1.2** contain overall two nitrogen atoms in either the 5,12- or the 6,11-position as a consequence of the disorder of **1.2**, where it can take on two different orientations. (b) Packing of **1.3**. View along the *b*-axis (left) and along the *a*-axis (right). (c) Packing of **1.2**. View along the *b*-axis (left) and along the *a*-axis (middle). View along the diagonal of the crystallographic *b*- and *c*-axes (right). (Copied from ref. 45 with modification)

Single crystals of **1.6** qualified for single crystal X-ray crystallography were obtained from solution in DMF or benzophenone. [46] In the crystal growing from DMF, the N-Hs of **1.6** form a hydrogen bond with molecules of DMF as shown in Figure 1.6a. In the crystal growing from benzophenone, which cannot form hydrogen bonds, the crystal structure of **1.6** changes to a herringbone arrangement which is a characteristic packing motif for pentacene and other electron rich π-systems, with four rings overlapped between neighboring molecules in the crystal as shown in Figure 1.6d. [47]

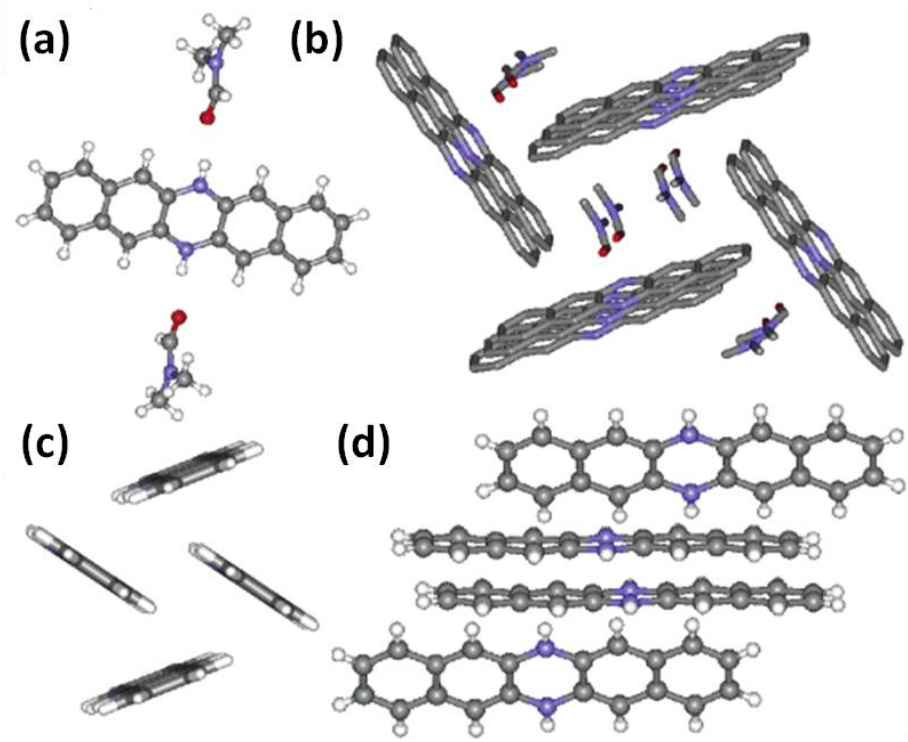

Figure 1.6 (a) Crystal structure of **1.6** from DMF showing two hydrogen bonds to DMF; (b) channels through the crystals. (c) Crystal structure of **1.6** from hot benzophenone showing a herringbone arrangement motif; (d) View of the crystal lattice showing slipping. (For the models: gray atoms are carbon, blue atoms are nitrogen, white atoms are hydrogen and red atoms are oxygen. Reprinted from ref. 47 with modification)

1.3.2 N-substituted N-heteroacenes derivatives

Because substituting NH groups in N-heteroacenes with varied groups generally increases solubility, it becomes easier to grow single crystals of these compounds from solution leading to the reported crystal structures. As shown in Figure 1.7, backbone of **1.18** bends at the methylated nitrogen atoms position with a bending angle of 160 °while **1.12** is essentially planar. Molecules of **1.18** form one dimensional stacks with the phenazine planes separated by 3.51 Å. Interestingly, the crystal lattice of **1.19** is found to contain water molecules which form H-bonds chain with unsubstituted N atoms of molecules **1.19** which are flat and stack with a π-to-π distance of 3.42 Å as shown in Figure 1.7c. [19] The crystal structure of compound **1.20a** shows

that the molecule is essentially planar. The molecules pack in a staggered sheet type structure which consist dimmers of **1.20a** by aligning the heterocyclic backbone face to face with a π-to-π distance of 3.58 Å and the phenyl groups facing in opposing directions. [20]

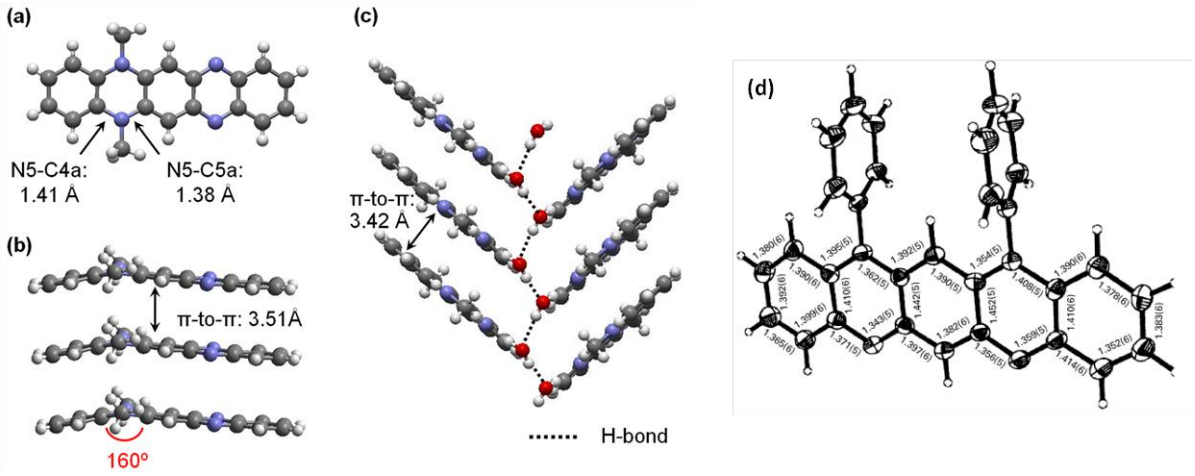

Figure 1.7 Crystal structures of **1.18**, **1.19** and **1.20**: (a) a single molecule of **1.18** with bond lengths highlighted; (b) π-stacks and the bending angle of **1.18**; (c) H-bonded chain of water molecules between two π-stacks of **1.19**. (d) a single molecule of **1.20** with bond lengths. (Reprinted from ref. 19 and ref. 20 with modification)

As shown in Figure 1.8a-b, the molecular plane of fluorubine backbone **1.21a** is nearly planar and the methyl group at N3 position is slightly twisted out of the face by approximately 10 °. Due to π-π interactions between the fluorubine cores, the molecules of **1.21a** form face-to-face packed dimers in the crystal lattice which were connected by two hexafluorophosphate anions to build up "molecular wires". [21] From solutions in mixed chloroform and methanol, Beckert obtained crystals of **1.22** and **1.23,** which contain solvent (chloroform) molecules in the lattice. Very similarly, as shown in Figure 1.8c-d, phenyl substituents of 1.22 are nearly perpendicular to the slightly twisted hexaazapentacene plane. Due to strong π-π interactions, the mesoionic derivative **1.22** forms face-to-face stacked dimmers, which themselves build highly symmetric molecular arrangements in the solid state.

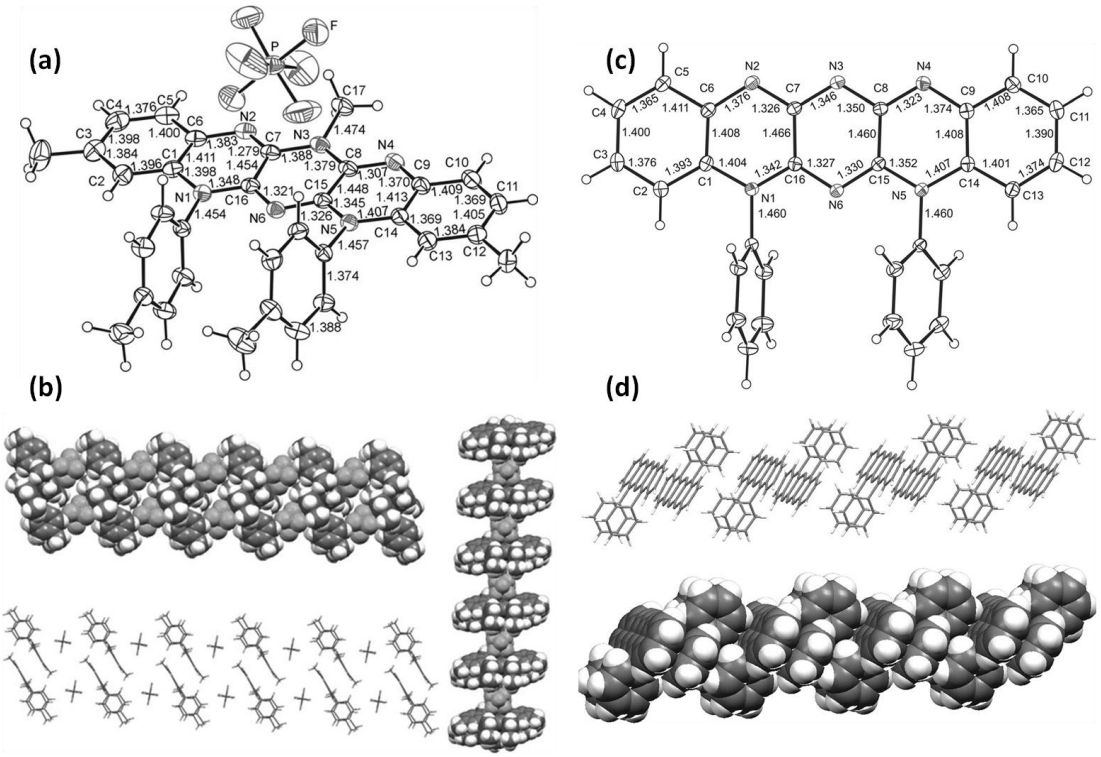

Figure 1.8 (a) Solid-state structure and bond lengths of the cationic fluorubine derivative **1.21a** (Ar=4-Me-C_6H_4, R=Me, X=PF_6). (b) Packing effects of the crystal lattice of the fluorubine derivative **1.21a**. (c) ORTEP plot of the molecular structure of the mesoionic fluorubine **1.22**. (d) The solid-state packing of the mesoionic fluorubine **1.22**. (50% probability ellipsoids, the co-crystallised chloroform molecules are omitted for clarity.) (Reprinted from ref. 21 and ref. 22 with modification)

1.3.3 C-substituted N-heteroacenes derivatives

Needle like single crystals of tetrachloro-diazapentacene **1.27** were obtained by the physical vapor transport method, while single crystals of tetrachloro-dihydrodiazapentacene **1.26** were obtained by sublimation under vacuum to avoid decomposition at higher temperature. Figure 1.9 shows their molecular packing: both compounds give a shifted π-π stacking rather than the herringbone arrangement motif in the presence of chlorine atoms, with π-π distances of 3.45 Å and 3.37 Å for **1.26** and **1.27**, respectively. The distances between adjacent chlorine atoms are in the range of 3.66-4.05 Å. [26]

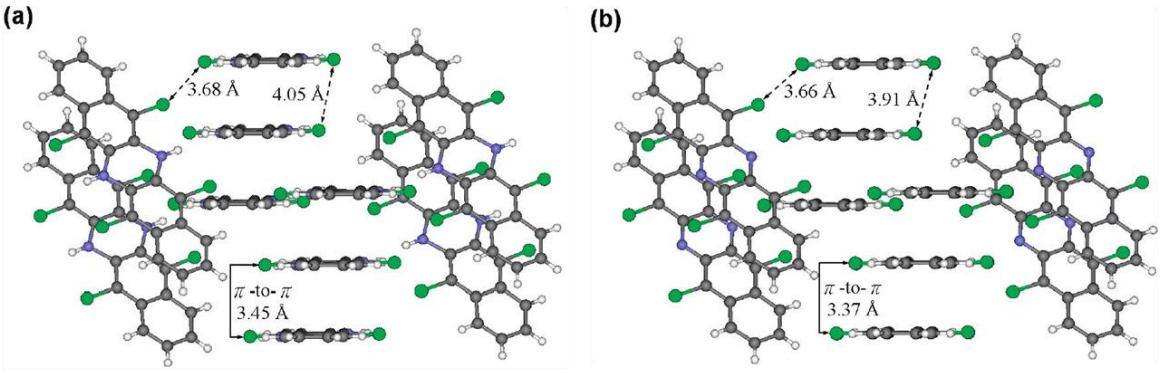

1.26 **1.27**

Figure 1.9 Molecular packing of **1.26** and **1.27**. (Reprinted from ref. 26 with small modification)

Silylethynylated N-heteroacenes exhibit different packing motifs depending on both the influence of trialkylsilyl groups and the nature of N-heteroacenes backbones.[30, 35-44] Most of triisopropylsilylethynylated N-heteropentacenes exhibit two dimension π-π stacking with a brickwork arrangement as shown in Figure 1.10a, which is also characteristic for packing of 6,13-bis(triisopropylsilylethynyl)-pentacene. This common molecular packing suggests the bulky triisopropylsilyl ethynyl groups play a key role in determining molecular packing and is adapted by many N-heteroacene molecules discussed in this chapter, such as **1.33a-c**, **1.35**, **1.39a**, **1.41a**, **1.44**, **1.48**, **1.51**, **1.53**, **1.55a-c** and so on. When the structure symmetry is broken, the molecular packing changes to the one dimensional π-stacking as observed in the crystal structure of **1.29**, **1.33c** and **1.39b**, possibly because of the difference of charge distribution or the shift of substitution position. With two pyrazine rings not shielded by the bulky triisopropyl groups, **1.49** exhibits a totally different packing mode. As shown in Figure 1.10c-d, molecules of **1.49** are first linked by double weak C-H···N hydrogen bonds to form a ribbon-like structure, and two H-bonded ribbons then form the bilayer π-π stacks in a herringbone motif.

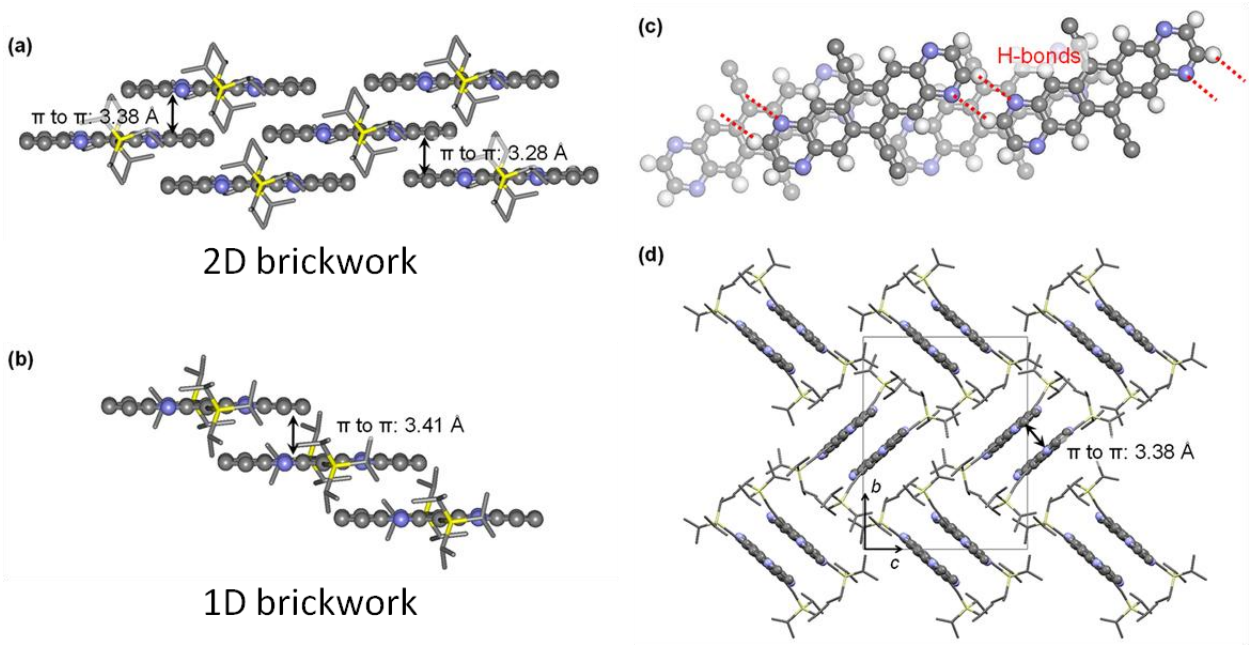

Figure 1.10 Molecular packing of **1.28**, **1.29**, and **1.49**: (a) π-stacks of **1.28** with 2D brickwork arrangement; (b) 1D stacks of **1.29**; (c) bilayer π-stacks of **1.49** showing weak C-H···N hydrogen bonds; (d) side view of bilayer π-stacks of **1.49** showing unit cell. (Reprinted from ref. 42)

1.3.4 N-heteroacenequinones

Because N-heteroacenequinones have poor solubility, the single crystals of N-heteroacenequinones were grown by the physical vapor transport technique. X-ray crystallographic analysis has revealed that the molecular packing of both **1.31** and **1.13** features unusual quadruple weak hydrogen bonds and π-π stacking as shown in Figure 1.11. Molecules of **1.13** form infinite one dimensional stack with a π-π distance of 3.39 Å. The neighboring stacks are linked by quadruple weak C-H ··N/O hydrogen bonds in a self-complementary ADAD-DADA pattern (D is hydrogen donor and A is hydrogen acceptor). Molecules of **1.31** form infinite stack in two directions with a π-π distance of 3.32 Å and quadruple weak C-H ··N/O DDAA-AADD hydrogen bonds pattern. [32] Miao and co-workers suggested that weak hydrogen

bonds between neighboring stacks and close π-π stacking lead to dense molecular packing which are expected to favor charge transport by enhancing orbital overlap.

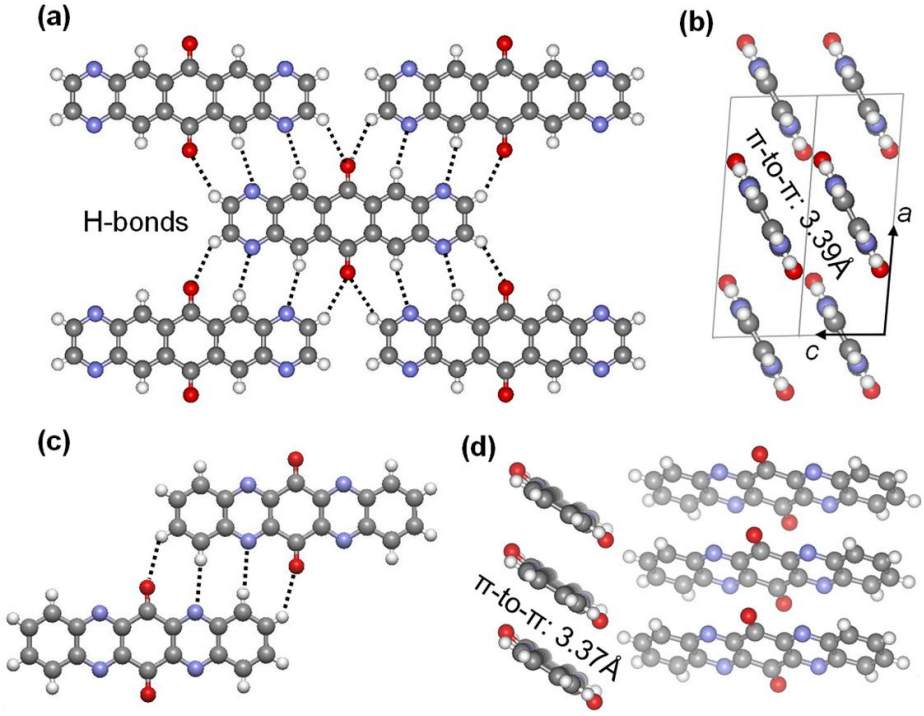

Figure 1.11 Crystal structures of **1.13** and **1.31**: (a) weak C-H···O/N hydrogen bonds (shown with dashed lines) between molecules of **1.13**; (b) π-π stacks of **1.13** as viewed along the *b* axis of unit cell; (c) weak C-H···O/N hydrogen bonds (shown with dashed lines) between two molecules of **1.31**; (d) π-π stacks of **1.31** viewed in two directions. (Reprinted from ref. 32)

1.4 N-heteroacenes as Electronic Materials: Computational and Experimental Studies

1.4.1 Organic Field Effect Transistors (OFETs)

Many N-heteroacenes have been found to function as organic semiconductors in organic field effect transistors (OFETs), which are elemental units of organic electronic circuits for varied applications such as flexible displays, radio-frequency identification tags and sensors.[48] A typical OFET consists of a layer of organic semiconductor, a dielectric layer and three electrodes (gate, drain and source) as shown in Figure 1.12. Organic semiconductors used in

OFETs are commonly classified as p-type (hole-transporting) and n-type (electron-transporting) depending on type of charge carrier (hole or electrons).[49] OFETs that have p-type organic semiconductors to transport holes are p-channel OFETs, while those have n-type organic semiconductors to transport electrons are n-channel OFETs.

OFETs that have a thin film of organic semiconductor as the active channel is also known as organic thin film transistors (OTFTs). When no gate voltage is applied (V_G=0), the OFET is in its "off" state with ideally no or practically a very low source-drain current (I_{DS}) at a source-drain bias (V_D). When a sufficiently high voltage (V_G is higher than the so-called ‘‘threshold voltage’’) is applied on the gate, mobile charge carriers are accumulated at the interface between the semiconductor and dielectric layer and the OFET is switched to its "on" state with a high source-drain current at a source-drain bias V_D. In this way, an OFET acts as an on/off switch. The key parameters for characterizing OFETs are the field effect mobility (μ_{FET}), threshold voltage (V_{th}) and *on/off* ratio. For practical applications, OFETs require high field effect mobility, which allows fast switching, high *on/off* ratio and relative low threshold voltage.[50]

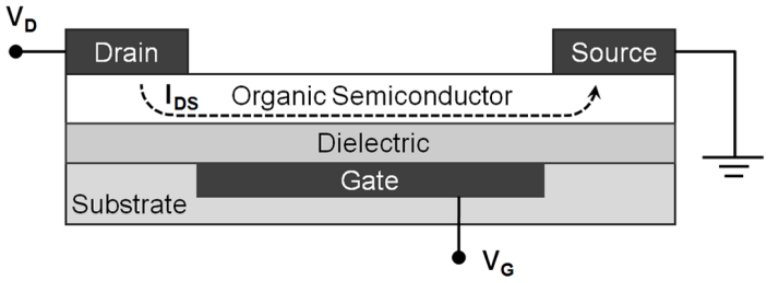

Figure 1.12 Schematic structure of an OFET (top contact and bottom gate) showing applied voltage (V_D and V_G) and source-drain current (I_{DS}). (Reprinted from ref. 5c)

To design high-performance organic semiconductors for OFETs, one need to consider both electronic structure and molecular packing, which are two basic factors for the molecules themselves to determine the performance of organic semiconductors.[51]

1.4.2 Computational studies

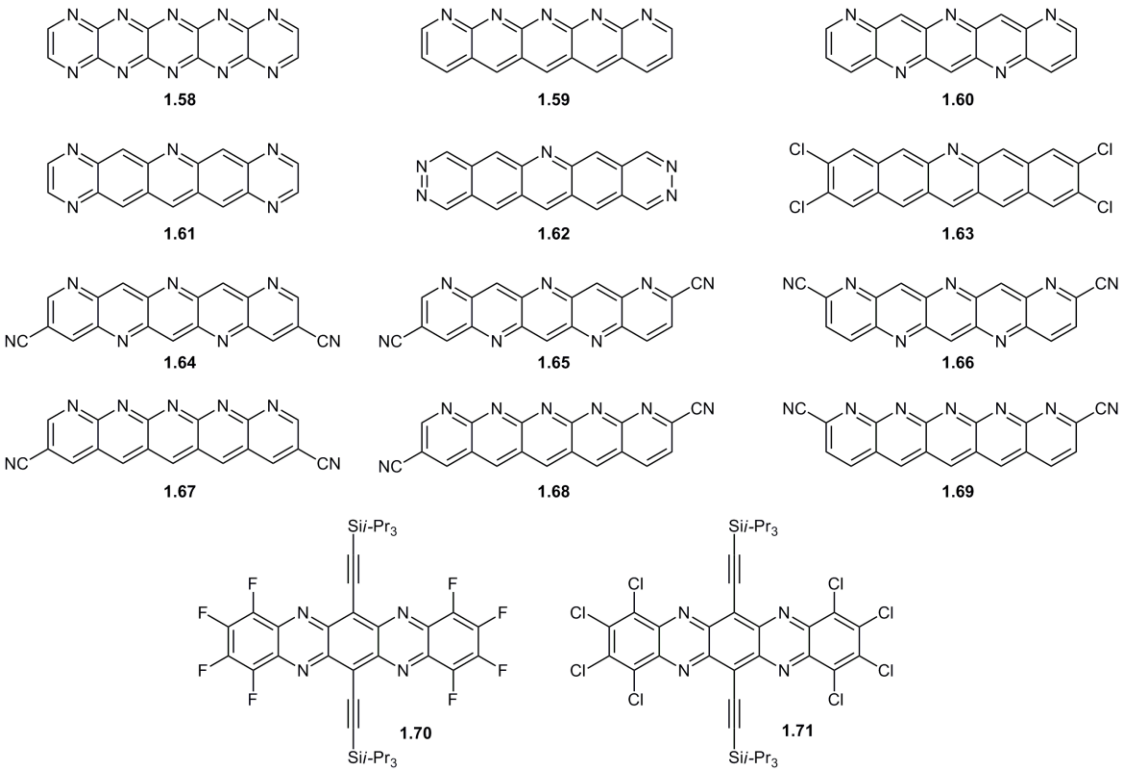

Figure 1.13 Theoretical studies of promising N-heteropentacenes derivatives for semiconductor materials by Chao, Houk and Kou.

In 2006, Chen and Chao firstly introduced series of N-heteropentacenes **1.58-1.63** (Figure 1.13) as potentially materials for n-type organic semiconductors.[52] All of these compounds show small reorganization energies (0.15–0.2 eV) and attractive electron affinity. Later on, Winkler and Houk extended the series and investigated other N-heteropentacenes more deeply.[53] By attaching nitrile substituent, they found CN-N-heteropentacenes **1.64-1.69** could

have lower LUMO energy levels and self-assembly behaviors in their solid states. The calculated reorganization energies values range between 0.13 and 0.15 eV, which are smaller than those calculated by Chen and Chao. Besides, Kuo and co-workers calculated the electron affinities and reorganization energies for a series of silylethynylated N-heteropentacenes, predicting that octafluoro- and octachloro- tetraazapentacenes (**1.70**-**1.71**) would be two very attractive n-type organic semicondcutor materials because of their low reorganization energies and large charge transfer integrals. [54]

On the basis of recent experimental studies, Ren and co-workers systematically investigated the effect of pyrazine and dihydropyrazine on structures and charge transport properties of N-heteropentacenes by DFT calculations. It is found that the introduction of pyrazine keeps the planar shape of molecule, and decreases the energy levels of HOMO and LUMO thus improving the stability toward oxidation and ability of accepting electrons. Small electron reorganization energies and large electronic coupling originated from their dense π-stacking give rise to high electron mobility, which are roughly in agreement with the experimental results. [55] In contrast with pyrazine, introduction of dihydropyrazine to pentacene is more helpful for promoting p-type organic semiconductor materials. Owing to electron donating property of dihydropyrazine, it results in high-lying LUMOs, which are adverse to electron injection and stability of radical anions. [56]

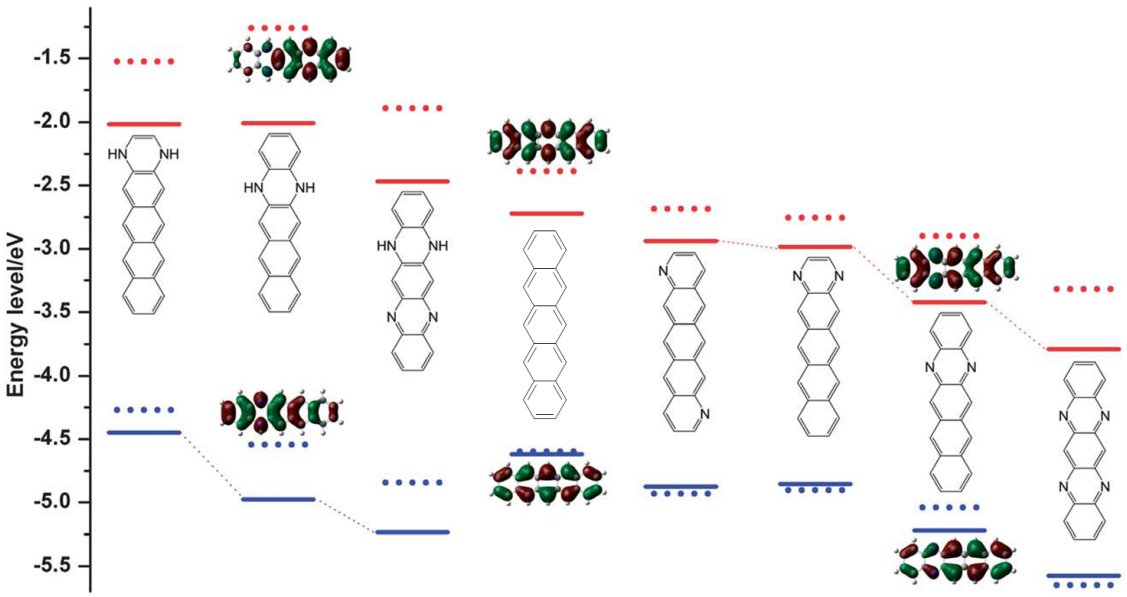

Figure 1.14 Relative HOMO and LUMO energy levels of N-heteropentacenes calculated by the B3LYP/6-31G* method. (Solid line: N-heteroacenes with TIPS ethynyl groups; dash line: N-heteroacenes without TIPS ethynyl groups.) (Reprinted from ref. 59)

Very recently, Shuai and co-workers calculated the electronic structures and charge carrier mobility of series of N-heteroacenes and dihydro-N-heteroacenes on the basis of reported molecular structures and crystal structures. [57] (Figure 1.14) They found that the dehydrogenation of dihydro-N-heteropentacenes leads to a more distinct stabilization of the LUMOs than that of the HOMOs, resulting in a significantly reduced band gap as well as a red-shifted absorption band. The absolute position of the frontier molecular orbitals depends upon the position of the nitrogen atoms in the N-heteroacenes backbone, demonstrating that internal pyrazine units feature lower energies levels than their terminal analogues which have been proved by experimental results. [43] Besides, the dehydrogenation of dihydro N-heteropentacenes derivatives is found to remarkably increase the electron transfer integrals and decrease the electron reorganization energies, thus regarded as a useful strategy for designing high performance n-type organic semiconductors.

1.4.3 Experimental studies

To the best of our knowledge, **1.12** is the first N-heteroacenes that were characterized in terms of electrical conductivity. [58] In 1991, Jenekhe reported that its methylsulfonate salt exhibited a conductivity of ~0.04 Scm^{-1} in compressed pellets and a two-orders-of-magnitude conductivity in single crystals at room temperature. 14 years later, Zhu and co-workers reported that **1.12** functioned as a p-type organic semiconductor in organic field effect transistors with a field effect mobility of 0.02 $cm^2V^{-1}s^{-1}$. [59]

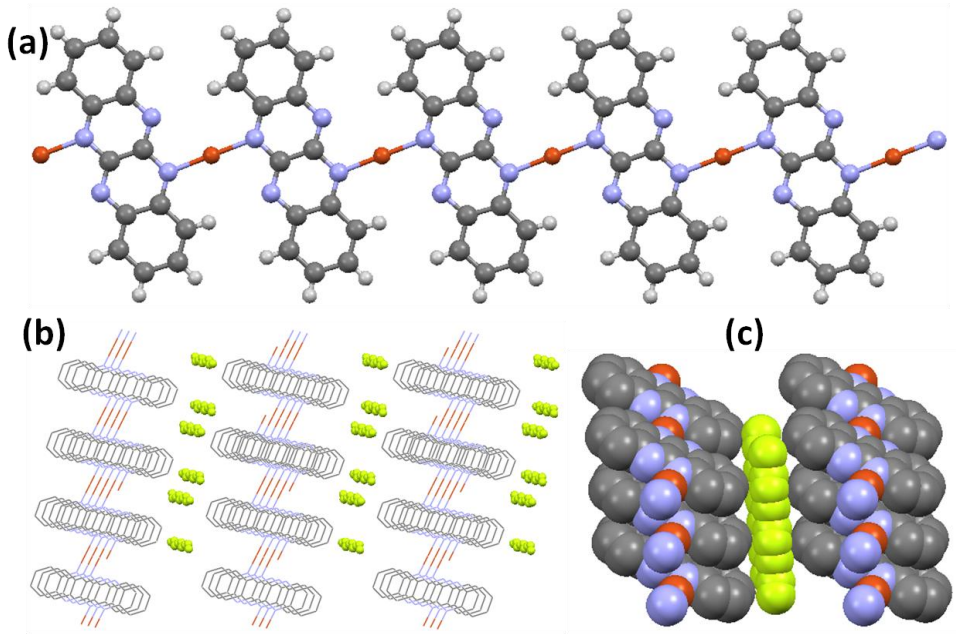

Figure 1.15 (a) The structure of 1D coordination polymer in [Cu (**1.5**) $F_{0.5}]_n$**;** (b) the segregated stacking of the coordination polymer along the *a* axis to create 2D stacking layers, which are separated by other layers constructed from disordered F^- along the *c* axis; (c) a perspective view along the *a* axis. (For the models: gray atoms are carbon, blue atoms are nitrogen, red atoms are copper and yellow atoms are fluoride.) (Reprinted from ref. 60)

In 2006, Makoto reported a copper(I) complex of **1.5** which is a new high conductive solids resulting from a coordinated polymer containing Cu^+ ions and **1.5** as acceptor. X-ray structure analysis shows a flat-ribbon structure with alternative linkage between the Cu^+ ions and

1.5, which are arranged in segregated stacks to form two dimensional stacking layers as conductive channels. However, further applications for other fully unsaturated N-heteroacenes have not yet emerged.[60]

In 2003, Nuckolls and co-workers extended their interests in organic semiconductors to the field of N-heteroacenes, demonstrating that **1.6** and **1.10** were viable substitutes for pentacene as p-type semiconductor with a hole mobility up to 5×10^{-5} $cm^2V^{-1}s^{-1}$ and 6×10^{-3} $cm^2V^{-1}s^{-1}$, respectively. [46] Further investigation on **1.6** led to interesting finding that **1.6** formed three crystalline polymorphs in the vacuum-deposited thin films and one polymorph yielded mobility as high as 0.45 $cm^2V^{-1}s^{-1}$, which was over 5000 times higher than those of the other two phases.[61] Besides **1.6** and **1.10**, methylated derivatives of **1.18** and **1.19** also exhibited p-type organic semiconductors behavior with mobility about 10^{-4} $cm^2V^{-1}s^{-1}$. [19]

Chlorinated dihydrodiazapentacene **1.26** functioned as a p-type semiconductor when deposited on a pentacene buffer layer exhibiting a hole mobility as high as 1.4 cm^2 $V^{-1}s^{-1}$. Chlorinated diazapentacene **1.27** functioned as an n-type semiconductor in OFETs fabricated directly on single crystals exhibiting very high electron mobility as high as 3.39 $cm^2V^{-1}s^{-1}$. [26]

Some N-heteroacenequinones functioned as promising n-type semiconductors in OTFT for their low lying and well delocalized LUMO energy levels benefiting from the electron deficient nature of N atoms and quinone structures. For example, **1.13** exhibited electron mobility up to 0.12 $cm^2V^{-1}s^{-1}$ in its polycrystalline films fabricated by vacuum-deposited method. However, **1.30** and **1.31** only exhibited lower electron mobility in the range of 10^{-5} $cm^2V^{-1}s^{-1}$. [32]

In 2010, Zhang and co-workers explored **1.53** and **1.55a-c** as high and balanced ambipolar thin film transistors, with mobility of 0.11 cm^2 $V^{-1}s^{-1}$ (hole) and 0.15 cm^2 $V^{-1}s^{-1}$

(electrons) for **1.53**, 0.08 cm^2 $V^{-1}s^{-1}$ (hole) and 0.09 cm^2 $V^{-1}s^{-1}$ (electrons) for **1.55b**, 0.12 cm^2 $V^{-1}s^{-1}$ (hole) and 0.14 cm^2 $V^{-1}s^{-1}$(electron) for **1.55c**. [44]

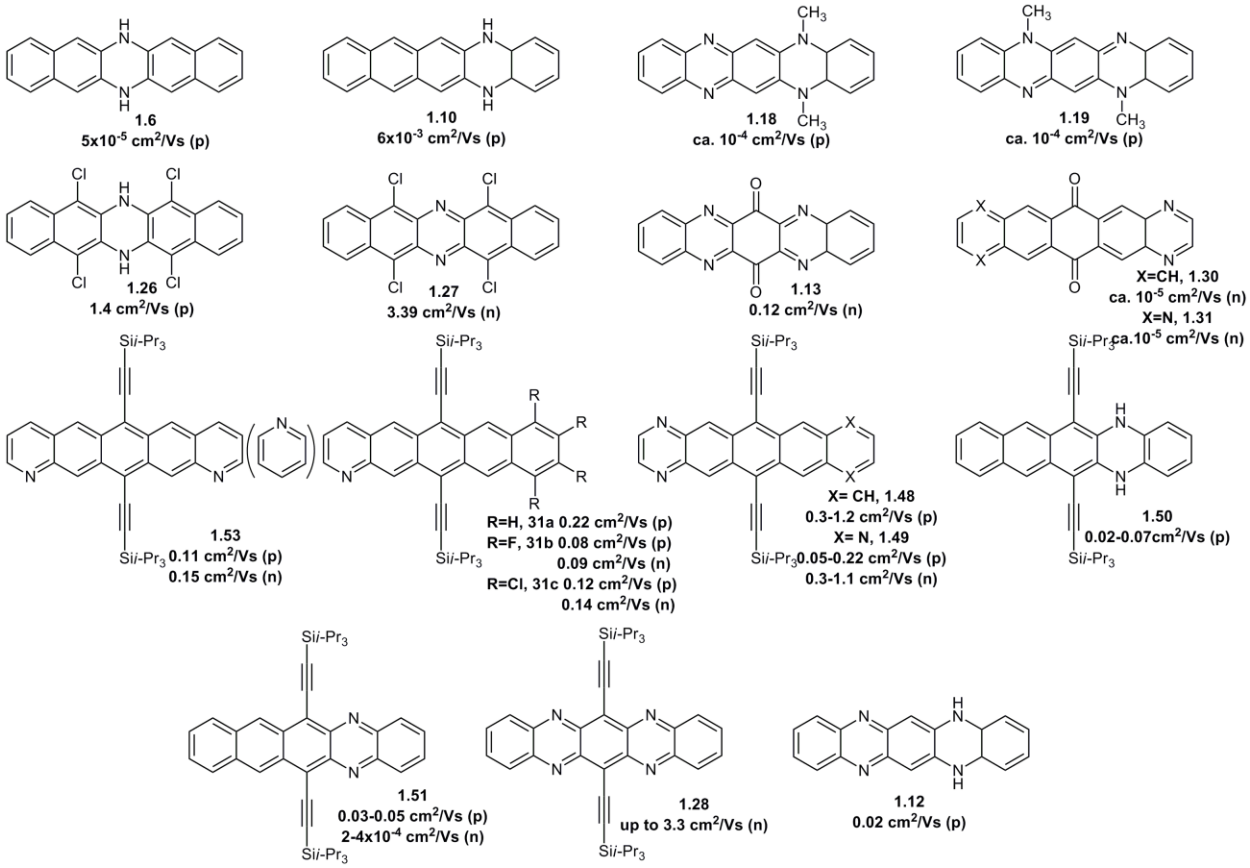

Figure 1.16 Summary of N-heteropentacenes exhibiting OFET properties.

Miao and co-workers systematically studied TIPS-N-heteropentacenes derivatives applications in thin film transistors from materials to devices. Based on their HOMO and LUMO energy levels, **1.50** and **1.48** functioned as p-type semiconductors with mobility of 0.02-0.07 cm^2 $V^{-1}s^{-1}$ and 0.3-1.2 cm^2 $V^{-1}s^{-1}$, respectively.[42] **1.49** and **1.51** functioned as ambiploar semiconductors with field effect properties in both p- and n-channel OFETs. [43] Particularly, **1.28** exhibited the highest electron mobility of 3.3 cm^2 $V^{-1}s^{-1}$ and the average electron mobility of 1.6 cm^2 $V^{-1}s^{-1}$ when the transistors were fabricated by vacuum-deposited method and tested under

vacuum. When the transistors were tested in ambient air, the electron mobility of **1.28** decreased to 0.3-0.5 $cm^2V^{-1}s^{-1}$, due to trapping of electrons by oxygen and water. When **1.28** was directly drop cast onto SiO_2, the mobility of resulting OTFTs dropped to 0.003 $cm^2\ V^{-1}s^{-1}$ because of the trapping of the mobile electrons by the Si-OH groups. [43] Single crystals OFETs of **1.28**, which fabricated by growing crystals of **1.28** on OTS-treated Si/SiO_2 and gluing silver strips onto them, exhibited field effect mobility up to 1.8 $cm^2\ V^{-1}s^{-1}$ but such single crystal devices are not suitable for practical application. [62] To fabricated high-performance solution-processed OTFTs of **1.28**, Miao's group recently developed a new strategy to enhance the surface energy of SAMs by inserting polar oxygen atoms into the long alkyl chain of phosphonic acids. SAMs of these phosphonic acids on a solution-processed high-*k* metal oxide layer have led to solution-processed n-channel OTFTs of **1.28** with average field effect mobility of up to 2.5 cm^2/Vs as well as low operational voltage. [30] Overall, **1.28** is the best-performing of N-heteroacenes so far with respect to electron-transport properties in thin-film transistors although its device stability in air still needs to be improved.

In conclusion, these results indicate that N-heteropentacenes and their derivatives are a general design for high-performance organic semiconductors with good opportunities for studying structure-property relationships. Particularly silylethynylated-N-heteropentacenes have been developed into one important branch of organic semiconductor materials, which may eventually obscure the robust stability, solution processed and high mobility requirements for practical application.

1.5 Reference

1 (a) Clar, E. *Aromatische Kohlenwasserstoffe*, Springer, Berlin. **1941**. (b) Clar, E. *Chem. Ber.* **1929**, *62*, 350.

2 Bendikov, M.; Wudl, F.; Perepichka, D. F. *Chem. Rev.* **2004**, *104*, 4891.

3 (a) Perepichka, D. F.; Bendikov, M.; Meng, H.; Wudl, F. *J. Am. Chem. Soc.* **2003**, *125*, 10190. (b) Chun, D.; Cheng, Y.; Wudl, F. *Angew. Chem. Int. Ed.* **2008**, *47*, 8380.

4 Anthony, J. E. *Angew. Chem. Int. Ed.* **2008**, *47*, 452. (b) Anthony, J. E. *Chem. Rev.* **2006,** *106*, 5028. (c) Payne, M. M.; Parkin, S. R.; Anthony, J. E. *J. Am. Chem. Soc.* **2005**, *127*, 8028.

5 (a) Bunz, U. H. F. *Chem. Eur. J.* **2009**, *15*, 6780. (b) Bunz, U. H. F. *Pure Appl. Chem.* **2010**, *82*, 953. (c) Miao, Q. *Synlett.* **2012**, 326. (d) Richards, G. J.; Hill, J. P.; Mori, T.; Ariga, K. *Org. Biomol. Chem.* **2011**, *9*, 5005. (e) Bunz, U. H. F.; Engelhart, J. U.; Lindner, B. D.; Schaffroth, M. *Angew. Chem. Int. Ed.* **2013**, *52*, 3810. (f) Winkler, M.; Houk, K. N. *J. Am. Chem. Soc.* **2007**, *129*, 1805.

6 Richards, G. J.; Hill, J. P.; Mori, T.; Ariga, K. *Org. Biomol. Chem.*, **2011**, *9*, 5005.

7 Hinsberg, O. *Liebigs Ann. Chem.*, **1901**, *319*, 257.

8 Mallouli, A.; Lepage, Y. *Synthesis*, **1980**, *09*, 689.

9 Kummer, F.; Zimmermann, H. *Ber. Bunsenges.* **1967**, *71*, 1119.

10 Badger, G. M.; Pettit, R. *J. Chem. Soc*. **1951**, 3211.

11 Leete, E.; Ekechukwu, O.; Delvigs, P. *J. Org. Chem.* **1966**, *31*, 3734.

12 Hinsberg, O.; Schwantes, E. *Chem. Ber.* **1903**, *36*, 4039.

13 (a) Switzer, J. L. US Patent 2.495.202, **1945**. (b) Graser, F. DE3504143, **1986**. (c) Foster, C. E. GB2.430.936, **2007**. (d) Fleischhauer, J.; Beckert, R. DE102007050673, **2007**.

14 (a) Richards, G. J.; Hill, J. P.; Subbaiyan, N. K.; D'Souza, F.; Karr, P. A.; Elsegood, M. R. J. ; Teat, S. J.; Mori, T.; Ariga, K.; *J. Org. Chem.* **2009**, *74*, 8914. (b) Ahmad, A. R.; Mehta, L. K.; Parrick, J. *J. Chem. Soc. Perkin Trans 1*, **1996**, 2443. (c) Akimoto, Y.; *Bull. Chem. Soc. Jpn.* **1956**, *29*, 460. (d) Akimoto, Y. *Bull. Chem. Soc. Jpn.* **1956**, *29*, 553.

15 Bergstrom, F. W.; Ogg, R. A., Jr. *J. Am. Chem. Soc.* **1931**, *53*, 245.

16 Quast, H.; Schön, N. *Liebigs Ann. Chem.* **1984**, 133.

17 (a) Armand, J.; Boulares, L.; Bellec, C.; Pinson, J. *Can. J. Chem.* **1987**, *65*, 1619. (b) Sawtschenko, L.; Jobst, K.; Neudeck, A.; Dunsch, L. *Electrochimica Acta* **1996**, *41*, 123.

18 (a) Goyette, M.-A.; Leclerc, M. *J. Electroanal. Chem.* **1995**, *382*, 17. (b) Casu, M. B.; Imperia, P.; Schrader, S.; Falk, B.; Jandke, M.; Strohriegl, P. *Synth. Met.* **2001**, *124*, 79. (c) Jenekhe, S. A. *Macromolecules*, **1991**, *24*, 1. (d) Ma, Y.; Sun, Y.; Liu, Y.; Gao, J.; Chen, S.; Sun, X.; Qiu, W.; Yu, G.; Cui, G.; Hu, W.; Zhu, D. *J. Mater. Chem.* **2005**, *15*, 4894.

19 Tang, Q.; Liu, J.; Chan, H. S.; Miao, Q. *Chem. Eur. J.* **2009**, *15*, 3965.

20 (a) Wudl, F.; Koutentis, P. A.; Weitz, A.; Mea, B.; Strassner, T.; Houk, K. N.; Khan, S. I. *Pure Appl. Chem.***1999**, *71*, 295. (b) Riley, A. E.; Mitchell, G. W.; Koutentis, P. A.; Bendikov, M.; Kaszynski, P.; Wudl, F.; Tolbert, S. H. *Adv. Funct. Mater.* **2003,** *13*, 531.

21 Fleischhauer, J.; Beckert, R.; Jüttke, Y.; Hornig, D.; Günther, W.; Birckner, E.; Grummt, U. W.; Görls, H. *Chem. Eur. J.*, **2009**, *15*, 12799.

22 Fleischhauer, J.; Zahn, S.; Beckert, R.; Grummt, U.-W.; Birckner, E.; Görls, H. *Chem. Eur. J.* **2012**, *18*, 4549.

23 Seillan, C.; Brisset, H.; Siri, O. *Org. Lett.* **2008**, *10*, 4013.

24 Li, G.; Wu, Y.; Gao, J.; Wang, C.; Li, J.; Zhang, H.; Zhao, Y.; Zhao, Y.; Zhang, Q. *J. Am. Chem. Soc.* **2012**, *134*, 20298.

25 Tang, M. L.; Oh, J. H.; Reichardt, A. D.; Bao, Z. *J. Am. Chem. Soc.* **2009**, *131*, 3733.

26 (a) Weng, S.-Z.; Shukla, P.; Kuo, M.-Y.; Chang, Y.-C.; Sheu, H.-S.; Chao, I.; Tao, Y.-T. *ACS Appl. Mater. Interfaces* **2009**, *1*, 2071. (b) Islam, M. M.; Pola, S.; Tao, Y.-T. *Chem. Commun.* **2011**, *47*, 6356.

27 (a) Anthony, J. E.; Eaton, D. L.; Parkin, S. R. *Org. Lett.* **2002**, *4*, 15. (b) Anthony, J. E.; Brooks, J. S.; Eaton, D. L.; Parkin, S. R. *J. Am. Chem. Soc.* **2001**, *123*, 9482.

28 (a) Payne, M. M.; Parkin, S. R.; Anthony, J. E. *J. Am. Chem. Soc.* **2005**, *127*, 8028. (b) Purrshothaman, B.; Parkin, S. R.; Anthony, J. E. *Org. Lett.* **2010**, *12*, 2060.

29 (a) Chun, D.; Cheng, Y.; Wudl, F. *Angew. Chem., Int. Ed.* **2008**, *47*, 8380. (b) Qu, H.; Chi, C. *Org. Lett.* **2010**, *12*, 3360. (c) Ref. 24.

30 (a) Miao, S.; Appleton, A. L.; Berger, N.; Barlow, S.; Marder, S. R.; Hardcastle, K. I.; Bunz, U. H. F. *Chem. Eur. J.* **2009**, *15*, 4990. (b) Liu, D.; Xu, X.; Su, Y.; He, Z.; Xu, J.; Miao, Q. *Angew. Chem. Int. Ed.* **2013,** *52*, 6222.

31 Cava, M. P.; Napier, D. R. *J. Am. Chem. Soc.* **1957**, *79*, 1701.

32 (a) Tang, Q.; Liang, Z.; Liu, J.; Xu, J.; Miao, Q. *Chem. Commun.* **2010**, 46, 2977. (b) Liang, Z.; Tang, Q.; Liu, J.; Li, J.; Yan, F.; Miao, Q. *Chem. Mater.* **2010**, *22*, 6438.

33 (a) Mateo-Alonso, A.; Kulisic, N.; Valenti, G.; Marcaccio, M.; Paolucci, F.; Prato, M. *Chem. Asian J.* **2010**, *5*, 482. (b) Richards, G. J.; Hill, J. P.; Subbaiyan, N. K.; Karr, P. A.; Elsegood, M. R. J.; Teat, S. J.; Mori, T.; Ariga, K. *J. Org. Chem.* **2009**, *74*, 8914. (c) Richards, G. J.; Hill, J. P.; Okamoto, K.; Shundo, A.; Akada, M.; Elsegood, M. R. J.; Mori, T.; Ariga, K. *Langmuir* **2009**, *25*, 8408. (d) Richards, G. J.; Hill, J. P.; Labuta, J.; Wakayama, Y.; Akada, M.; Ariga, K. *Phys. Chem. Chem. Phys.* **2011**, *13*, 4868. (e) More, S.; Bhosale, R.; Choudhary, S.; Mateo-Alonso, A. *Org. Lett.* **2012**, *14*, 4170.

34 (a) Gao, B.; Wang, M.; Cheng, Y.; Wang, L.; Jing, X.; Wang. F. *J. Am. Chem. Soc.* **2008**, *130*, 8297. (b) Dubois, D.; Moninot, G.; Kutner, W.; Jones, M. T.; Kadish, K. M. *J. Phys. Chem.* **1992**, *96*, 7137. (c) Fogel, Y.; Kastler, M.; Wang, Z.; Andrienko, D.; Bodwell, G. J.; Müllen, K. *J. Am. Chem. Soc.* **2007**, *129*, 11743. (d) McGrath, K. K.; Jang, K.; Robins, K. A.; Lee, D.-C. *Chem. Eur. J.* **2009**, *15*, 4070. (f) Kaafarani, B. R.; Kondo, T.; Yu, J. S.; Zhang, Q.; Dattilo, D.; Risko, C.; Jones, S. C.; Barlow, S.; Domercq, B.; Amy, F.; Kahn, A.; Bredas, J. L.; Kippelen, B.; Marder, S. R. *J. Am. Chem. Soc.* **2005**, *127*, 16358. (g) Tong, C.; Zhao, W.; Luo, J.; Mao, H.; Chen, W.; H. Chan,S. O.; Chi, C. *Org. Lett.* **2012**, *14*, 494.

35 (a) Appleton, A. L.; Brombosz, S. M.; Barlow, S.; Sears, J. S.; Bredas, J. L.; Marder, S. R.; Bunz, U. H. F. *Nat. Commun.* **2010**, *1*, 91. (b) Lindner, B. D.; Engelhart, J. U.; Marken, M.; Tverskoy, O.; Appleton, A. L.; Rominger, F.; Hardcastle, K. I.; Enders, M.; Bunz, U. H. F. *Chem. Eur. J.* **2012**, *18*, 4627. (c) Appleton, A. L.; Barlow, S.; Marder, S. R.; Hardcastle, K. I.; Bunz, U. H. F. *Synlett.* **2011**, 1983.

36 (a) Hartwig, J. F. *Acc. Chem. Res.* **1998**, *31*, 852. (b) Wolfe, J. P.; Wagaw, S.; Marcoux, J. F.; Buchwald, S. L. *Acc. Chem. Res.* **1998**, *31*, 805.

37 Tverskoy, O.; Rominger, F.; Peters, A.; Himmel, H.-J.; Bunz, U. H. F. *Angew. Chem. Int. Ed.* **2011**, *50*, 3557.

38 Lindner, B. D.; Engelhart, J. U.; Tverskoy, O.; Appleton, A. L.; Rominger, F.; Peters, A.; Himmel, H. J.; Bunz, U. H. F. *Angew. Chem. Int. Ed.* **2011**, *50*, 8588.

39 Engelhart, J. U.; Lindner, B. D.; Tverskoy, O.; Rominger, F.; Bunz, U. H. F. *Org. Lett.* **2012**, *14*, 1008.

40 Engelhart, J. U.; Lindner, B. D.; Tverskoy, O.; Schaffroth, M.; Rominger, F.; Bunz, U. H. F. *J. Org. Chem.* **2013**, *78*, 1249.

41 Anthony, J. E.; Brooks, J. S.; Eaton, D. L.; Parkin, S. R. *J. Am. Chem. Soc.* **2001**, *123*, 9482.

42 Liang, Z.; Tang, Q.; Mao, R.; Liu D.; Xu, J.; Miao, Q. *Adv. Mater.* **2011**, *23*, 5514.

43 Liang, Z.; Tang, Q.; Xu, J.; Miao, Q. *Adv. Mater.* **2011**, *23*, 1535.

44 (a) Liu, Y.-Y.; Song, C.-L.; Zeng, W.-J.; Zhou, K.-G.; Shi, Z.-F.; Ma, C.-B.; Yang, F.; Zhang, H.-L.; Gong, X. *J. Am. Chem. Soc.* **2010**, *132*, 16349. (b) Song, C. L.; Ma, C.-B.; Yang, F.; Zeng, W.-J.; Zhang, H.-L.; Gong, X. *Org. Lett.* **2011**, 2880.

45 Miao, S.; Brombosz, S. M.; Schleyer, P. v. R.; Wu, J. I.; Barlow, S.; Marder, S. R.; Hardcastle, K. I.; Bunz, U. H. F. *J. Am. Chem. Soc.* **2008**, *130*, 7339.

46 Miao, Q.; Nguyen, T.-Q.; Someya, T.; Blanchet, G. B.; Nuckolls, C. *J. Am. Chem. Soc.* **2003**, *125*, 10284.

47 (a) Matthews, C. C.; Bros, A. B.; Baas, J.; Meetsma, A.; deBoer, J.-L.; Palsera, T. T. M. *Acta Crystallogr.* **2001**, *C57*, 939. (d) Campbell, R. B.; Robertson, J. M.; Trotter, J. *Acta Crystallogr.* **1961**, *14*, 705. (c) Thalladi, V.; Smolka, T.; Gehrke, A.; Boese, R.; Sustmann, R. *New J. Chem.* **2000**, *24*, 143. (d) Hunter, C. A.; Sanders, J. K. M. *J. Am. Chem. Soc.* **1990**, *112*, 5525.

48 (a) Jang, J. *Materials Today* **2006**, *9*, 46. (b) Gelinck, G.; Heremans, P.; Nomoto, K.; Anthopoulos, T. *Adv. Mater.* **2010**, *22*, 3778. (c) Someya, T.; Dodabalapur, A.; Huang, J.; See, K. C.; Katz, H. E. *Adv. Mater.* ***2010***, *22*, 3799. (d) Mabeck, J. T.; Malliaras, G. G. *Anal. Bioanal. Chem.* **2006**, *384*, 343.

49 Murphy A. R.; Fréchet, J. M. J. *Chem. Rev.* **2007**, *107*, 1066.

50 Katz, H. E.; Bao, Z.; Gilat, S. L. *Acc. Chem. Res.* **2001**, *34*, 359.

51 (a) Tang, M. L.; Reichardt, A. D.; Wei, P.; Bao, Z. *J. Am. Chem. Soc.* **2009**, *131*, 5264. (b) Anthony, J. E. *Chem. Rev.* **2006**, *106*, 5028. (c) Brédas, J.-L.; Calbert, J. P.; da Silva, D. A.;

Cornil, J. *Proc. Natl. Acad. Sci. U.S.A.* **2002**, 99, 5804. (d) Brédas, J.-L.; Beljonne, D.; Coropceanu, V.; Cornil, J. *Chem. Rev.* **2004**, *104*, 4931.

52 Chen, H.-Y.; Chao, I. *ChemPhysChem* **2006**, *7*, 2003.

53 Winkler, M.; Houk, K. N. *J. Am. Chem. Soc.* **2007**, *129*, 1805.

54 Li, C.-H.; Huang, C.-H.; Kuo, M.-Y. *Phys. Chem. Chem. Phys.* **2011**, *13*, 11148.

55 Chen, X.; Guo, J.; Zou, L.; Ren, A.; Fan, J. *J. Phys. Chem. C* **2011**, *115*, 21416.

56 Chen, X.; Zou, L.; Fan, J.; Zhang, S.; Ren, A. *Org. Electron.* **2012**, *13*, 2832.

57 Tang, X.-D.; Liao,Y.; Geng, H.; Shuai, Z.-G. *J. Mater. Chem.* **2012**, *22*, 18181.

58 Jenekhe, S. A. *Macromolecules*, **1991**, *24*, 1.

59 Y. Ma, Y. Sun, Y. Liu, J. Gao, S. Chen, X. Sun, W. Qiu, G. Yu, G. Cui, W. Hu, D. Zhu, *J. Mater. Chem.* **2005**, *15*, 4894.

60 Tadokoro, M;. Yasuzuka, S.; Nakamura, M.; Shinoda, T.; Tatenuma, T.; Mitsumi, M.; Ozawa, Y. ; Toriumi, K.; Yoshino, H.; Shiomi, D.; Sato, K.; Takui, T.; Mori, T.; Murata; K. *Angew. Chem. Int. Ed.* **2006**, *45*, 5144.

61 Tang, Q.; Zhang, D.; Wang, S.; Ke, N.; Xu, J.; Yu, J. C.; Miao, Q. *Chem. Mater.* **2009**, *21*, 1400.

62 Wang, C.; Liang, Z.; Liu, Y.; Wang, X.; Zhao, N.; Miao, Q.; Hu, W.; Xu, J. *J. Mater. Chem.* **2011**, *21*, 15201.

Chapter 2 Hydrogen-Bonded Dihydrotetraazapentacenes*

2.1 Introduction

N-heteropentacenes, which have N atoms inserted into the backbone of pentacene, have recently been found as a new family of organic semiconductors with high performance in organic field effect transistors (OFETs). [1] A combination of varied number, position and valence state of N atoms in N-heteropentacenes can in principle yield a large number of structurally-related π-backbones, and thus brings great opportunities for developing novel organic semiconductors with tunable electronic structure, stability, solubility and molecular packing. Unlike pentacene, N-heteropentacenes are capable of hydrogen bonds with nitrogen atoms. As found from the known crystal structures, N-heteropentacenes form both classical and weak hydrogen bonds. N-heteropentacenes were found to form classical hydrogen bonds with solvent molecules, such as DMF and water, in the crystal lattice.(see Chapter 1.5) Having aromatic C-H as the hydrogen donor, the weak hydrogen bonds (C-H···N) between N-heteropentacene molecules were first predicted for self-complementary N-rich pentacenes. [2] As recently found in the crystal structure, silylethynylated 1, 4, 8, 11-tetraazapentacene forms double weak hydrogen bonds, which lead to a packing motif different from the common two dimensional π-stacking of silylethynylated N-heteropentacenes. Owing to the greater strength, classical hydrogen bonds are in principle more powerful in directing the molecular packing of N-heteropentacenes. However, classical hydrogen bonds between N-heteropentacene molecules were not reported to the best of our knowledge.

---

* This Section is reprinted with small modification from: Zikai He, Danqing Liu, Renxin Mao, Qin Tang, Qian Miao*. *Org. Lett.*, **2012**, *14*, 1050. Synthesis, Characterization and crystal growth were done by me. Crystal structures were solved by Ms. Hoi Shan Chan. Thin film transistor fabrication and characterization was done by Dr. Qin Tang and Ms. Danqing Liu. DFT calculation was done by Mr. Renxin Mao.

To explore how classical N-H···N hydrogen bonds tune the properties of N-heteropentacenes, we have designed a new dihydrodiazapentacene (**2.1**) that has adjacent pyrazine and dihydropyrazine rings at one end of the pentacene backbone as shown in Figure 2.1. This design allows self-complementary N-H···N hydrogen bonds in the solid state as detailed in this chapter. Following the success of silylethynylated pentacenes [3] and N-heteropentacenes [4] as soluble and stable organic semiconductor with high charge carrier mobility, triisopropylsilylethynyl groups are introduced to **2.1** leading to **2.2** and **2.3**. Particularly, the NH groups of **2.2** are exposed as found from the space-filling model shown in Figure 2.2, and thus are available for hydrogen bonding. On the other hand, the NH groups of **2.3** are shielded by the bulky triisopropylsilyl groups as found from the space-filling model, and thus are not able to form hydrogen bonds with a hydrogen-bond acceptor. Studying UV-vis absorption of **2.2** and **2.3** in different solvents has led to an interesting finding on solvent-dependent absorption caused by hydrogen bonding. It is found that these new members of N-heteropentacenes function as p-type organic semiconductors in thin film transistors. Particularly, **2.3** exhibits field effect mobility as high as 0.7 $cm^2V^{-1}s^{-1}$.

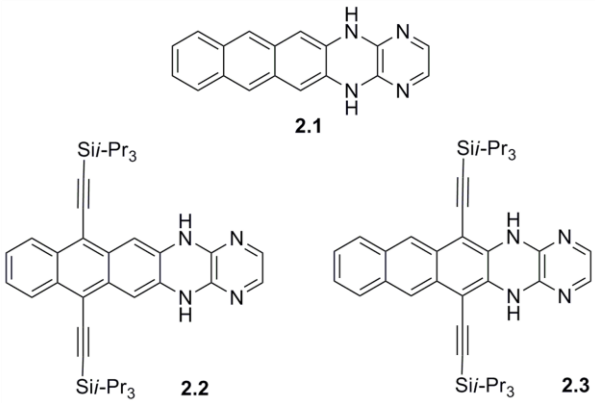

Figure 2.1 Molecular structures of 5, 14-dihydro-1,4,5,14-tetraazapentacene (**2.1**) and its silylethynylated derivatives (**2.2** and **2.3**).

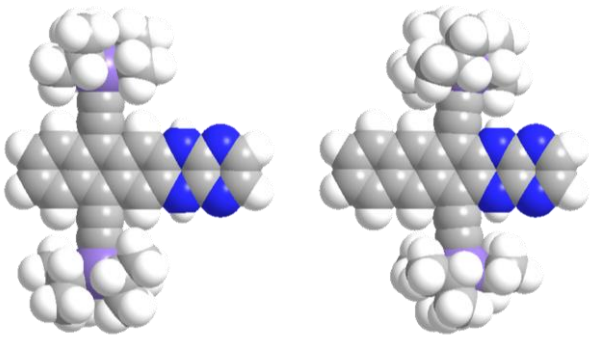

Figure 2.2 Space-filling models of **2.2** and **2.3** as optimized at B3LYP/6-31g(d,p) level of density function theory (DFT) (C, N, Si and H atoms are shown in grey, blue, violet and white, respectively)**.**

2.2 Results and Discussion

2.2.1 Synthesis

Shown in Scheme 2.1 are the syntheses of **2.1**-**2.3** in two ways. **2.1** and **2.2** were synthesized from 2,3-diaminopyrazine and the corresponding dihydroxyanthranenes (**2.4** and **2.5** respectively) by solvent-free condensation at 205 to 215 °C. In comparison with the synthesis of 5,14-dihydro-5,14-diazapentacene from solvent-free condensation of 2,3-dihydroxyanthracene and 1,2-diaminobenzene at 160 °C, the synthesis of **2.1** needs higher temperature because 2,3-diaminopyrazine has less nucleophilic amino groups due to the electron-deficient nature of pyrazine. The low yield of **2.2** may be attributed to the low stability of **2.5** during heating or reduced reactivity of **2.5** due to presence of alkynyl groups ortho to the hydroxyl groups. Unlike **2.1** and **2.2**, compound **2.3** was synthesized by palladium catalyzed coupling of **2.6** and 2, 3-dichloropyrazine using 1, 1'-bis(diphenylphosphino)ferrocene (dppf) as ligand and Cs_2CO_3 as base. This condition was a modification from Bunz's synthesis of an isomer of **2.2** and **2.3** from

1, 4-bis(triisopropylsilyl)-2,3-diaminonaphthalene and 2,3-dichloroquinoxaline using biaryl phophane ligands and Hünig base.[5]

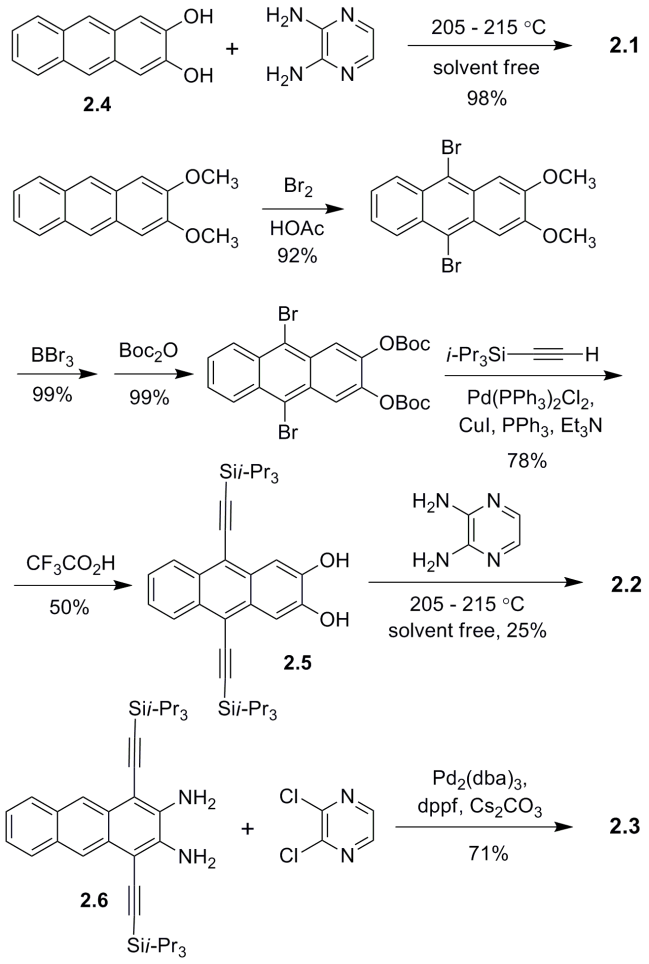

Scheme 2.1 Synthesis of **2.1-2.3**.

2.2.2 Structures

Molecules **2.1-2.3** may each in principle exist as three isomers, which arise from varying the position of H atoms that are bonded to N atoms. As the representative, the three isomers of **2.1** are shown in Figure 2.3. According to Clar's aromatic sextet rule,[6] **2.1** is more favorable energetically than **2.1'** and **2.1''** because **2.1** has two aromatic sextet rings while **2.1'** and **2.1''**

have only one. The ^{1}H NMR of **2.1** show four singlet peaks and two peaks of characteristic AA'XX' patterns, in agreement with the C_{2v} symmetry thus excluding the structure of **2.1''**. Moreover, the H2 and H3 of **2.1** (red shown in Figure 2.3) exhibits a chemical shift at 7.11 ppm, which is very close to the chemical shift (7.13 ppm) of the corresponding hydrogen atoms in 2, 3-diaminopyrazine.[7] As shown in Figure 2.3, the N5-C5a and N5-C4a bonds are both longer than the N4-C4a bond, and the N5-C5a bond has the same length as the N-C bond (1.39 Å) in 6,13-dihydro-6,13-diazapentacene. These bond lengths support the structure of **2.1**, which has dihydropyrazine as the second ring.

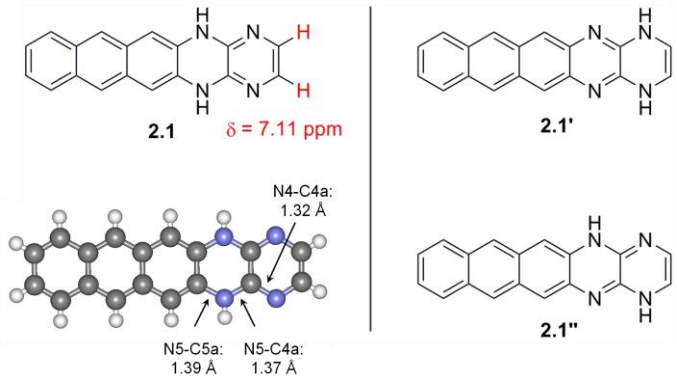

Figure 2.3 Possible isomeric structures of **2.1** and the crystal structure of **2.1**. (C, N, and H atoms are shown in grey, blue, and white, respectively)

The electronic structures of **2.1**-**2.3** were studied using both experimental and computer methods. Cyclic voltammograms of **2.1**-**2.3** (shown in the Experimental Section) exhibited one irreversible oxidation wave but did not show any reduction waves in the testing window. Based on the oxidation peak potential vs. ferrocenium/ferrocene, the highest occupied molecular orbital (HOMO) energy levels of **2.1**-**2.3** were estimated as -4.80 eV, -5.13 eV and -5.17 eV, respectively.[8] The HOMO-LUMO gap was determined based on the absorption edge in the UV-

vis absorption spectrum from a solution in DMF or CH_2Cl_2, the energy levels of LUMO was calculated from the HOMO energy levels and optical gap. HOMO and LUMO energy levels were also calculated at the B3LYP level of density functional theory (DF) with 6-311++G(d,p)//6-31G(d, p) basis sets. As depicted graphically in the Figure 2.4, **2.1** and **2.3** have well delocalized electron distribution in their HOMOs and LUMOs, while **2.2** has its HOMO and LUMO more localized on benzene rings than on dihydropyrazine and pyrazine rings. The calculated HOMO energy levels of **2.1**-**2.3** are very close (about -5.4 eV) and lower than the experimental values. The above results on electronic structures were summarized in Table 2.1 and suggest that **2.1**-**2.3** can function as p-type organic semiconductors.

Table 2.1 Reduction/oxidation potentials, absorption edge [a] and frontier orbital energy levels.

	2.1	**2.2**	**2.3**
E_{ox} vs. Fc^+/Fc (V)	0.00	0.33	0.37
E_{red} vs. Fc^+/Fc (V)	NA	NA	NA
Absorption Edge (nm)[a]	474	518	492
Optical Gap (eV)	2.62	2.39	2.52
HOMO (eV)[b]	-4.80	-5.13	-5.17
LUMO (eV)[c]	-2.19	-2.82	-2.65

[a] The UV-vis absorption spectra were recorded from solutions in DMF or CH_2Cl_2 of 5×10^{-5} mol/L. [b] Calculated from $E_{HOMO} = -4.80eV - E_{ox}$. [c] Calculated from E_{LUMO} = optical gap + E_{HOMO}.

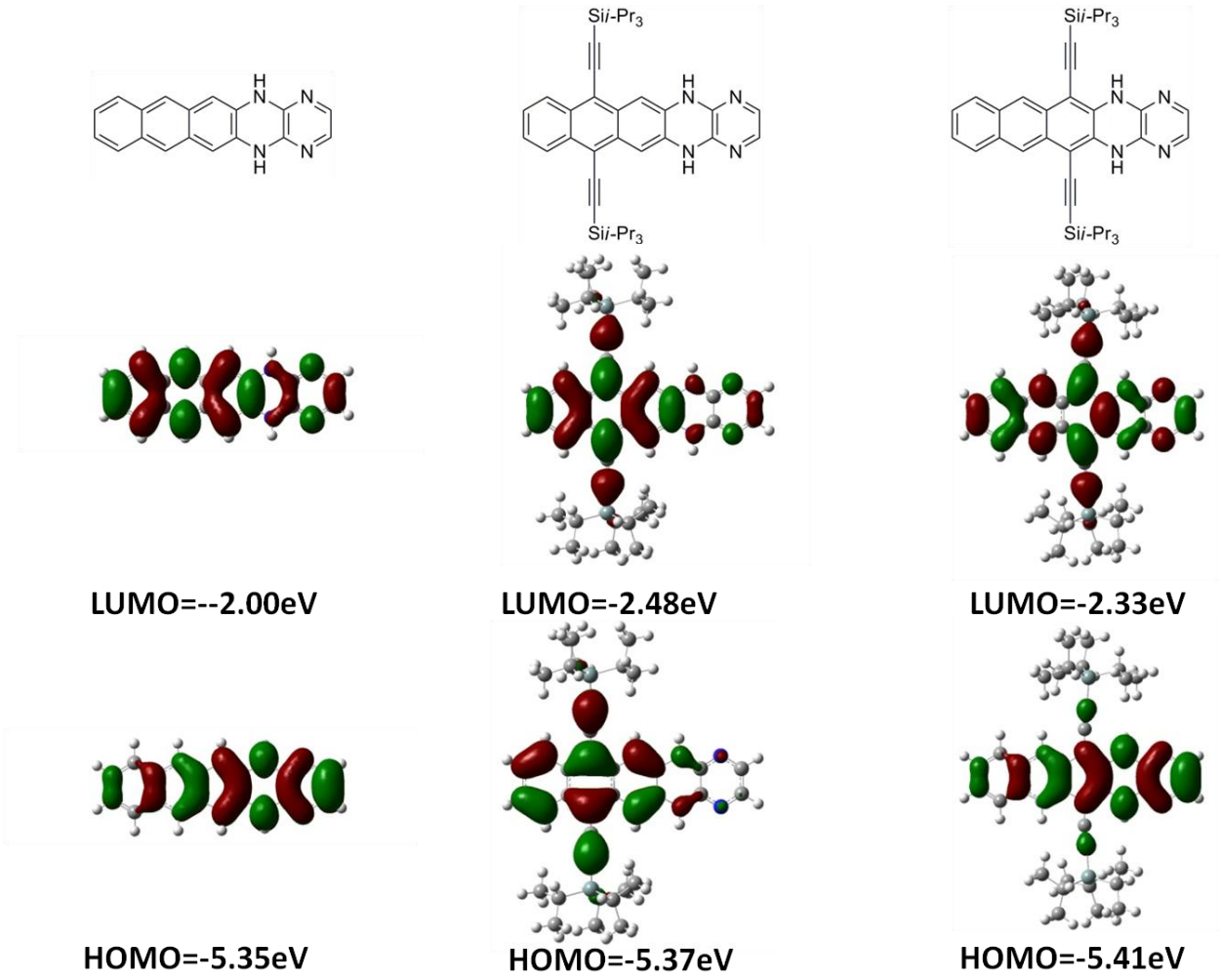

Figure 2.4 Calculated frontier molecular orbitals of **2.1**-**2.3** with the energy levels.

2.2.3 Molecular Packing

Single crystals of **2.1** and **2.3** were grown by physical vapor transport and from solution in ethyl acetate, respectively. X-ray crystallographic analysis on these single crystals has revealed their crystal structures. Molecules of **2.1** form hydrogen-bonded ribbons, which stack in two directions. As shown in Figure 2.5a, molecules of **2.1** are linked by double N-H···N hydrogen bonds, which have the N-to-N distance of 3.05 Å, the H-to-N distance of 2.25 Å and the N-H-N angle of 154.7°. As shown in Figure 2.5b, two stacks of **2.1** are arranged in a

herringbone pattern with a distance of 3.42 Å between the π-planes, and the two neighboring molecules of **2.1** in each π-stack have an offset arrangement with a relative shift along the long molecular axis. In the crystal lattice, each molecule of **2.1** occupies a volume of 320.14 $Å^3$, which is smaller than the volume occupied by 6, 13-dihydro-6,13-diazapentacene (333.92 $Å^3$ per molecule) [9] and 6,13-diazapentacene (333.89 $Å^3$ per molecule).[10] This suggests that hydrogen bonds between N-heteropentacene molecules can be helpful in forming dense packing. As shown in Figure 2.5c, **2.3** exhibits π-stacking of two-dimensional brickwork arrangement, which is typical of silylethynylated pentacenes [3] and N-heteropentacenes.[4] The distance between π planes of **2.3** is 3.35 to 3.36 Å. No hydrogen bonds are found between molecules of **2.3** in the crystal structures because the NH groups are shielded by the bulky triisopropylsilyl groups.

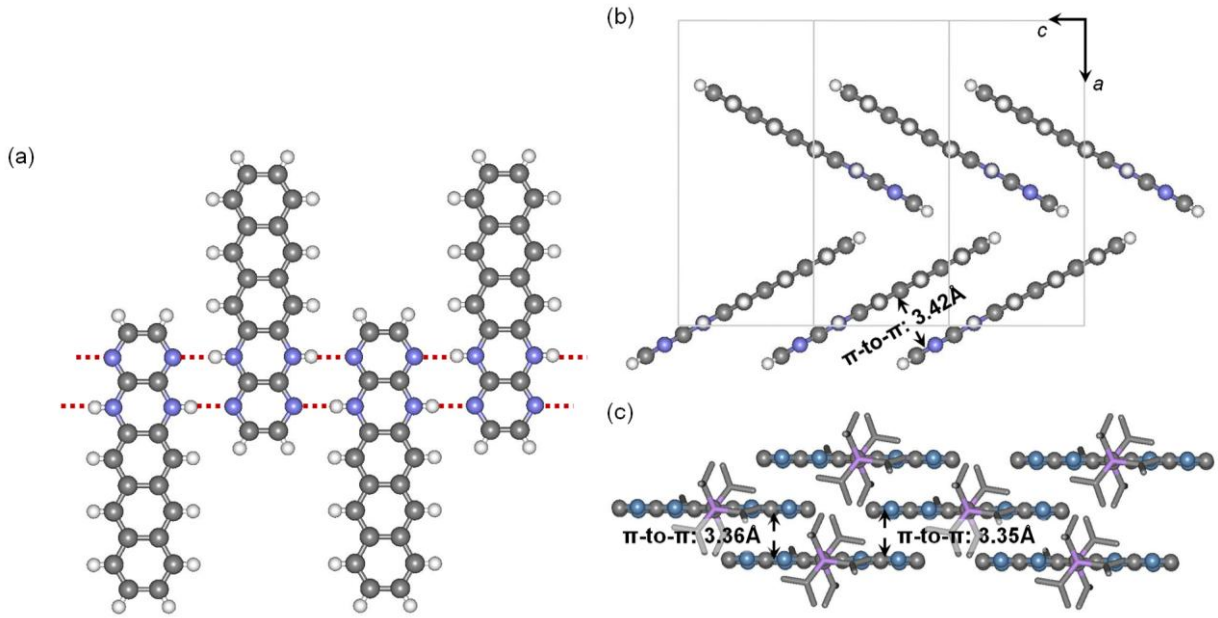

Figure 2.5 Molecular packing of **2.1** and **2.3** in crystals: (a) hydrogen-bonded ribbon of **2.1** with hydrogen bonds shown in red; (b) π-stacks of **2.1** as viewed along the *b* axis of unit cell; (c) π-stacks of **2.3** with brickwork arrangement. (The N-heteropentacene cores are shown as ball-stick model and the silylethynyl substituents are shown in stick model. Hydrogen atoms are removed for clarification. The grayish-blue colored atoms of **2.3** contain both nitrogen and carbon atoms due to disorder.)

2.2.4 Hydrogen Bonding in Solution

Compound **2.1** is only soluble in highly polar solvents, such as DMSO and DMF, while **2.2** and **2.3** are soluble in a variety of organic solvents including benzene, CH_2Cl_2, acetone and THF. Dissolving **2.2** and **2.3** in varied solvents has led to an interesting finding that **2.2** exhibits apparent solvent-dependent absorption, while **2.3** does not show apparent color changes in different solvents. As shown in Figure 2.6a, the solution of **2.2** in CH_2Cl_2 appears yellow but orange in DMSO. This color change is in relation to a red shift of largest-wavelength absorption by 35 nm. Such solvent-dependent color variation may possibly be explained in terms of solvatochromism, which a well-known phenomenon of color changes due to a change in solvent polarity. The widely accepted explanation for solvatochromism is that the ground state and the Franck-Condon excited state of a polar chromophore are stabilized by polar solvent molecules by different degree.[11] To determine whether the solvent-caused color change of **2.2** is a solvatochromic effect, the absorption spectra of **2.2** were recorded in varied solvents. As shown in Figure 2.6b, the measured values of longest-wavelength absorption were first plotted against the dielectric constant of the corresponding solvent. The data for **2.2** do not show a positive correlation between the longest-wavelength absorption and the solvent dielectric constant although DMSO leads to a red shift of absorption. This indicates that the solvent-caused color change of **2.2** should not be described by classical solvatochromism.

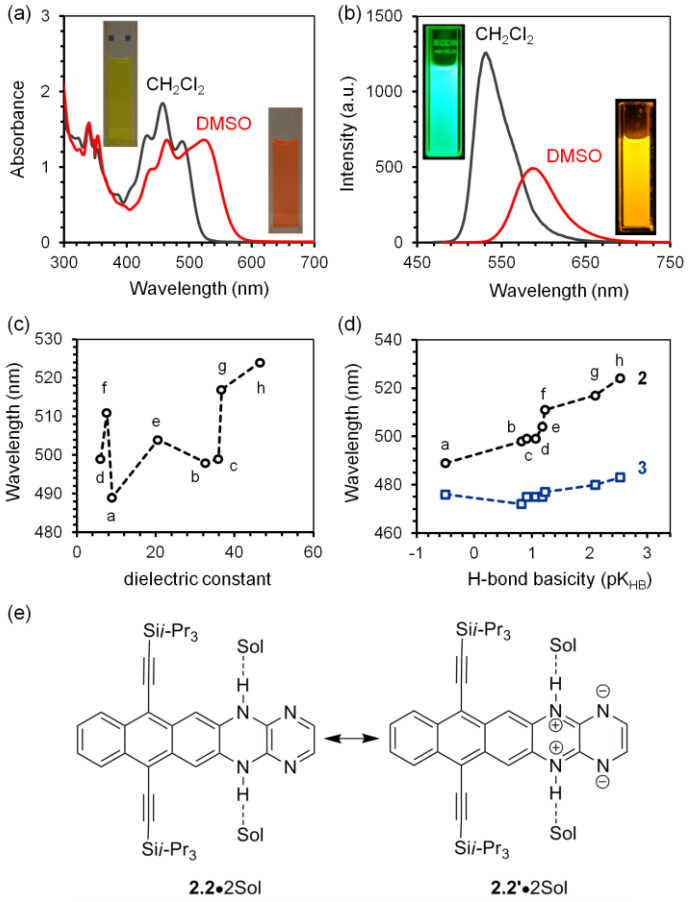

Figure 2.6 (a) Absorption spectra of **2.2** in CH_2Cl_2 and DMSO (1×10^{-5} mol/L); (b) Fluoresence spectra of **2.2** in CH_2Cl_2 and DMSO (1×10^{-5} mol/L); (c) the longest-wavelength absorption of **2.2** in varied solvents versus the dielectric constant of solvent (a: CH_2Cl_2, b: CH_3OH, c: CH_3CN, d: ethyl acetate, e: acetone, f: THF, g: DMF, h: DMSO); (d) the longest-wavelength absorption of **2.2** in varied solvents versus the hydrogen bond basicity of solvent; (e) resonance structures for hydrogen-bonded complex of **2.2** and solvent molecules (Sol).

On the other hand, the chemical shift for N-H of **2.2** exhibits a large down-field shift when the solvent changes from CD_2Cl_2 to DMSO-d_6, indicating formation of hydrogen bonds between **2.2** and DMSO. To test whether the solvent-caused color change of **2.2** depends on hydrogen bonding with solvent molecules, the measured values of longest-wavelength absorption were plotted against the solvent hydrogen-bond basicity parameter (pK_{HB}) as shown

in Figure 2.6c. The positive correlation presented in Figure 2.6d indicates that the solvent-caused color change of **2.2** in fact depends on the hydrogen-bond basicity of solvents. In contrast, the longest-wavelength absorption of **2.3** does not exhibit apparent shift in various solvents because its shielded N-H groups are unavailable or at least much less available for hydrogen bonds with solvent molecules. This dependence can be understood in terms of the hydrogen-bonded complex **2.2**•2Sol and its resonance form **2.2'**•2Sol as shown in Figure 2.6d. The resonance form **2.2'** is expected to contribute to the longer-wavelength absorption because it has a diazatetracene substructure with greater conjugation. Therefore the factors that stabilize **2.2'** should lead to red shift of absorption band. The higher hydrogen-bond basicity a solvent has, the stronger hydrogen bond it forms with **2.2**. As a result of a stronger hydrogen bond, the N-H bond should be weakened by a greater degree leading to more negative charge on the nitrogen atoms. Such hydrogen-bond-induced negative charge can partially counterbalance the positive charge on nitrogen atoms in **2.2'** and thus stabilize the resonance form **2.2'**. With stabilization by stronger hydrogen bonds, **2.2'** can make greater contribution to the resonance structure of **2.2** leading to red shift of absorption, which depends on the hydrogen bond basicity of solvent molecules.

2.2.5 Thin Film Transistors

Semiconductor properties of **2.1** and **2.3** were tested in vacuum-deposited thin film transistors, which have octadecyltrimethoxysilane (OTMS) modified SiO_2 as dielectrics,[12] vacuum-deposited gold as top-contact drain and source electrodes and heavily doped silicon as a bottom gate electrode. However, efforts to fabricate devices from **2.2** by thermal evaporation happened to fail because it decomposed during heating under vacuum. The X-ray diffractions (XRD) from the films of **2.1** did not show any peaks indicating the amorphous nature of **2.1** in

the film. On the other hand, XRD of **2.3** exhibited four peaks in accordance with the (001), (002), (003) and (005) diffractions derived from the single crystal structures, indicating a highly crystalline film. It is found that both **2.1** and **2.3** functioned as p-type semiconductors with field effect mobility of 4–6 $\times 10^{-4}$ and 0.3–0.7 $cm^2V^{-1}s^{-1}$, respectively. The low field effect mobility of **2.1** should be attributed to the amorphous nature of its vacuum deposited film as it is well known that the field effect mobility is very sensitive to the crystallinity of the thin film.[13] The disordered arrangement of **2.1** in the thin films prevents evaluating the effect of hydrogen bonding on charge transport by comparing the field effect mobilities of **2.1** and other N-heteropentacenes that do not form hydrogen bonds in the solid state. Shown in Figure 2.7 are the typical transfer *I-V* curves for the thin film transistors of **2.3**. From the transfer *I-V* curve, a field-effect mobility of 0.5 $cm^2V^{-1}s^{-1}$ is measured in the saturation regime using the equation: $I_{DS} = (\mu WC_i/2L)(V_G - V_T)^2$ and C_i of 11nF/cm^2 for 300nm SiO_2. On/off ratio of the drain current obtained between 0 and -80 V gate bias is greater than 1×10^5.

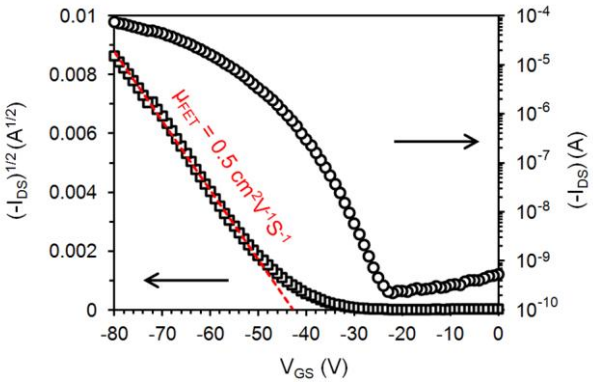

Figure 2.7 Drain current (I_{DS}) versus gate voltage (V_{GS}) with drain voltage (V_{DS}) of –50 V for a thin film transistor of **2.3** with the active channel of W = 1 mm and L = 50 μm as measured in air.

2.3 Conclusion

In conclusion, the above study has explored three new members of N-heteropentacenes that have adjacent pyrazine and dihydropyrazine rings at one end of the pentacene backbone. These designs not only allow self-complementary N-H ···N hydrogen bonds in the solid state but also lead to interesting findings on solvent-dependent UV-vis absorptions. Such solvent dependence should not be described with the classical solvotachromism in relation to solvent polarity, but can be attributed to hydrogen bonds that stabilize the resonance form of greater conjugation.

2.4 Experimental

2.4.1 Synthesis

General: The reagents and starting materials employed were commercially available and used without any further purification if not specified elsewhere. 1H-NMR or 13C-NMR spectra were recorded on a Brucker ADVANCE III 400MHz spectrometer. Mass spectra were recorded on a Therno Finnigan MAT 95 XL spectrometer. X-ray crystallography data were collected on a Bruker AXS Kappa ApexII Duo Diffractometer. UV-Vis and steady-state fluorescence spectra were taken on a Cary 5G UV-Vis-NIR spectrophotometer and a Hitachi F-4500 spectrofluorometer respectively. Melting points, without correction, were measured using a Nikon Polarizing Microscope ECLIPSE 50i POL equipped with an INTEC HCS302 heating stage.

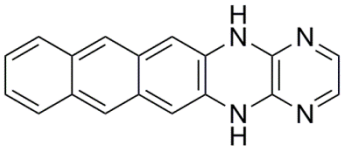

5,14-dihydro-1,4,5,14-tetraazapentacene (2.1)

2,3-Dihydroxyanthracene (440 mg, 2 mmol) and 2,3-diaminopyrazine (267 mg, 2.4 mmol) were mixed well and ground together with a mortar and pestle. The resulted mixture was heated at 205 to 215 ℃ for 3 hours under N_2 atmosphere. The crude product was cooled down to room temperature and ground with acetone. The resulting slurry was filtered, washed by acetone for several times, and dried under vacuum with P_2O_5. 560 mg of 5,14-dihydro-1,4,5,14-tetraazapentacene was obtained as brown powder in a yield of 98%. ^{1}H-NMR (DMSO-d_6) δ (ppm): 6.77 (s, 2H), 7,11 (s, 2H), 7.27 (dd, J_1=6.4Hz, J_2=3.2Hz, 2H), 7.76 (dd, J_1=6.4Hz, J_2=3.2Hz, 2H), 7.87 (s, 2H), 9.84 (s, 2H). ^{13}C-NMR (DMSO-d_6) δ (ppm): 105.7, 123.1, 124.9, 127.8, 130.4, 131.3, 132.8, 141.0, 142.3. HRMS (EI^+):cacld. for $C_{18}H_{12}N_4$ ($[M]^+$): 284.1056, found: 284.1050. Melting point: 366-367 ℃.

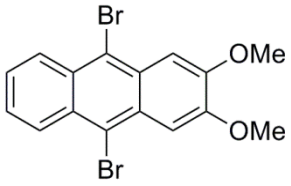

9,10-dibromo-2,3-dimethoxyanthracene

To a suspension of 2,3-dimethoxyanthracene (478 mg, 2 mmol) in 40ml of acetic acid added a solution of bromine (0.23 ml, 4.5 mmol) in 2.3ml of acetic acid over 5 minutes. Yellow solid formed immediately. The resulting mixture was stirred for another 1 hour at room temperature, and then quenched with saturated aqueous solution of $Na_2S_2O_3$. The yellow solid was filtered,

washed with water for several times and dried under vacuum with P_2O_5, yielding 732 mg of 9,10-dibromo-2,3-dimethoxyanthracene in a yield of 92%. ^{1}H-NMR ($CDCl_3$) δ(ppm): 4.12 (s, 6H), 7.57 (dd, J_1 = 6.0Hz, J_2 = 2.8Hz, 2H), 7.75 (s, 2H), 8.49 (dd, J_1 = 6.0 Hz, J_2 = 2.8 Hz, 2H).^{13}C-NMR ($CDCl_3$) δ (ppm): 56.3, 105.6, 120.9, 126.7, 127.9, 128.1, 130.1, 151.6. HRMS(EI^+): cacld. for $C_{16}H_{12}Br_2O_2$ ($[M]^+$): 395.9179, found: 395.9192. Melting point: 218-220 ℃.

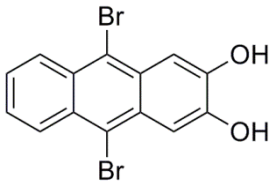

9.10-dibromoanthracene-2,3-diol

To a solution of 9,10-dibromo-2,3-dimethoxyanthracene (722 mg, 1.8 mmol) in 50ml of anhydrous dichloromethane at 0 ℃ under an atmosphere of N_2 was added 18ml (18 mmol) of boron tribromide solution (1 M) in dichloromethane. The resulting mixture was heated to reflux for 3 hours under N_2. After cooled down to room temperature, the reaction mixture was quenched with ice-water, and then extracted with diethyl ether for three times. The organic layers were combined and dried with anhydrous sodium sulfate. Removal of solvents under reduced pressure yielded 650 mg of 9,10-dibromo-anthracene-2,3-diol as brown powder in a yield of 99 %. ^{1}H-NMR (Acetone-d_6) δ(ppm): 7.57-7.61 (m, 2H), 7.90 (s, 2H), 8.39-8.43 (m, 2H), 9.39 (s, 2H).^{13}C-NMR (Acetone-d_6) δ(ppm): 109.3, 120.2, 127.4, 128.3, 129.2, 130.3, 150.2. HRMS (EI^+): cacld. for $C_{14}H_8Br_2O_2$ ($[M]^+$): 367.8866, found: 367.8851. Melting point: 168-171 ℃ (decomposed).

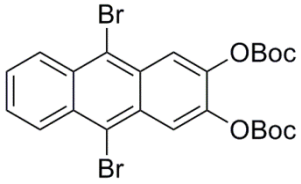

9,10-dibromo- 2,3-bis(*tert*-butyoxycarbonyloxy)-anthracene

To a solution of 9.10-dibromoanthracene-2,3-diol (654 mg, 1.8 mmol) in 20 ml of anhydrous THF at 0 ℃ were added 4-dimethylaminopyridine (21.7 mg, 0.18 mmol) and di-tert-butyl dicarbonate (1.55 g, 7.2 mmol). The resulting reaction mixture was warmed to room temperature and stirred over night, then quenched with saturated aqueous solution of NH_4Cl and extracted with ethyl acetate. The extracts were dried over anhydrous Na_2SO_4, concentrated under reduced pressure. The crude product was purified by column chromatography on silica gel using CH_2Cl_2: hexane (1 : 2) as eluent yielding 1.01 g of 9,10-dibromo- 2,3-bis(*tert*-butyoxycarbonyloxy)-anthracene as yellow crystal in a yield of 99%. ^{1}H-NMR ($CDCl_3$) δ (ppm): 1.61(s, 18H), 7.60 (dd, J_1 = 6.8Hz, J_2 = 3.2 Hz, 2H), 8.49 (dd, J_1 = 6.8Hz, J_2 = 3.2 Hz, 2H), 8.51 (s, 2H).^{13}C-NMR ($CDCl_3$) δ (ppm): 27.8, 84.5, 121.0, 122.9, 127.9, 128.4, 129.3, 131.2, 143.4, 150.7. HRMS (EI^+): cacld. for $C_{24}H_{24}Br_2O_6$ ($[M]^+$): 567.9916, found:567.9930. Melting point: 127-129 ℃.

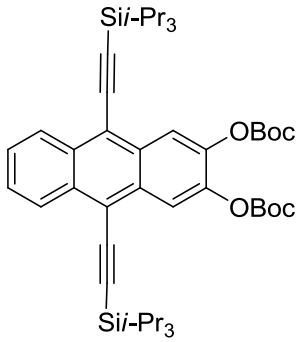

9,10-bis((triisopropylsilyl)ethynyl)-2,3-bis(tert-butyoxycarbonyloxy)-anthracene

Under an atmosphere of N_2, a mixture of 9,10-dibromo-2,3-bis(*tert*-butyoxycarbonyloxy) anthracene (568 mg, 1.0 mmol), $Pd(PPh_3)_2Cl_2$ (70 mg, 0.1mmol), CuI (38 mg, 0.2mmol), PPh_3 (52 mg, 0.2 mmol) was dissolved in 5.0 ml Et_3N (N_2 purged before use). To the resulting solution was added triisopropylsilyl acetylene (1.0 ml, 4.5 mmol) under an atmosphere of N_2. The resulting reaction mixture was heated to reflux for 2 days, then cooled down to room temperature and concentrated under reduced pressure. The crude product was purified by column chromatography on silica gel using CH_2Cl_2: Hexane (1 : 3 to 1 : 2) yielding 591 mg of 9,10-bis((triisopropylsilyl)ethynyl)-2,3- bis(tert-butyoxycarbonyloxy)-anthracene as yellow crystal in a yield of 78%. ^{1}H-NMR ($CDCl_3$) δ (ppm): 1.24-1.25(m, 42H), 1.59 (s, 18H), 7.60 (dd, J_1 = 6.4Hz, J_2 = 3.2Hz, 2H), 8.50 (s, 2H), 8.59 (dd, J_1 = 6.4Hz, J_2 = 3.2 Hz, 2H).^{13}C-NMR ($CDCl_3$) δ (ppm):11.6, 19.0, 27.7, 84.1, 103.0, 105.5, 118.7, 119.9, 127.2, 127.3, 130.8, 132.6, 142.8, 150.9. HRMS (EI^+): cacld. for $C_{46}H_{66}O_6Si_2$ ($[M]^+$): 770.4392, found:770.4355. Melting point: 186-188 ℃.

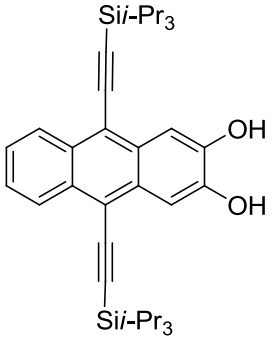

9,10-bis((triisopropylsilyl)ethynyl) -anthracene-2,3-diol (2.5)

To a solution of 9,10-bis((triisopropylsilyl)ethynyl)-2,3-bis(tert-butyoxycarbonyloxy)-anthracene (300 mg, 0.39 mmol) in 20 ml of CH_2Cl_2 was added 2.0 ml of trifluoroacetic acid slowly. The resulting reaction was stirred for 6 hours at room temperature. After quenched by $NaHCO_3$

solution, the organic layer was separated and the aqueous layer was extracted with CH_2Cl_2 for three times. The organic layers were combined and dried with anhydrous sodium sulfate, filtered, and concentrated under reduced pressure. The crude product was purified by column chromatography on silica gel using CH_2Cl_2: Hexane (1: 1) to pure CH_2Cl_2 as eluent yielding 114 mg of 9,10-bis((triisopropylsilyl)ethynyl) -anthracene-2,3-diol as blue crystal in a yield of 50%. ^{1}H-NMR ($CDCl_3$) δ (ppm): 1.25-1.26 (m, 42H), 6.15 (s, 2H), 7.52 (dd, J_1 = 6.4 Hz, J_2 = 3.2 Hz, 2H), 7.97 (s, 2H), 8.54 (dd, J_1 = 6.4Hz, J_2 = 3.2 Hz, 2H).^{13}C-NMR ($CDCl_3$) δ(ppm):11.7, 19.1, 103.9, 104.0, 108.7, 116.6, 126.2, 127.0, 130.1, 131.7, 146.1. HRMS (EI^+): cacld. for $C_{36}H_{50}O_2Si_2$ ($[M]^+$): 570.3344, found: 570.3355. Melting point: 148 ℃ (decomposed).

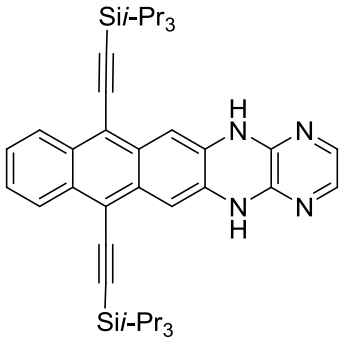

7,12-bis((triisopropylsilyl)ethynyl)-5,14-dihydro-1,4,5,14-tetraazapentacene (2.2)

9,10-bis((triisopropylsilyl)ethynyl)-2,3-diol-anthracene (114 mg, 0.2 mmol) and 2,3-diaminopyrazine (112 mg, 1.0 mmol) were mixed well and ground together with a mortar and pestle. The resulted mixture was heated at 205 to 215 ℃ for 0.5 hours under an atmosphere of N_2. The crude product was cooled down to room temperature, and then purified by column chromatography on silica gel using CH_2Cl_2： ethyl acetate (20： 1 to 10： 1) as eluent yielding 40 mg of 7,12-bis((triisopropylsilyl)ethynyl) -5,14-dihydro-1,4,5,14-tetraazapentacene as yellow powder in a yield of 25%. ^{1}H-NMR ($CDCl_3$) δ (ppm): 1.24-1.26(m, 42H), 6.73 (s, 2H), 7.27 (s,

2H), 7.34 (s, 2H), 7.46 (dd, J_1 = 6.4 Hz, J_2 = 3.2 Hz, 2H), 8.39 (dd, J_1 = 6.4 Hz, J_2=3.2 Hz, 2H).^{13}C-NMR ($CDCl_3$) δ (ppm): 11.6, 19.1, 103.5, 104.0, 106.6, 115.9, 126.4, 126.9, 131.4, 131.7, 132.2, 133.2, 141.6. HRMS (EI^+): cacld. for $C_{40}H_{52}N_4Si_2$ ($[M]^+$): 644.3725, found: 644.3715. Melting point: 239-240 ℃ (Acetone).

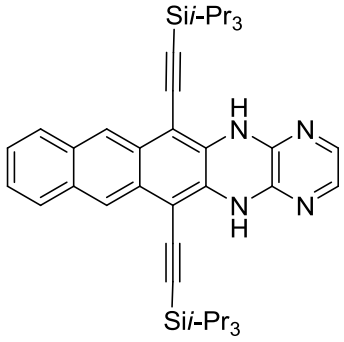

6,13-bis((triisopropylsilyl)ethynyl)-5,14-dihydro-1,4,5,14-tetraazapentacene (2.3)

Under atmosphere of N_2, 5.0 ml of toluene was added to a mixture of 1,4-bis((triisopropylsilyl) ethynyl)-anthracene-2,3-diamine [14] (191 mg, 0.34 mmol), 2,3-dichloropyrazine (60 mg, 0.40 mmol), $Pd_2(dba)_3$ (31 mg, 0.04 mmol), 1,1'-bis(diphenylphosphino)ferrocene (28 mg, 0.06 mmol) and Cs_2CO_3 (328 mg, 1.01 mmol). The resulting mixture was heated to reflux for 2 days, then cooled down to room temperature and concentrated under reduced pressure. The crude product was cooled down to room temperature, and then purified by column chromatography on silica gel using CH_2Cl_2 : Hexane (1 : 2 to 1 : 1) as eluent yielding 154 mg of 6,13-bis((triisopropylsilyl) ethynyl)-5,14-dihydro-1,4,5,14- tetraazapentacene as yellow crystals in a yield of 71%. ^{1}H-NMR ($CDCl_3$) δ (ppm): 1.23-1.26 (m, 42H), 7.25 (s, 2H), 7.35 (s, 2H), 7.37 (dd, J_1 = 6.4 Hz, J_2 = 3.2Hz, 2H), 7.80(dd, J_1=6.4Hz, J_2=3.2Hz, 2H) 8.37(s, 2H).^{13}C-NMR ($CDCl_3$) δ (ppm): 11.5, 19.0, 99.7, 105.5, 123.6, 125.7, 128.0, 128.2, 132.0, 133.6, 134.6, 140.6. HRMS (EI^+): cacld. for

$C_{40}H_{53}N_4Si_2$ ($[M+H]^+$): 645.3803, found ($[M+H]^+$): 645.3846. Melting point: 289-290 ℃ (Ethyl Acetate).

2.4.2 Cyclic Voltammetry

Cyclic voltammetry was performed in a solution of anhydrous DMF or a solution of anhydrous CH_2Cl_2 both with 0.1M tetrabutylammonium hexafluorophosphate (Bu_4NPF_6) as supporting electrolyte, at a scan rate of 50 mV s^{-1}. A platinum bead was used as a working electrode, a platinum wire was used as an auxiliary electrode, and a silver wire was used as a psedo-reference. $FeCp_2^+/FeCp_2^0$ or $CoCp_2^+/CoCp_2^0$ was used as an internal standard. Potentials were recorded versus $FeCp_2^+/FeCp_2^0$. The commonly used HOMO energy level of ferrocene is −4.80 eV, and $CoCp_2^+/CoCp_2^0$ is -1.35V vs $FeCp_2^+/FeCp_2^0$ as measured using $FeCp_2^+/FeCp_2^0$ as an internal standard.

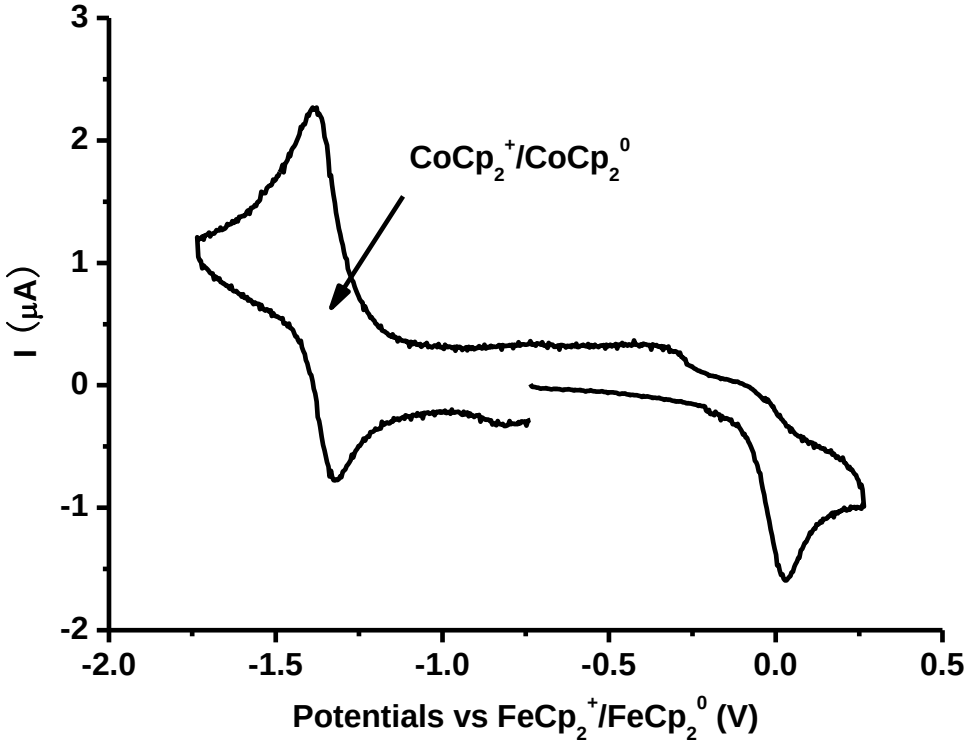

Figure 2.8 Cyclic voltammogram of **2.1** recorded in DMF with $CoCp_2^+/CoCp_2^0$ as the internal standard.

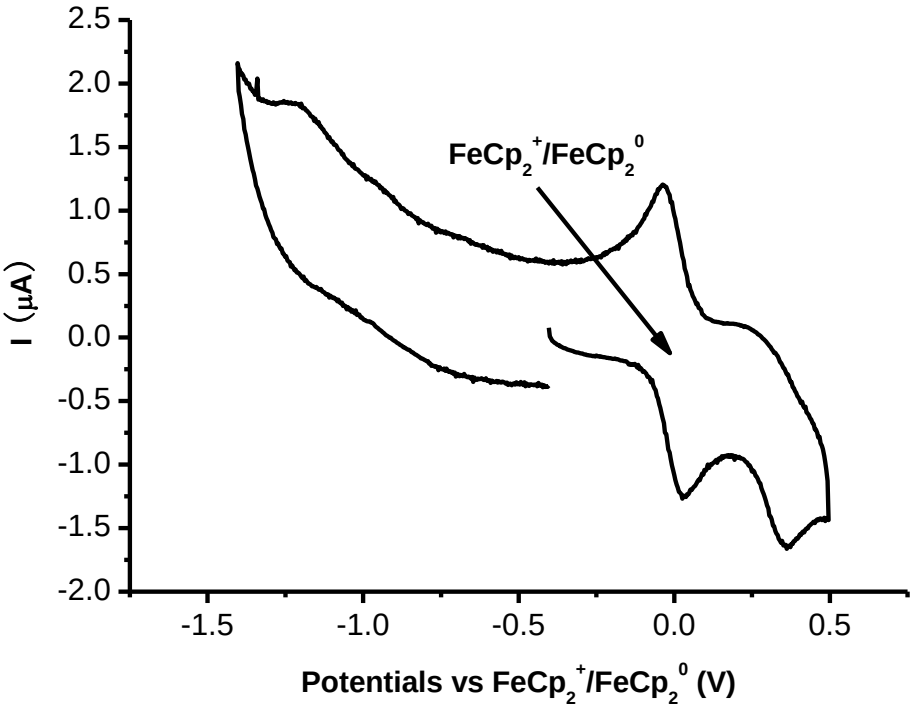

Figure 2.9 Cyclic voltammogram of **2.2** recorded in CH_2Cl_2 with $FeCp_2^+/FeCp_2^0$ as the internal standard.

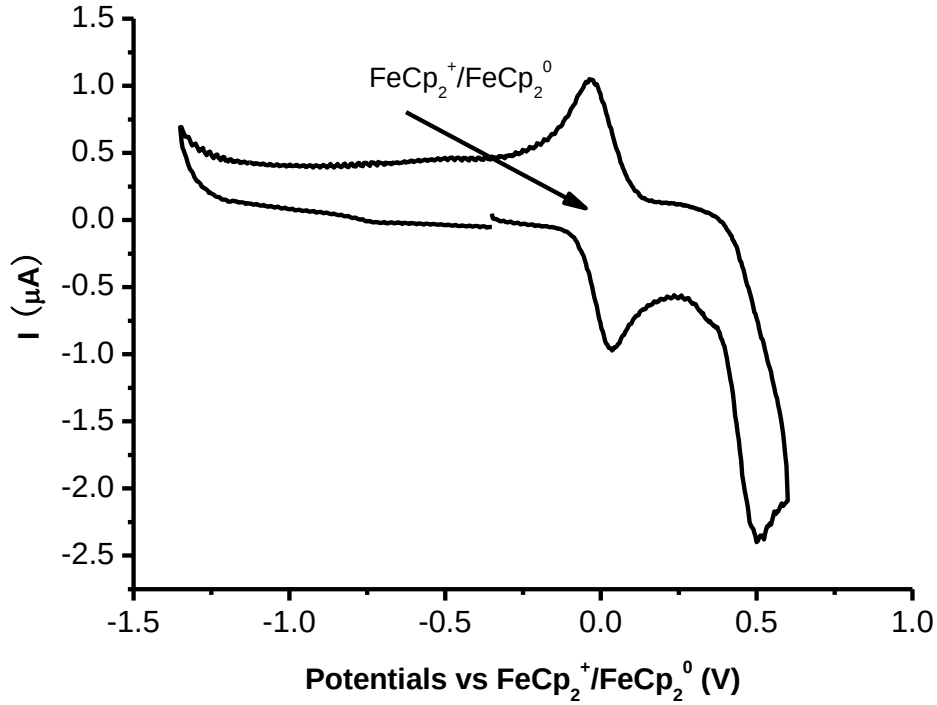

Figure 2.10 Cyclic voltammogram of **2.3** recorded in CH_2Cl_2 with $FeCp_2^+/FeCp_2^0$ as the internal standard.

2.4.3 UV-vis absorption sepectroscopy

UV-vis absorption spectra were recorded from solutions of **2.1**-**2.3** in DMF (for **2.1**) or dichloromethane (for **2.2** and **2.3**) at a concentration of 5×10^{-5} mol/L.

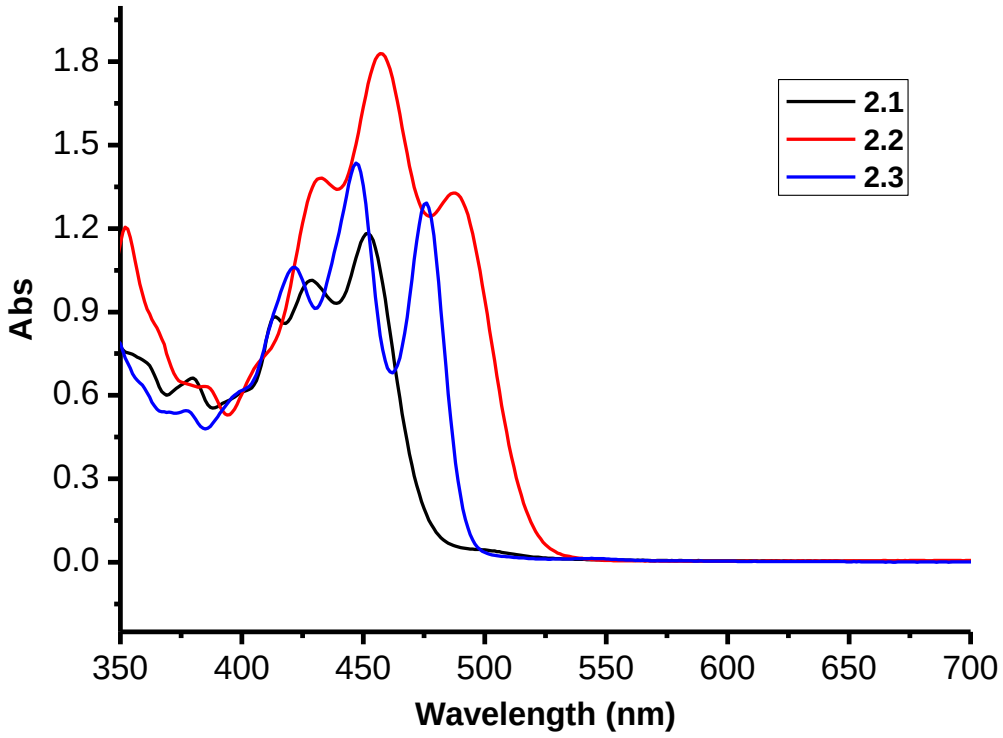

Figure 2.11 Absorption spectra of **2.1**, **2.2** and **2.3** as recorded from solutions of **2.1** in DMF and **2.2** and **2.3** in CH_2Cl_2 at the same concentration of 5×10^{-5} mol/L.

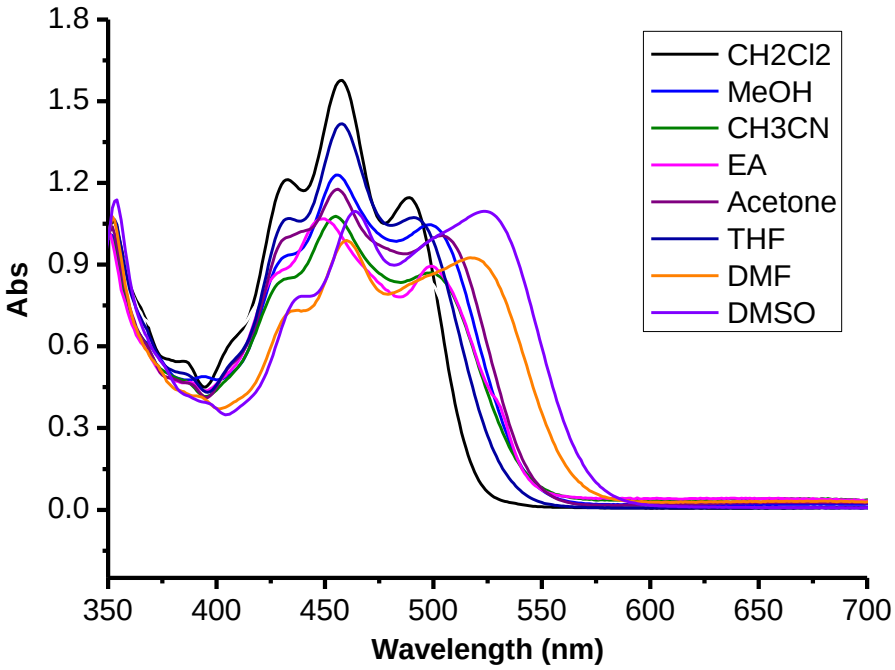

Figure 2.12 UV-vis absorption of **2.2** in different solvents at the same concentration of 5×10^{-5} mol/L.

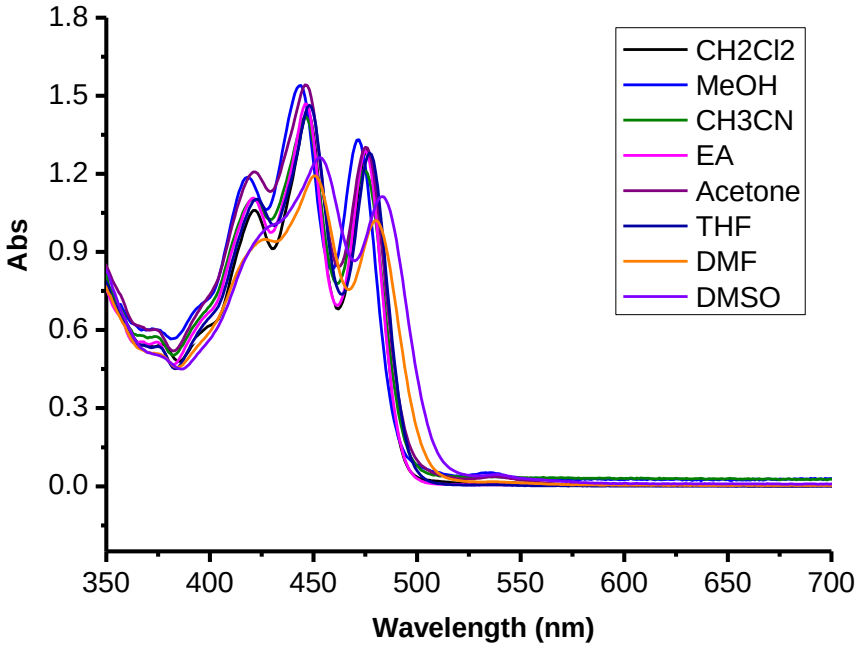

Figure 2.13 UV-vis absorption of **2.3** in different solvents at the same concentration of 5×10^{-5} mol/L.

2.4.4 Fabrication and Characterization of Vacuum-Deposited Thin Films and Transistors

The dielectric SiO_2 surface was modified with a self-assembled monolayer of octadecyl-trimethoxysilane (OTMS) by following the reported procedures.[12] The semiconductor thin films were deposited using an Edwards Auto 306 vacuum coater with a Turbomolecular pump at a pressure of 2.0×10^{-6} torr or lower, with a deposition rate of ca. 2 nm/min to desired thickness. During vacuum deposition the distance between source and substrate was 18.5 cm, and the substrate was kept at room temperature. Top contact drain and source gold electrodes were vacuum-deposited through a shadow mask onto the films in the same vacuum chamber, and the resulting semiconducting channels were 50μm(L)×1mm(W), 100μm(L)×1mm(W), 150μm(L)×1mm(W), 50μm(L)×2mm(W) and 100μm(L)×2mm(W). In these transistors highly n-doped silicon functioned as gate electrode and OTMS-treated 300 nm- thick SiO_2 functioned as dielectrics.

Atomic Force Microscopy (AFM): Thin films deposited on OTMS treated SiO_2/Si were used for AFM studies. The topographic images were obtained using a Nanoscope IIIa Multimode Microscope from Digital Instruments. The AFM images were collected using tapping mode and in air under ambient conditions. The topographic images were collected from multiple samples, and for each sample, different regions were scanned to ensure reproducibility.

X-ray diffraction (XRD): XRD data were recorded with a SmartLab X-Ray Refractometer from the 50 nm-thick thin films, which were vacuum-deposited on OTMS-treated SiO_2 surface at a substrate temperature of 25 ℃.

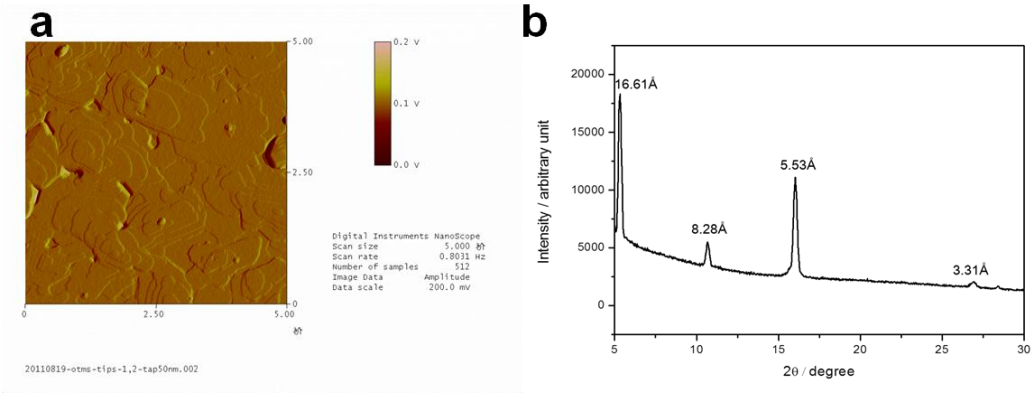

Figure 2.14 (a) AFM image and (b) X-ray diffractions from of a 50 nm-thick film of **2.3**.

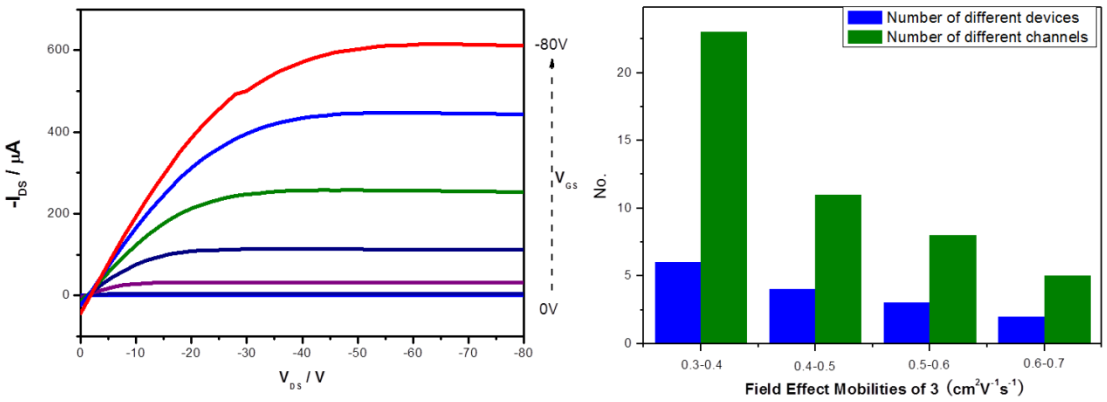

Figure 2.15 (Left) Drain current (I_{DS}) versus drain voltage (V_{DS}) with varying gated voltage (V_{GS}, from 0 to −80 V in −10 V steps) for typical thin film transistors of **3** deposited on OTMS-treated SiO_2 at substrate temperature of room temperature with channel dimension of W = 1 mm and L = 50 μm and (Right) Summary of thin film transistor performance of **3** deposited on OTMS-treated SiO_2 under high vacuum.

Electrical Characterization: The current-voltage measurement was carried out on a probe station with a Keithley 4200 Semiconductor Characterization System at room temperature in ambient air. The field effect mobility was measured from transfer I-V curves in the saturation

regime using the equation: $I_{DS} = (\mu WC_i/2L)(V_G - V_T)^2$, where I_{DS} is the drain current, μ is field effect mobility, C_i is the capacitance per unit area for 300 nm SiO_2 (11 nF cm^{-2}), W is the channel width, L is the channel length, and V_G and V_T are the gate and threshold voltage, respectively.

2.5 Reference

1. Miao, Q. *Synlett*, **2012**, *23*, 326.
2. Winkler, M.; Houk, K. N. *J. Am. Chem. Soc.* **2007**, *129*, 1805.
3. Anthony, J. E. *Angew. Chem. Int. Ed.* **2008**, *47*, 452.
4. (a) Liu, Y.-Y.; Song, C.-L.; Zeng, W.-J.; Zhou, K.-G.; Shi, Z.-F.; Ma, C.-B.; Yang, F.; Zhang, H.-L.; Gong, X. *J. Am. Chem. Soc.* **2010**, *132*, 16349. (b) Liang, Z.; Tang, Q.; Xu, J.; Miao, Q. *Adv. Mater.* **2011**, *23*, 1535. (c) Song, C. L.; Ma, C.-B.; Yang, F.; Zeng, W.-J.; Zhang, H.-L.; Gong, X. *Org. Lett.* **2011**, 2880. (d) Wang, C.; Liang, Z.; Liu, Y.; Wang, X.; Zhao, N.; Miao, Q.; Hu, W.; Xu, J. *J. Mater. Chem.* **2011**, *21*, 15201. (e) Liang, Z.; Tang, Q.; Mao, R.; Liu D.; Xu, J.; Miao, Q. *Adv. Mater.* **2011**, *23*, 5514.
5. Tverskoy, O.; Rominger, F.; Peters, A.; Himmel, H.-J.; Bunz, U. H. F. *Angew. Chem. Int. Ed.* **2011**, *50*, 3557.
6. (a) Clar, E. *The Aromatic Sextet*, Wiley: New York, **1972**. (b) Harvey, R. G. *Polycyclic Aromatic Hydrocarbons*, Wiley-VCH: New York, **1997**.
7. The 1H NMR spectra of **2.1** and 2,3-diaminopyrazine were both measured in DMSO-d_6.
8. The commonly used HOMO energy level of ferrocene is −4.80 eV. See: (a) Pommerehne, J.; Vestweber, H.; Guss, W.; Mahrt, R. F.; Bässler, H.; Porsch, M.; Daub, J. *Adv. Mater.* **1995**,

7, 551. (b) D'Andrade, B. W.; Datta, S.; Forrest, S. R.; Djurovich, P.; Polikarpov, E.; Thompson, M. E. *Org. Electron.* **2005**, *6*, 11.

9. Tang, Q.; Zhang, D.; Wang, S.; Ke, N.; Xu, J.; Yu, J. C.; Miao, Q. *Chem. Mater.* **2009**, *21*, 1400.
10. Miao, Q. PhD thesis, Columbia University, **2005**.
11. Reichardt, C.; Welton, T. Solvents and Solvent Effects in Organic Chemistry, 4th Ed. Wiley-VCH, **2011**, Weinheim.
12. Ito, Y.; Virkar, A. A.; Mannsfeld, S.; Oh, J. H.; Toney, M.; Locklin, A.; Bao, Z. *J. Am. Chem. Soc.* **2009**, *131*, 9396.
13. Dimitrakopoulos, C. D.; Malenfant, P. R. L. *Adv. Mater.* **2002**, *14*, 99.
14. Appleton, A. L.; Brombosz, S. M.; Barlow, S.; Sears, J. S.; Bredas, J.-L.; Marder, S. R.; Bunz, U. H. F. *Nat. Commun.* **2010**, *1*, 91.

Chapter 3 Highly Electron-Deficient Hexaazapentacenes and Their Dihydro Precursors*

3.1 Introduction

N-heteropentacenes, following the parent hydrocarbon, pentacene, have recently arisen as a new family of organic semiconductors exhibiting high performance in organic field effect transistors (OFETs). [1] Unlike pentacene, N-heteropentacenes have their properties, including solubility, electronic structures, molecular packing and semiconductor properties, highly dependent on the pattern of N atoms, which is defined by the number, position and valence state of N atoms in the pentacene backbone.[2, 3] Unprecedented patterns of N atoms therefore have good opportunities leading to new findings on N-heteropentacenes.[3, 4]

Here we report novel silylethynylated N-heteropentacenes (**3.1a-c**) that have three adjacent pyrazine rings at the center of pentacene backbone as shown in Figure 3.1. These hexaazapentacenes clearly differentiate themselves from the long-known fluorubine [5] and recently reported N-substituted fluorubines [6] by having all the six N atoms in the imine (unsaturated) form. With this unprecedented pattern of N-atoms, **3.1a-c** are found to exhibit the record low energy level of lowest unoccupied molecular orbital (LUMO) for N-heteropentacenes and able to oxidize dihydroanthracene to anthracene. The synthetic precursors of **3.1a-c** are the corresponding dihydrohexaazapentacenes **3.2a-c** (shown in Scheme 3.1), which exhibit interesting H-bonding that is not observed from fluorubine or N-substituted fluorubines.

---

* This Section is reprinted with small modification from: Zikai He, Renxin Mao, Danqing Liu, Qian Miao*. *Org. Lett.*, **2012**, *16*, 4190. Synthesis, characterization and crystal growth were done by me. Crystal structures were solved by Ms. Hoi Shan Chan. Thin film transistor fabrication and characterization was done by Ms. Danqing Liu. DFT calculation was done by Mr. Renxin Mao and me.

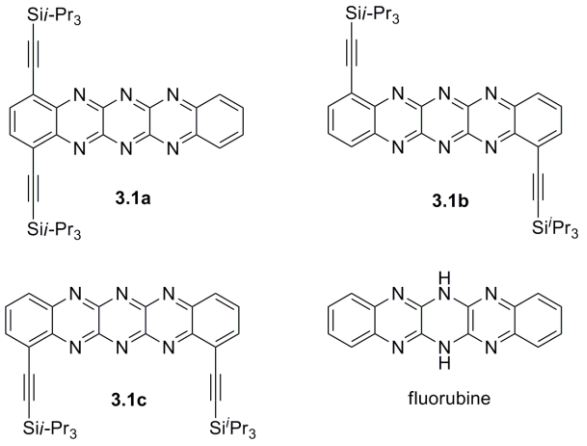

Figure 3.1 Structures of silylethynylated hexaazapentacenes (**3.1a-c**) and fluorubine.

3.2 Results and Discussion

3.2.1 Synthesis

Shown in Scheme 3.1 is the synthesis of **3.1a-c**, which started with the construction of dihydrohexaazapentacene backbone from dichlorodicyanopyrazine by two subsequent nucleophilic substitutions. Among the three isomers of dibromo-dihydrohexaazapentacene, **3.3b** and **3.3c** were yielded as a nearly 1:1 mixture, which was used in the next step without separation due to their low solubility. Sonogashira reaction of **3.3a-c** with triisopropylacetylene resulted in dihydrohexaazapentacenes **3.2a-c**, and **3.2b** and **3.2c** were separated conveniently using column chromatography on silica gel. It is worth noting that this Sonogashira reaction required long reaction time (at least 48 hours) because of the poor solubility and low reactivity of **3.3a-c**. Dihydrohexaazapentacenes **3.2a-c** exhibited very different R_f (ratio to the front) values on silica gel thin layer chromatography (TLC). The highest R_f value and lowest solubility of **3.2a** can be attributed to the fact that its N atoms are shielded by the bulky triisopropylsilyl groups on the both sides of the pentacene backbone. In contrast, the lowest R_f value and highest solubility of **3.2c** can be attributed to its completely exposed N atoms on one side, which lead to stronger

interactions with the silica gel and polar solvent molecules. Unlike most of the reported silylethynylated dihydro-N-heteropentacenes,[7] **3.2a-c** are resistant to oxidation by MnO_2 [8] as well as O_2 in air, DDQ and pyridinium chlorochromate (PCC). PbO_2 was finally found effective to oxidize **3.2a-c** to the corresponding hexazapentacenes (**3.1a-c**) almost quantitatively. Similar to the previously reported hexaazahexacene,[9] **3.1a-c** changed gradually back to **3.2a-c**, respectively, when their solutions or solids were stored in air under ambient light for several days. However, the mechanism for this reaction remains an unanswered question.

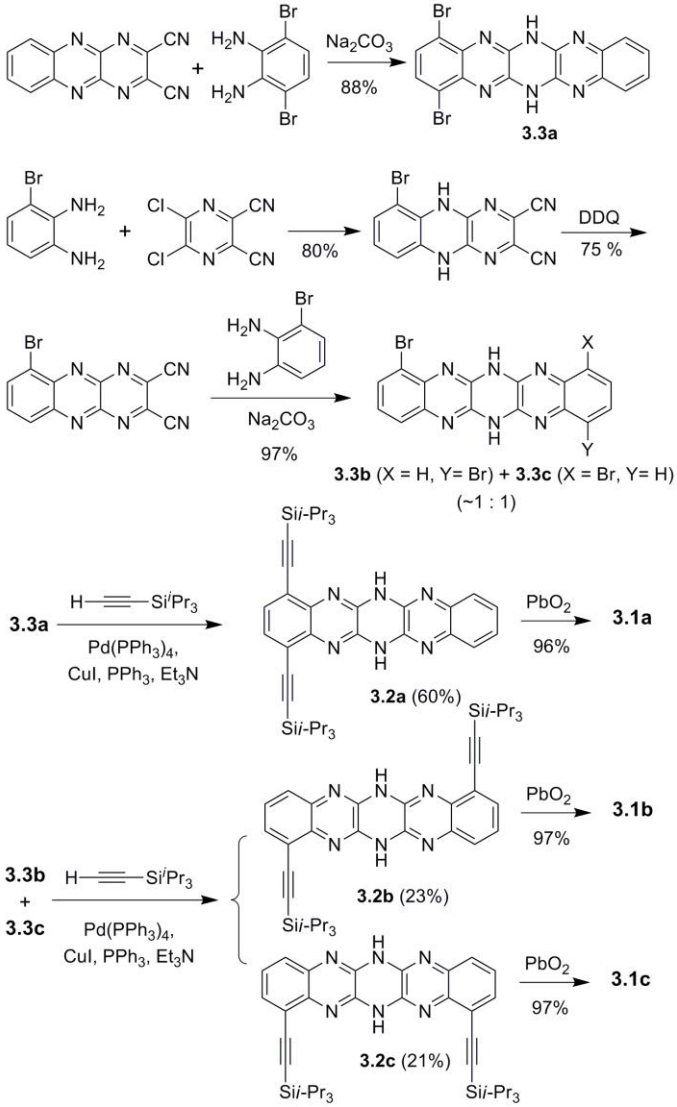

Scheme 3.1 Synthesis of hexaazapentacenes **3.1a-c**.

3.2.2 Structures

Actually, the backbone studied here, 6,13-dihydro-5,6,7,12,13,14-hexaazapentacene and its derivatives were known for about a century, called fluorubine.[10] However, effective synthesis and fully characterization was not reported until recently, [11] particularly fluorubine itself and saturated forms. Fluorubine and its derivatives may each in principle exist as four isomers by varying the position of H atoms that are bonded to N atoms. As the representative, the four isomers of fluorubine are shown in Figure 3.2. According to calculations by Wu and co-workers, dihydroazapentacenes are stabilized by ethenamine conjugation.[8] Electron deficient ethenamine will increase the delocalized of N lone pair electrons, leading higher stability. **Fluorubine** is more energetically favorable than other three ones because it was stabilized and benefits substantially from four dihydropyrazine imidamide (N-doped-ethenamine) conjugations. Moreover, we calculated the heats of hydrogenation $\Delta H(H_2)$ for the fluorubine from their parent hexaazapentacene.[8] Although they loss aromaticity in hyrogenation, they are stabilized by imidamide conjugations and/or ethenamine conjugations involving the N lone pairs, so $\Delta H(H_2)$ for four isomers is exothermic. $\Delta H(H_2)$ should become increasing exothermic as the stability increases. The DFT results are in agreement with our conclusion that **Fluorubine** is the most stable isomer because it releases most heat after hydrogenation. On the other hand, the 1H NMR of fluorubine shows one singlet peak related to NH groups and two sets of peaks with characteristic AA'XX' patterns, in agreement with the D_{2h} symmetry thus excluding other three structures. As shown in Figure 3.2, in the single crystals of **3.1a** and **3.2b**, the C5a-N6 bond is longer than the C5a-N5 bond in **3.1a**; and the C5a-N6 and C6a-N6 bonds are longer than the C12a-N12 bond and C13a-N14 in **3.2b**. These bond lengths support the structure of **Fluorubine**, which has dihydropyrazine as the third ring.

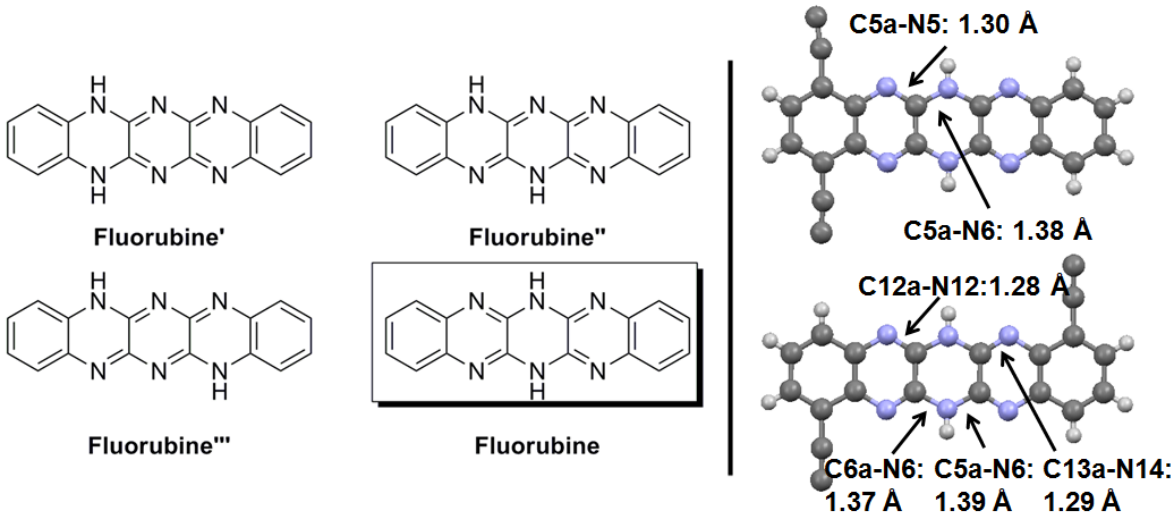

Figure 3.2 Possible isomeric structures of fluorubine and the crystal structure of **3.2a** and **3.2b**. (C, N, and H atoms are shown in grey, blue, and white, respectively).

3.2.3 Electronic Structures and DFT calculations

Hexaazapentacenes **3.1a-c** form green solution while dihydrohexazapentacenes **3.2a-c** form yellow solution with strong green fluorescence. In comparison to the reported tetraazapentacenes that have two silylethynyl groups attached to the internal rings,[3, 9] **3.1a**, **3.1b** and **3.1c** exhibit blue-shifted, weaker and broader longest-wavelength absorptions at 630 nm, 597 nm and 588 nm, respectively, as shown in Figure 3.5. The cyclic voltammograms of **3.1a-c** (shown in the Experimental Section) exhibit two reversible one-electron reduction waves in the testing window. The first half-wave reduction potential vs. ferrocenium/ferrocene is −0.26 V for **3.1a**, −0.23 V for **3.1b**, and −0.29 V for **3.1c**, from which the lowest unoccupied molecular orbital (LUMO) energy levels of **3.1a-c** are estimated as −4.54 eV, −4.57 eV and −4.51 eV, respectively.[12] **3.1a-c** have lower LUMO energy levels than the reported silylethynylated monoazapentacene, diazapentacenes and tetraazapentacenes that do not have extra substituents. Particularly, **3.1b** has the lowest LUMO energy level among all the known N-heteropentacenens

including those that have extra electron-withdrawing substituents, such as fluorine and nitro groups. The record low LUMO energy levels of **3.1a-c** are in agreement with the earlier conclusion that the LUMO energy level of N-heteropentacene goes down with the increasing number of unsaturated N atoms, [2] particularly in the internal rings of pentacene.[3] From the longest-wavelength absorptions (optical gaps) and LUMO energy levels, the energy level of highest occupied molecular orbital (HOMO) was estimated as −6.14 eV for **3.1a**, −6.33 eV for **3.1b** and −6.28 eV for **3.1c**. The very close LUMO energy levels and slightly different HOMO energy levels of **3.1a-c** suggest that C-C triple bonds have different contributions to the HOMO and LUMO. This is in agreement with the calculated HOMOs, which are delocalized to C-C triple bonds, and the calculated LUMOs, which are almost localized on the hexaazapentacene backbone.[13] On the other hand, the cyclic voltammograms of **3.2a-c** (shown in the Experimental Section) exhibit one irreversible oxidation wave and one irreversible reduction wave. From the peak potentials of these oxidation and reduction waves, the HOMO and LUMO energy levels of **3.2a-c** were estimated as shown in Table 3.1.

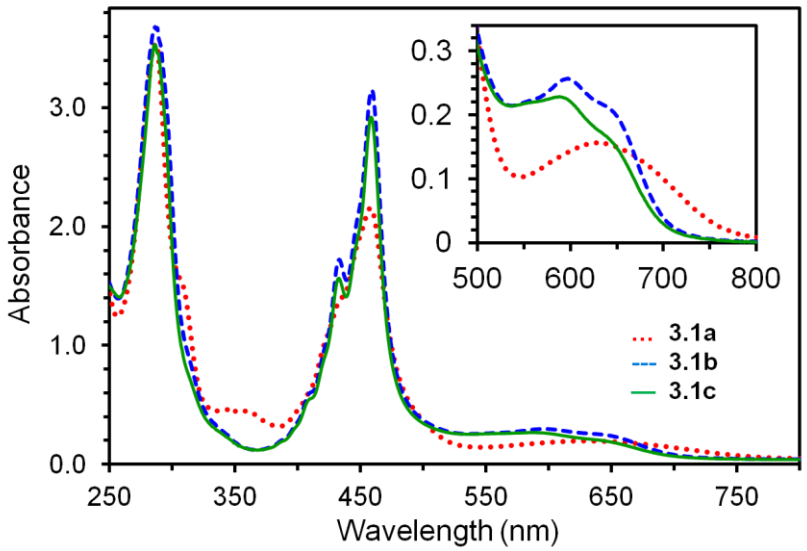

Figure 3.5 UV-vis absorption spectra of **3.1a-c** in CH_2Cl_2 (5×10^{-5}mol/L)

The frontier molecular orbitals were calculated using the following simplified model molecules with the Gaussian 09 software package. The geometries of these model molecules were first optimized at the B3LYP level of density functional theory (DFT) with the 6-31G(d, p) basis set, and the HOMO and LUMO were then calculated with the 6-311++G(d, p) basis set.

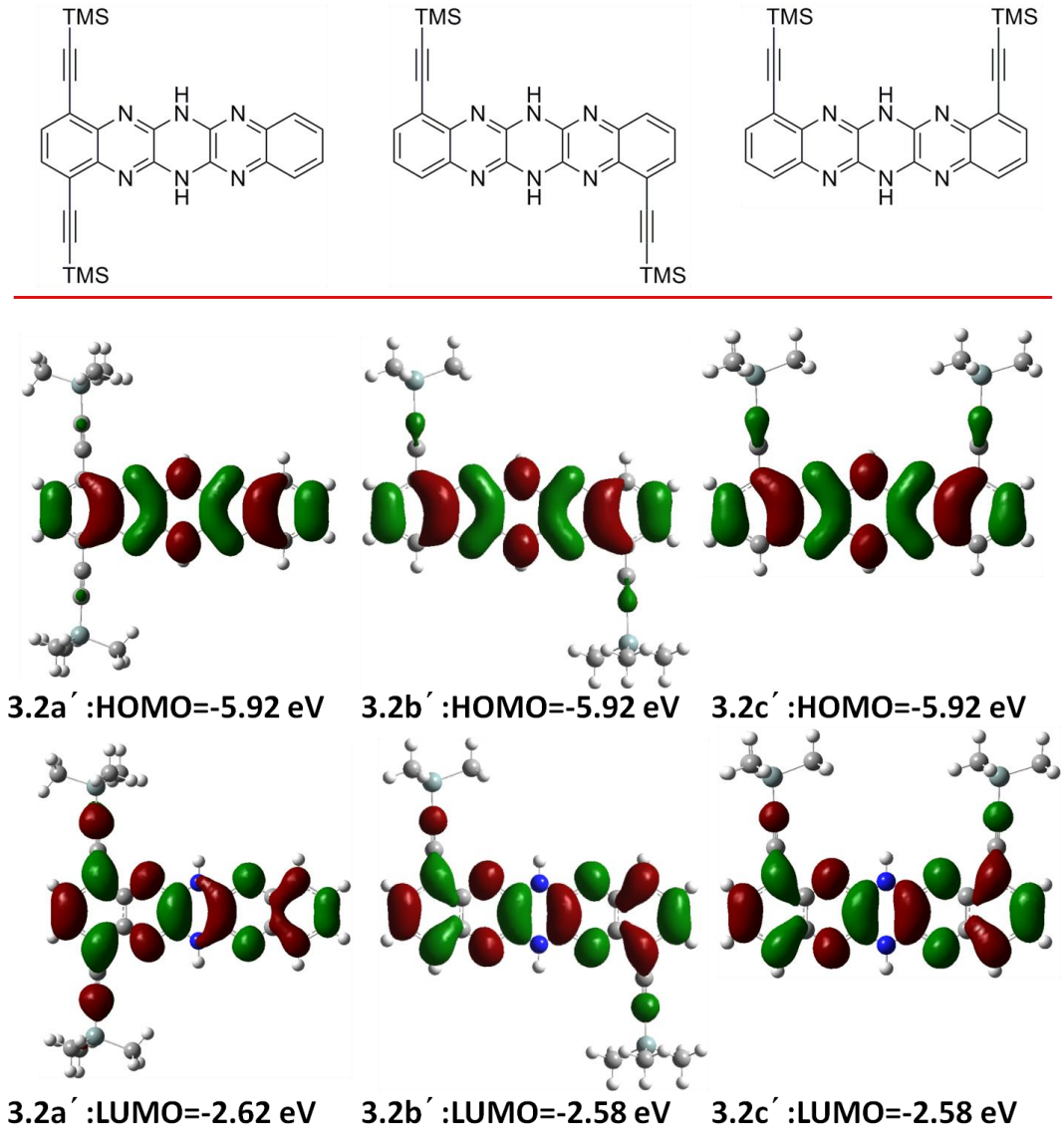

Figure 3.3 Calculated frontier molecular orbitals of **3.2a'-c'** with the energy levels.

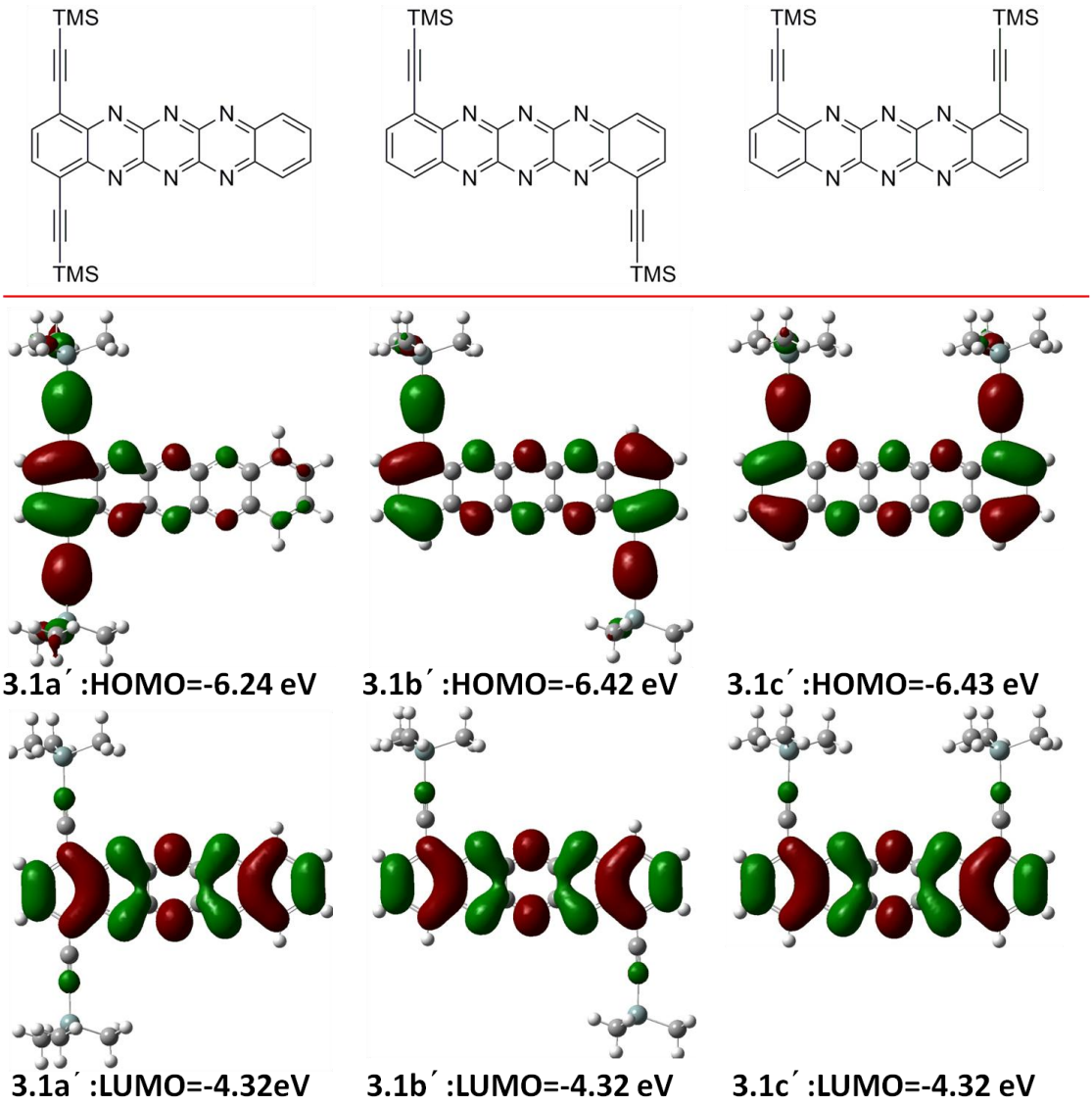

Figure 3.4 Calculated frontier molecular orbitals of **3.1a'-c'** with the energy levels.

The low LUMO energy levels of **3.1a-c** suggest that they may function as n-type semiconductors although the instability in the solid state limits their potential applications.[14] However, our attempts of fabricating thin film transistors of **3.1a-c** appeared unsuccessful because these compounds decomposed during thermal evaporation and formed disordered films with poor morphology during solution-based process. On the other hand, the relatively high

LUMO energy levels and relatively low HOMO energy levels of **3.2a-c** suggest that these compounds are not suitable candidates for either n-type or p-type semiconductors.

Table 3.1 Computational, electrochemical and optical data for **3.1a-c** and **3.2a-c**.

	Computational [a]		Electrochemical [b]				Optical [c]	
	HOMO (eV)	LUMO (eV)	E_{ox} (V)	E_{red} (V)	HOMO (eV)	LUMO (eV)	λ_{max} (nm)	Optical gap (eV)
3.1a	−6.24	−4.32	—	−0.26	—	−4.54	630	1.60
3.1b	−6.42	−4.32	—	−0.23	—	−4.57	593	1.76
3.1c	−6.43	−4.32	—	−0.29	—	−4.52	588	1.76
3.2a	−5.92	−2.62	0.81	−1.48	−5.61	−3.32	481	2.48
3.2b	−5.92	−2.58	0.79	−1.54	−5.59	−3.26	477	2.55
3.2c	−5.92	−2.58	0.80	−1.46	−5.60	−3.34	481	2.53

[a] HOMO and LUMO energy levels were calculated at the B3LYP level of DFT with 6-311++G(d,p)//6-31G(d, p) basis sets using the corresponding trimethylsilyl-substituted molecules as simplified models. [b] Potentials are reported versus ferrocenium/ferrocene as half-wave potential for reversible waves and peak wave for irreversible waves. HOMO and LUMO energy levels were estimated from HOMO = −4.80 – E_{ox} (eV) and LUMO = −4.80 − E_{red} (eV). [c] λ_{max} is for the longest-wavelength absorption as recorded from solutions in CH_2Cl_2 of 5×10^{-5}mol/L; and the optical gap is estimated from the absorption edge as recorded from the same solutions.

3.2.4 Oxidative Property

The very low LUMO energy levels of **3.1a-c** suggest that they can function as oxidants in organic reactions. To test the oxidizing ability of these hexaazapentacenes, **3.1a** was selected as the representative and used as the oxidant in the stoichiometric and catalytic oxidation of 9, 10-

dihydroanthracene. When 1 equivalent of **3.1a** was used the oxidant, dihydroanthracene was completely oxidized to anthracene after 16 hours as shown in Table 3.2 (entry 2). Because the reduction product of **3.1a** in this reaction is **3.2a**, which can be oxidized back to **3.1a** by PbO_2, it is possible to oxidize dihydroanthracene with **3.1a** in a catalytic manner with PbO_2 as the second oxidant. When 0.3 equivalent of **3.1a** and 30 equivalents of PbO_2 were used as the oxidant, dihydroanthracene was oxidized to anthracene in a yield of 89% as shown in Table 3.2 (entry 4). In control experiments, PbO_2 itself oxidized dihydroanthracene slowly to not only anthracene but also anthraquinone, which was however not observed from the crude products of the reactions using **3.1a** as the oxidant. The mechanism for this dehydrogenation reaction by **3.1a** presumably involves a transfer of hydride or a hydrogen atom from the benzyl group to the pyrazine nitrogen as suggested by its two reversible one-electron reductions.

Table 3.2 Oxidation of 9,10-dihydroanthracene by **3.1a** and PbO_2.

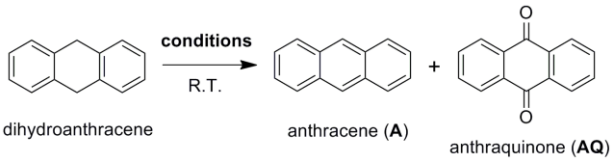

Entry	Conditions [a]	Products [b]	
		A	**AQ**
1	**1a** (1eq.), 2 h	55%	0%
2	**1a** (1eq.), 16 h	100%	0%
3	**1a** (0.3 eq.), PbO_2 (30 eq.), 2 h	22%	0%
4	**1a** (0.3 eq.), PbO_2 (30 eq.), 29 h	89%	0%
5	PbO_2 (30 eq.), 16 h	6%	3%
6	PbO_2 (30 eq.), 29 h	14%	13%

[a] The reactions were carried out in $CHCl_3$ at room temperature. [b] The yield was determined by 1H NMR from the crude product.

3.2.5 Molecular Packing

With adjacent pyrazine and dihydropyrazine rings that are not shielded by the bulky triisopropylsilyl groups, molecules of **3.2a-c** can in principle form intermolecular hydrogen bonds with each other. To study such hydrogen bonds, single crystals of **3.2a** and **3.2b** were grown from solutions in ethyl acetate and subject to X-ray crystallographic analysis. On the other hand, **3.2c** was very difficultly crystallized from common organic solvents. Shown in Figure 3.6a is the crystal structure of **3.2a**, which exhibits a one-dimensional face-to-face π-stacking with head-to-tail arrangement. It is found that neighboring molecules of **3.2a** stack with each other with two slightly different arrangements alternating in one stack. One arrangement has the two π-faces separated by 3.26 Å and the two silicon atoms of neighboring molecules separated by 7.42 Å. In comparison, the other arrangement has two π-faces separated by 3.35 Å and the two silicon atoms of neighboring molecules separated by 13.75 Å, which is accompanied with a shift along the long axis of pentacene backbone. Intermolecular hydrogen bonds are not observed between the π-stacks of **3.2a** since the N-H moiety of each molecule of **3.2a** is somehow blocked by the triisopropyl groups of neighboring molecule in the same stack. Unlike its isomer **3.2a**, **3.2b** exhibits intermolecular hydrogen bonds but lacks π-π interactions in its crystal structure. As shown in Figure 3.6a, molecules of **3.2b** form a hydrogen-bonded ribbon, which has a shape of "X" as viewed along the *a* axis of the unit cell. The double hydrogen bonds between molecules of **3.2b** as shown in Figure 3.6c have the N-to-N distances of 3.06 Å and 3.12 Å, the H-to-N distances of 2.28 Å and 2.30 Å, and the N-H-N angles of 151.6 ° and 158.7 °. The N-to-N and H-to-N distances for the hydrogen bonds of **3.2b** are slightly larger than those found for the hydrogen bonds of unsubstituted dihydrotetraazapentacene [4] possibly due to the steric hindrance of bulky triisopropylsilyl groups.

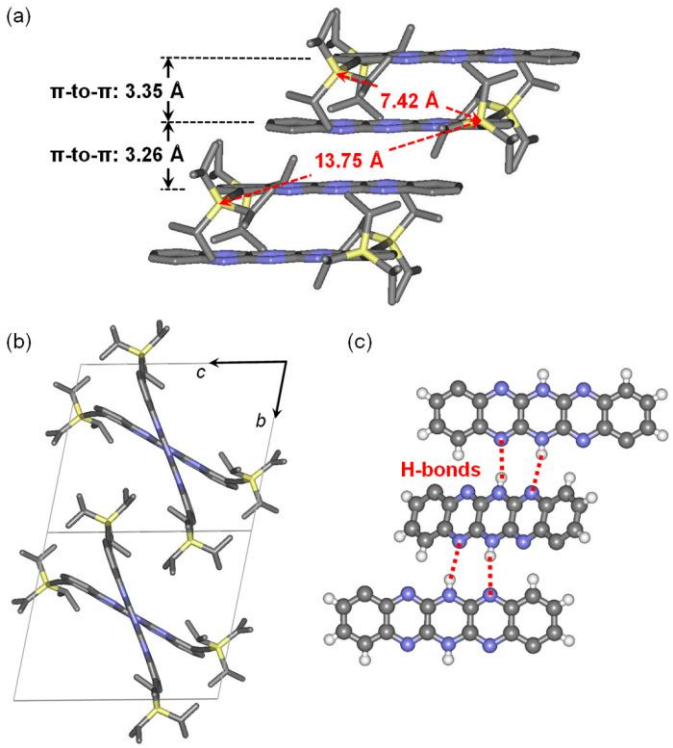

Figure 3.6 (a) Crystal structure of **3.2a** showing π-stacking; (b) crystal structure of **3.2b** view along the *a* axis of its unit cell; (c) hydrogen bonds between molecules of **3.2b** in the crystal structure. (Carbon, nitrogen, hydrogen and silicon atoms are shown in grey, blue, white and light yellow, respectively. For clarity, hydrogen atoms are removed in Figure a and b and triisopropylethynyl groups are removed in Figure c.)

3.2.6 Hydrogen Bonding in Solution

Although crystal structures of **3.2c** were not available as evidence for hydrogen bonds, intermolecular hydrogen bonds of **3.2c** were found in solution with ^{1}H NMR spectroscopy. Among the two active protons of **3.2c**, only one is available for intermolecular hydrogen bonds, while the other is shielded by the two bulky triisopropylsilyl groups. As shown in Figure 3.7, when a solution of **3.2c** in $CDCl_3$ (2 mol/L) is cooled from 22 to -40 ℃, the broad peak for exposed N-H (highlighted in magenta) exhibits a significant down-field shift of 2.1 ppm, while

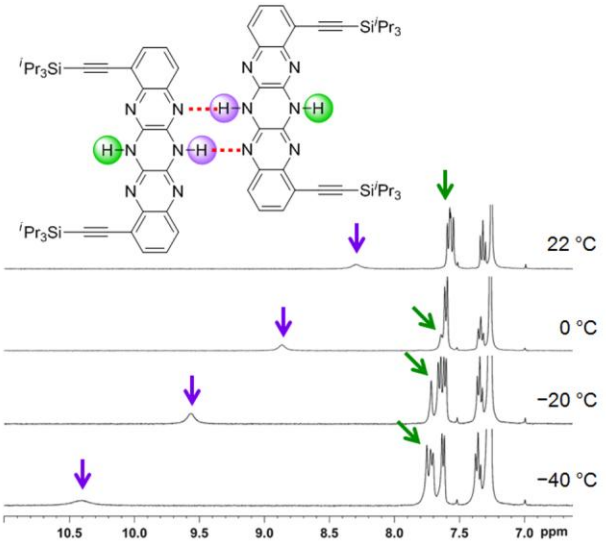

Figure 3.7 H-bonded dimer of **3.2c** and selected 1H NMR spectra of **3.2c** when cooled from 22 °C to −40 °C.

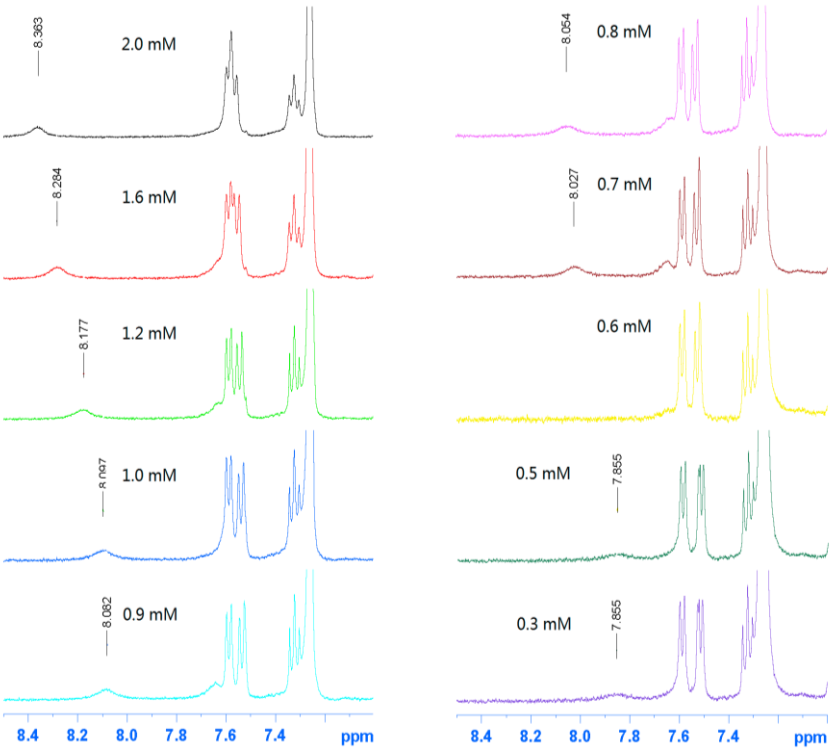

Figure 3.8 1H NMR spectra for **3.2c** in $CDCl_3$ with different concentrations at 20 ℃.

the signal of shielded N-H (highlighted in green) only shifts to down field by less than 0.2 ppm. This indicates formation of intermolecular hydrogen bonds, [15] which is accompanied with less dynamic molecules at lower temperature. Although the low solubility of **3.2c** in non-H-bonding solvents prevented varying its concentration by a large degree, when a solution of **3.2c** in $CDCl_3$ increased its concentration from 0.3 mmol/L to 2 mmol/L, the broad peak for exposed N-H exhibited a down-field shift of 0.5 ppm as shown in the Figure 3.8 which also excluded the possibility of H-bonding with water in $CDCl_3$.

3.3 Conclusion

In summary, reported above are three highly electron-deficient silylethynylated hexaazapentacenes (**3.1a-c**) with unprecedented pattern of N-atoms and their dihydro precursors (**3.2a-c**). These hexaazapentacenes (**3.1a-c**) are found to exhibit LUMO energy levels lower than -4.50 eV and thus able to oxidize dihydroanthracene to anthracene in both stoichiometric and catalytic reactions. Among the three isomeric dihydrohexaazapentacenes, **3.2b** exhibits interesting hydrogen bonding in crystals and **3.2c** exhibits hydrogen bonding in solution, while the crystal structure of **3.2a** lacks hydrogen bond but is dominated by π-stacking possibly in relation to the arrangement of bulky substituents. The instability of hexaazapentacenes **3.1a-c** in ambient conditions suggest a maximum number of pyridine or pyrazine-type nitrogen atoms for n-type organic semiconductors based on N-heteropentacenes.

3.4 Experimental

3.4.1 Synthesis

General: The reagents and starting materials employed were commercially available and used without any further purification if not specified elsewhere. 1H-NMR or 13C-NMR spectra

were recorded on a Brucker ADVANCE III 400MHz spectrometer. Mass spectra were recorded on a Therno Finnigan MAT 95 XL spectrometer. X-ray crystallography data were collected on a Bruker AXS Kappa ApexII Duo Diffractometer. UV-Vis and steady-state fluorescence spectra were taken on a Cary 5G UV-Vis-NIR spectrophotometer and a Hitachi F-4500 spectrofluorometer respectively. Melting points, without correction, were measured using a Nikon Polarizing Microscope ECLIPSE 50i POL equipped with an INTEC HCS302 heating stage.

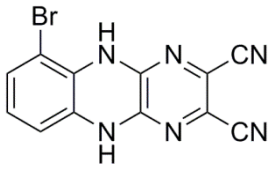

6-bromo-5,10-dihydro-2,3-dicyanopyrazinoquinoxaline

A mixture of 1-bromo-2,3-diaminobenzene [16] (374 mg, 2.0 mmol) and 2,3-dichloro-5,6-dicyanopyrazine (440 mg, 2.2 mmol) in 1,4-dioxane (10 mL) was refluxed over night. After cooled to room temperature, the resulting orange solids were filtered and washed with water and diethyl ether for several times, yielding 504 mg (80%) of 6-bromo-5,10-dihydro-2,3-dicyanopyrazinoquinoxaline as orange crystalline powders, which contained residue solvent of 1,4-dioxane. Such solvent residue could not be removed under vacuum indicating 1,4-dioxane molecules are crystallized within the lattice possibly by forming hydrogen bonds with the product. ^{1}H-NMR (DMSO-d_6) δ (ppm): 10.49 (s, 1H), 9.46 (s, 1H), 6.86 (d, J=8.0Hz, 1H), 6.58 (t, J=8.0Hz, 1H), 6.38 (d, J=8.0Hz, 1H). ^{13}C-NMR (DMSO-d_6) δ (ppm): 107.8, 113.9, 114.9, 122.5, 123.9, 125.0, 127.4, 128.6, 131.6, 147.7. HRMS (EI^+): cacld. for $C_{12}H_5BrN_6$ ($[M]^+$): 311.9763, calcd. For ([M]+): 311.9754. Melting point: 359-361 ℃.

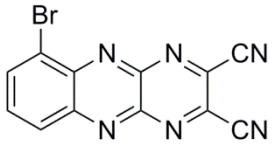

6-bromo-2,3-dicyanopyrazinoquinoxaline

A mixture of 6-bromo-5,10-dihydro-2,3-dicyanopyrazinoquinoxaline (626 mg, 2.0 mmol) and 2,3-dichloro-5,6-dicyanoquinone (DDQ) (545 mg, 2.4 mmol) in anhydrous THF (10 mL) was stirred at room temperature over night under an N_2 atmosphere. The resulting red suspension was filtered and washed with diethyl ether for several times, yielding 560 mg (75%) of 6-bromo-2,3-dicyanopyrazinoquinoxaline. ^{1}H-NMR (DMSO-d_6) δ (ppm): 8.68 (bs, 1H), 8.49 (bs, 1H), 8.16 (bs, 1H). ^{13}C-NMR (DMSO-d_6) δ (ppm): 114.1, 123.8, 130.1, 135.8, 136.2, 136.5, 138.3, 142.1, 142.5, 144.1, 147.5. Melting point: 309-311 ℃.

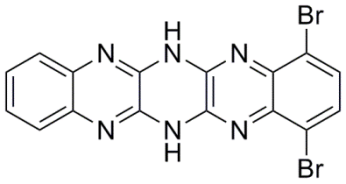

1,4-dibromo-6,13-dihydro-5,6,7,12,13,14-hexaazapentacene (3.3a)

A mixture of 2,3-dicyanopyrazinoquinoxaline (232 mg, 1.0 mmol), 1,4-dibromo-2,3-diaminobenzene [17] (532 mg, 2.0 mmol), and sodium carbonate (640 mg, 6.0 mmol) in N,N-dimethylformamide (8 mL) was refluxed for 3 h. The mixture was allowed to cool to room temperature overnight and diluted by water (50 ml). The resulting precipitate was filtered, rinsed with water and diethyl ether for several times, yielding 390 mg of (88%) 1,4-dibromo-6,13-dihydro-5,6,7,12,13,14-hexaazapentacene as dark brown solids. 1H-NMR (DMSO-d6) δ (ppm):

11.10 (bs, 2H), 7.22 (dd, J_1 = 5.6 Hz, J_2 = 3.6 Hz, 2H), 7.16 (s, 2H), 7.09 (dd, J_1 = 5.6 Hz, J_2 = 3.6 Hz, 2H). HRMS (EI^+): cacld. for $C_{16}H_8Br_2N_6$ ($[M]^+$): 443.9151 found: 443.9161.

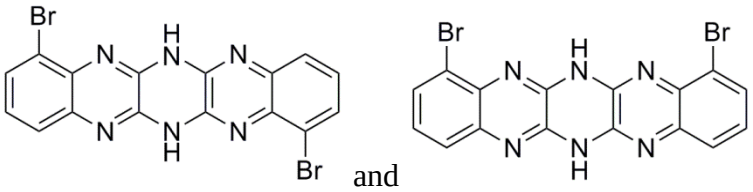

1,8-dibromo-6,13-dihydro-5,6,7,12,13,14-hexaazapentacene (3.3b) and 1,11-dibromo-6,13-dihydro-5,6,7,12,13,14-hexaazapentacene (3.3c)

A mixture of 6-bromo-2,3-dicyanopyrazinoquinoxaline (311 mg, 1.0 mmol), 1-bromo-2,3-diaminobenzene (374 mg, 2.0 mmol), and sodium carbonate (640 mg, 6.0 mmol) in N,N-dimethylformamide (8 mL) was refluxed for 3 h.[18] The mixture was allowed to cool to room temperature overnight and diluted by water (50 ml). The resulting precipitate was filtered, rinsed with water and diethyl ether for several times, yielding a mixture of the two products as a dark brown solid (432mg, 97%). ^{1}H-NMR (DMSO-d_6) δ (ppm): 11.35 (bs, 2H), 7.39 (m, 2H), 7.20 (m, 2H), 6.99 (m, 2H). HRMS (EI^+): cacld. for $C_{16}H_8Br_2N_6$ ($[M]^+$): 443.9151. found: 443.9190.

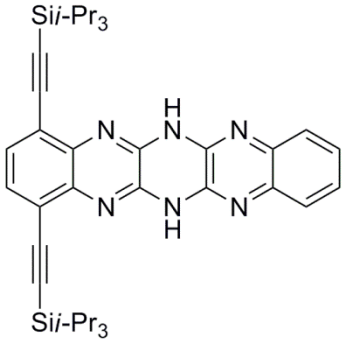

1,4-bis((triisopropylsilyl)ethynyl)-6,13-dihydro-5,6,7,12,13,14-hexaazapentacene (3.2a)

Under an atmosphere of N_2, a mixture of 1,4-dibromo-6,13-dihydro-5,6,7,12,13,14 -hexaazapentacene (355 mg, 0.8 mmol), $Pd(PPh_3)_4$ (92 mg, 0.08 mmol), CuI (31 mg, 0.16 mmol) and PPh_3 (21 mg, 0.08 mmol) was dissolved in 4 ml of Et_3N (N_2 purged before use) and 4 ml of toluene (N_2 purged before use). To the resulting suspension was added triisopropylsilyl acetylene (0.7 ml, 3.1 mmol) under an atmosphere of N_2. The resulting reaction mixture was sonicated for 10 minutes and heated to reflux for 2 days, then cooled to room temperature and concentrated under reduced pressure. The crude product was purified by column chromatography on silica gel using CH_2Cl_2: hexane = 2:1 as eluent yielding 310 mg (60%) of 1,4-bis((triisopropylsilyl)ethynyl)-6,13-dihydro-5,6,7,12,13,14 -hexaazapentacene as yellow solid. ^{1}H-NMR ($CDCl_3$) δ (ppm): 1.19 (m, 42H), 7.45 (m, 8H), 7.58 (m, 4H), 7.59 (bs, 2H), 7.88 (bs, 2H). ^{13}C-NMR (THF-d_8) δ (ppm):12.4, 19.2, 97.3, 106.3, 121.7, 127.2, 127.3, 131.7, 140.1, 140.8, 142.4, 143.0. HRMS (EI^+): cacld. for $C_{38}H_{50}N_6Si_2$ ($[M]^+$): 646.3630, found: 646.3640. Melting point: 285 ℃ (decomposed, ethyl acetate).

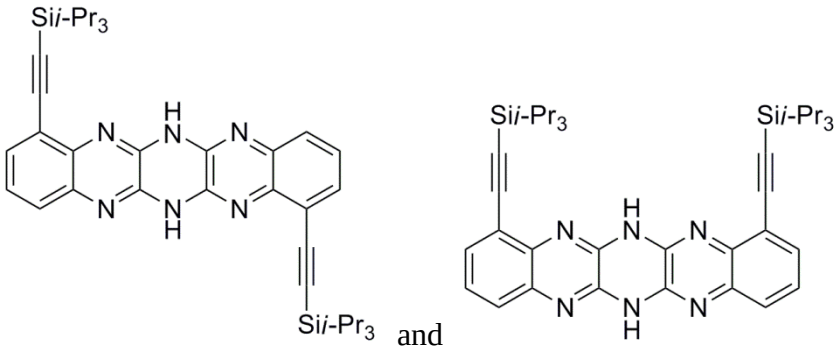

and

1,8-bis((triisopropylsilyl)ethynyl)-6,13-dihydro-5,6,7,12,13,14-hexaazapentacene (3.2b) and **1,11-bis((triisopropylsilyl)ethynyl)-6,13-dihydro-5,6,7,12,13,14-hexaazapentacene (3.2c)**

Under an atmosphere of N_2, $Pd(PPh_3)_4$ (116 mg, 0.1 mmol), CuI (20 mg, 0.1 mmol), PPh_3 (10 mg, 0.05 mmol) and a mixture of 1,8-dibromo-6,13-dihydro-5,6,7,12,13,14 -

hexaazapentacene and 1,11-dibromo-6,13-dihydro-5,6,7,12,13,14-hexaazapentacene (222 mg, 0.5 mmol) were dissolved in 8 ml of Et_3N (N_2 purged before use) and 8 ml of toluene (N_2 purged before use). To the resulting suspension was added triisopropylsilyl acetylene (0.7 ml, 3.1 mmol) under an atmosphere of N_2. The resulting reaction mixture was sonicated for 10 minutes and heated to reflux for 4 days, then cooled down to room temperature and concentrated under reduced pressure. The crude product was purified by column chromatography on silica gel using CH_2Cl_2: Hexane = 3:1 to 4:1) as eluent, yielding 76 mg (23%) of 1,8-bis((triisopropylsilyl)ethynyl)-6,13-dihydro-5,6,7,12,13,14-hexaazapentacene as yellow solid. Changing eluent to CH_2Cl_2: Ethyl Acetate (10:1 to 9:1) yielded 67 mg (21%) of 1,11-bis((triisopropylsilyl)ethynyl)-6,13-dihydro-5,6,7,12,13,14-hexaazapentacene as yellow solid.

1,8-bis((triisopropylsilyl)ethynyl)-6,13-dihydro-5,6,7,12,13,14-hexaazapentacene

^{1}H-NMR ($CDCl_3$) δ (ppm): 1.19 (m, 42H), 7.33 (t, J = 8.0Hz, 2H), 7.52 (d, J=8.0Hz, 2H), 7.59 (d, J=8.0Hz, 2H), 8.02 (bs, 2H).^{13}C-NMR (THF-d_8) δ (ppm):12.4, 19.2, 95.4, 106.5, 121.4, 126.5, 127.8, 132.9, 140.2, 140.7, 142.7, 142.8. HRMS (ESI^+): cacld. for $C_{38}H_{51}N_6Si_2$ ($[M+H]^+$): 647.3708, found: 647.3722. Melting point: 348-349 ℃ (Ethyl Acetate).

1,11-bis((triisopropylsilyl)ethynyl)-6,13-dihydro-5,6,7,12,13,14-hexaazapentacene

^{1}H-NMR (CD_2Cl_2) δ (ppm): 1.21 (m, 42H), 7.35 (t, J = 7.6Hz, 2H), 7.58 (m, 4H), 7.79 (bs, 1H), 8.34 (bs, 1H). ^{13}C-NMR (THF-d_8) δ (ppm):12.4, 19.2, 95.5, 106.6, 121.4, 126.6, 127.9, 132.9, 140.2, 140.7, 142.6, 142.7. HRMS (ESI^+): cacld. for $C_{38}H_{51}N_6Si_2$ ($[M+H]^+$): 647.3708, found: 647.3695. Melting point: >380 ℃ (decomposed, ethyl acetate).

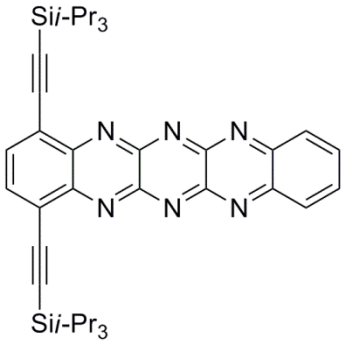

1,4-bis((triisopropylsilyl)ethynyl)-5,6,7,12,13,14-hexaazapentacene (3.1a)

PbO_2 (3 g, 12.5 mmol) was added to a solution of 1,4-bis((triisopropylsilyl)ethynyl)-6,13-dihydro-5,6,7,12,13,14-hexaazapentacene (60 mg, 0.1 mmol) in 10 ml of CH_2Cl_2. The resulting dark green mixture was stirred at room temperature for 24 hours in dark, then filtered through a thin pad of Celite and washed with CH_2Cl_2 to remove PbO_2. The filtrate was concentrated under a reduced pressure, and purified by column chromatography on silica gel using CH_2Cl_2: Ethyl Acetate (20:1 to 10:1) yielding 58 mg of 1,4-bis((triisopropylsilyl)ethynyl)-5,6,7,12,13,14-hexaazapentacene as brown solid in a yield of 96%. ^{1}H-NMR ($CDCl_3$) δ (ppm): 1.29-1.26(m, 42H), 8.03 (dd, J_1 = 7.2 Hz, J_2 = 3.2 Hz, 2H), 8.11 (s, 2H), 8.46 (dd, J_1 = 7.2Hz, J_2 = 3.2 Hz, 2H).^{13}C-NMR ($CDCl_3$) δ (ppm):11.6, 19.0, 102.3, 103.9, 125.6, 130.9, 135.0, 138.0, 146.1, 146.5, 149.4, 150.3. HRMS (ESI^+): cacld. for $C_{38}H_{49}N_6Si_2$ ($[M+H]^+$): 645.3552, found:645.3546. Melting point: 198 ℃ (decomposed).

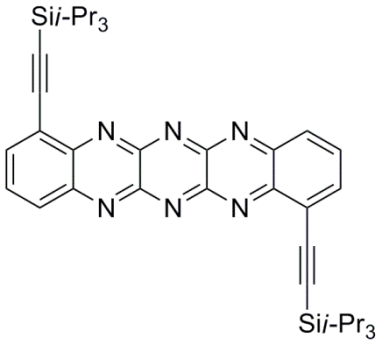

1,8-bis((triisopropylsilyl)ethynyl)-5,6,7,12,13,14-hexaazapentacene (3.1b)

PbO_2 (3 g, 12.5 mmol) was added to a solution of 1,8-bis((triisopropylsilyl)ethynyl)-6,13-dihydro-5,6,7,12,13,14-hexaazapentacene (30 mg, 0.05 mmol) in 20 ml of CH_2Cl_2. The resulting dark green mixture was stirred at room temperature for 10 mins in dark, then filtered through a thin pad of Celite and washed with CH_2Cl_2 to remove PbO_2. The filtrate was concentrated under a reduced pressure and purified by column chromatography on silica gel using CH_2Cl_2: Ethyl Acetate (10:1 to 9:1) yielding 29 mg of 1,8-bis((triisopropylsilyl)ethynyl)-5,6,7,12,13,14-hexaazapentacene as brown solid in a yield of 97%. ^{1}H-NMR ($CDCl_3$) δ (ppm): 1.27 (m, 42H), 7.98 (dd, J_1 = 8.8 Hz, J_2 = 7.2 Hz, 2H), 8.21 (d, J= 6.4Hz, 2H), 8.40 (d, J_1 = 8.8Hz, 2H).^{13}C-NMR ($CDCl_3$) δ (ppm):11.6, 19.0, 102.1, 102.4, 125.9, 130.9, 134.6, 138.5, 146.4, 146.4, 149.5, 150.2. HRMS (ESI^+): cacld. for $C_{38}H_{49}N_6Si_2$ ($[M+H]^+$): 645.3552, found:645.3545. Melting point: 190 ℃ (decomposed).

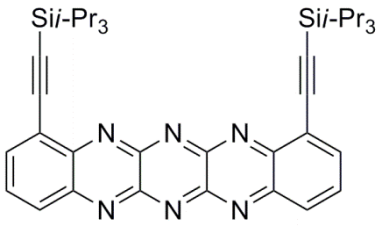

1,11-bis((triisopropylsilyl)ethynyl)-5,6,7,12,13,14-hexaazapentacene (3.1c)

PbO_2(3 g, 12.5 mmol) was added to a solution of 1,11-bis((triisopropylsilyl)ethynyl)-6,13- dihydro-5,6,7,12,13,14-hexaazapentacene (30 mg, 0.05 mmol) in 10 ml of CH_2Cl_2. The resulting dark green mixture was stirred at room temperature for 30 mins in dark and then filtered through a thin pad of Celite and washed with CH_2Cl_2 to remove PbO_2. The filtrate was concentrated under a reduced pressure and purified by column chromatography on silica gel using CH_2Cl_2: Ethyl Acetate (10:1 to 9:1) yielding 29 mg of 1,11-bis((triisopropylsilyl)ethynyl)-

5,6,7,12,13,14-hexaazapentacene as brown solid in a yield of 97%. ^{1}H-NMR ($CDCl_3$) δ (ppm): 1.30 (m, 42H), 7.97 (dd, J_1 = 8.8 Hz, J_2 = 6.8 Hz, 2H), 8.18 (dd, J_1 = 6.8Hz, J_2 = 0.8 Hz, 2H), 8.38 (dd, J_1 = 6.8Hz, J_2 = 0.8 Hz, 2H).^{13}C-NMR ($CDCl_3$) δ (ppm):11.6, 19.0, 102.1, 102.7, 125.9, 130.9, 134.7, 137.7, 146.3, 146.5, 149.7, 150.1. HRMS (ESI^+): cacld. for $C_{38}H_{49}N_6Si_2$ ($[M+H]^+$): 645.3552, found:645.3588. Melting point: 180 ℃ (decomposed, ethyl acetate).

3.4.2 Cyclic Voltammetry

Cyclic voltammetry was performed in a solution of anhydrous CH_2Cl_2 with 0.1M tetrabutylammonium hexafluorophosphate (Bu_4NPF_6) as supporting electrolyte, at a scan rate of 100mV s^{-1}. A platinum bead was used as a working electrode, a platinum wire was used as an auxiliary electrode, and a silver wire was used as a pseudo-reference. $FeCp_2^+/FeCp_2^0$ or $CoCp_2^+/CoCp_2^0$ was used as an internal standard. Potentials were recorded versus $FeCp_2^+/FeCp_2^0$, which has a HOMO energy level of -4.80 eV. $CoCp_2^+/CoCp_2^0$ is known as -1.35V vs. $FeCp_2^+/FeCp_2^0$.

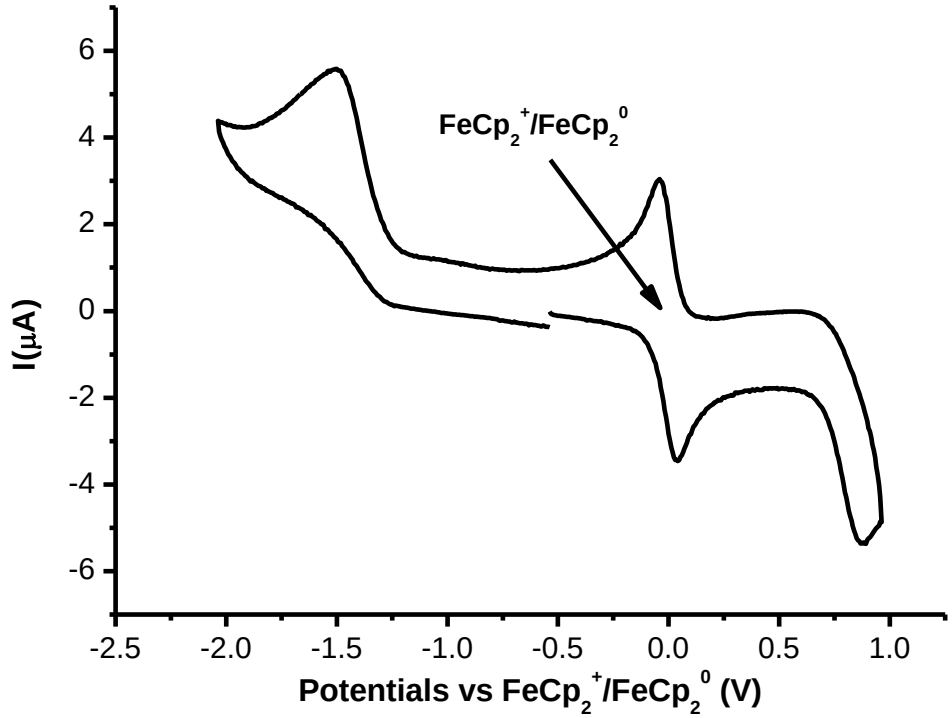

Figure 3.9 Cyclic voltammogram of 1,4-bis((triisopropylsilyl)ethynyl)-6,13-dihydro- 5,6,7,12,13,14-hexaazapentacene (**3.2a**) recorded in CH_2Cl_2.

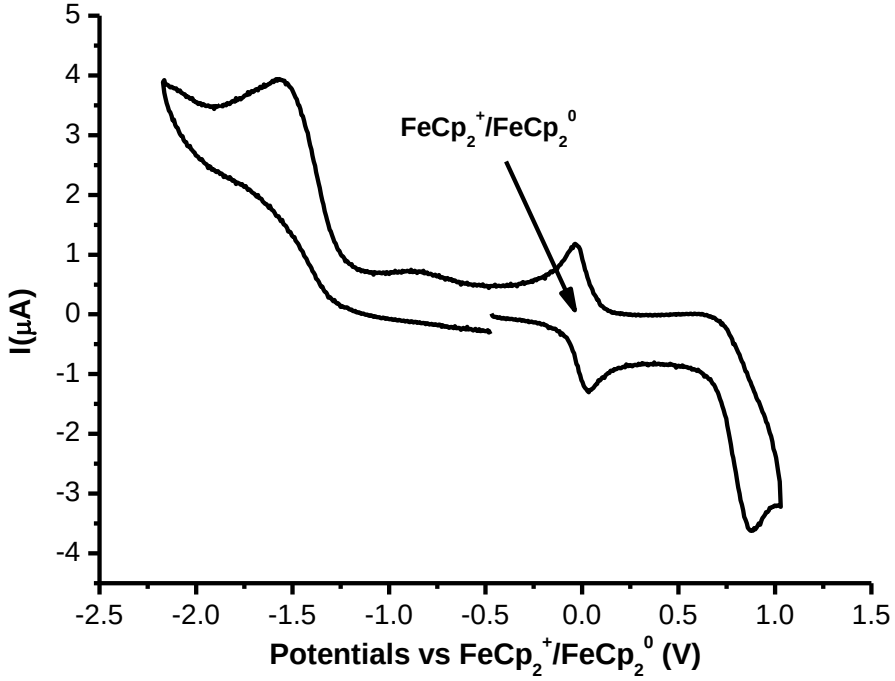

Figure 3.10 Cyclic voltammogram of 1,8-bis((triisopropylsilyl)ethynyl)-6,13-dihydro- 5,6,7,12,13,14-hexaazapentacene (**3.2b**) recorded in CH_2Cl_2.

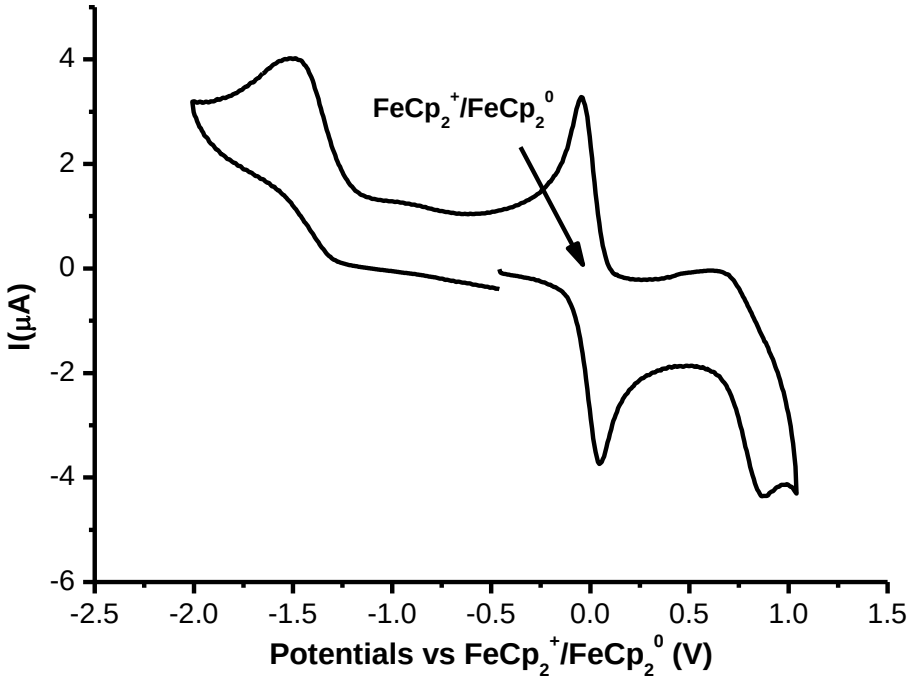

Figure 3.11 Cyclic voltammogram of 1,11-bis((triisopropylsilyl)ethynyl)-6,13-dihydro- 5,6,7,12,13,14-hexaazapentacene (**3.2c**) recorded in CH_2Cl_2.

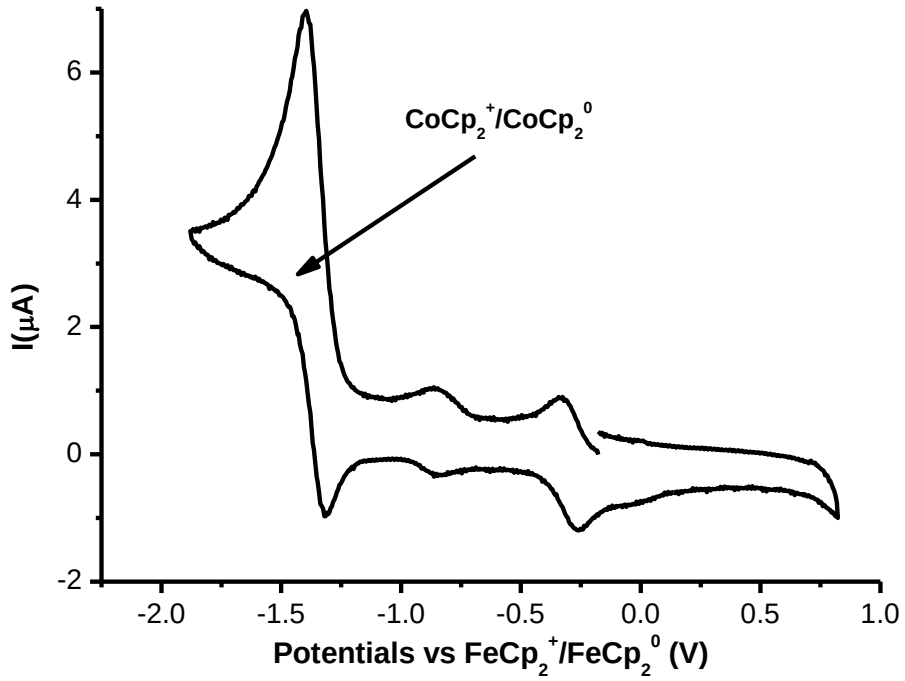

Figure 3.12 Cyclic voltammogram of 1,4-bis((triisopropylsilyl)ethynyl)-5,6,7,12,13,14 -hexaazapentacene (**3.1a**) recorded in CH_2Cl_2.

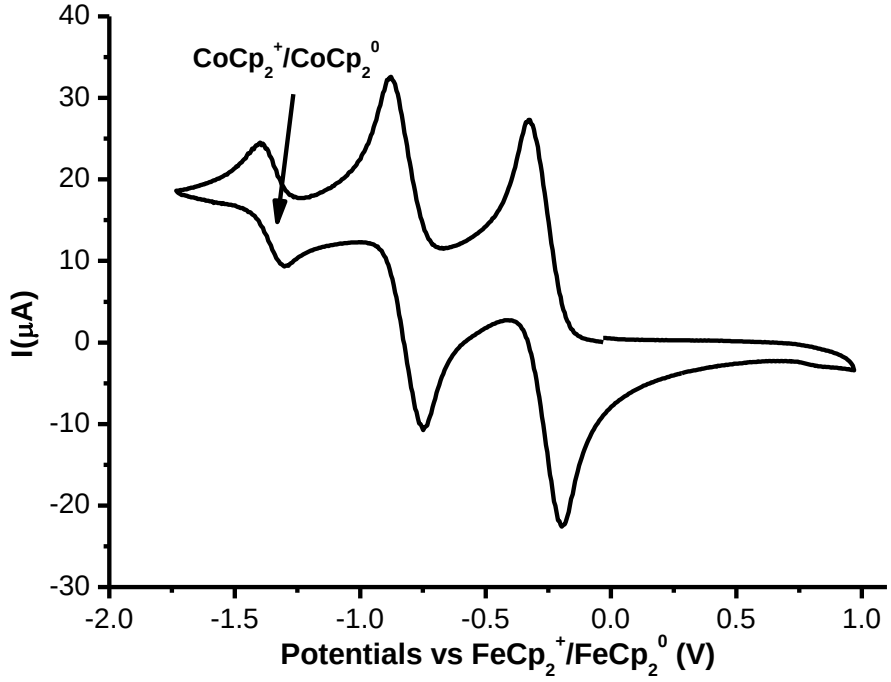

Figure 3.13 Cyclic voltammogram of 1,8-bis((triisopropylsilyl)ethynyl)-5,6,7,12,13,14-hexaazapentacene (**3.1b**) recorded in CH_2Cl_2.

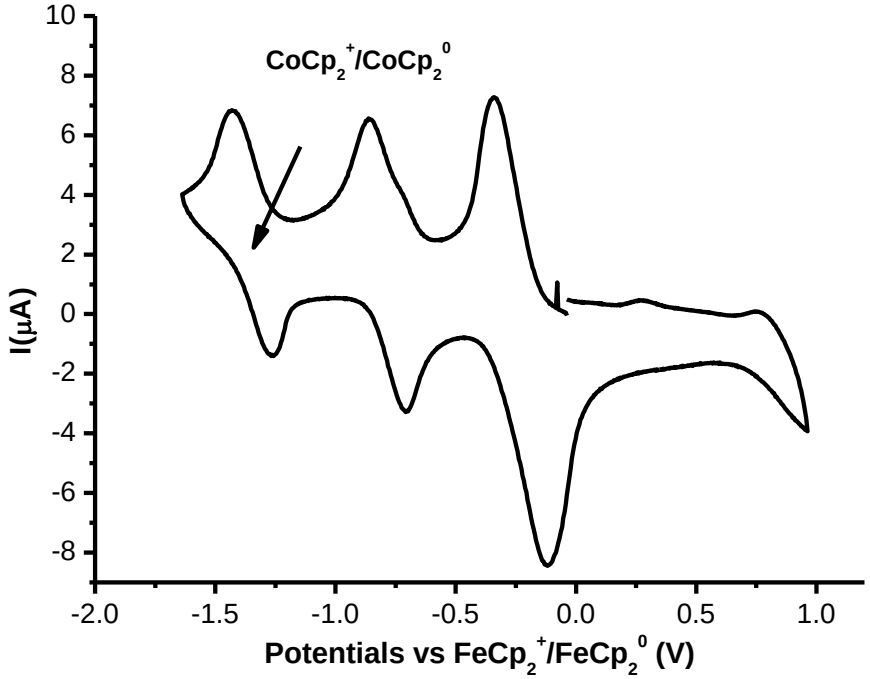

Figure 3.14 Cyclic voltammogram of 1,11-bis((triisopropylsilyl)ethynyl)-5,6,7,12,13,14-hexaazapentacene (**3.1c**) recorded in CH_2Cl_2.

3.4.3 UV-vis absorption sepectroscopy

UV-vis absorption spectra and fluorescence spectra were recorded from solutions in dichloromethane with a concentration of 5×10^{-5} mol/L.

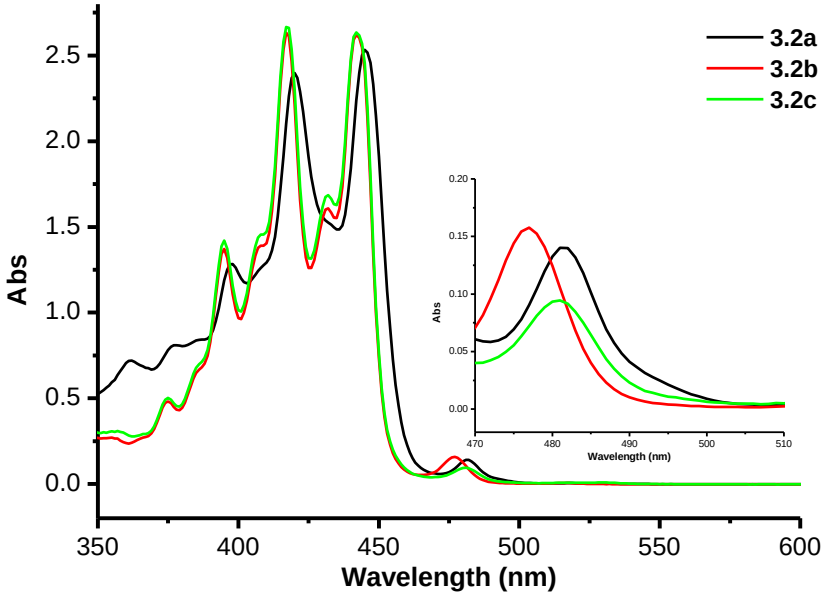

Figure 3.15 Absorption spectra of **3.2a**, **3.2b** and **3.2c** as recorded from solutions of CH_2Cl_2 at the same concentration of 5×10^{-5} mol/L.

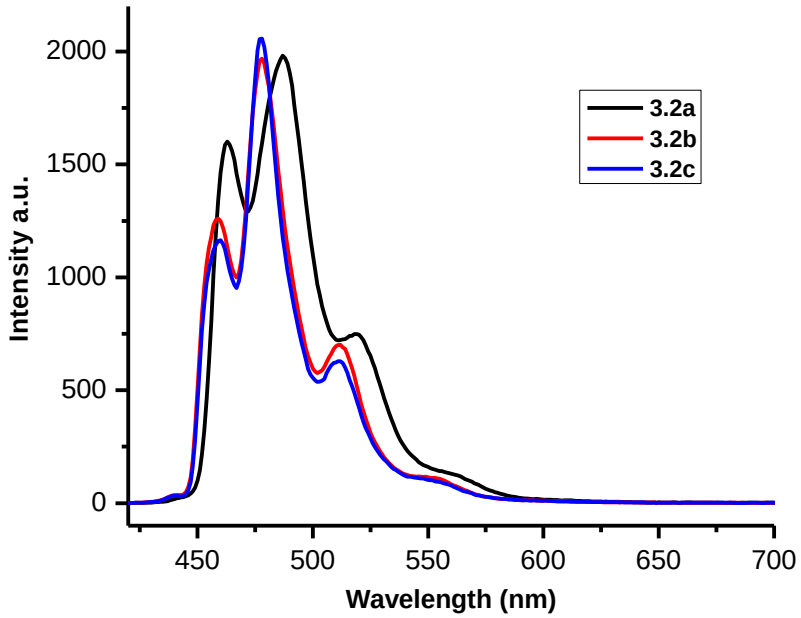

Figure 3.16 Fluorescence spectra of **3.2a**, **3.2b** and **3.2c** as recorded from solutions of CH_2Cl_2 excited at 410nm.

3.5 Reference

1 Miao, Q. *Synlett*, **2012**, *23*, 326.

2 Winkler, M.; Houk, K. N. *J. Am. Chem. Soc.* **2007**, *129*, 1805.

3 Liang, Z.; Tang, Q.; Mao, R.; Liu D.; Xu, J.; Miao, Q. *Adv. Mater.* **2011**, 23, 5514.

4 He, Z.; Liu, D.; Mao, R.; Tang, Q.; Miao, Q. *Org. Lett.* **2012**, *14*, 1050.

5 (a) Hinsberg, O.; Schwantes, E. *Chem. Ber.* **1903**, *36*, 4039. (b) Bergstrom, F. W.; Ogg, R. A. Jr. *J. Am. Chem. Soc.* **1931**, *53*, 245.

6 (a) Fleischhauer, J.; Beckert, R.; Jüttke, Y.; Hornig, D.; Günther, W.; Birckner, E.; Grummt, U.-W.; Görls, H. *Chem. Eur. J.* **2009**, *15*, 12799. (b) Fleischhauer, J.; Zahn, S.; Beckert, R.; Grummt, U.-W.; Birckner, E.; Görls, H. *Chem. Eur. J.* **2012**, *18*, 4549.

7 (a) Liang, Z.; Tang, Q.; Xu, J.; Miao, Q. *Adv. Mater.* **2011**, *23*, 1535. (b) Tverskoy, O.; Rominger, F.; Peters, A.; Himmel, H.-J.; Bunz, U. H. F. *Angew. Chem. Int. Ed.* **2011**, *50*, 3557. (c) Miao, S.; Appleton, A. L.; Berger, N.; Barlow, S.; Marder, S. R.; Hardcastle, K. I.; Bunz, U. H. F. *Chem. Eur. J.* **2009**, *15*, 4990.

8 Miao, S.; Brombosz, S. M.; Schleyer, P. v. R.; Wu, J. I.; Barlow, S.; Marder, S. R.; Hardcastle, K. I.; Bunz, U. H. F. *J. Am. Chem. Soc.* **2008**, *130*, 7339.

9 Lindner, B. D.; Engelhart, J. U.; Tverskoy, O.; Appleton, A. L.; Rominger, F.; Peters, A.; Himmel, H.-J.; Bunz, U. H. F. *Angew. Chem. Int. Ed.* **2011**, *50*, 8588.

10 Bergstrom, F. W.; Ogg, R. A. *J. Am, Chem. Soc.* **1931**, *53*, 245.

11. Fleischhauer, J.; Beckert, R.; Jüttke, Y.; Hornig, D.; Günther, W.; Birckner, E.; Grummt, U. W.; Görls, H. *Chem. Eur. J.* **2009**, *15*, 12799.

12 The commonly used HOMO energy level of ferrocene is −4.80 eV. See: (a) Pommerehne, J.; Vestweber, H.; Guss, W.; Mahrt, R. F.; Bässler, H.; Porsch, M.; Daub, J. *Adv. Mater.* **1995**,

7, 551. (b) D'Andrade, B. W.; Datta, S.; Forrest, S. R.; Djurovich, P.; Polikarpov, E.; Thompson, M. E. *Org. Electron.* **2005**, *6*, 11.

13 The frontier molecular orbitals of **3.1a-c** and **3.2a-c** were also calculated with the Gaussian 09 software package using simplified model molecules, which have smaller trimethylsilyl groups replacing the triisopropylsilyl groups. The geometries of these model molecules were first optimized at the B3LYP level of density functional theory (DFT) with the 6-31G(d, p) basis set, and the HOMO and LUMO were then calculated with the 6-311++G(d, p) basis set.

14 Newman, C. R.; Frisbie, C. D.; da Silva Filho, D. A.; Brédas, J.-L.; Ewbank, P. C.; Mann, K. R. *Chem. Mater.* **2004**, *16*, 4436.

15 Palmans, A. R. A.; Vekemans, J. A. J.; Fischer, H.; Hikmet, H.; Meijer, E. W. *Chem. Eur. J.* **1997**, *3*, 300.

17. Bijleveld, J. C.; Shahid, M.; Gilot, J.; Wienk, M. M.; Janssen, R. A. J. *Adv. Funct. Mater.* **2009**, *19*, 3262.

17 Dominguez, Z.; Khuong, T.-A. V.; Dang, H.; Sanrame, C. N.; Nunez, J. E.; Garcia-Garibay, M. A. *J. Am. Chem. Soc.* **2003**, *125*, 8827.

18 Richards, G. J.; Hill, J. P.; Subbaiyan, N. K.; D'Souza, F.; Karr, P. A.; Elsegood, M. R. J.; Teat, S. J.; Mori, T.; Ariga, K. *J. Org. Chem.*, **2009**, *74*, 8914.

Chapter 4 An Air Stable Solution-Processed High-Mobility N-Type Organic Semiconductor from Electron-Deficient Thiadiazolophenazine*

4.1 Introduction

Organic thin film transistors (OTFTs) are essential building blocks of large-area, flexible and low-cost organic electronics, and offer promising applications in various technology areas. [1] The ultimate success of OTFTs requires developing organic semiconductors that combine high field effect mobility, good solution-processability and robust stability under ambient air, moisture, and light exposure. [2] Although the field effect mobility of leading organic semiconductors in OTFTs has reached or even exceeded the value of amorphous silicon (~1 $cm^2V^{-1}s^{-1}$), organic semiconductors that can meet all the above requirements are still rare. [3] Such challenge is particularly true for n-type (electron-transporting) organic semiconductors, [4] because of the instability of organic anions.[5]

To have a good chance of being stable in air, n-type organic semiconductors should have reduction potentials lower than that of oxygen and water so that the reduced molecules (often radical anions) are not quenched by oxygen and water. [6] To achieve a sufficiently low reduction potential, it is often necessary to apply more than one types of electron-withdrawing moieties to lower the energy level of lowest unoccupied molecular orbital (LUMO). Electron deficiency does have a strong impact on the injection of charges at the electrode, but does not necessarily have impact on the electron mobility of an n-type semiconductor. [6] It is the precise nature of π-

---

* Synthesis, characterization, DFT calculation and crystal growth were done by me. Crystal structures were solved by Ms. Hoi Shan Chan. Thin film transistor fabrication and characterization was done by Danqing Liu.

stacking, rather than simply the presence of π-stacking interactions that governs the charge carrier mobility [6] because electronic coupling between molecules are determined by not only the spatial overlap of molecular orbitals but also the phase relationship between the orbitals. [7] To better control the precise nature of π-stacking, other strong supramolecular interactions can be introduced because the exact molecular packing is determined by the sum of all kinds of supramolecular interactions. When designing air-stable high-mobility n-type semiconductors, we recognized that thiadiazole is useful in both lowering LUMO energy level and tuning molecular packing because it is not only an electron-deficient heterocycle but able to form strong dipole-dipole interactions between N and S atoms. Such dipole-dipole interactions arise from the charge-separated resonance form of thiadiazole as shown in Figure 4.1.

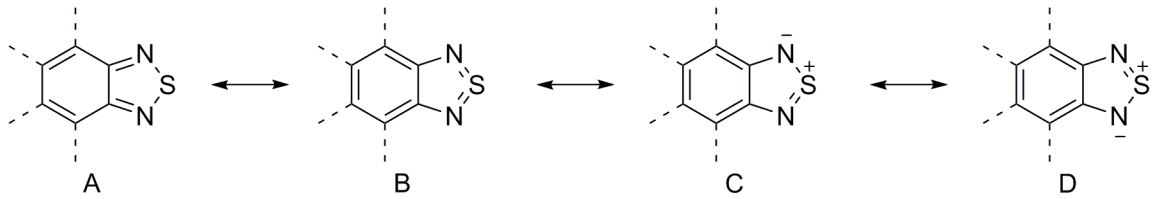

Figure 4.1 The resonance structures of benzo[2,1,3]thiadiazole.

Reported here is a new n-type organic semiconductor based on π-electron deficient thiadiazolophenazine (**4.1** as shown in Figure 4.2). Although aceno[2,1,3]thiadiazoles (e.g. **4.3**) were firstly synthesized in 2009 [8] and later were successfully applied as p-type organic semiconductors in single crystal field effect transistors (**4.4**), [9] thiadiazole-fused arenes were not reported as no n-type organic semiconductors to the best of our knowledge. Regarding the design of **4.1**, the following issues are worth noting. First, **4.1** has three electron-withdrawing moieties, namely thiadiazole, pyrazine and chlorine, combined in one molecule to achieve a sufficiently

low LUMO energy level. Second, the strong dipole-dipole interactions between thiadiazole moieties can enforce a close crystal packing with a self-complementary head-to-head arrangement. Third, following the success of silylethynylated pentacenes [10] and N-heteropentacenes [1] as soluble and stable organic semiconductors with high charge carrier mobility, triisopropylsilylethynyl (TIPS) groups are introduced to **4.1** not only to increase solubility but also to induce one-dimensional π-stacking with a brickwork arrangement. It is found that **4.1** functions as a solution-processed air stable n-type organic semiconductor with field effect mobility up to 0.7 $cm^2V^{-1}s^{-1}$ as measured in air.

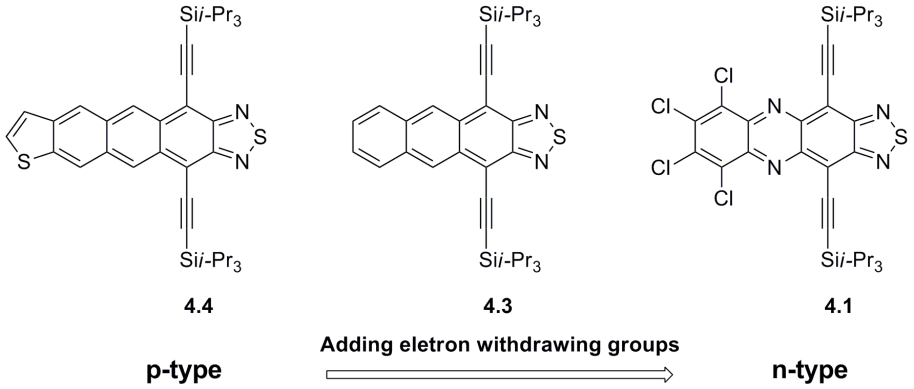

Figure 4.2 Molecular structures of aceno[2,1,3]thiadiazoles **4.1, 4.3** and **4.4**.

4.2 Results and Discussion

4.2.1 Synthesis

Shown in Scheme 4.1 is the synthesis of **4.1**. Reaction of p-chlornil with potassium phthalimide, followed by treatment of hydrazine and thionyl chloride, afforded the starting material benzo[1,2-c;4,5-c']bis[2,1,5]thiadiazole-4,8-dione (BBT-p-quinone, **4.5**). [8a] Nucleophilic addition of triisopropyl-ethynylide to **4.5** yielded the corresponding diol, which was directly reduced by sodium hypophosphite and potassium iodide in acetic acid and toluene (V/V=1:1)

yielding 4,8-bis(triisopropylsilylethynyl)-benzo[1,2-c:4,5-c']bis([1,2,5]thiadiazole) (TIPS-BBT, **4.2**) as dark purple crystal with metallic luster in a yield of 30% for two steps. The ortho-diamine **4.6** was obtained by $LiAlH_4$ reduction of **4.2**, and condensation of **4.6** with o-chlornil gave **4.1** as black crystals in a yield of 15%. The low yield of **4.1** may be attributed to the low reactivity of amine groups due to electron-withdrawing nature of thiadiazole and the steric effect of bulky TIPS. **4.3** was synthesized as the reported procedures explored by Bunz and co-workers for comparison. [8]

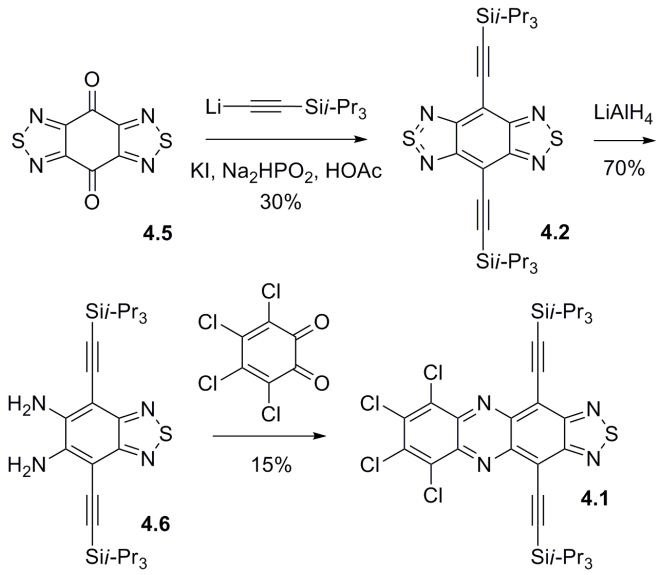

Scheme 4.1 Synthesis of hexaazapentacenes **4.1-4.2**.

4.4.2 Molecular Packing

With one or two [2,1,3]thiadiazole rings that are terminated at π−backbone, molecules of **4.1-4.2** can in principle form intermolecular S-N dipole interaction with each other. To study such interaction, single crystals of **4.1** and **4.2** were grown from solutions in ethyl acetate and subject to X-ray crystallographic analysis. Shown in Figure 4.3a is the crystal structure of **4.2**, molecules of **4.2** are linked by double S-N dipole-diploe interactions forming a linear ribbon,

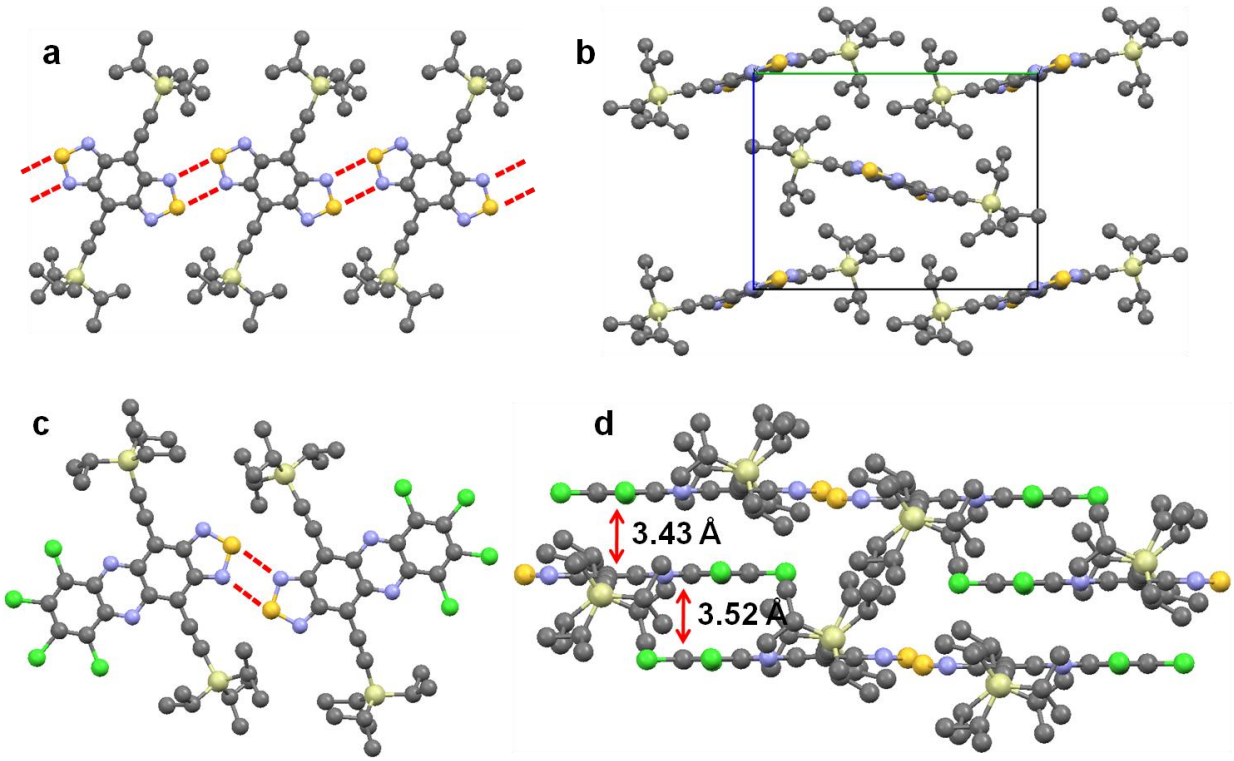

Figure 4.3 (a) Crystal structure of **4.2** showing S-N dipole interactions; (b) crystal structure of **4.2** view along the *a* axis of its unit cell; (c) S-N dipole interactions between molecules of **4.1** in the crystal structure. (d) Crystal structure of **4.1** showing π-stacking with distance. (Carbon, nitrogen, chlorine, silicon and sulfur atoms are shown in grey, blue, green and light yellow, respectively. For clarity, hydrogen atoms are removed.)

with the N-to-N distance of 3.135 Å, S-to-N distance of 3.141 Å and S-to-S distance of 3.884 Å. This intermolecular S-to-N distance is smaller than the sum of van der Waals radii of S and N atoms (1.55 Å for N and 1.80 Å for S) by 0.21 Å. As shown in Figure 4.3b, ribbons of **4.2** are arranged in a herringbone pattern and there are no cofacial π-π interactions between the π-backbone of **4.2**, which are shielded by the bulk triisopropyl groups. The absence of cofacial π-π interactions between the π-backbone suggests that **4.2** may not function as a good organic semiconductor. As shown in Figure 4.3c, two molecules of **4.1** are linked by S-N dipole-dipole interactions forming a head-to-head dimer, where the N-to-N distance is 2.881 Å, the S-to-N

distance is 2.920 Å and the S-to-S distance is 3.722 Å. This intermolecular S-to-N distance is significantly smaller than the sum of van der Waals radii of S and N atoms (1.55 Å for N and 1.80 Å for S) by 0.43 Å indicating a strong dipole-dipole interaction. In comparison**,** the dipole-dipole interactions of **4.1** have a shorter S-to-N distance than that of **4.2.** This can be attributed to the bending of TIPS-ethyl groups of **4.1** leading to smaller repulsion between the neighboring bulky TIPS groups and shorter distance of thiadiazole motifs. As shown in Figure 4.3d, viewed along *a* axis, molecules of **4.1** exhibit a one-dimensional face-to-face π-stacking with head-to-tail arrangement. It is found that neighboring molecules of **4.1** stack with each other with two slightly different arrangements alternating in one stack. One arrangement has the two π-faces separated by 3.43 Å with relative stronger π-π overlap between the two molecules (about three rings overlap), while the other arrangement has two π-faces separated by 3.52 Å with smaller π-π overlap between the two molecules (about one rings). Such one-dimensional π-stacking and π-π distances are expected to provide a charge transport pathway, which is of key importance for OTFTs.

4.2.3 Electronic Structures and DFT Calculations

The electronic structures of **4.1** and **4.2** were investigated with both experimental and computational methods. Figure 4.4 shows the UV-vis absorption and fluorescence spectra of **4.1**-**4.3** as measured from their solutions of CH_2Cl_2 (1×10^{-5} M). **4.2** form a red solution with the longest wavelength absorption at 590 nm and exhibits strong reddish fluorescence with an emission peaking at 620 nm when excited with a light at 380 nm. **4.1** form a green solution with the longest wavelength absorption at 710 nm and exhibits much weaker fluorescence with an emission peak at 699 nm when excited at 420 nm. In comparison to the reported **4.3, 4.1** exhibits

very similar but slightly red-shifted longest-wavelength absorptions (11 nm) and emission (10 nm) for its N insertion and tetrachloride substitution as shown in Figure 4.4. [11]

The cyclic voltammograms of **4.1** and **4.2** (shown in the Experimental Section) exhibit two reversible one-electron reduction waves in the testing window. The first half-wave reduction potential vs. ferrocenium/ferrocene is −0.91 V for **4.2** and −0.62 V for **4.1** from which the lowest unoccupied molecular orbital (LUMO) energy levels of **4.2** and **4.1** are estimated as −3.79 eV and −4.18 eV, respectively. [12] The HOMO-LUMO gaps of **4.2** and **4.1** are 1.97 eV and 1.75 eV, respectively, as estimated from their absorption edge at 628 nm and 710 nm. From the optical gap and LUMO energy level, the HOMO is estimated as −5.76 eV for **4.2** and −5.93 eV for **4.1**, respectively. In comparison, **4.3** exhibits two reversible one-electron reduction waves and one reversible one-electron oxidation wave. From the half-wave electrochemical potentials, the HOMO and LUMO energy levels of **4.3** are estimated as −5.53 eV and −3.62 eV, respectively. These results are summarized in Table 4.1 for comparison. **4.2** has lower LUMO and HOMO energy levels than **4.3** in agreement with the electron deficient nature of thiadizole. **4.1** has the lowest LUMO and HOMO energy levels because of the extra electron-withdrawing pyrazine and Cl atoms, and the low LUMO at −4.18 eV makes it a good candidate for air stable n-type semiconductor. [6]

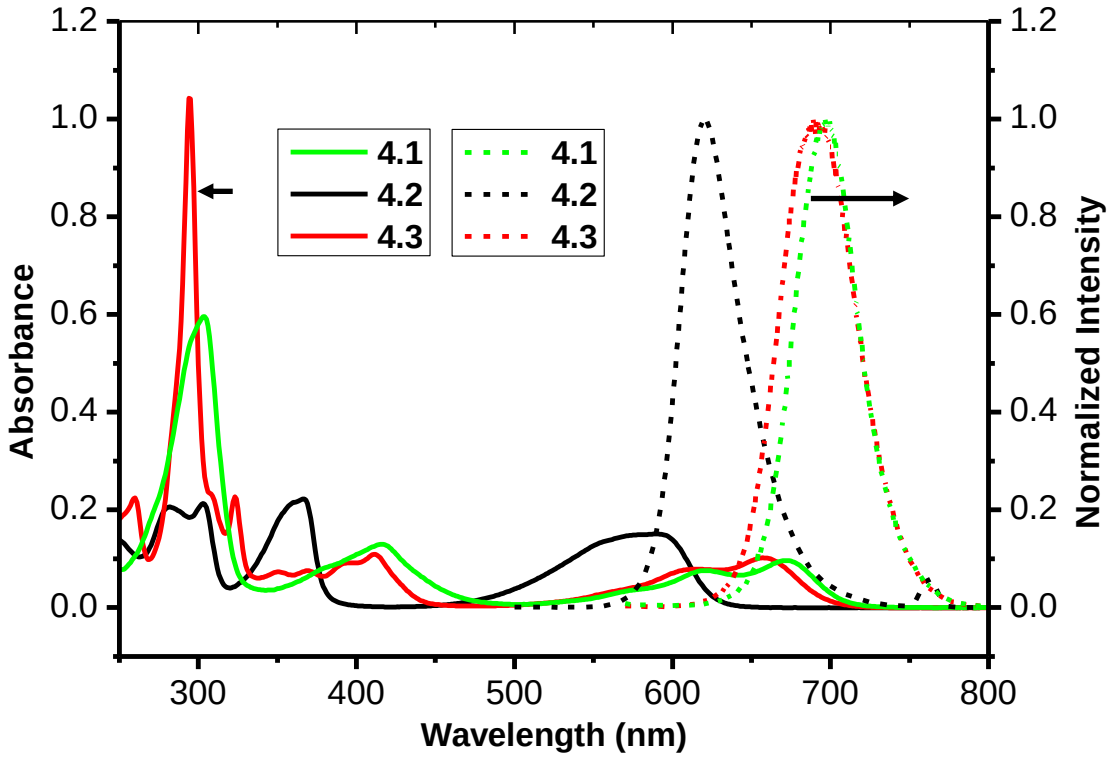

Figure 4.4 UV-vis absorption and fluorescence spectra of **4.1-4.3** in CH_2Cl_2 (1×10^{-5}mol/L)

Table 4.1 Electrochemical potentials, absorption edge, and frontier orbital energy levels for **4.1-4.3**.

	Electrochemical				Optical	
	E_{ox} [a] (V)	E_{red} [a] (V)	HOMO (eV)	LUMO (eV)	λ_{edge} [b] (nm)	Optical gap (eV)
4.1	—	−0.62	−5.93[c]	−4.18	710	1.75
4.2	—	−0.91	−5.76[c]	−3.79	628	1.97
4.3	0.73	−1.18	−5.53	−3.62	699	1.77

[a] Potentials are reported versus ferrocenium/ferrocene as half-wave potential for reversible waves. HOMO and LUMO energy levels were estimated from HOMO = −4.80 – E_{ox} (eV) and LUMO = −4.80 − E_{red} (eV). [b] λmax is for the longest-wavelength absorption as recorded from solutions in CH2Cl2 of 1×10^{-5}mol/L; and the optical gap is estimated from the absorption edge as recorded from the same solutions. [c] HOMO-LUMO = Optical gap.

4.2.4 Thin Film Transistors

Semiconductor properties of **4.1** were tested in solution processed thin film transistors. To fabrication solution-processed OTFTs, a solution of **4.1** (0.25% in hexane) was drop-cast onto the octadecylphoshponic acid (ODPA) modified AlO_y/TiO_x dielectric. [13] The transistor was completed by depositing a layer of gold onto the organic film through a shadow mask to form top-contact source and drain electrodes under a high vacuum. The resulting devices had highly doped silicon as the gate electrode and vacuum-deposited gold as top-contact drain. The X-ray diffractions (XRD) from the films of **4.1** exhibited one intense peak and three minor peaks in accordance with the (001), (002), (003) and (005) diffractions derived from the single crystal structures, indicating a highly crystalline film. (see the Experimental Section) It is found that **4.1** functioned as n-type semiconductors with field effect mobility in the range of 0.1 to 0.7 $cm^2V^{-1}s^{-1}$. The mobility did not change when measured under vacuum or in ambient air. Shown in Figure 4.5 are the typical transfer *I-V* curves for the best-performing OTFT of **4.1** as test in ambient air. From the transfer *I-V* curve, a field-effect mobility of 0.72 $cm^2V^{-1}s^{-1}$ is measured in the saturation regime using the equation: $I_{DS} = (\mu WC_i/2L)(V_G - V_T)^2$ and C_i of 200nF/cm^2 for ODPA-modified AlO_y/TiO_x dielectric. On/off ratio of the drain current obtained between 0.2 and -3 V gate bias is greater than 1×10^3.

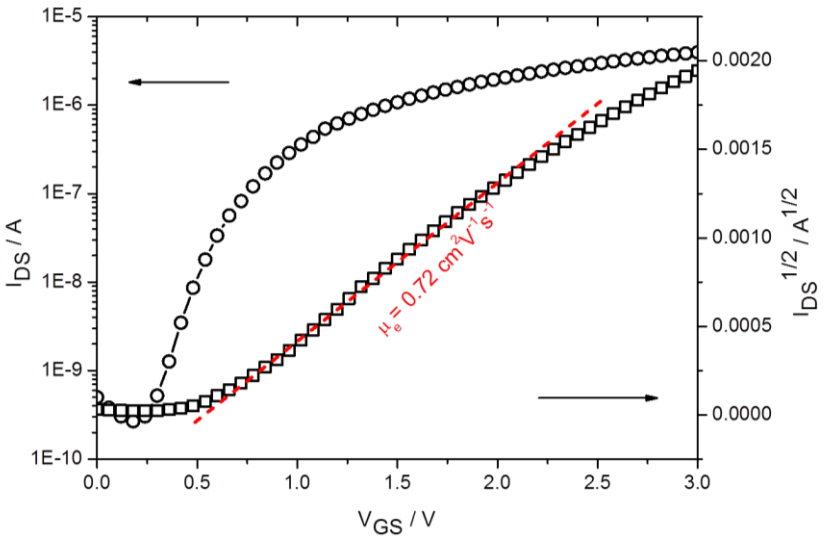

Figure 4.5 Drain current (I_{DS}) versus gate voltage (V_{GS}) with drain voltage (V_{DS}) of 3 V for a thin film transistor of **4.1** with the active channel of W = 1 mm and L = 100 μm as measured in air.

4.3 Conclusion

In summary, reported above is an electron-deficient silylethynylated aceno[2,1,3]thiadiazole (**4.1**), which is designed to combine electron-withdrawing moieties of thiadiazole, pyrazine and chlorine. A typical S-N dipole-dipole interaction was found in their crystal packing. Particularly **4.1** was found to exhibit a low LUMO energy level of -4.18 eV and function as an air stable n-type organic semiconductor in solution-processed OTFTs with field effect mobility as high as 0.7 $cm^2v^{-1}s^{-1}$.

4.4 Expermental

4.4.1 Synthesis

General: The reagents and starting materials employed were commercially available and used without any further purification if not specified elsewhere. Anhydrous and oxygen-free

THF was purified by an Advanced Technology Pure-Solv PS-MD-4 system. 1H-NMR or 13C-NMR spectra were recorded on a Brucker ADVANCE III 400MHz spectrometer. Mass spectra were recorded on a Therno Finnigan MAT 95 XL spectrometer. X-ray crystallography data were collected on a Bruker AXS Kappa ApexII Duo Diffractometer. UV-Vis and steady-state fluorescence spectra were taken on a Cary 5G UV-Vis-NIR spectrophotometer and a Hitachi F-4500 spectrofluorometer respectively. Melting points, without correction, were measured using a Nikon Polarizing Microscope ECLIPSE 50i POL equipped with an INTEC HCS302 heating stage.

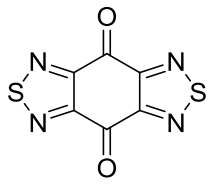

benzo[1,2-c;4,5-c']bis[2,1,5]thiadiazole-4,8-dione (4.5)

A mixture of *p*-chlornil (7.38 g, 30 mmol) and potassium phthalimide (24.45 g, 132 mmol) in CH_3CN (450 mL) was heated to reflux for 2 days. Upon completion of the reaction, the mixture was filtered. The resulting solids were washed with the filtrate was colorless. The green solid was collected and dried in vacuum. Then the green solid and hydrazine hydrate (50%, 30 mL) were mixtured and stirred at 60 ℃ overnight. The mixture was filtered and the resulting dark-brown solids were washed with water, and dried in vacuum yielding 3 g (60%) of 2, 3, 5, 6-tetraamino-benzoquinone which was used in the next step without purification. A mixture of 2,3,5,6-tetraamino-benzoquinone (1.68 g, 10 mmol) in $SOCl_2$ (18 mL) was refluxed for 24 h. The excess $SOCl_2$ was removed in vacuum. The residue was purified by recrystallization from

DMF for three times yielding benzo[1,2-c;4,5-c']bis[2,1,5]thiadiazole-4,8-dione as brown solids (2 g, 90%).[14]

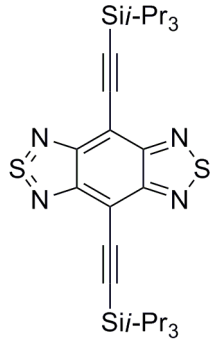

4,8-bis(triisopropylsilylethynyl)-benzo[1,2-c;4,5-c']bis[2,1,5]thiadiazole (**4.2**)

To an oven-dried Schlenk flask was added triisopropylsilylacetylene (2.0 mL, 9.0 mmol) and anhydrous and oxygen-free THF (10 mL). To the resulting solution as cooled at 0 ℃, was added 6.25 ml (10.0 mmol) 1.6 M n-butyllithium in hexane. The reaction mixture was stirred at room temperature for 1 h, and then benzo[1,2-c;4,5-c']bis[2,1,5]thiadiazole-4,8-dione (0.672 g, 3 mmol) was added to it. The mixture was heated to reflux with stirring for 12 h and then quenched with wet diethyl ether. After concentrated under reduced pressure, the residue was dissolved in hexane/ethyl acetate (V/V=4:1) and filtered through a pad of silica gel. The filtrate was collected and concentrated under reduced pressure yielding the corresponding diol (1.2 g, 66%), which was used in the next step without further purification and characterization. A mixture of 59mg (0.1 mmol) of diol, 120 mg of KI and 60 mg of NaH_2PO_2 in 25ml of acetic acid/toluene (V/V=1:1) was heated to reflux for 45 min. After cooling to room temperature, H_2O (20 mL) was added to the mixture and the aqueous solution was extracted with hexanes (3×20 mL). The combined organic layers were concentrated under reduced pressure. The residue was purified by chromatography on silica gel using a mixture solvent of hexane/CH_2Cl_2 (v/v, 7:1) solvent as the

eluent yielding 4,8-bis(triisopropylsilylethynyl)-benzo[1,2-c;4,5-c']bis[2,1,5]thiadiazole (25 mg, 45%) as dark-purple crystals.

^{1}H-NMR ($CDCl_3$) δ(ppm): 1.25(m). ^{13}C-NMR($CDCl_3$) δ(ppm): 11.6, 18.9, 101.1, 106.3, 111.1, 155.5. HRMS (EI^+): cacld. for $C_{28}H_{42}N_4S_2Si_2$ ([M]+): 554.2384, found: 554.2372. Melting point: 253-255 ℃ (ethyl acetate).

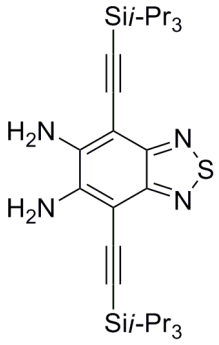

4,7-bis(triisopropylsilylethynyl)-5,6-diamino-benzo[2,1,3]thiadiazole (**4.6**)

111 mg (0.2 mmol) of 4,8-bis(triisopropylsilylethynyl)-benzo[1,2-c;4,5-c']bis[2,1,5]thiadiazole was dissolved in anhydrous and oxygen-free THF (10 mL) in a dried Schlenk-tube under nitrogen. $LiAlH_4$ (76 mg, 2.0 mmol) was added into the solution in portions at 0 ℃. After stirring for 3 h at room temperature the mixture was cooled down to 0 ℃ again and treated with a saturated NH_4Cl aqueous solution. The mixture was diluted with water (30 mL) and extracted with diethyl ether (30 mL) for three times. The organic layers were combined, dried over anhydrous Na_2SO_4 and concentrated under reduced pressure. The crude product was purified by column chromatography using CH_2Cl_2/hexane (V/V=1:1) as the eluent yielding 4,7-bis(triisopropylsilylethynyl)-5,6-diamino-benzo[2,1,3]thiadiazole as yellow solids (95 mg, 90%).

^{1}H-NMR ($CDCl_3$) δ(ppm): 4.26 (bs, 4H), 1.19 (m, 42H). ^{13}C-NMR($CDCl_3$) δ(ppm): 11.4, 18.9, 97.0, 99.7, 103.4, 143.6, 150.5. HRMS (EI^+): cacld. for $C_{28}H_{46}N_4SSi_2$ ([M]+): 526.2976, found: 526.2981. Melting point: 207-209 ℃.

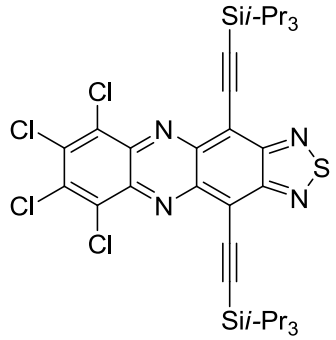

4,11-bis((triisopropylsilyl)ethynyl)-6,7,8,9-tetrachloro-[1,2,5]thiadiazolo-[3,4-b]phenazine (4.1)

Under an atmosphere of N_2, a mixture of 4,7-bis(triisopropylsilylethynyl)-5,6-diamino-benzo[2,1,3]thiadiazole (106 mg, 0.2 mmol) and *o*-chlornil (100 mg, 0.4 mmol) was dissolved in 10 ml of ethanol/acetic acid (V/V=3:1). The resulting suspension was heated to reflux over night. After cooled down to room temperature, 50ml of water was added and resulting mixture was extracted by diethyl ether for three times. The combined organic layer was dried over anhydrous Na_2SO_4 and concentrated under reduced pressure. The crude product was purified by column chromatography using CH_2Cl_2/hexane (V/V=1:5) as the eluent yielding dark solids. The obtained dark solids were dissolved in dichloromethane and an excess PbO_2 (2g) was added. After being stirring for 20 minutes, the reaction mixture was filtrated through a pad of Celite and the filtrate as concentrated under reduced pressure. The residue was purified by column chromatography using CH_2Cl_2/hexane (V/V=1:5) as the eluent yielding 22 mg (15%) of 4,11-bis((triisopropylsilyl)ethynyl)-6,7,8,9-tetrachloro-[1,2,5]thiadiazolo-[3,4-b]phenazine as black

crystals. ^{1}H-NMR ($CDCl_3$) δ(ppm): 1.30(m). ^{13}C-NMR ($CDCl_3$) δ(ppm): 11.7, 19.0, 101.5, 113.9, 115.3, 132.4, 135.9, 140.2, 141.8, 155.8. HRMS (EI^+): cacld. for $C_{34}H_{44}N_4Cl_4SSi_2$ ([M+2H]+): 738.1550, found: 738.1569. Melting point: 299-301 ℃. (ethyl acetate)

4.4.2 Cyclic Voltammetry

Cyclic voltammetry was performed in a solution of anhydrous CH_2Cl_2 with 0.1M tetrabutylammonium hexafluorophosphate (Bu_4NPF_6) as supporting electrolyte, at a scan rate of 100mV s^{-1}. A platinum bead was used as a working electrode, a platinum wire was used as an auxiliary electrode, and a silver wire was used as a pseudo-reference. $FeCp_2^+/FeCp_2^0$ was used as an internal standard. Potentials were recorded versus $FeCp_2^+/FeCp_2^0$, which has a HOMO energy level of -4.80 eV.

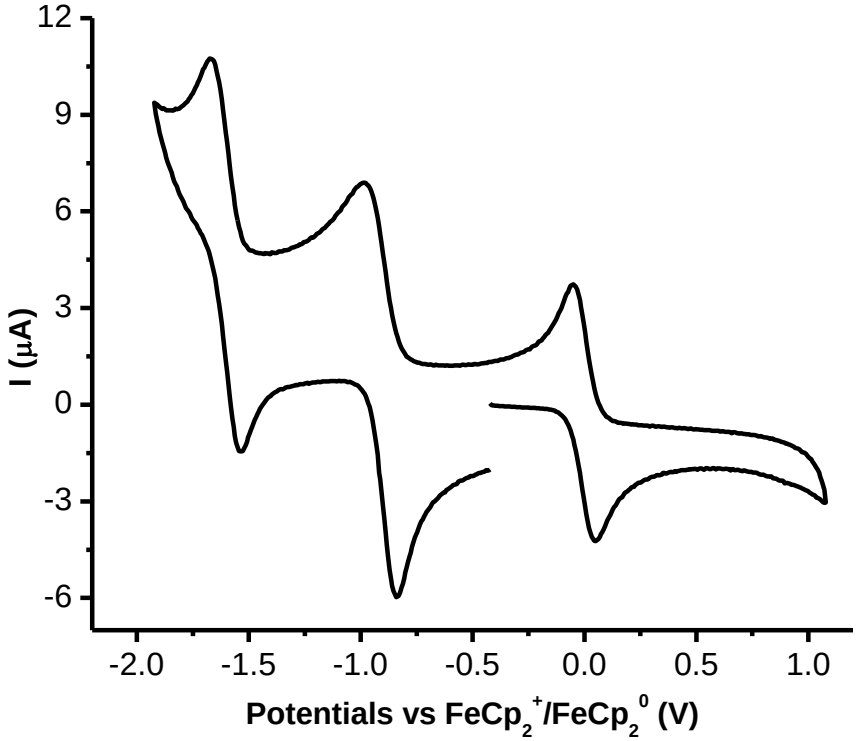

Figure 4.6 Cyclic voltammogram of 4,8-bis(triisopropylsilylethynyl)-benzo[1,2-c;4,5-c']bis[2,1,5]thiadiazole (**4.2**) recorded in CH_2Cl_2.

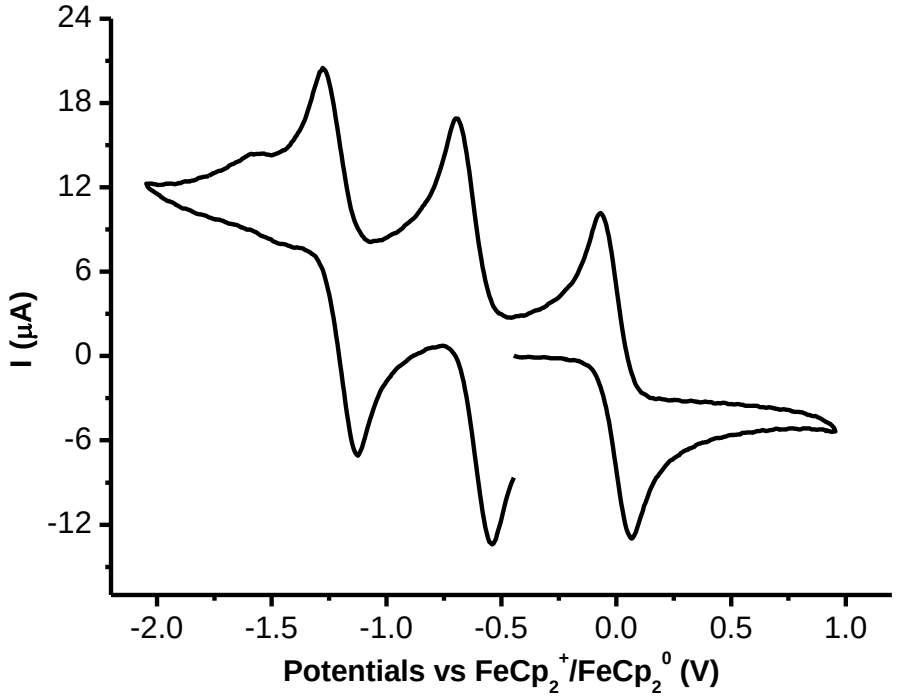

Figure 4.7 Cyclic voltammogram of 4,11-bis((triisopropylsilyl)ethynyl)-6,7,8,9-tetrachloro-[1,2,5]thiadiazolo-[3,4-b]phenazino (**4.1**) recorded in CH_2Cl_2.

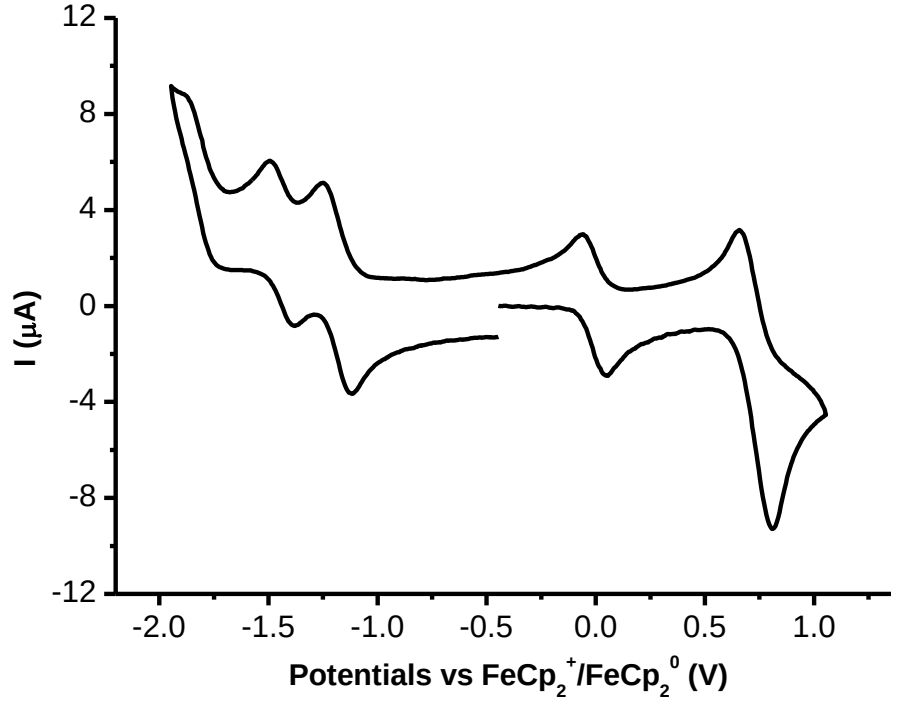

Figure 4.8 Cyclic voltammogram of 4,11-bis((triisopropylsilyl)ethynyl)-[1,2,5]thiadiazolo-anthracene (**4.3**) recorded in CH_2Cl_2.

4.4.3 Characterization of Solution-Processed Thin Films and Transistors

Atomic Force Microscopy (AFM): Thin films deposited on ODPA treated AlO_y/TiO_x dielectric were used for AFM studies. The topographic images were obtained using a Nanoscope IIIa Multimode Microscope from Digital Instruments. The AFM images were collected using tapping mode and in air under ambient conditions. The topographic images were collected from multiple samples, and for each sample, different regions were scanned to ensure reproducibility.

X-ray diffraction (XRD): XRD data were recorded with a SmartLab X-Ray Refractometer at a substrate temperature of 25 ℃.

Electrical Characterization: The current-voltage measurement was carried out on a probe station with a Keithley 4200 Semiconductor Characterization System at room temperature in ambient air. The field effect mobility was measured from transfer I-V curves in the saturation regime using the equation: $I_{DS} = (\mu WC_i/2L)(V_G–V_T)^2$, where I_{DS} is the drain current, μ is field effect mobility, C_i of 200 nF/cm^2 for ODPA-modified AlO_y/TiO_x dielectric, W is the channel width, L is the channel length, and V_G and V_T are the gate and threshold voltage, respectively.

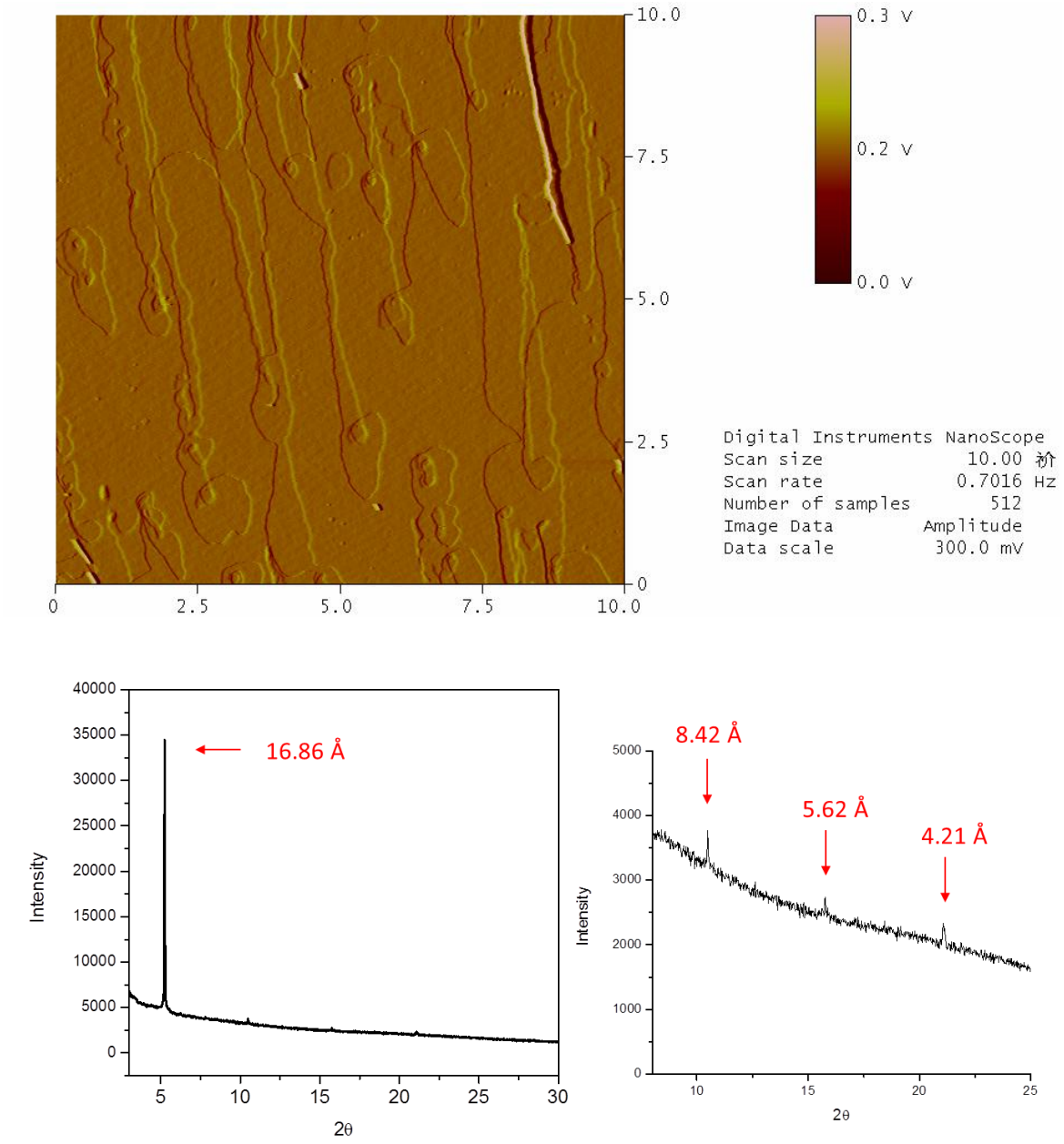

Figure 4.9 (a) AFM image and (b) X-ray diffractions from of a solution-processed films of **4.1**

4.5 Reference

1. (a) Miao, Q., *Synlett*, **2012**, *23*, 326. (b) Liu, Y.-Y.; Song, C.-L.; Zeng, W.-J.; Zhou, K.-G.; Shi, Z.-F.; Ma, C.-B.; Yang, F.; Zhang, H.-L.; Gong, X. *J. Am. Chem. Soc.* **2010**, *132*, 16349. (c) Liang, Z.; Tang, Q.; Xu, J.; Miao, Q. *Adv. Mater.* **2011**, *23*, 1535. (d) Liang, Z.; Tang, Q.; Mao, R.; Liu D.; Xu, J.; Miao, Q. *Adv. Mater.* **2011**, *23*, 5514. (e) Liu, D.; Xu, X.; Su, Y.; He, Z.; Xu, J.; Miao, Q. *Angew. Chem. Int. Ed.* **2013**, *52*, 6222. (f) Sokolov, A. N.; Tee, B. C.-K.; Bettinger, C. J.; Tok, J. B.-H.; Bao, Z. N. *Acc. Chem. Res.* **2012**, *45*, 361. (g) Di, C. A.; Zhang, F. J.; Zhu, D. B. *Adv. Mater.* **2012**, *25*, 313. (h) Chang, J.-W.; Wang, C.-G.; Huang, C.-Y.; Tsai, T.-D.; Guo, T.-F.; Wen, T.-C. *Adv. Mater.* **2011**, *23*, 4077. (i) Chen, Z.; Lee, M. J.; Shahid Ashraf, R.; Gu, Y.; Albert-Seifried, S.; Meedom Nielsen, M.; Schroeder, B.; Anthopoulos, T. D.; Heeney, M.; McCulloch, I.; Sirringhaus, H. *Adv. Mater.* **2012**, *24*, 647. (j) Dodabalapur, A. *Mater. Today* **2006**, *9*, 24. (k) B.Mannsfeld, S. C.; Tee, B. C.-K.; Stoltenberg, R.; Chen, C. V. H.-H.; Barman, S.; O.Muir, B. V.; Sokolov, A. N.; Reese, C.; Bao, Z. *Nat. Mater.* **2010**, *9*, 859.
2. Facchetti, A. *Mater. Today*, **2007**, *3*, 28.
3 For recent reviews on organic semiconductors for OTFTs, see: (a) Murphy, A. R.; Fréchet, J. M. *Chem. Rev.* **2007**, *107*, 1066. (b) Allard, S.; Forster, M.; Souharce, B.; Thiem, H.; Scherf, U. *Angew. Chem. Int. Ed.* **2008**, *47*, 4070. (c) Dong, H.; Wang, C.; Hu, W. *Chem. Commun.* **2010**, *46*, 5211.
4 For reviews on n-type organic semiconductors and n-channel OTFTs, see: (a) Newman, C. R.; Frisbie, C. D.; da Silva Filho, D. A.; Brédas, J. L.; Ewbank, P. C.; Mann, K. R. *Chem. Mater.* **2004**, *16*, 4436. (b) Zaumseil, J.; Sirringhaus, H. *Chem. Rev.* **2007**, *107*, 1296.

5 de Leeuw, D. M.; Simenon, M. M. J.; Brown, A. R.; Einerhand, R. E. F. *Synth. Met.* **1997**, *87*, 53.

6 Anthony, J. E.; Facchetti, A.; Heeney, M.; Marder, S. R.; Zhan, X. *Adv. Mater.* **2010**, *22*, 3876.

7 (a) Brédas, J.-L.; Calbert, J. P.; da Silva, D. A.; Cornil, J. *Proc. Natl. Acad. Sci. U.S.A.* **2002**, 99, 5804. (b) Brédas, J.-L.; Beljonne, D.; Coropceanu, V.; Cornil, J. *Chem. Rev.* **2004**, *104*, 4931.

8 (a) Appleton, A. L.; Miao, S.; Bromosz, S. M.; Berger, S. J.; Barlow, S.; Marder, S. R.; Lawrence, B. M.; Hardcastle, K. I.; Bunz, U. H. F. *Org. Lett.* **2009**, *11*, 5222. (b) Linder, T.; Badiola, E.; Baumgartner, T.; Sutherland, T. *Org. Lett.* **2010**, *12*, 4520.

9 Lei, T.; Zhou, Y.; Cheng, C.-Y.; Cao, Y.; Peng, Y.; Bian, J.; Pei, J. *Org. Lett.* **2011**, *13*, 2642.

10. Anthony, J. E. *Angew. Chem. Int. Ed.* **2008**, *47*, 452.

11 Appleton, A. L.; Brombosz, S. M.; Barlow, S.; Sears,J. S.; Bredas, J. L.; Marder, S. R.; Bunz, U. H. F. *Nat. Commun.* **2010**, *1*, 91.

12 The commonly used HOMO energy level of ferrocene is −4.80 eV. See: (a) Pommerehne, J.; Vestweber, H.; Guss, W.; Mahrt, R. F.; Bässler, H.; Porsch, M.; Daub, J. *Adv. Mater.* **1995**, *7*, 551. (b) D'Andrade, B. W.; Datta, S.; Forrest, S. R.; Djurovich, P.; Polikarpov, E.; Thompson, M. E. *Org. Electron.* **2005**, *6*, 11.

13. Su, Y.; Wang, C.; Xie, W.; Xie, F.; Chen, J.; Zhao, N.; Xu, J. *ACS Appl. Mater. Interfaces*, **2011**, *3*, 4662.

14 (a) Anzenbacher, P. Jr.; Palacios, M. A.; Jursíková, K.; Marquez, M. *Org. Lett.* **2005**, *7*, 5027. (b) Neidlein, R.; Dao, T.V.; Gieren, A.; Kokkinidis, M.; Wilckens, R.; Geserich, H. P. *Chem. Ber*. **1982**, *115*, 2898.

Chapter 5 Conjugated Macrocycles of Phenanthrene: Self-Assembly, Semiconductor Properties and a New Segment of [6, 6]-Carbon Nanotube*

5.1 Introduction

Conjugated macrocycle molecules [1] have recently received considerable attention in organic chemistry [2] and supramolecular chemistry [3], [4] as well as materials science [5] because of their roles as building blocks for both carbon-rich nano-structures with intrinsic cavities [6] and functional materials as applied, for example, in fluorescent sensors [7] and organic electronic devices.[8] Although benzene is by far the most commonly employed aromatic building block for the known conjugated macrocycles, [9] the less explored polycyclic aromatic hydrocarbon (PAH) building blocks have larger π-surfaces with more interesting optical and electrical properties. [10]

The building block explored herein is phenanthrene, [11, 12] whose linear oligomers are known as organic semiconductors.[13] In view of this, we envisioned that (nearly) flat conjugated macrocycles of phenanthrenes **5.1**-**5.3** (shown in Figure 5.1) are candidates of organic semiconductors. To explore structure-property relationship, particularly how the self-assembly and semiconductor property of conjugated macrocycles depend on their size, **5.1**-**5.3** were designed to have different linkers connecting three phenanthrene units. Unlike **5.1**-**5.3**, macrocycle **5.4** (shown in Figure 5.1) has a coronal π-backbone, which is a new segment of [6,6]-carbon nanotube.

---

* Portions of this chapter are adapted from a paper submitted to *Chem. Sci.* Synthesis, characterization and DFT calculations were done by me. Synthesis and characterization of **5.1** and **5.3** were done by Mr. Xing Zheng and me. Thin film transistor fabrication and characterization were done by Ms. Xiaomin Xu. SEM images were taken by Dr. Tian Ming.

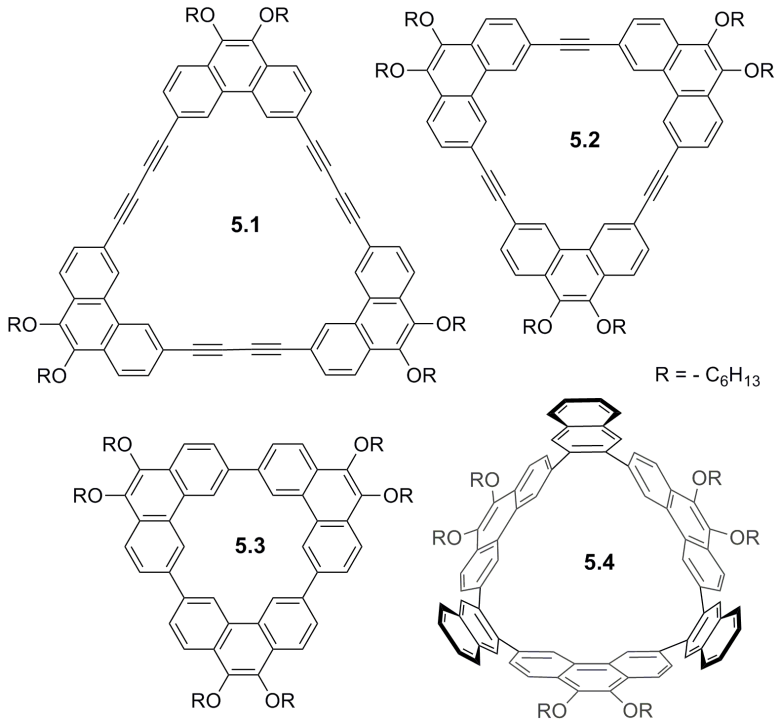

Figure 5.1 Structures of conjugated macrocycles of phenanthrene (**5.1**-**5.4**).

Recent years have witnessed significant steps toward organic synthesis of carbon nanotubes of single chirality,[14, 15, 16] which is still the bottleneck for fundamental studies and advanced applications of carbon nanotubes.[17] New advances in the chemistry of hoop-shaped π-molecules,[18, 19] particularly, synthesis of cycloparaphenylenes by Jasti, [20] Itami [21] and Yamago,[22] have provided not only short segments but also potential synthetic templates of carbon nanotubes. On the basis of these syntheses and Scott's proof-of-concept approach to metal-free growth of carbon nanotubes with Diels-Alder reactions,[23] uniform carbon nanotubes of single chirality and predefined diameter have become a reachable target of organic synthesis.[14] Replacing benzene rings in cycloparaphenylenes with larger arenes leads to hoop-shaped cyclic oligo-arenes, which are also known as π-extended nanorings and are expected to be closer precursors of carbon

nanobelts and nanotubes.[24] By selecting arene units and linking positions, one can design new segments of carbon nanotubes with varied chirality. Such π-extended nanorings were not synthesized until very recently, and have only four known members, namely, cyclo[13]paraphenylene-2,6-naphthylene, [25] [9]cyclo-1,4-naphthylene,[24] [4]-cyclo-2,8-chrysenylene [26] and [4]-cyclo-3,9-chrysenylene.[27] Unlike these reported π-extended nanorings, **5.4** has two different arene units, e.g. phenanthrene and naphthalene, singly bonded in one macrocycle and its naphthalene units are linked at the 2,3-positions rather than the 1,4-positions. Shown in Figure 5.2a is an energy-minimized model for **5.4**, which has the hexyl side chains replaced by methyl groups for simplification. The π-backbone of **5.4** is a new segment of [6,6]-carbon nanotube as displayed in Figure 5.2b.

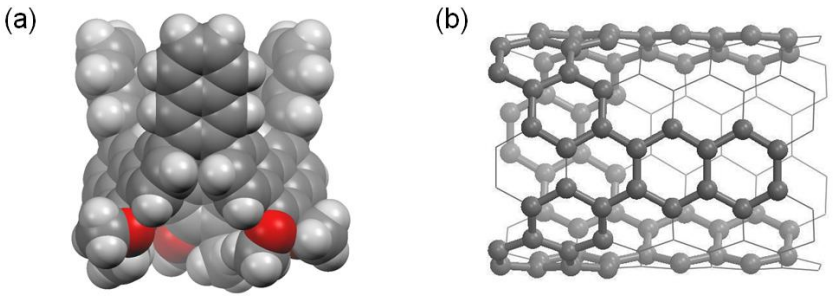

Figure 5.2 (a) CPK model of **5.4'**, a simplified analogue of **5.4** with hexyl groups replaced by methyl groups as optimized at the B3LYP level of DFT with the 6-31G(d,p) basis set; (b) skeleton of **5.4** embedded in [6,6]-carbon nanotube.

5.2 Results and Discussion

5.2.1 Synthesis

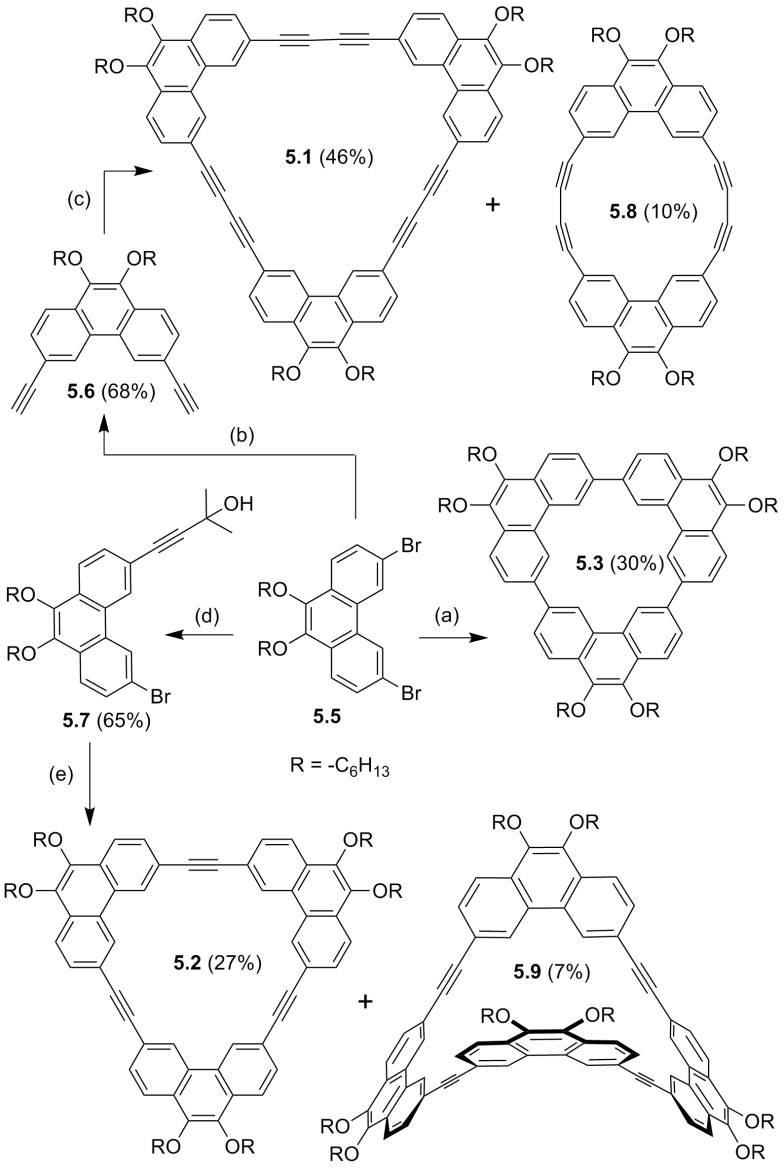

Scheme 5.1 Synthesis of macrocycles **5.1**-**5.3**.[a]

[a] Reagents and conditions: (a) $Ni(cod)_2$, 1,5-cyclooctadiene, 2,2′-bipyridine. (d) 2-methyl-3-butyn-2-ol, $Pd(PPh_3)_2Cl_2$, PPh_3, CuI, Et_3N. (b) (i) trimethylsilylacetylene, $Pd(PPh_3)_2Cl_2$, PPh_3, CuI, Et_3N; (ii) KOH. (c) $Cu(OAc)_2$, pyridine. (e) NaOH, *n*-Bu_4NBr, $Pd(PPh_3)_4$, CuI.

Shown in Scheme 5.1 is the synthesis of **5.1-5.3** starting from 3,6-dibromophenanthrene (**5.5**), which was prepared by modifying a reported procedure.[28] Eglinton reaction of diyne **5.6** led to cyclic trimerization and dimerization yielding **5.1** in an isolated yield of 46% and **5.8** in an isolated yield of 10%, respectively. Sonogashira reaction of **5.7** led to cyclization yielding trimeric and tetrameric macrocycles **5.2** and **5.9**, respectively. The isolated yield of **5.2** is 27%, which corresponds to a yield of 65% for each coupling with in-situ deprotection and is comparable to the yield of dehydrobenzo[12]annulenes from the cyclic trimerization of 1,2-dialkoxy-3-iodo-4-(trimethylsilyl)ethynylbenzenes under a similar Sonogashira reaction condition.[29] Nickel(0)-mediated Yamamoto-type coupling of **5.5** led to the smallest macrocycle **5.3** in an isolated of 30%, which is higher than the yields of cyclotrimerization of 9,10-didecylphenyl-3,6-dichlorophenanthrene (12%) [12] and 7,10-dibromo-2,3-bis(dodecyloxy) -triphenylene (21%) [30] under similar conditions but in 5-fold dilution solution. The relatively good yields of macrocycles **5.1-5.3** can be partially attributed to the shape and rigidity of phenanthrene.

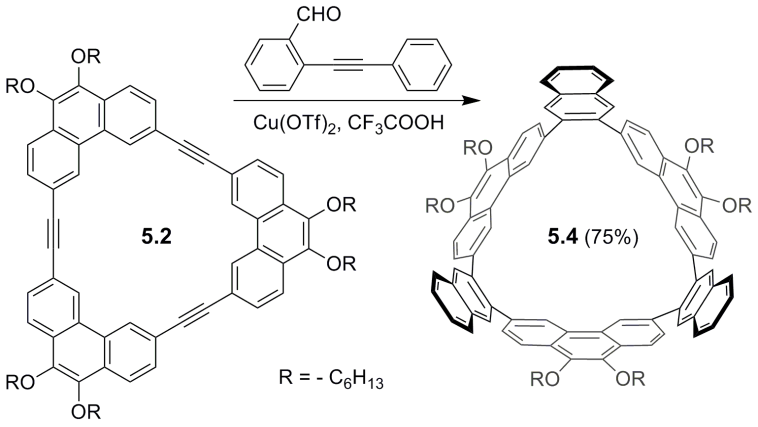

Scheme 5.2 Synthesis of coronal macrocycle **5.4**.

Unlike the synthesis of reported π-extended nanorings, which directly linked naphalene [24] or chrysene subunits,[26, 27] the strategy used here is to convert the synthetically accessible flat macrocycle **5.2** into the coronal nanoring **5.4** by benzannulation.[31] As shown in Scheme 5.2, Lewis acid-catalyzed [4+2] benzannulation [32] between 2-(phenylethynyl)benzaldehyde and each alkyne moiety in **5.2** led to **5.4** in a yield of 75%, which corresponds to a high yield of 91% for each benzannulation reaction. The structure of these macrocycles **5.1**-**5.4** was confirmed by ^{1}H NMR, ^{13}C NMR and MALDI-TOF MS.

Benzannulation on the three alkyne moieties of **5.2** can in principle lead to two isomers depending on whether the benzannulation occurs on the same side of the flat macrocycle **5.2**. The ^{1}H NMR spectrum of **5.4** in toluene-d_8 exhibits six sets of peaks in the aromatic region, which are in agreement with a C3-symmetric structure with all the three naphthalene moieties on the same side. Variable-temperature ^{1}H NMR spectrum of **5.4** was almost unchanged in the range of −40 ℃ to 95 ℃ (shown in the Supporting Information) indicating **5.4** is a rigid molecule. Such rigidity is in agreement with the single bond linkages at the 2,3-positions of naphthalene and the 3,6-positions of phenanthrene. The intrinsic cavity in **5.4** suggests it may function as a molecular host in solution or crystals although no direct evidences were found from our preliminary experiments.

5.2.2 Optical Properties and Frontier Molecular Orbitals

Macrocycles **5.1** and **5.2** are soluble in common organic solvents resulting in light yellow solution with green fluorescence when irradiated with UV light. In comparison, **5.3** is almost colorless in solution with bluish-green fluorescence when irradiated with UV light. As

shown in Figure 5.3, the UV-vis absorption spectra from solutions in CH_2Cl_2 exhibit longest-wavelength absorption at 406 nm for **5.1**, 407 nm for **5.2**, and 388 nm for **5.3**, from which the optical gaps of **5.1**, **5.2** and **5.3** are determined as 3.05 eV, 3.05 eV and 3.20 eV, respectively. In accordance to the red-shifted longest-wavelength absorption, the fluorescence spectra of **5.1** and **5.2** also exhibit red-shifted emission relative to **5.3** as shown Figure 5.3.

The frontier molecular orbitals of **5.1-5.3** were calculated at the B3LYP level of density functional theory (DFT) with the 6-311++G(d, p) basis set using simplified model molecules **5.1'-5.3'** (shown in the Supporting Information), which have smaller methyl groups replacing the hexyl groups in **5.1-5.3**. As shown in the Supporting Information, **5.1-5.3** have their HOMO and LUMO delocalized on the three phenanthrene rings as well as the *sp* C atoms. The energy level of highest occupied molecular orbital (HOMO) is calculated as −5.54 eV for **5.1**, −5.32 eV for **5.2** and −5.45 eV for **5.3**, and the energy level of lowest unoccupied molecular orbital (LUMO) is calculated as −2.42 eV for **5.1**, −2.31 eV for **5.2** and −1.92 eV for **5.3**. The HOMO-LUMO gaps of **5.1-5.3** as calculated from these energy levels are in agreement with the experimental optical gaps. The larger HOMO-LUMO gap of **5.3** relative to those of **5.1** and **5.2** can be attributed to the atomic crowdedness, which drives the molecule out of plane and results less effective conjugation.[33] The delocalized and relatively high HOMO of **5.1-5.3** suggests that these macrocycles may function as p-type semiconductors in the solid state.

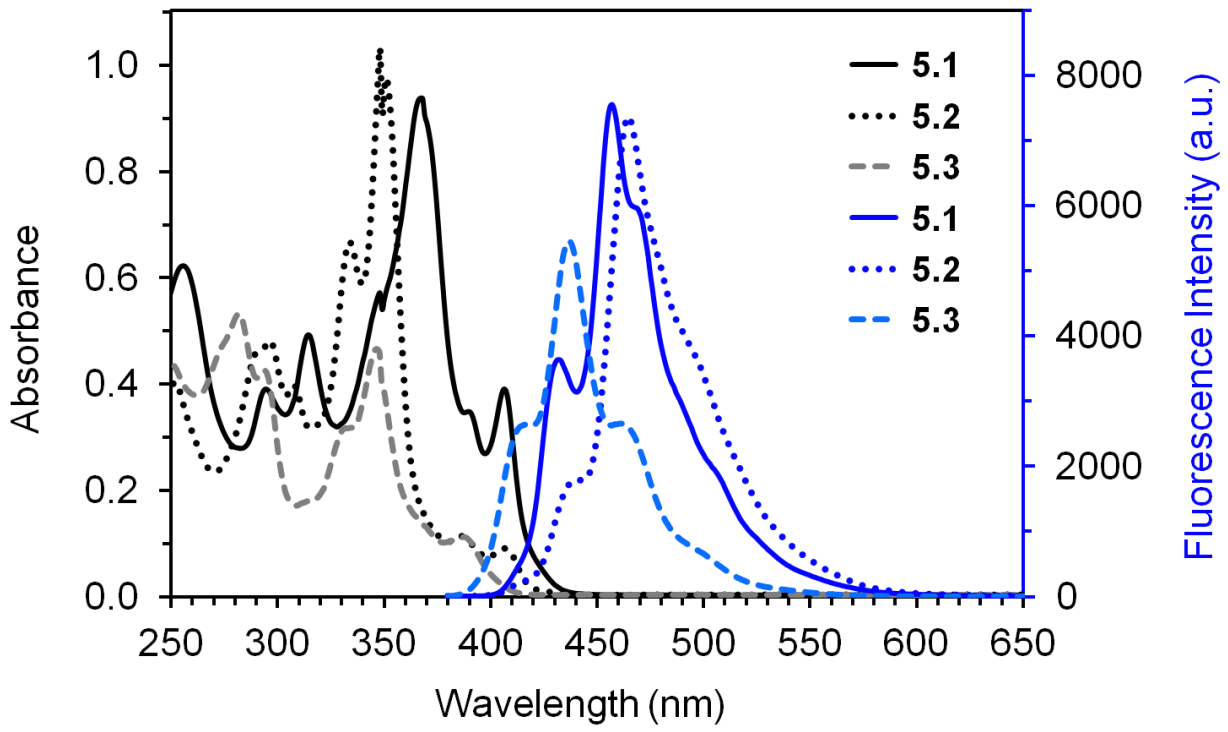

Figure 5.3 UV-vis absorption and fluorescence (excited at 360 nm) spectra of **5.1-5.3** in CH_2Cl_2 (5×10^{-6} mol/L).

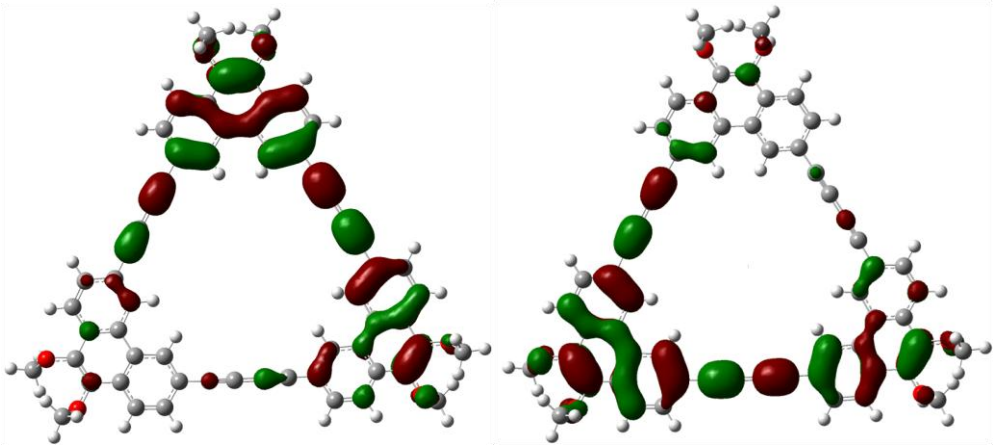

5.1'-HOMO1: -5.56eV **5.1'-HOMO2: -5.56eV**

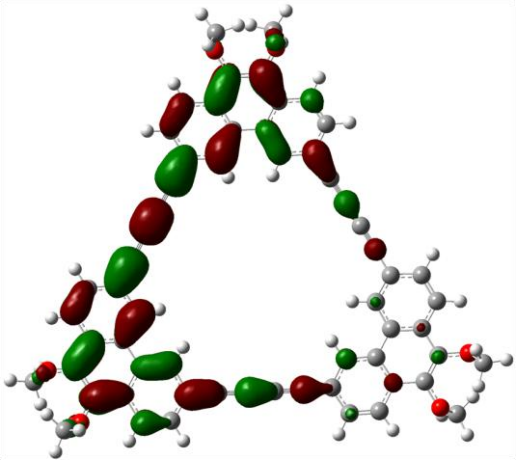

5.1'-LUMO1: -2.10eV

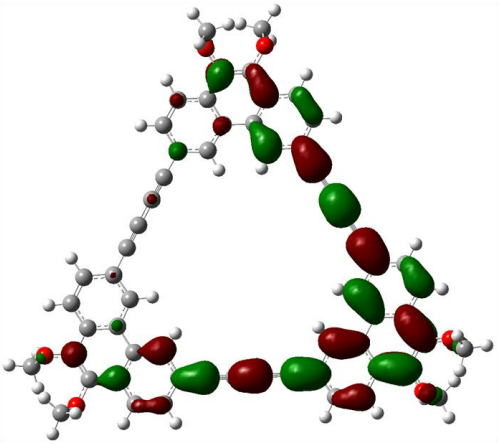

5.1'-LUMO2: -2.10eV

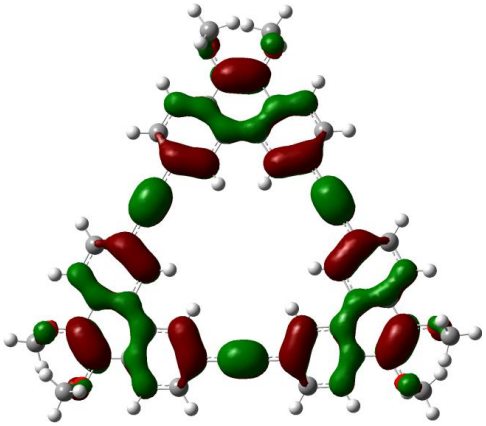

5.2'-HOMO: -5.32eV

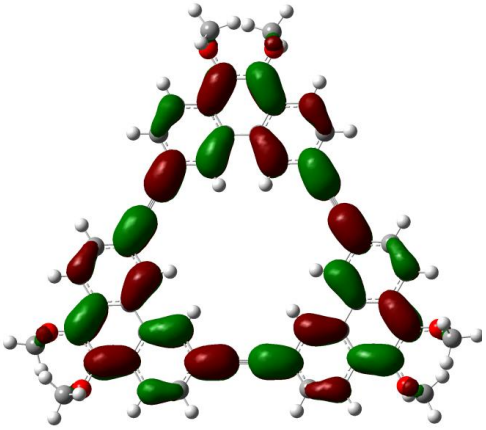

5.2'-LUMO: -2.31eV

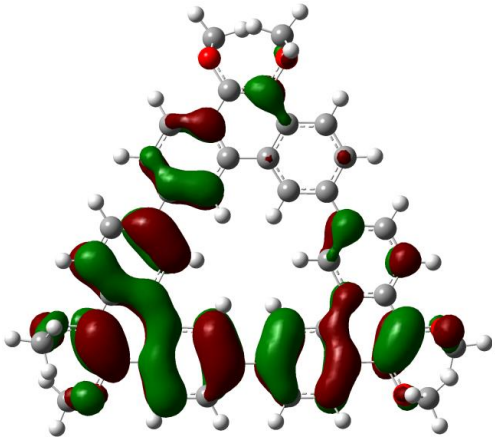

5.3'-HOMO1: -5.45eV

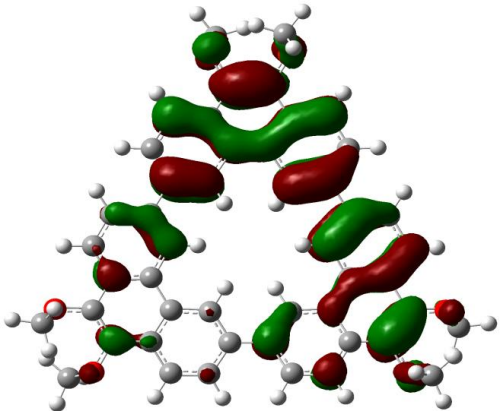

5.3'-HOMO2: -5.45eV

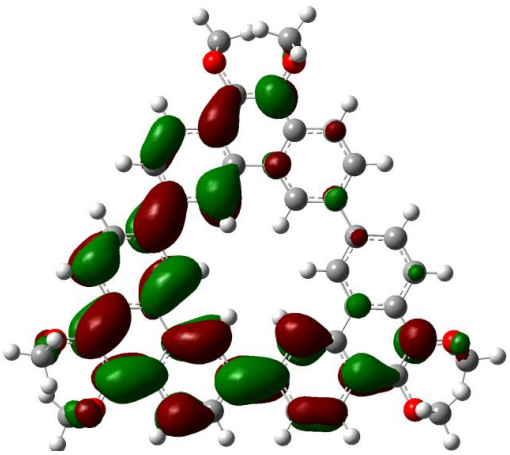

5.3'-LUMO: -1.92eV

Figure 5.4 Calculated HOMO and LUMO energy levels of **5.1'-5.3'**.

Macrocycle **5.4** has a coronal shape of C3 symmetry with dihedral angels of 67.6 ° and 76.7 ° between neighboring planes of phenanthrene and naphthalene as found from the energy-minimized model (shown in Figure 5.2a). To evaluate the conjugation between phenanthrene and naphthalene units in **5.4**, the UV-vis absorption and fluorescence spectra of **5.4** are compared with those of the corresponding monomers, 9,10-dihexyloxyphenanthrene (**5.10**) and naphthalene (**5.11**). As shown in Figure 5.5a, the solution of **5.4** has stronger and red-shifted absorption in comparison to the mixed solution of **5.10** and **5.11**, which has the same concentration for each chromaphore. As shown in Figure 5.5b, the mixed solution of **5.10** and **5.11** has a weak emission band corresponding to naphthalene and a strong emission band corresponding to phenanthrene, while the solution of **5.4** only has a stronger and red-shifted emission band corresponding to phenanthrene when excited at the same wavelength. The absence of the weak emission band corresponding to naphthalene is due to energy transfer from naphthalene to phenanthrene in **5.4** in view of the overlap between the emission of **5.11** and the absorption of **5.10**. The enhanced and red-shifted absorption and emission of **5.4** suggest

considerable conjugation between the phenanthrene and naphthalene units, which is in agreement with the delocalized distribution of LUMO. Shown in Figure 5.6 are the HOMO and LUMO of **5.4** as calculated at the B3LYP level of density functional theory (DFT) with the 6-311++G(d, p) basis set using the simplified model molecule **5.4'**. It is found that the HOMO contains two degenerate orbitals, which are both essentially localized on phenanthrene rings, and the LUMO is fully delocalized on all the phenanthrene and naphthalene rings.

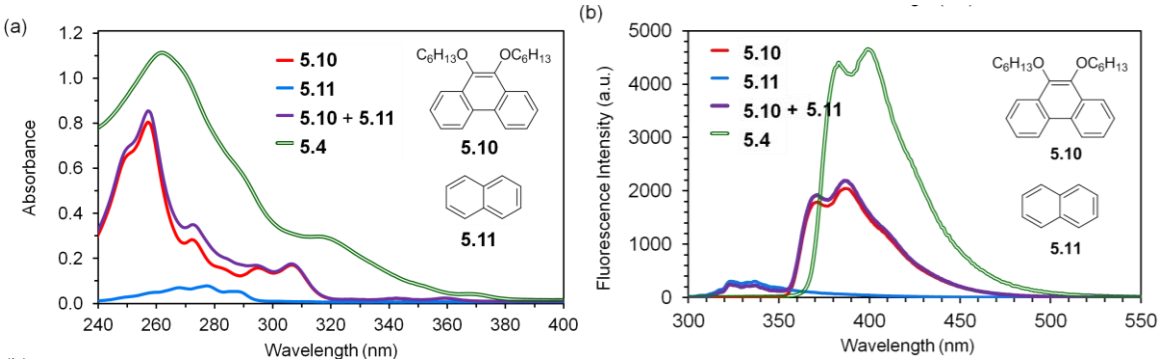

Figure 5.5 (a) UV-vis absorption and (b) fluorescence (excited at 280 nm) spectra of **5.4** and the corresponding monomers in CH_2Cl_2 (the concentration of **5.4** is 5×10^{-6} mol/L, and the concentration of each momomer is 1.5×10^{-5} mol/L).

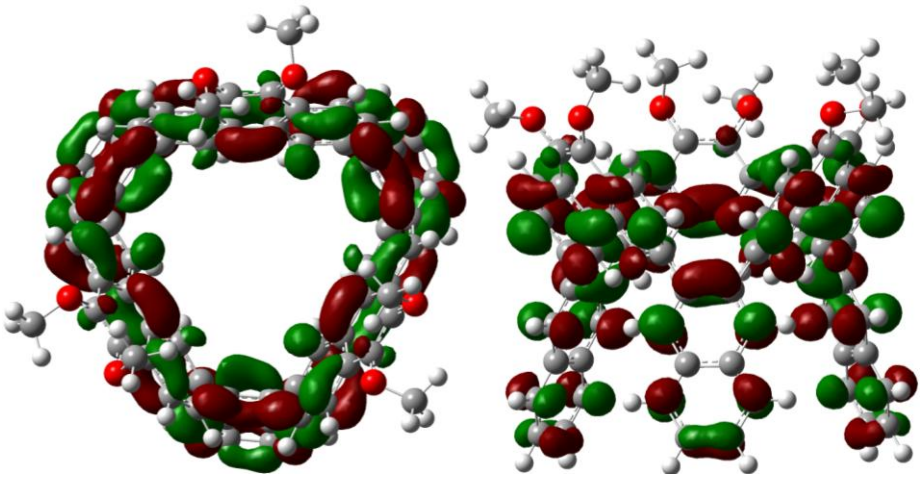

5.4'-LUMO: -1.62eV (from different views)

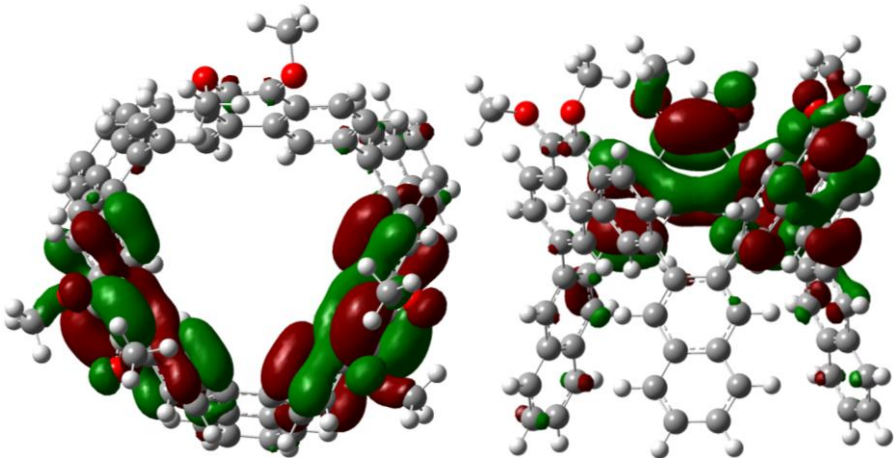

5.4'-HOMO1: -5.68eV (from different views)

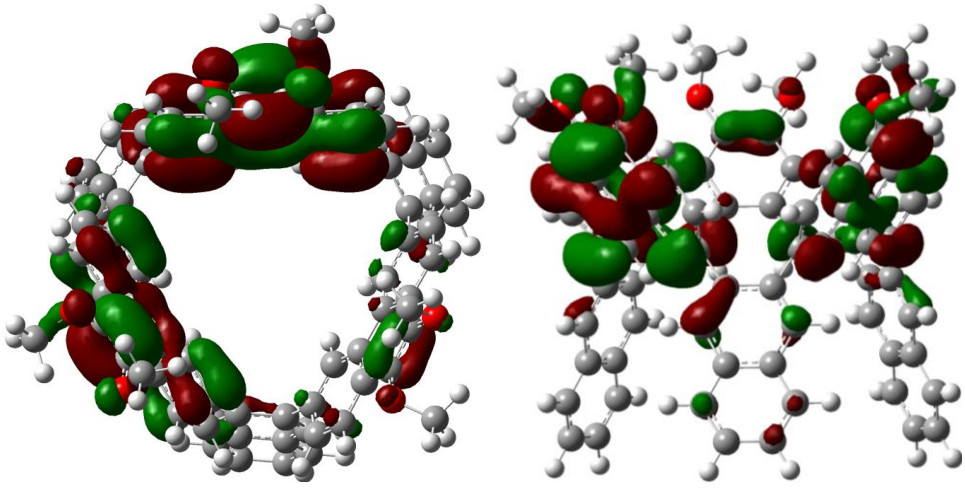

5.4'-HOMO2: -5.68eV (from different views)

Figure 5.6 Calculated HOMO and LUMO of **5.4'**.

5.2.3 Self-Assembly

It became evident during routine characterization of **5.1**-**5.3** with ^{1}H NMR spectroscopy that the aromatic chemical shifts of **5.1** and **5.3** were dependent on concentration. At room temperature, the chemical shift of H_a, the proton inside the macrocycle, in **5.3** varied from δ = 9.63 to 9.08 ppm as the concentration changed from 0.21 to 71 mM as shown in Figure 5.7a. In

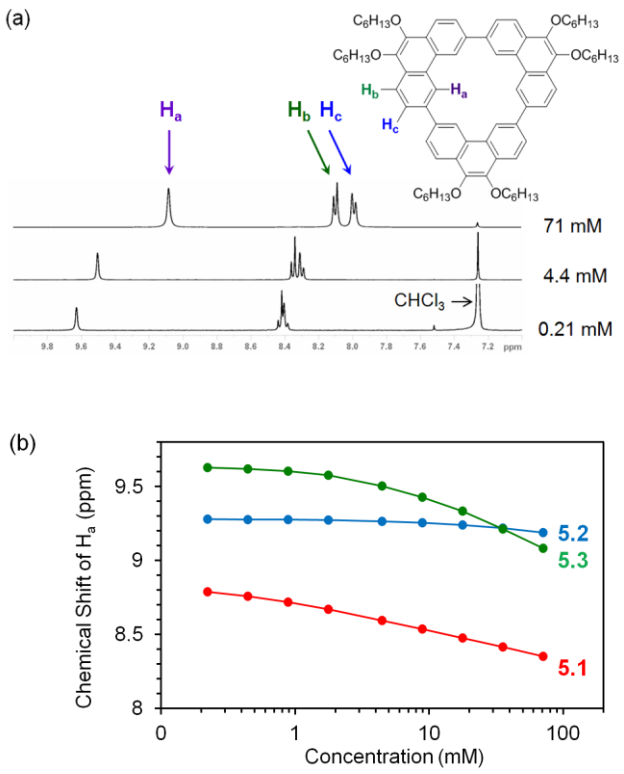

Figure 5.7 (a) Selected ^{1}H NMR spectra of **5.3** with varied concentration in $CDCl_3$ at room temperature; (b) concentration dependence of ^{1}H NMR chemical shifts for H_a of **5.1**-**5.3** in $CDCl_3$ at room temperature.

comparison, the chemical shifts of the aromatic protons outside the macrocycle (H_b and H_c) varied from δ = 8.44 to 8.11 ppm and from 8.40 to 8.00 ppm, respectively, in the same concentration range. As shown in Figure 5.7b, the chemical shift of H_a in **5.1** exhibited an apparent but smaller up-field shift from 8.79 to 8.35 ppm as the concentration rose from 0.21 to 71 mM. These observations suggest that **5.1** and **5.3** self-associate in chloroform solution with π-π stacking, and the up-field shift of aromatic protons can be attributed to the influence of the ring current from the neighboring molecule. In contrast, the chemical shift of H_a in **5.2** exhibited a very small up-field shift of 0.09 ppm in the same concentration range, which suggests that the

self-aggregation of **5.2** is negligible. Unlike **5.1**, the 1,8-pyrenylene-ethynylene macrocycle, which differs from **5.1** by replacing phenanthrene units with pyrene, is not reported to self-aggregate in solution.[9]

To quantify the self-aggregation of macrocycles **5.1** and **5.3**, the association constants were calculated using the monomer-dimer model, which is the simplest and most commonly used model in studying aggregation of arylene-ethynylene macrocycles.[3] By assuming that monomer–dimer equilibrium is the only association process, such a model can be used in systems where dimerization is the predominant process and the association into higher aggregates is negligible.[34] With an assumption that measured chemical shift is the weighted average that of the monomer and dimer, this model gave a good fit of the experimental data as detailed in the experimental section yielding association constants of 98 L $\cdot$mol^{-1} and 17 L $\cdot$mol^{-1} for **5.1** and **5.3**, respectively.[35] These values are lower than the association constant of cyclo-7,10-tris-triphenylenyl macrocycle (444 L $\cdot$mol^{-1}), which also self-aggregate in solution as observed with varied-concentration ^{1}H NMR.[36]

In relation to fabrication of organic thin film transistors (OTFTs), the self-assemblies of **5.1**-**5.3** in drop-cast films were studied. Depending on the boiling point of solvent used for drop casting, the films formed with 20 to 120 seconds. In such a relatively fast process, **5.1** and **5.3** were found to easily form birefringent films as observed with a polarized light microscope. When a solution of **5.1** in cyclohexane was drop-cast onto the SiO_2 surface of a silicon wafer, the resulting film contained sub-micrometer scaled fibers as shown in Figure 5.8a, which were found with scanning electron microscopy (SEM). Formation of such sub-micrometer scaled fibers suggests preferential self-assembly of **5.1** in one direction, which is in agreement with the self-association with π-π stacking in solution. When a solution of **5.3** in THF and acetone (1:1) was

drop-cast onto a silicon wafer, whose SiO_2 surface was pretreated with a self-assembled monolayer of octadecyltrimethoxysilane (OTMS),[37] the resulting film contained highly birefringent crystalline domains in micrometer scale as shown in Figure 5.8b. In contrast, drop-casting solutions of **5.2** in a variety of solvents onto silicon wafers (with or without pre-treatment of organosilanes) often led to amorphous films, which appeared dark under a polarized light microscope and exhibited structureless surface in the atomic force microscopy (AFM) images. These findings are in agreement with the fact that the macrocycle **5.2** does not self-associate in solution.

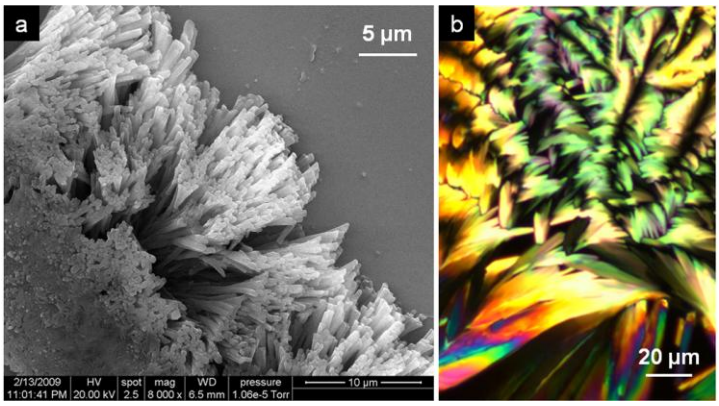

Figure 5.8 (a) SEM image for fibers of **5.1** as formed by drop-casting a solution in cyclohexane onto SiO_2; (b) reflection polarized light micrograph of a film of **5.3** as cast from a solution in THF and acetone (1:1) onto OTMS-modified SiO_2.

5.2.4 Semiconductor Properties

To explore the potential of the flat macrocycles **5.1**-**5.3** as semiconductors, we first tested them in as-cast films with a field effect transistor structure. A solution of **5.1**-**5.3** in THF or a mixed solvent of THF and acetone was drop-cast onto a silicon wafer, which had its SiO_2 surface pretreated with a self-assembled monolayer of octadecyltrimethoxysilane.[37] The resulting film of

5.3, for instance, as observed with a polarized light microscope is displayed in Figure 5.9b. The transistor was completed by depositing a layer of gold onto the organic film through a shadow mask to form top-contact source and drain electrodes. As measured in ambient air from these devices, **5.1** and **5.3** functioned as p-type semiconductors with field effect mobility of 2.4×10^{-4} $cm^2V^{-1}s^{-1}$ and 4.4×10^{-5} $cm^2V^{-1}s^{-1}$, respectively. In contrast, the as-cast films of **5.2** appeared insulating presumably due to the disordered nature of the film.

With flexible alkyl chains surrounding rigid π-planes, molecules of **5.1**-**5.3** may reorganize themselves upon thermal annealing, which is widely used in treating organic thin films to enhance the ordering of molecules. In view of this, the drop-cast films of **5.1**-**5.3** were heated at 120 ℃ for 10 minutes and then cooled in air to room temperature. After this annealing the amorphous film of **5.2** turned birefringent when observed with a polarized microscope. X-ray diffraction from the annealed film of **5.2** exhibited a major peak at $2\theta = 3.70°$ (*d*-spacing: 23.87 Å) along with three minor peaks. With top-contact drain and source electrodes of gold, the annealed film of **5.2** behaved as a p-type semiconductor with field effect mobility up to 7.0×10^{-4} $cm^2V^{-1}s^{-1}$. Unlike **5.2**, the annealed films of **5.1** and **5.3** behaved as p-type semiconductors with their field effect mobilities almost unchanged. The negligible effect of annealing on the films of **5.1** and **5.3** can be attributed to the molecular ordering that already exists in the as-cast films, which is related to the self-association of **5.1** and **5.3** in solution. The best-performing OTFT of **5.2** was fabricated by drop-casting or spin-coating a solution of **5.2** in toluene onto a silicon wafer, which had its SiO_2 surface pretreated with a self-assembled monolayer of phenyltrichlorosilane,[38] and subsequent annealing at 120 ℃. The resulting film contained broken birefringent fibers as shown in the polarized light micrograph in Figure 5.9a, and exhibited a field effect mobility of 1.2×10^{-3} $cm^2V^{-1}s^{-1}$. This mobility was extracted from the transfer I-V

curves shown in Figure 5.9b using the equation: $I_{DS} = (\mu WC_i/2L)(V_G–V_T)^2$, where I_{DS} is the drain current, μ is field effect mobility, C_i is the capacitance per unit area for the 300 nm thick SiO_2, W is the channel width, L is the channel length, and V_G and V_T are the gate and threshold voltage, respectively.

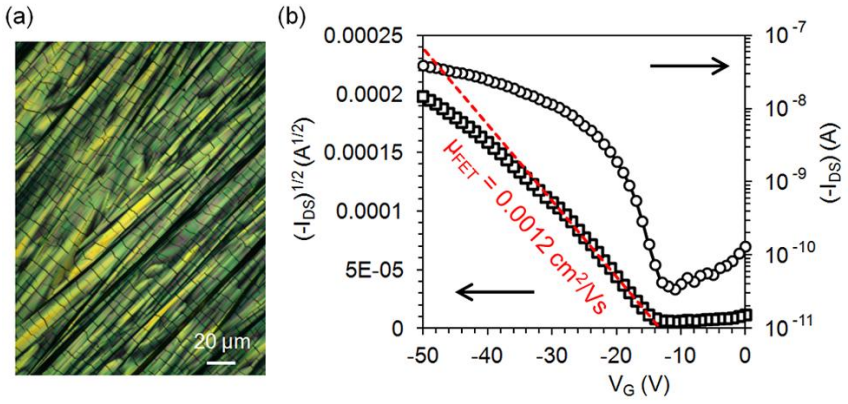

Figure 5.9 (a) Reflection polarized light micrograph of the annealed film of **5.2**; (b) drain current (I_{DS}) versus gate voltage (V_G) with drain voltage (V_{DS}) at −50 V for the best-performing OTFT of **5.2** with the active channel of W = 1 mm and L = 150 μm as measured in air.

To better understand the reorganization of **5.2** during the annealing process, **5.2** was further investigated with differential scanning calorimetry (DSC). The DSC trace revealed two phase transitions in the heating cycle, namely, a minor peak at 95 ℃ corresponding to a transition from one crystalline polymorph to another with the reorganization of alkyl side chains, [39] and a more pronounced one at 178 ℃ corresponding to melting. The phase between 95 ℃ and 178 ℃ is not a liquid crystal but a different polymorph of crystal because the powder X-ray diffractions from **5.2** in this temperature range exhibit multiple peaks typical for crystalline powders and the transition at 95 ℃ involves an enthalpy change (ca. 5 kJ mol^{-1}) that is much smaller than the typical value for a transition from crystals to liquid crystals. Here the lower-

temperature and higher-temperature polymorphs are named as K1 and K2, respectively. The reorganization of **5.2** during the annealing process can thus be related to formation of K2, which subsequently transits to K1 upon cooling. The transition from K2 to K1 likely leads to breaking of crystals as shown in Figure 5.9a.

5.3 Conclusion

In summary, we have explored phenanthrene as a useful building block for conjugated macrocycles. Macrocycles **5.1**-**5.3** are found to function as p-type organic semiconductors in solution-processed thin film transistors, and their field effect mobility as measured from as-cast films is dependent on their ability of self-aggregation in solution. Another interesting finding from this study is that Lewis acid-catalyzed [4+2] benzannulation on the flat macrocycle **5.2** leads to the coronal macrocycle **5.4**, whose π-backbone is a new segment of [6,6]-carbon nanotube. This suggests a new strategy to synthesize π-extended nanorings from flat conjugated macrocycles that are more easily accessed.

5.4 Expermental

5.4.1 Synthesis

General: The reagents and starting materials employed were commercially available and used without any further purification if not specified elsewhere. 1H-NMR or 13C-NMR spectra were recorded on a Brucker ADVANCE III 400MHz spectrometer. Mass spectra were recorded on a Therno Finnigan MAT 95 XL spectrometer. X-ray crystallography data were collected on a Bruker AXS Kappa ApexII Duo Diffractometer. UV-Vis and steady-state fluorescence spectra were taken on a Cary 5G UV-Vis-NIR spectrophotometer and a Hitachi F-4500 spectrofluorometer respectively. Melting points, without correction, were measured using a Nikon Polarizing Microscope ECLIPSE 50i POL equipped with an INTEC HCS302 heating stage. Differential Scanning Calorimetry (DSC) was performed on Perkin Elmer Differential Scanning Calorimeter Pyris 1.

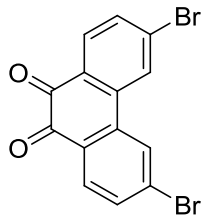

3, 6-dibromophenanthrene-9, 10-dione and

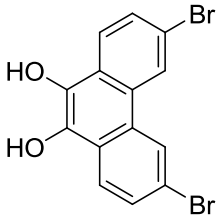

3, 6-dibromophenanthrene-9, 10-diol were synthesized according to the literature.[40]

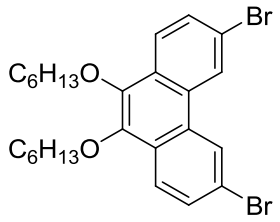

3, 6-dibromo-9, 10-bis(hexyloxy)phenanthrene

To a mixture of 3,6-dibromophenanthrene-9,10-diol (4.208 g, 11.43 mmol) and K_2CO_3 (11.80 g, 85.5 mmol) in 24 ml DMF, which was purged with nitrogen for 30 minutes, was added 1-bromohexane (24.0 ml, 182.88 mmol) via a syringe under a nitrogen atmosphere at room temperature. The resulting solution was stirred under a N_2 atmosphere at room temperature overnight. The solution was then poured into water and extracted with CH_2Cl_2, for three times. The organic layer was combined, washed with brine, dried with anhydrous Na_2SO_4 and concentrated under reduced pressure to remove the CH_2Cl_2 and excessive 1-bromohexane. The pure product was recrystallized from ethanol to yield 3,6-dibromo-9,10-bis(hexyloxy)phenanthrene (3.378 g, 52%). ^{1}H-NMR($CDCl_3$) δ(ppm): 8.64(s, 2H), 8.10(d, J=9.0 Hz, 2H), 7.71(dd, J_1=6.15 Hz, J_2=1.8 Hz, 2H), 4.18(t, J=6.6 Hz, 4H), 1.88(m, 4H), 1.38(m,8H), 0.92(t, J=6.9 Hz, 6H). ^{13}C-NMR($CDCl_3$) δ(ppm): 14.1, 22.6, 25.9, 30.4, 31.7, 73.7, 120.3, 124.2, 125.4, 128.7, 128.8, 130.4, 143.1. These data are consistent with the reported literature.

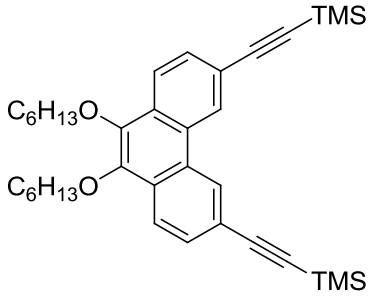

3,6-bis(trimethylsilylethynyl)-9,10-bis(hexyloxy)-phenanthrene

To a mixture of 3,6-dibromo-9,10-bis(hexyloxy)phenanthrene (1.072 g, 2.00 mmol), CuI (70.3 mg, 36.91 mmol), PPh_3 (120.7 mg, 0.46 mmol) and $Pd(PPh_3)_2Cl_2$ (75.0 mg, 0.10 mmol) in 20.0 ml anhydrous and oxygen-free toluene and 1.12 ml triethylamine was added (trimethylsilyl)acetylene (3.6 ml, 16.0 mmol) via a syringe under a nitrogen atmosphere at room temperature. The resulting solution was stirred under a nitrogen atmosphere and refluxed overnight. After reaction, the crude product was extracted with diethyl ether for three times. The organic layer was combined, washed with water, brine, dried with anhydrous Na_2SO_4 and concentrated under reduced pressure. Column chromatography on silica gel (dichloromethane: hexane=1:10) yielded 3,6-bis(trimethylsilylethynyl)-9,10-bis(hexyloxy)- phenanthrene (0.882 g, 77.31%). ^{1}H-NMR($CDCl_3$) δ(ppm): 8.76(s, 2H), 8.15(d, J=8.48 Hz, 2H), 7.68(d, J=8.48 Hz, 2H), 4.19(t, J=6.68 Hz, 4H), 1.90(m, 4H), 1.56(m, 4H), 1.39(m, 8H), 0.95(t, J=6.84 Hz, 6H), 0.35(s, 18H). ^{13}C-NMR($CDCl_3$) δ(ppm): 0.1, 14.1, 22.7, 25.9, 30.4, 31.7, 73.7, 94.8, 105.6, 120.5, 122.3, 126.7, 127.7, 129.6, 130.0, 143.8. These data are consistent with the reported literature.

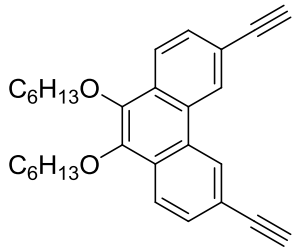

3,6-diethynyl-9,10-bis(hexyloxy)phenanthrene

To a solution of 3,6-bis(trimethylsilylethynyl)-9,10-bis(hexyloxy)-phenanthrene (0.882 g, 1.55 mmol) in 10.0 ml THF was added 2M KOH (3.0 ml, 6.0 mmol). The resulting solution was stirred under air at room temperature overnight. After reaction, saturated 3ml NH_4Cl was added and the solution was extracted with CH_2Cl_2 for three times. The organic layer was combined and

washed with brine, dried with anhydrous Na_2SO_4 and removed under reduced pressure. The crude product was purified by flash column chromatography on silica gel using (dichloromethane: hexane=1:10) as eluent and yielded 3,6-diethynyl-9,10-bis(hexyloxy) phenanthrene (0.576 g, 88.0%). ^{1}H-NMR ($CDCl_3$) δ(ppm): 8.76(s, 2H), 8.18(d, J=8.44 Hz, 2H), 7.70(dd, J_1=8.44 Hz, J_2=1.24 Hz, 2H), 4.20(t, J=6.72 Hz, 4H), 3.22(s, 2H), 1.90(m, 4H), 1.56(m, 4H), 1.38(m, 8H), 0.93(t, J=2.48 Hz, 6H). ^{13}C-NMR($CDCl_3$) δ(ppm): 143.9, 130.1, 129.9, 127.6, 126.9, 122.5, 119.5, 84.1, 77.8, 73.8, 31.7, 30.4, 25.9, 22.7, 14.1. These data are consistent with the reported literature.

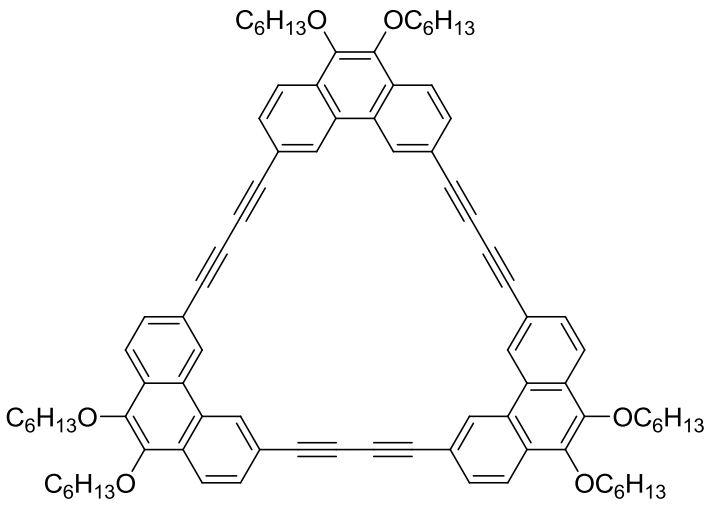

5.1

Cyclic-tri(3,6-diethynyl-9,10-bis(hexyloxy)-phenanthrene) (5.1) and

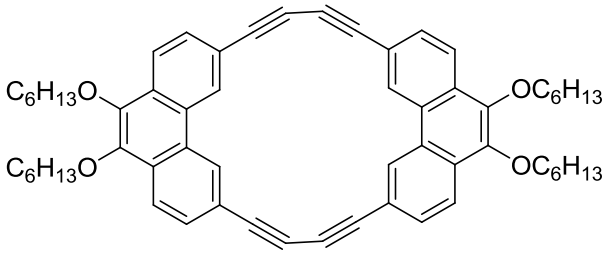

5.8

Cyclic-bis(3,6-diethynyl-9,10-bis(hexyloxy)phenanthrene) (5.8)

To a solution of $Cu(OAc)_2$ (31.70 g, 174.0 mmol) in 200.0 ml of pyridine and 20.0 ml CH_3OH was added 3,6-diethynyl-9,10-bis(hexyloxy)phenanthrene (2.47 g, 5.8 mmol), which was dissolved in 150.0 ml pyridine, by dropping over 2 hours. The resulting mixture was stirred at 55 ℃ overnight. Then the reaction mixture was cooled to room temperature and 200ml methanol was added into the solution. The mixture was filtered and the resulting solid was washed thoroughly with water, methanol successively. Then the solid was submitted to column by using (dichloromethane: hexane=1:3) as eluent and the pure Cyclic-tri(3,6-diethynyl-9,10-bis(hexyloxy)phenanthrene) and cyclic-bis(3,6-diethynyl-9,10-bis(hexyloxy)phenanthrene) were yielded separately. Recrystalized Cyclic-bis(3,6-diethynyl-9,10-bis(hexyloxy)phenanthrene) from CH_2Cl_2 to get pure product (238.2 mg, 9.7%) as yellow crystal. Precipitated Cyclic-tri(3,6-diethynyl-9,10-bis(hexyloxy)phenanthrene) from EtOH to get pure product (1.132 g, 46%) as yellow solid.

Cyclic-bis(3,6-diethynyl-9,10-bis(hexyloxy)phenanthrene) ^{1}H-NMR ($CDCl_3$) δ(ppm): 9.94(s, 4H), 8.00(d, J=8.44 Hz, 4H), 7.37(d, J=8.36 Hz, 4H), 4.17(t, J=6.68 Hz, 8H), 1.88(m, 8H), 1.55(m, 8H), 1.38(m, 16H), 0.93(t, J=6.84 Hz, 12H). ^{13}C-NMR($CDCl_3$) δ(ppm): 14.1, 22.6, 25.8, 30.4, 31.7, 73.8, 90.9, 119.9, 122.5, 125.8, 127.9, 130.2, 133.9, 144.7. HRMS (MALDI-TOF): calcd. for $C_{60}H_{64}O_4$ ($[M]^+$): 848.4805, found: 848.4807.

Cyclic-tri(3, 6-diethynyl-9, 10-bis(hexyloxy)phenanthrene) Melting point: 244 ℃. ^{1}H-NMR ($CDCl_3$, 1mg/ml) δ(ppm): 8.71 (s, 6H), 8.10 (d, J=8.8 Hz, 6H), 7.67 (d, J=8.8 Hz, 6H), 4.20 (t, J=6.8 Hz, 12H), 1.94 (m, 12H), 1.60 (m, 12H), 1.43 (m, 24H), 0.97 (t, J=6.8 Hz, 18H). ^{13}C-NMR($CDCl_3$) δ(ppm): 14.2, 22.8, 26.0, 30.6, 31.9, 73.4, 75.4, 82.7, 119.2, 121.7, 126.9, 127.3,

128.9, 129.2, 143.6. HRMS (MALDI-TOF): calcd. for $C_{90}H_{97}O_6$ ($[M+H]^+$): 1273.7285, found: 1273.7358.

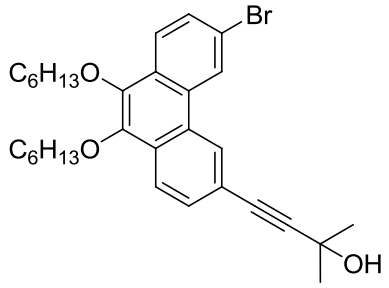

3-(2'-methyl-2'-ol-but-3'-nyl)-6-bromo-9,10-bis(hexyloxy)-phenanthrene

To a mixture of 3,6-dibromo-9,10-bis(hexyloxy)phenanthrene (1.731 g, 3.23 mmol), CuI (123.0 mg, 0.65 mmol), PPh_3 (169.4 mg, 0.65 mmol) and $Pd(PPh_3)_2Cl_2$ (72.5 mg, 0.10 mmol) in 40ml anhydrous and oxygen-free THF and 1.35 ml triethylamine was added 2-methylbut-3-yn-2-ol (0.31 ml, 3.23 mmol) via a syringe under a nitrogen atmosphere at room temperature. The resulting solution was stirred under a nitrogen atmosphere at room temperature overnight. After reaction, the crude product was extracted with diethyl ether for three times. The organic layer was combined, washed with water, brine, dried with anhydrous Na_2SO_4 and concentrated under reduced pressure. Column chromatography on silica gel (dichloromethane100%) yielded 3-(2'-methyl-2'-ol-but-3'-nyl)-6-bromo-9,10-bis(hexyloxy) phenanthrene (0.979 g, 65%). ^{1}H-NMR($CDCl_3$) δ(ppm): 8.60 (d, J=1.2 Hz, 1H), 8.48(s, 1H), 8.06(d, J=8.8Hz, 1H), 8.03(d, J=8.8 Hz, 1H), 7.65(dd, J_1=8.8 Hz, J_2=1.6 Hz, 1H), 7.55(d, J=8.4 Hz, 1H), 4.14(t, J=6.8 Hz, 4H), 2.87(s, 1H), 1.87(m, 4H), 1.74(s, 6H), 1.54(m, 4H), 1.38(m, 8H), 0.94(m, 6H). ^{13}C-NMR($CDCl_3$) δ(ppm): 143.5, 143.0, 130.0, 129.8, 129.3, 129.2, 128.3, 126.9, 126.1, 125.2, 124.0, 122.1, 120.2, 120.0, 94.5, 82.4, 73.7, 73.6, 65.6, 31.6, 31.5, 30.3, 25.8, 22.6, 14.00. HRMS (MALDI-TOF): calcd. for $C_{31}H_{39}{}^{79}BrO_3$ ($[M]^+$): 538.2083, found: 538.1006.

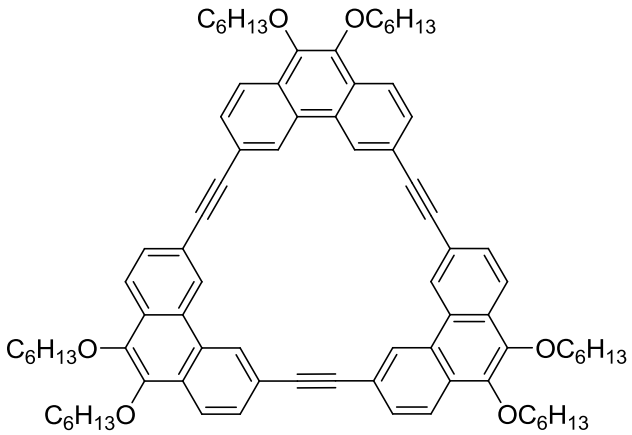

5.2

Cyclic-tri(3-ethynyl-9,10-bis(hexyloxy)phenanthrene) (5.2) and

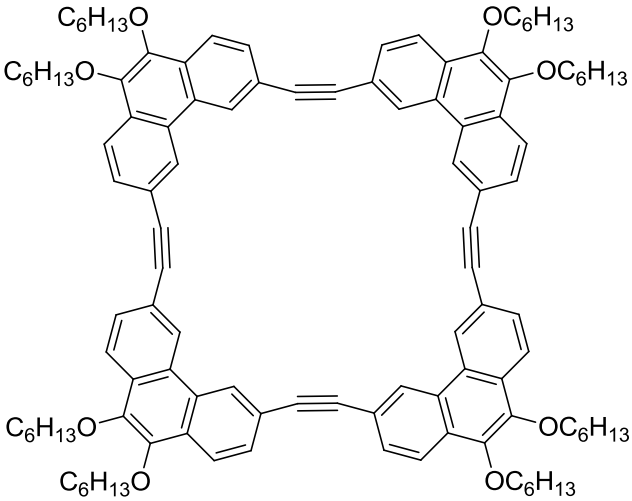

Cyclic-tetra(3-ethynyl-9,10-bis(hexyloxy)phenanthrene) (5.8)

A mixture of 3-(2'-methyl-2'-ol-but-3'-nyl)-6-bromo-9,10-bis(hexyloxy)-phenanthrene (760 mg, 1.4 mmol), CuI (13.5 mg, 0.07 mmol), *n*Bu_4NBr (22.5 mg, 0.07 mmol) and $Pd(PPh_3)_4$ (81 mg, 0.07 mmol) in 30ml oxygen-free benzene and 5 ml 5M aqueous NaOH solution was heated to 90℃ under a nitrogen atmosphere for 24 hours. After reaction, the crude product was extracted with diethyl ether for three times. The organic layer was combined, washed with water, brine, dried with anhydrous Na_2SO_4 and concentrated under reduced pressure. Column chromatography

on silica gel (dichloromethane: hexane = 1:4) yielded yellow solid cyclic-tri(3-ethynyl-9,10-bis(hexyloxy)phenanthrene) (0.150 g, 27%) and near white solid tetra-tri(3-ethynyl-9,10-bis(hexyloxy)phenanthrene) (0.040 g, 7%).

Cyclic-tri(3-ethynyl-9, 10-bis(hexyloxy)phenanthrene) (**2**) Melting point: 178 ℃. ^{1}H-NMR ($CDCl_3$, 1mg/ml) δ(ppm): 9.2 8(s, 6H), 8.24 (d, J=8.8 Hz, 6H), 7.81 (d, J=8.8 Hz, 6H), 4.25 (t, J=6.8 Hz, 12H), 1.95 (m, 12H), 1.61 (m, 12H), 1.43 (m, 24H), 0.96 (t, J=6.8 Hz, 18H). ^{13}C-NMR($CDCl_3$) δ(ppm): 14.3, 22.9, 26.1, 30.7, 31.9, 73.9, 91.2, 120.9, 122.5, 127.2, 128.2, 129.4, 129.5, 144.1. HRMS (MALDI-TOF): calcd. for $C_{84}H_{96}O_6$ ($[M]^+$): 1200.7207, found: 1200.7151.

Cyclic-tetra(3-ethynyl-9, 10-bis(hexyloxy)phenanthrene) (8) 1H-NMR (CDCl3) δ(ppm): 8.86 (s, 8H), 8.24 (d, J=8.4 Hz, 8H), 7.80 (dd, J_1=8.4 Hz, J_2=1.2Hz, 8H), 4.24 (t, J=6.8 Hz, 16H), 1.95 (m, 16H), 1.59 (m, 16H), 1.39 (m, 32H), 0.95 (t, J=6.8 Hz, 24H). ^{13}C-NMR($CDCl_3$) δ(ppm): 14.2, 22.8, 26.1, 30.6, 31.9, 73.9, 90.2, 120.8, 122.6, 126.2, 128.0, 129.7, 130.1, 144.0. HRMS (MALDI-TOF): calcd. for $C_{112}H_{128}O_8$ ($[M]^+$): 1601.9643, found: 1601.9590.

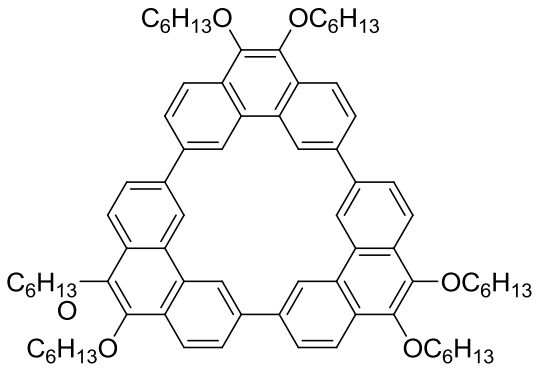

5.3

Cyclic-tri(9,10-bis(hexyloxy)phenanthrene) (5.3)

Bis(cyclooctadiene)nickel (660.2 mg, 2.4 mmol, 2.4 equiv), cyclooctadiene (0.295 ml, 2.4 mmol, 2.4 equiv), and 2,2′-bipyridine (374.9 mg, 2.4 mmol, 2.4 equiv) were dissolved in 10.0 ml dry N,N-dimethylformamide (DMF) in a Schlenk tube reactor. The mixture was heated at 60 ℃ under Argon for 45 minutes with stirring to produce the catalyst, and then a solution of 3,6-dibromo-9,10-bis(hexyloxy)phenanthrene (536 mg, 1.0 mmol) in dry DMF (12.0 ml) was added. The reaction was heated to 75 ℃ for 2 days. The resulting mixture was poured into a mixture of methanol (50.0 ml) and concentrated hydrochloric acid (25.0 ml) and stirred overnight. The brown precipitated solid was filtered off and washed with H_2O and MeOH. Column chromatography (hexane: CH_2Cl_2 = 3:1) yielded product (110mg, 30%) as colorless oil. Precipitate from MeOH to get white solid. ^{1}H-NMR ($CDCl_3$, 10mg/ml) δ (ppm): 9.43(s, 6H), 8.31(d, J=8.8Hz, 6H), 8.25(d, J=8.8Hz, 6H), 4.30(t, J=7.2Hz, 12H), 2.01(m, 12H), 1.68(m, 12H), 1.47(m, 24H), 1.00(t, J=7.2Hz, 18H). ^{13}C-NMR ($CDCl_3$) δ (ppm): 14.1, 22.7, 26.0, 30.6, 31.8, 73.9, 119.1, 123.3, 124.0, 128.9, 129.5, 135.0, 143.5. HRMS (MALDI-TOF): calcd. for $C_{78}H_{96}O_6$ ($[M]^+$): 1128.7207, found: 1128.7208.

Melting point: 320 ℃ (Decomposed).

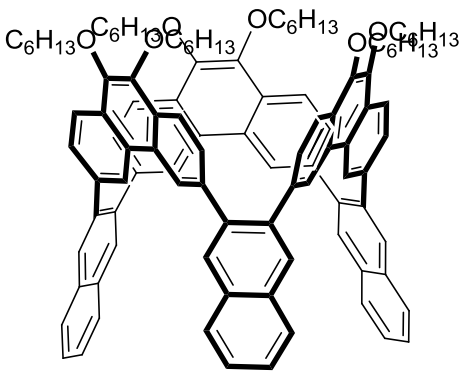

5.4

Cyclic-tri(3-(1’,2’-naphthyl)-9,10-bis(hexyloxy)phenanthrene) (5.4)

To a mixture of Cyclic-tri(3-ethynyl-9,10-bis(hexyloxy)phenanthrene) (48 mg, 0.04 mmol) and $Cu(OTf)_2$ (9.0 mg, 0.024mmol) in 1,2-dichloroethane (10 mL) were added 2-phenylethynyl-benzaldehyde (50mg, 0.24 mmol) and CF_3COOH (20 uL, 0.264 mmol) successively at room temperature under N_2 atmosphere. The resulting mixture was stirred at 100 ℃ for 3 hours and then cooled to room temperature. A saturated aqueous solution of $NaHCO_3$ was added, and the mixture was extracted with ether three times. The combined extracts were washed with brine, dried with anhydrous Na_2SO_4, and evaporated to leave the crude product, which was purified by silica gel column chromatography using dichloromethane: hexane = 1:5 as an eluent to give Cyclic-tri(3-(1',2'-naphthyl)-9,10- bis(hexyloxy)phenanthrene) (45 mg, 0.03 mmol) in 75% yield. ^{1}H-NMR (CD_2Cl_2) δ (ppm): 8.289(s, 6H), 8.006(d, J=8.4Hz, 6H), 7.880(m, 12H), 7.704(dd, J_1=8.4Hz, J_2=1.2Hz, 6H), 7.508(dd, J_1=8.4Hz, J_2=1.2Hz, 6H),4.052(t, J=7.2Hz, 12H), 1.847(m, 12H), 1.525(m, 12H), 1.363(m, 24H), 0,931(t, J=7.2Hz, 18H). ^{13}C-NMR (CD_2Cl_2) δ (ppm): 14.3, 23.1, 26.3, 30.8, 32.2, 73.8, 121.2, 124.1, 126.7, 128.0, 128.5, 128.7, 129.7, 129.7, 132.7, 139.5, 140.9, 143.4. HRMS (MALDI-TOF): calcd. for $C_{108}H_{114}O_6$ ($[M]^+$): 1507.8649, found: 1507.8585. Melting point: 143-144 ℃.

5.4.2 NMR spectra for 5.4 at different temperature

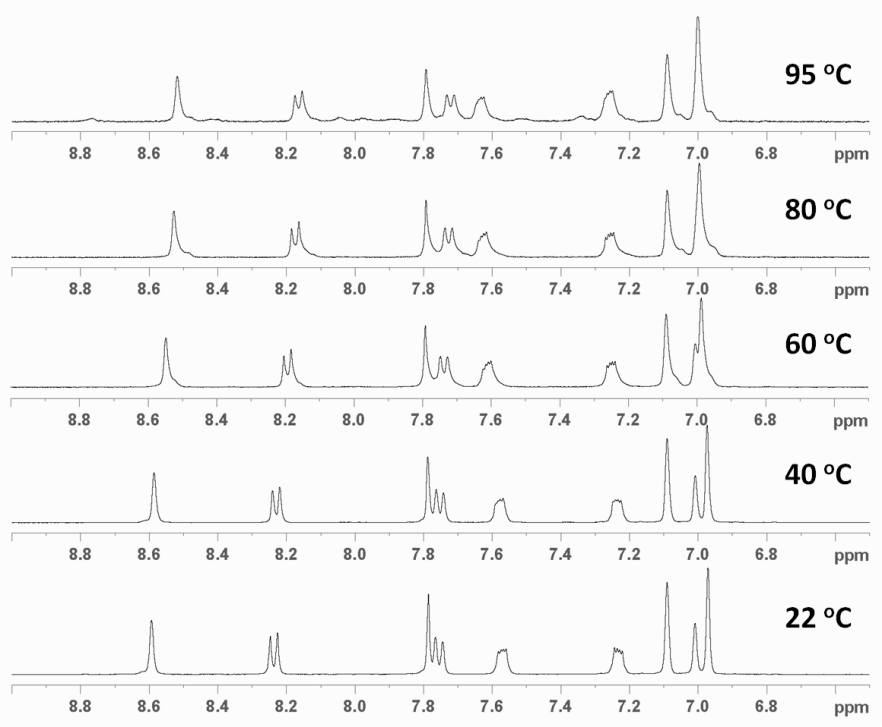

Figure 5.10 ^{1}H NMR spectra for **5.4** in toluene-d_8 at different temperature. (22 ℃ to 95 ℃)

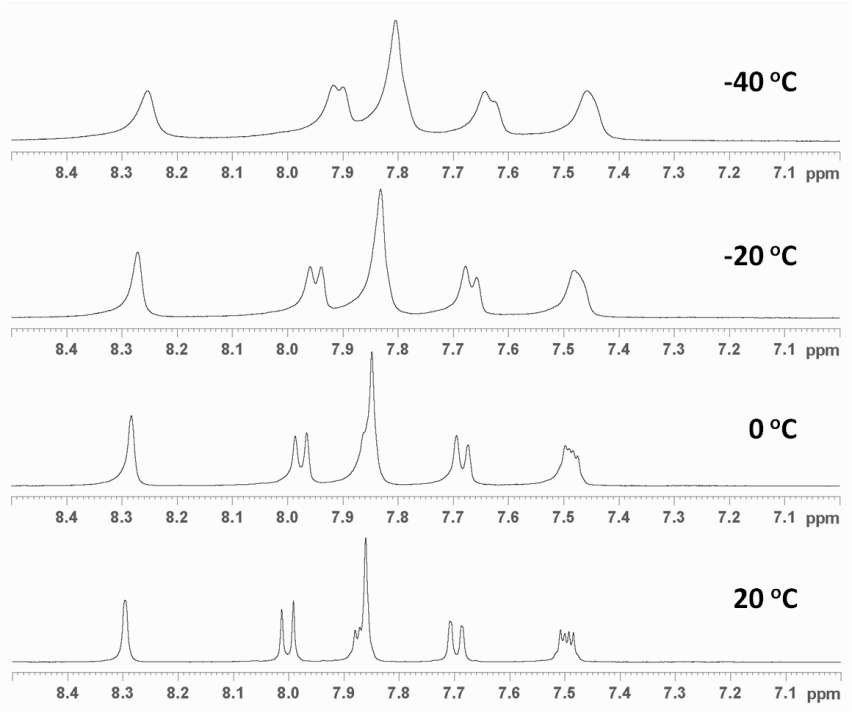

Figure 5.11 ^{1}H NMR spectra for **5.4** in CD_2Cl_2 at different temperature. (22 ℃ to -40 ℃)

5.4.3 1H NMR Data Analysis

The method described here is based on that developed by Horman and Dreux. [41] For dimerization of M, the following equilibrium is assumed:

$$2M \underset{}{\overset{K_{assoc}}{\rightleftharpoons}} M_2$$

$$K_{assoc} = \frac{[M_2]}{[M]^2} \quad \ldots\ldots\ldots\ldots\ldots\ldots\ldots\ldots (1)$$

If it is assumed that the measured chemical shift (δ) is the weighted average that of the monomer (δ_0) and dimer (δ_2):

$$\delta = f_0\delta_0 + f_2\delta_2;\ (f_0 + f_2 = 1)\ldots\ldots\ldots\ldots\ldots\ldots (2)$$

Total concentration of monomer (c):

$$c = [M] + 2[M_2] = [M] + 2K_{assoc}[M]^2\ldots\ldots\ldots (3)$$

From (1) and (2), K_{assoc}, δ, δ_0, δ_2 and c are related by the following expression:

$$\delta = f_0\delta_0 + f_2\delta_2 = f_0\delta_0 + (1\text{-}f_0)\,\delta_2 = f_0(\delta_0\text{-}\delta_2) + \delta_2 = \frac{[M]}{c}(\delta_0\text{-}\delta_2) + \delta_2\ldots\ldots\ldots\ldots\ldots\ldots\ldots (4)$$

From (3), we can get $[M] = \frac{-1+\sqrt{1^2-4\times 2K_{assoc}(-c)}}{2\times 2K_{assoc}}$, which was used in (4) to get following equation:

$$\delta = \delta_0 + \frac{1+4K_{assoc}c-\sqrt{1+8K_{assoc}c}}{4K_{assoc}c}(\delta_2 - \delta_0) \quad \ldots\ldots\ldots\ldots\ldots\ldots (5)$$

For each system, chemical shift (δ) are measured to different total concentration of monomer (c), chemical of the monomer (δ_0), dimer (δ_2) and the association constant K_{assoc} are wanted.

When $A=\delta_2$; $B=2(\delta_2\text{-}\delta_0)$; $C=8\,K_{assoc}$, the equation (5) is of the following form:

$$\delta = A - \frac{B}{1+\sqrt{1+Cc}} \quad \ldots\ldots\ldots\ldots\ldots\ldots (6)$$

The curve fitting was done simply by using Origin 8.5 to give A, B and C as shown here.

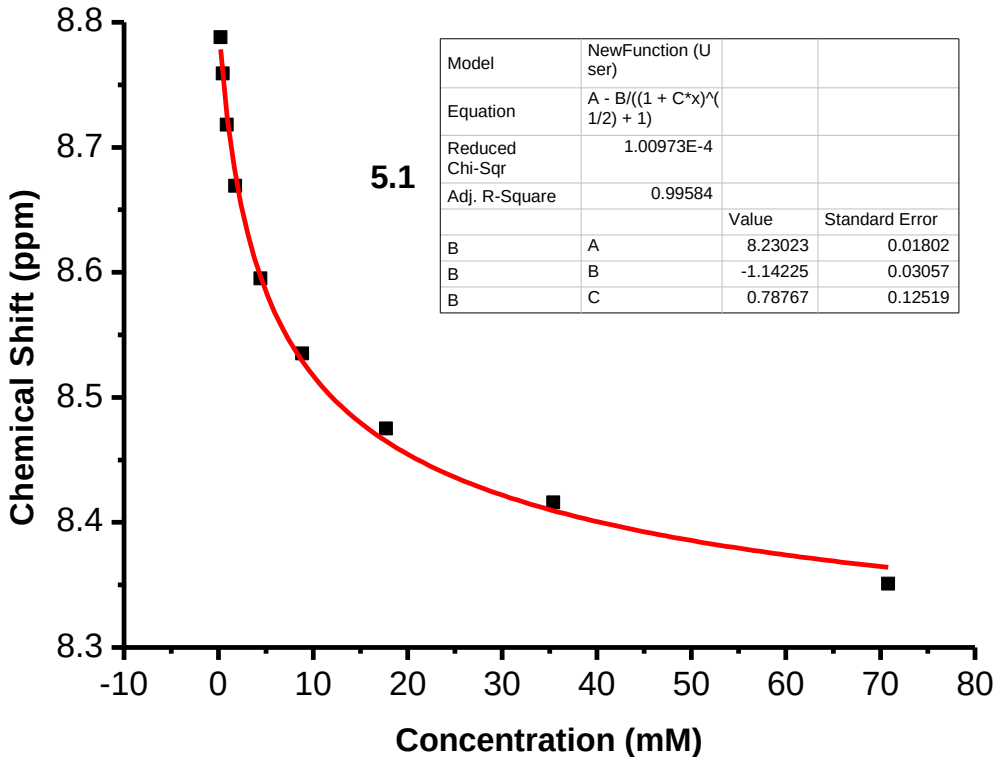

Figure 5.12 Chemical shift of selected aromatic proton of **5.1** at different concentration and curve fitting results.

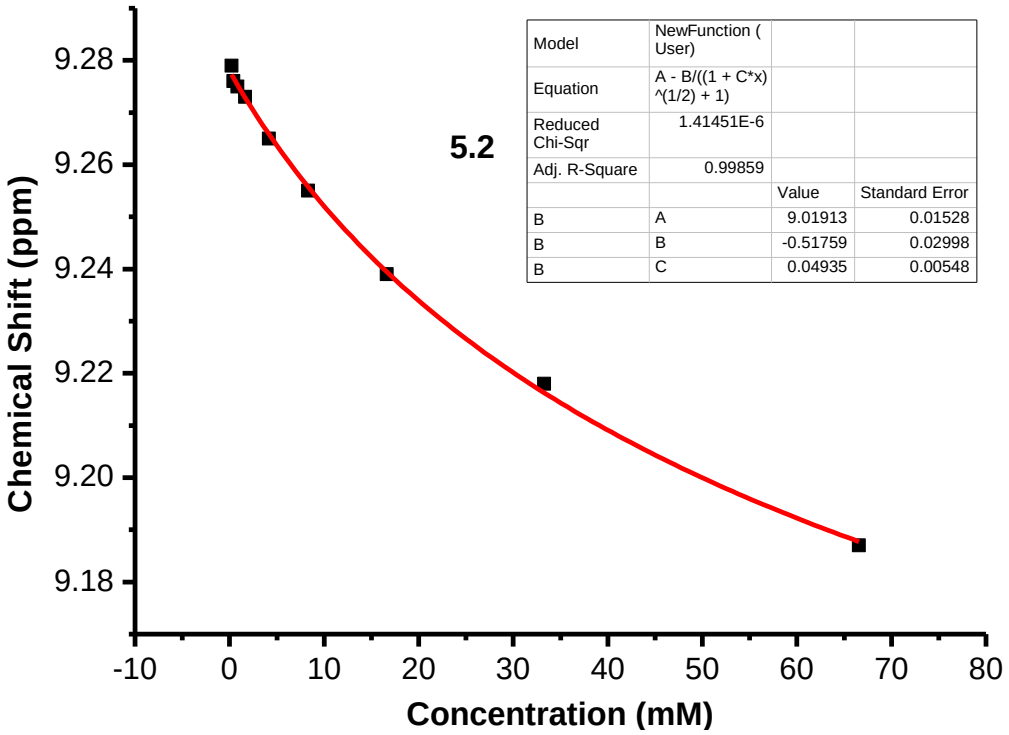

Figure 5.13 Chemical shift of selected aromatic proton of **5.2** at different concentration and curve

fitting results.

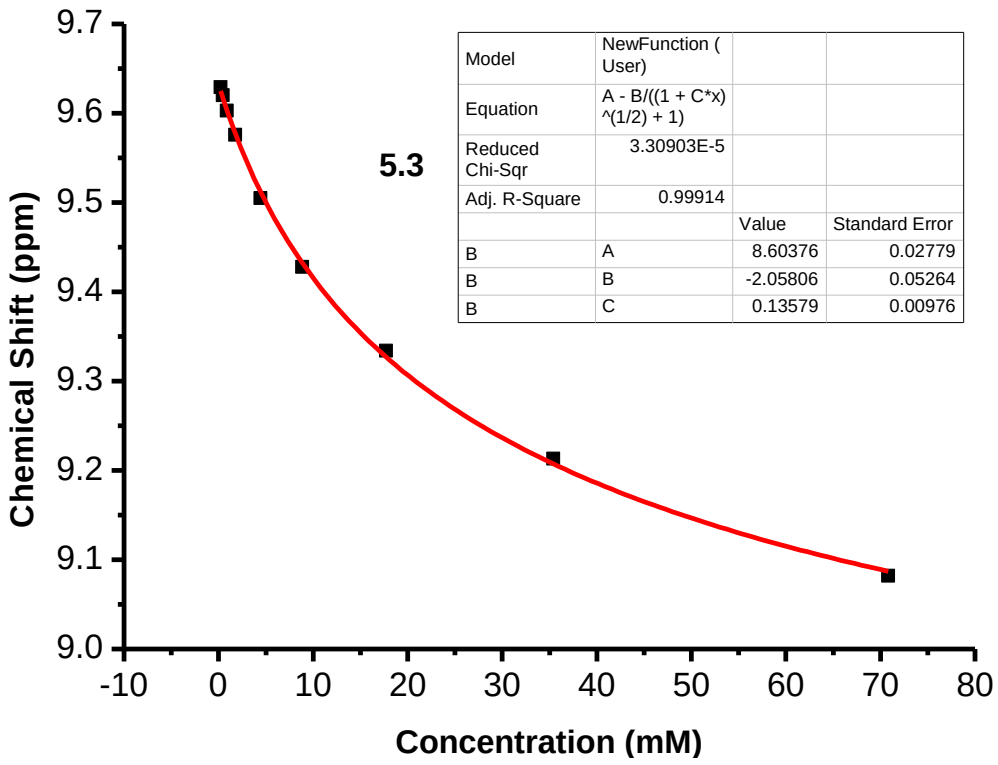

Figure 5.14 Chemical shift of selected aromatic proton of **5.3** at different concentration and curve fitting results.

Table 5-1 Summary of chemical shifts of selected proton Hα at different concentration and curve fitting results.

Concentration for 5.1 and 5.3 (mM in $CDCl_3$)	**Chemical Shift (ppm)**		**Concentration for 5.2 (mM in $CDCl_3$)**	**Chemical Shift (ppm)**
	5.1	**5.3**		**5.2**
0.22	8.788	9.629	0.21	9.279
0.44	8.759	9.62	0.41	9.276
0.89	8.718	9.603	0.84	9.275
1.77	8.669	9.576	1.66	9.273

4.43	8.595	9.505	4.16	9.265
8.85	8.535	9.428	8.32	9.255
17.71	8.475	9.334	16.65	9.239
35.41	8.416	9.213	33.29	9.218
70.82	8.351	9.082	66.57	9.187

Curve Fitting Results

δ_2 (ppm)	8.230	8.604	9.019
δ_0 (ppm)	8.801	9.633	9.278
K_{assoc} (M^{-1})	98	17	6

5.4.4 Cyclic coltammetry and estimation of HOMO/LUMO energy levels of 5.4

Cyclic voltammetry was performed in a solution of anhydrous CH_2Cl_2 with 0.1M tetrabutylammonium hexafluorophosphate (Bu_4NPF_6) as supporting electrolyte, at a scan rate of 100mV s^{-1}. A platinum bead was used as a working electrode, a platinum wire was used as an auxiliary electrode, and a silver wire was used as a pseudo-reference. $FeCp_2^+/FeCp_2^0$ was used as an internal standard. Potentials were recorded versus $FeCp_2^+/FeCp_2^0$, which has a HOMO energy level of -4.80 eV.

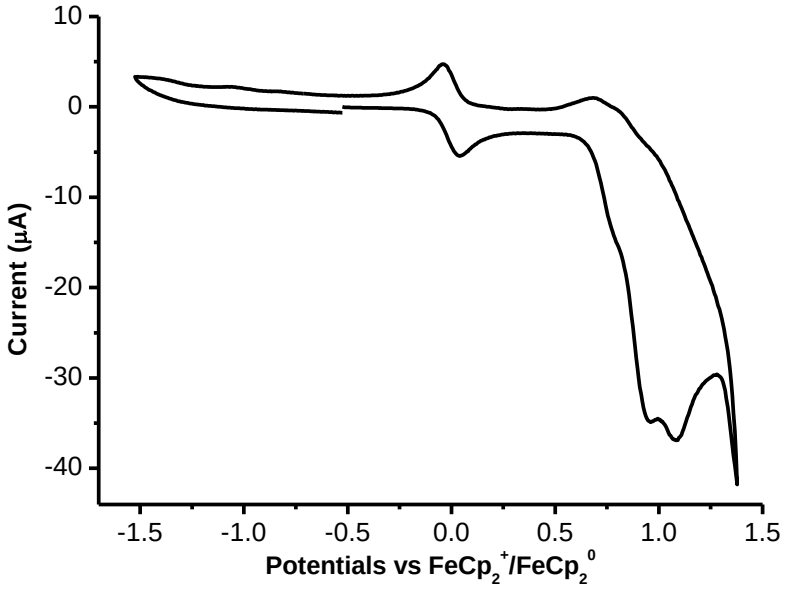

Figure 5.15 Cyclic voltammogram of **5.4** recorded in CH_2Cl_2.

Table 5-2 HOMO and LUMO Energy Levels of **5.4**.

	Computational [a]		Electrochemical	
	HOMO (eV)	LUMO (eV)	HOMO (eV)[b]	LUMO (eV)[c]
5.4	-5.68	-1.62	-5.72	-2.54

[a] HOMO and LUMO energy levels were calculated at the B3LYP level of DFT with 6-311++G(d,p)//6-31G(d, p) basis sets using the corresponding molecule (OMe for OC_6H_{13}) as simplified models. [b] HOMO energy level is estimated from HOMO = $-4.80 - E_{ox}$ (eV). [c] LUMO energy level is estimated from LUMO = HOMO − optical gap; the optical gap is estimated from the absorption edge as recorded from the same solution.

5.4.5 Differential Scanning Calorimetry of 5.2

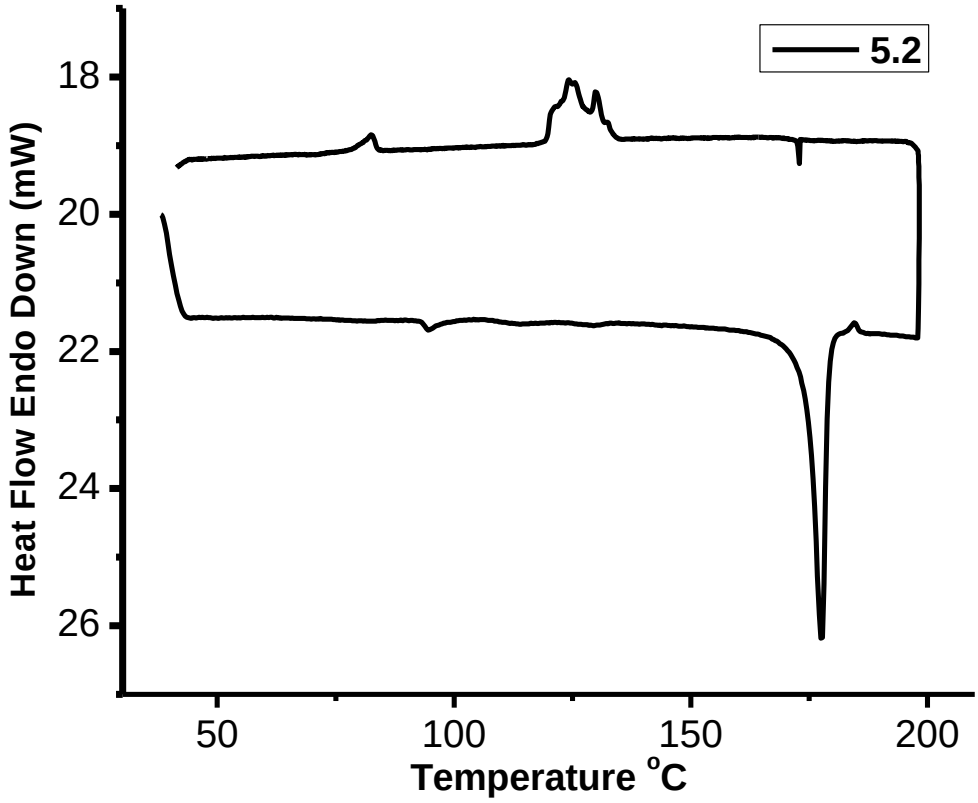

Figure 5.16 DSC thermogram of **5.2** (0.8mg) at a heating rate of 10 ℃/min.

5.4.6 Fabrication and Characterization of Solution-Processed Thin Films and Transistors of 5.1-5.3

❖ **Deposition of thin films and fabrication of transistors**

(1) **Typical for 5.1 – 5.3**

Organic thin films were deposited by drop-casting solutions onto octadecyltrimethoxysilane (OTMS) modified SiO_2/Si wafer at room temperature in air ambient. Selective thermal annealing process was done by heating at 120 ℃ for 10 minutes and cooled in air to room temperature. After deposition of organic layer, the devices were placed in a vacuum oven at room temperature overnight to totally remove the organic solvent. Using an Edwards Auto 306 vacuum coater with a Turbomolecular pump at a pressure of 2.0×10^{-6} torr or lower, top contact drain and source

gold electrodes were vacuum-deposited through a shadow mask onto the films, and the resulting semiconducting channels were 50μm(L)×1mm(W), 100μm(L)×1mm(W), 150μm(L)×1mm(W), 50μm(L)×2mm(W) and 100μm(L)×2mm(W).

A self-assembled monolayer of octadecyltrimethoxysilane (OTMS) was fabricated on SiO_2 surface following the reported procedure: a 3 mM solution of OTMS in trichloroethylene (TCE) was cast to a SiO_2/Si wafer, which was washed with a piranha solution (70:30 H_2SO_4/H_2O_2) and then treated with oxygen plasma. The solution was allowed to partially assemble for 10 seconds then the substrate was spun at 3000 rpm for 10 seconds. Following spin-casting the substrate was put in a closed container with a small vial which contains 10mL of ammonium hydroxide solution (30% in water) for 10h at room temperature. The substrate were then rinsed with deionized water and sonicated in toluene for 10 minutes.

(2) **Particular for 5.2**

The best performance thin film devices of **5.2** were deposited either by drop-casting solutions (1mg in 0.6mL Toluene) directly under the substrate temperature of 120℃ or by spin-coating solutions (5mg in 0.2mL Toluene) through the "on-the-fly-dispensing approach" [42] onto phenyltrichlorosilane (PTS) modiefied SiO_2/Si wafer in air ambient. The spin-coated devices were then put onto hot plate with 120℃ substrate temperature for thermal annealing. After that, all the devices were placed in vacuum oven overnight to totally remove the solvent. Top contact drain and source gold electrodes were finally vacuum-deposited in the same vacuum chamber, creating 50μm(L)×1mm(W), 100μm(L)×1mm(W), 150μm(L)×1mm(W), 50μm(L)×2mm(W) and 100μm(L)×2mm(W) semiconducting channels.

A self-assembled monolayer of phenyltrichlorosilane (PTS) was fabricated on SiO_2 surface by immersing the Piranha cleaned wafer into a toluene solution of PTS (3 wt%) and heated at 90℃ for 15 h.

❖ **Characterization of the Thin Films**

(1) Reflection polarized light micrograph: Polarized optical images of the thin films were obtained using Nikon 50IPOL microscope.

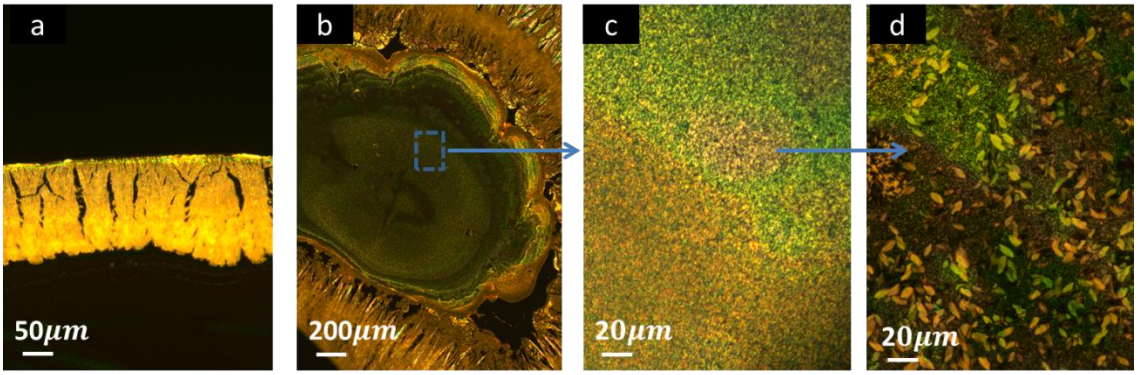

Figure 5.17 Reflected polarized-light micrographs for the films of **5.1** directly drop casted at room temperature (a) from 0.2wt% cyclohexane solution onto bare SiO_2 surface showing sub-micrometer scaled fibers, (b) from 0.17wt% THF solution onto OTMS-modified SiO_2 surface. Figure (c) shows the inner part of (b) with continuous and even thin film suitable for fabricating the thin film transistors; after thermal annealing by heated at 120 ℃ for 10 minutes and cooled in air to room temperature, larger dispersed crystallites formed in such film as shown in (d).

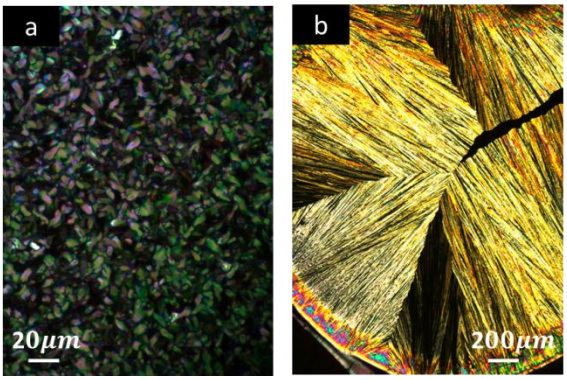

Figure 5.18 Reflected polarized-light micrographs for the films of **5.2** drop casted (a) from 0.17wt% THF solution onto OTMS-modified SiO_2 surface, heated at 120 ℃ for 10 minutes and then cooled in air to room temperature, showing continuous small crystallites, (b) from 0.17wt% toluene solution onto PTS-modified SiO_2 surface with the substrate temperature of 120 ℃, showing birefringent fibers aligned with long-range ordering.

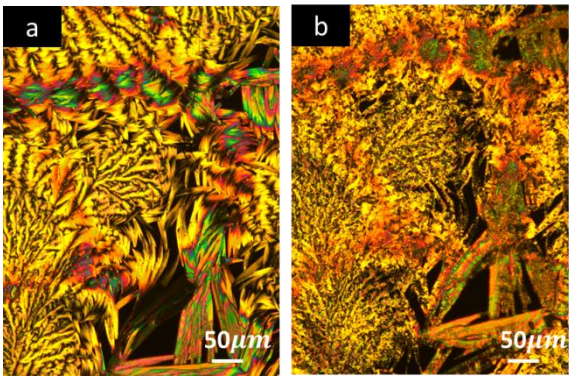

Figure 5.19 Reflected polarized-light micrographs for the films of **5.3** drop casted from 0.17wt% THF and acetone (1:1) mixed solution onto OTMS-modified SiO_2 surface, (a) without thermal annealing, (b) with thermal annealing by heated at 120 ℃ for 10 minutes and then cooled in air to room temperature.

(2) X-ray diffraction (XRD) XRD data were recorded on a SmartLab X-Ray Refractometer of the powders or the thin films deposited by solution process.

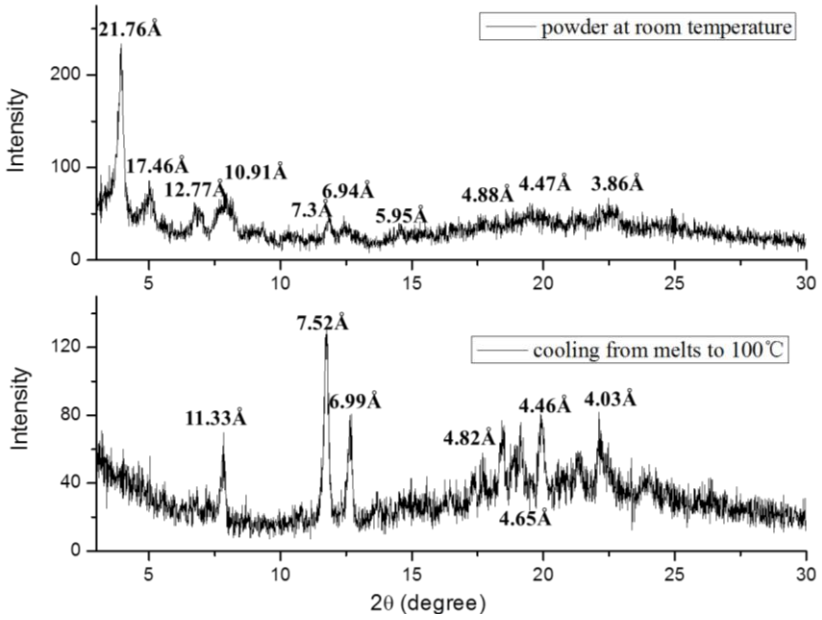

Figure 5.20 X-ray diffraction from the powder of **5.2** at room temperature (the above one), and cooling from melts to 100 ℃ exhibiting a different polymorph of crystal (the below one).

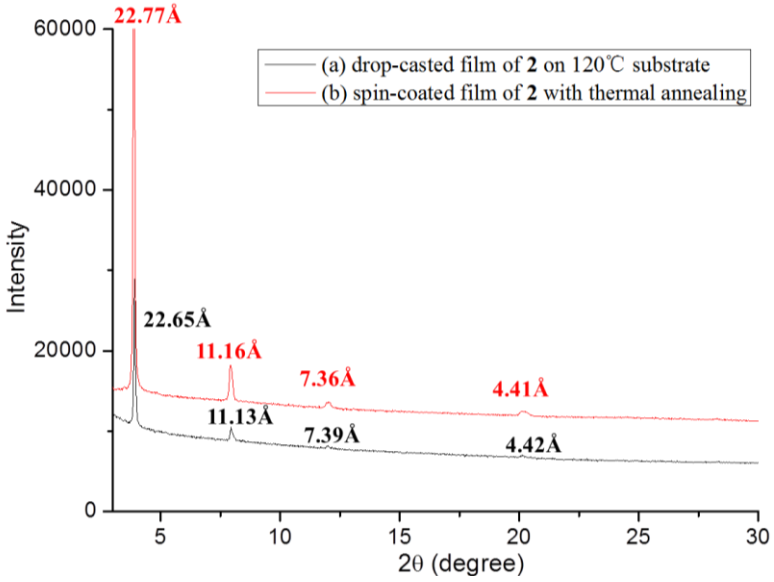

Figure 5.21 X-ray diffraction from thin film of **5.2** (a) drop-casted from 0.17wt% toluene solution onto PTS-modified SiO_2 surface with the substrate temperature of 120 ℃, (b) spin-coated from 2.5wt% toluene solution onto PTS-modified SiO_2 surface, annealing at 120 ℃ followed.

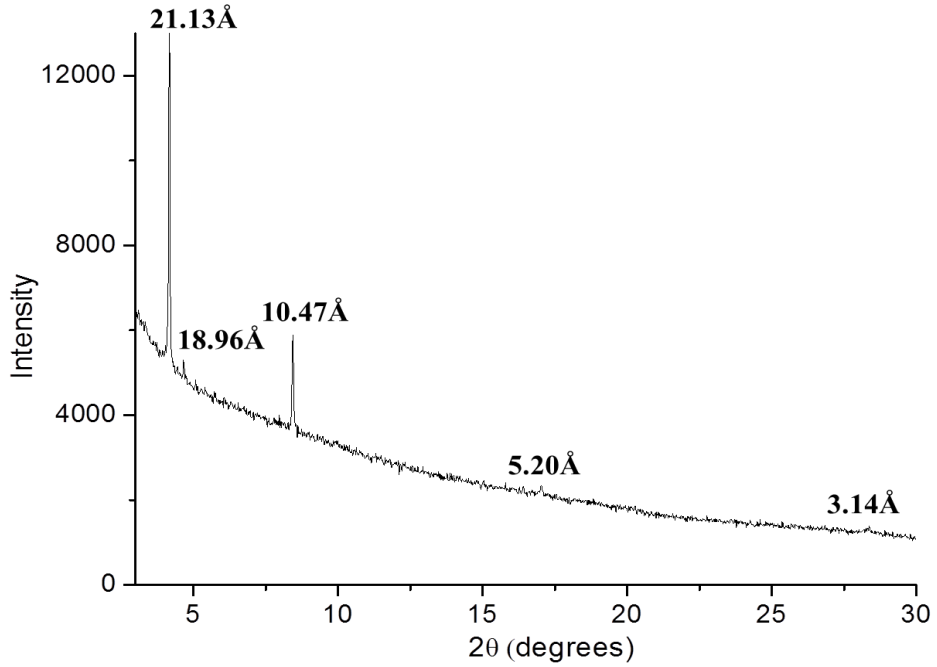

Figure 5.22 X-ray diffraction from thin film of **5.3** in 0.17wt% THF and acetone (1:1) mixed solution as-cast onto OTMS-modified SiO_2 surface.

(3) Atomic Force Microscopy (AFM)

Thin films deposited through solution process were used for AFM studies. The topographic images were obtained using a Nanoscope IIIa Multimode Microscope from Digital Instruments, using tapping mode and in air under ambient condition. The topographic images were collected from multiple samples, and for each sample, different regions were scanned to ensure reproducibility.

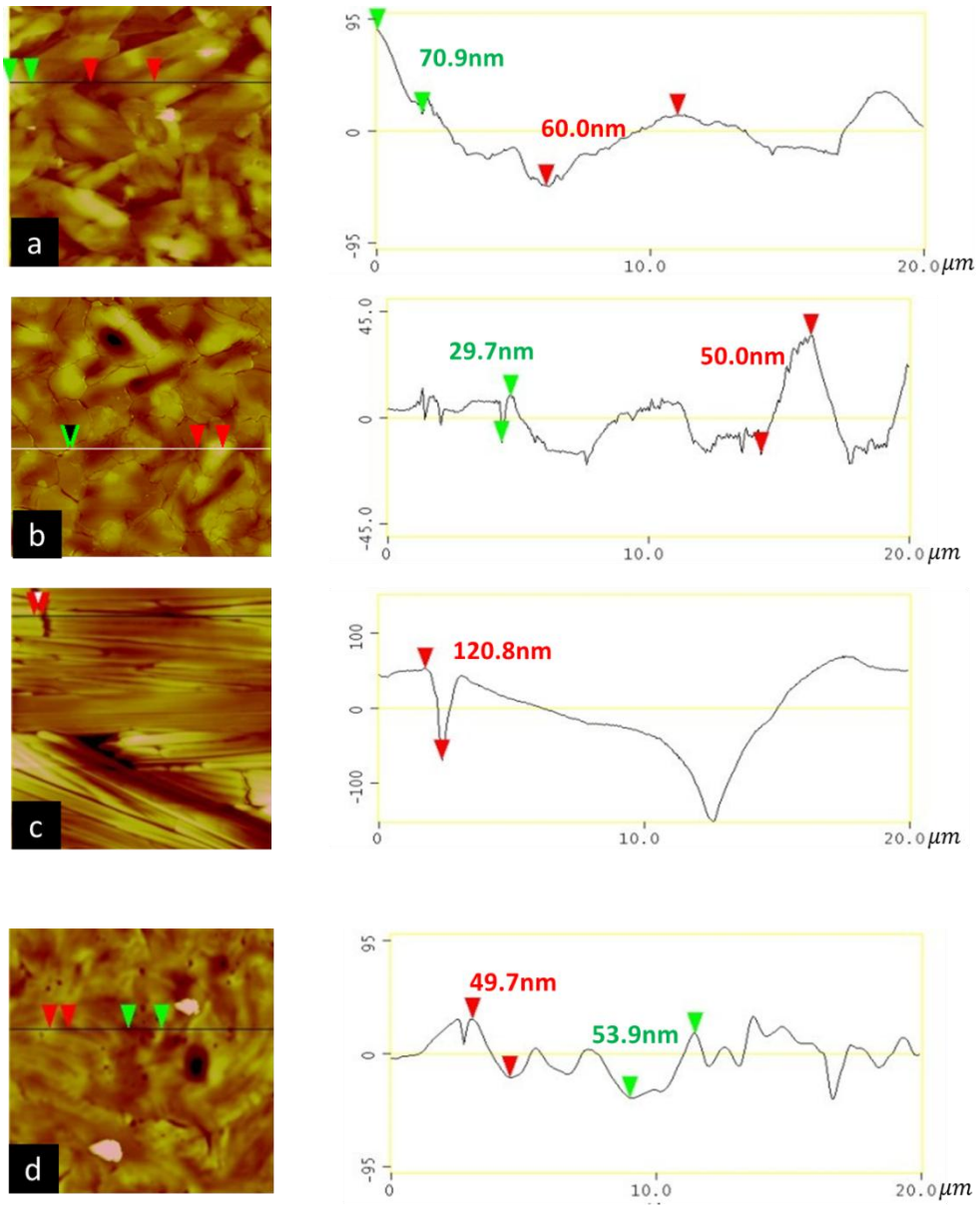

Figure 5.23 AFM section analysis for thin films of (a) **5.1** in 0.17wt% THF solution as-cast onto OTMS-modified SiO_2 surface, (b) **5.2** in 2.5wt% toluene solution spin-coated onto PTS-modified SiO_2 surface, annealing at 120 ℃ followed, (c) **5.2** in 0.17wt% toluene solution drop-casted onto PTS-modified SiO_2 surface, subsequent annealing at 120 ℃, (d) **5.3** in 0.17wt% THF and acetone (1:1) mixed solution as-cast onto OTMS-modified SiO_2 surface

❖ **Electrical Characterization of Thin Film Transistors**

The current-voltage measurement was carried out on a JANIS ST-500-20-4TX probe station with a Keithley 4200 Semiconductor Characterization System at room temperature in ambient air.

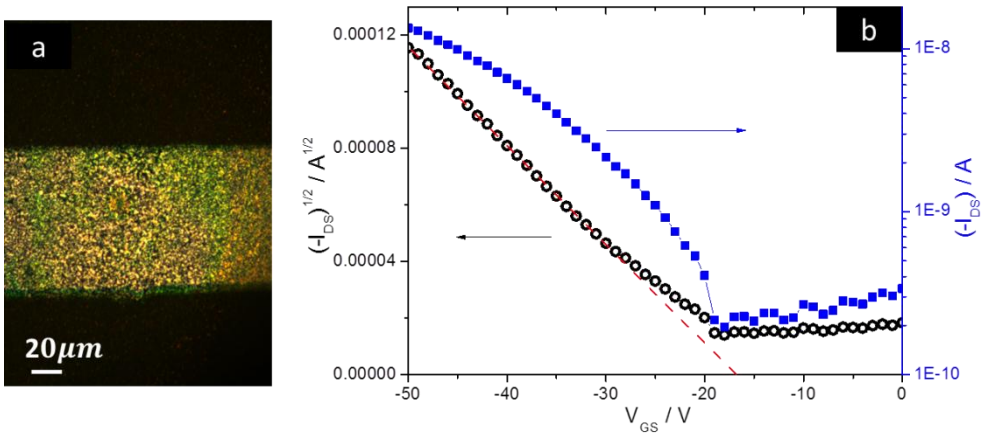

Figure 5.24 (a) Reflection polarized light micrograph of the device made from **5.1** by drop-casting 0.17wt% THF solution onto OTMS-modified SiO_2 surface at room temperature, showing the active channel of W = 1 mm and L = 100 μm. (b) Transfer curves of the thin film transistor shown in (a) with a hole mobility of 2.4E-4 cm^2/V s (tested in the air).

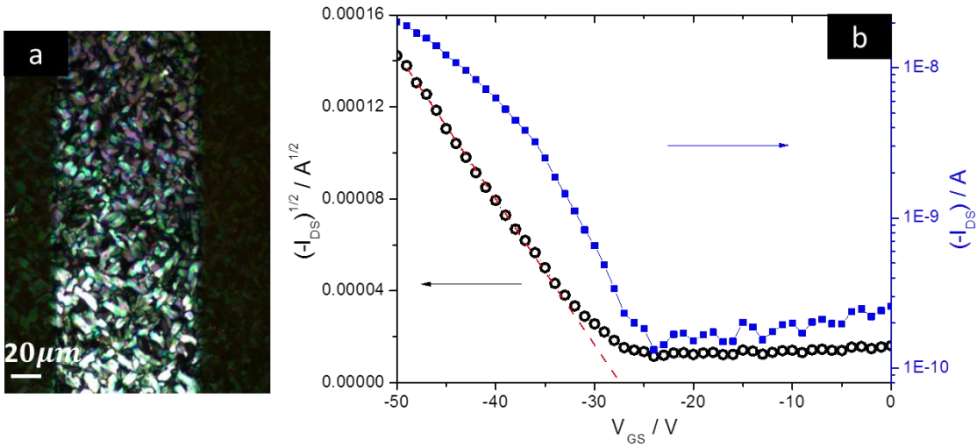

Figure 5.25 (a) Reflection polarized light micrograph of the device made from **5.2** by drop-casting 0.17wt% THF solution onto OTMS-modified SiO_2 surface, with thermal annealing at 120 ℃ for 10 minutes, showing the active channel of W = 1 mm and L = 100 μm. (b) Transfer curves of the thin film transistor shown in (a) with a hole mobility of 7.0E-4 cm^2/V s (tested in the air).

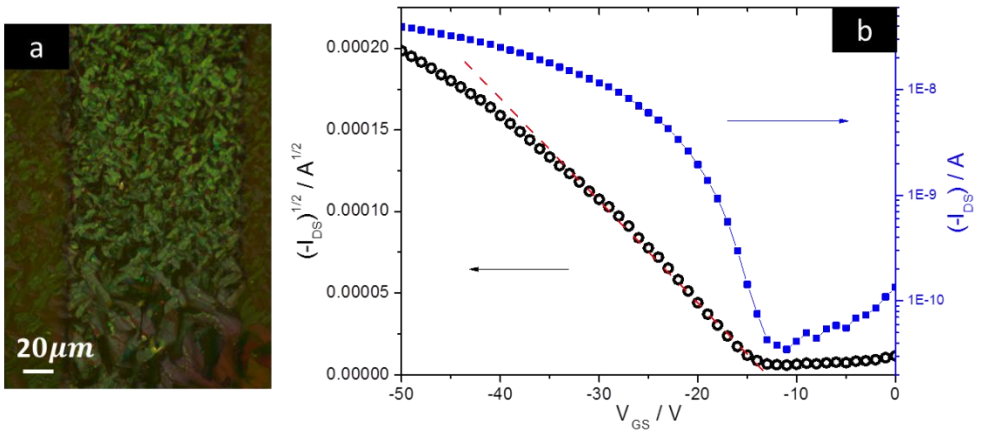

Figure 5.26 (a) Reflection polarized light micrograph of the device made from **5.2** by spin-coating 2.5wt% toluene solution onto PTS-modified SiO_2 surface and annealing at 120 ℃ followed, showing the active channel of W = 1 mm and L = 100 μm. (b) Transfer curves of the thin film transistor shown in (a) with a hole mobility of 1.2E-4 cm^2/V s (tested in the air).

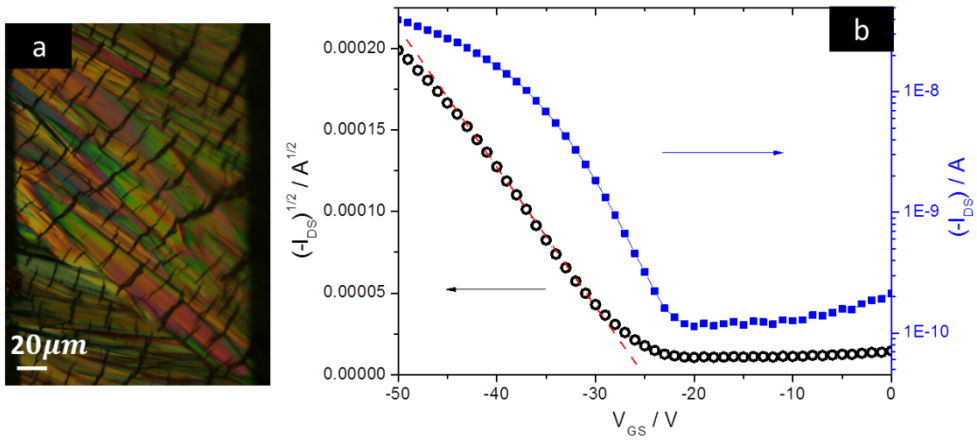

Figure 5.27 (a) Reflection polarized light micrograph of the device made from **5.2** by drop-casting 0.17wt% toluene solution onto PTS-modified SiO2 surface under substrate temperature of 120 ℃, showing the active channel of W = 1 mm and L = 150 μm. (b) Transfer curves of the thin film transistor shown in (a) with a hole mobility of 1.3E-4 cm^2/V s (tested in the air).

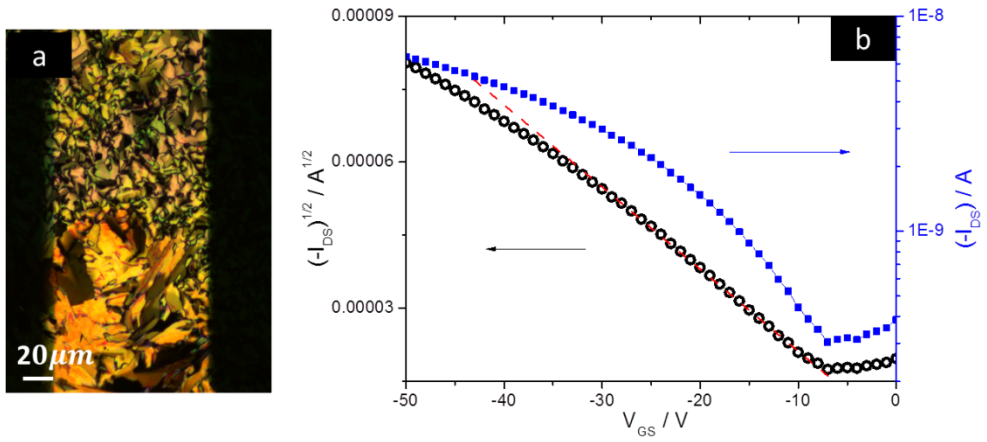

Figure 5.28 (a) Reflection polarized light micrograph of the device made from **5.3** by drop-casting 0.17wt% THF and acetone (1:1) mixed solution onto OTMS-modified SiO_2 surface at room temperature, showing the active channel of W = 1 mm and L = 100 μm. (b) Transfer curves of the thin film transistor shown in (a) with a hole mobility of 4.4E-5 cm^2/V s (tested in the air).

5.5 Reference

1. Iyoda, M.; Yamakawa, J.; Rahman, M. J. *Angew. Chem., Int. Ed.* **2011**, *50*, 10522.
2. (a) Zhang, W.; Moore, J. S. *Angew. Chem., Int. Ed.* **2006**, *45*, 4416.(b) Marsden, J. A.; Palmer, G. J.; Haley, M. M. *Eur. J. Org. Chem.* **2003**, *13*, 2355.(c) Spitler, E. L.; Johnson, C. A. II; Haley, M. M. *Chem. Rev.* **2006**, *106*, 5344.
3. Zhao, D.; Moore, J. S. *Chem. Commun.* **2003**, 807.
4. (a) Höger, S. *Pure Appl. Chem.*, **2010**, *82*, 821. (b) Grave, C.; Schlüter, A. D. *Eur. J. Org. Chem.* **2002**, 3075.
5. Höger, S. *Chem. Eur. J.* **2004**, *10*, 1320.
6. Bunz, U. H. F.; Rubin, Y.; Tobe, Y. *Chem. Soc. Rev.* **1999**, *28*, 107.

7. Naddo, T.; Che, Y.; Zhang, W.; Balakrishnan, K.; Yang, X.; Yen, M.; Zhao, J.; Moore, J. S.; Zhang, L. *J. Am. Chem. Soc.* **2007**, *129*, 6978.

8. (a) Zhao, W.; Tang, Q.; Chan, H.S.; Xu, J.; Lo, K.Y.; Miao, Q. *Chem. Commun.* **2008**, 4324. (b) Luo, J.; Yan, Q.; Li, T.; Zhu, N.; Bai. C.; Cao. Y.; Wang, J.; Pei. J.; Zhao, D. *Chem. Commun.* **2010**, *46*, 5725.

9. Venkataramana, G.; Dongare, P.; Dawe, L. N.; Thompson, d. W.; Zhao, Y.; Bodwell, G. J. *Org. Lett.* **2011**, *13*, 2240.

10. For recent examples of conjugated macrocycles with PAH building blocks, see: (a) Chen, S.; Yan, Q.; Li, T.; Zhao, D. *Org. Lett.* **2010**, *12*, 4784. (b) Toyota, S.; Goichi, M.; Kotani, M. *Angew. Chem., Int. Ed.* **2004**, *43*, 2248. (c) Chan, J. M. W.; Tischler, J. R.; Kooi, S. E.; Bulovic, V.; Swager, T. M. *J. Am. Chem. Soc.* **2009**, *131*, 5659. (d) Höger, S.; Cheng, X. H.; Ramminger, A.-D.; Enkelmann, V.; Rapp, A.; Mondeshki, M.; Schnell, I. *Angew. Chem. Int. Ed.* **2005**, *44*, 2801. (e) Zhang, L.; Gopee, H.; Hughes, D. L.; Cammidge, A. N. *Chem. Commun.* **2010**, *46*, 4255. (f) Nakamura, K.; Okubo, H.; Yamaguchi, M. *Org. Lett.* **2001**, *3*, 1097. (g) Liu, W.-J.; Zhou, Y.; Zhou, Q.-F.; Ma, Y.; Pei, J. *Org. Lett.* **2008**, *10*, 2123.

11. Morimoto, M.; Akiyama, S.; Misumi, S.; Nakagawa, M. *Bull. Chem. Soc. Jpn.* **1962**, *35*, 857.

12. Pisula, W.; Kastler, M.; Yang, C.; Enkelmann, V.; Müllen, K. *Chem. Asian J.* **2007**, *2*, 51.

13. Tian, H.; Shi, J.; Dong, S.; Yan, D.; Wang, L.; Geng, Y.; Wang, F. *Chem. Comm.* **2006**, 3498.

14. Schrettl, S.; Frauenrath, H. *Angew. Chem. Int. Ed.* **2012**, *51*, 6569.

15. Bunz, U. H. F.; Menning, S.; Martín, N. *Angew. Chem., Int. Ed.* **2012**, *50*, 7094.

16. Scott, L. T.; Jackson, E. A.; Zhang, Q.; Steinberg, B. D.; Bancu, M.; Li, B. *J. Am. Chem. Soc.* **2012**, *134*, 107.

17. Omachi, H.; Segawa, Y.; Itami, K. *Acc. Chem. Res.* **2012**, *45*, 1378.

18. For recent reviews, see: (a) Gleiter, R.; Esser, B.; Kornmayer, S. C. *Acc. Chem. Res.* **2009**, *42*, 1108. (b) Hirst, E. S.; Jasti, R. *J. Org. Chem.* **2012**, *77*, 10473. (c) Ref. 17.

19. For examples other than cycloparaphenylenes, see: (a) Esser, B.; Rominger, F.; Gleiter, R. *J. Am. Chem. Soc.* **2008**, *130*, 6716. (b) Esser, B.; Bandyopadhyay, A.; Rominger, F.; Gleiter, R. *Chem. Eur. J.* **2009**, *15*, 3368. (c) Stuparu, M.; Gramlich, V.; Stanger, A.; Schlüter, A. D. *J. Org. Chem.* **2007**, *72*, 424. (d) Standera, M.; Häfliger, R.; Gershoni-Poranne, R.; Stanger, A.; Jeschke, G.; van Beek, J. D.; Bertschi, L.; Schlüter, A. D. *Chem. Eur. J.* **2011**, *17*, 12163. (e) Merner, B. L.; Dawe, L. N.; Bodwell, G. J. *Angew. Chem., Int. Ed.* **2009**, *48*, 5487.

20. (a) Jasti, R.; Bhattacharjee, J.; Neaton, J. B.; Bertozzi, C. R. *J. Am. Chem. Soc.* **2008**, *130*, 17646. (b) Sisto, T. J.; Golder, M. R.; Hirst, E. S.; Jasti, R. *J. Am. Chem. Soc.* **2011**, *133*, 15800. (c) Xia, J.; Jasti, R. *Angew. Chem., Int. Ed.* **2012**, *51*, 2474. (d) Xia, J.; Bacon, J. W.; Jasti, R.; *Chem. Sci.* **2012**, *3*, 3018. (e) Xia, J.; Golder, M. R.; Foster, M. E.; Wong, B. M.; Jasti, R. *J. Am. Chem. Soc.* **2012**, *134*, 19709.

21. (a) Takaba, H.; Omachi, H.; Yamamoto, Y.; Bouffard, J.; Itami, K. *Angew. Chem., Int. Ed.* **2009**, *48*, 6112. (b) Omachi, H.; Matsuura, S.; Segawa, Y.; Itami, K. *Angew. Chem., Int. Ed.* **2010**, *49*, 10202. (c) Segawa, Y.; Miyamoto, S.; Omachi, H.; Matsuura, S.; Senel, P.; Sasamori, T.; Tokitoh, N.; Itami, K. *Angew. Chem., Int. Ed.* **2011**, *50*, 3244. (d) Ishii, Y.; Nakanishi, Y.; Omachi, H.; Matsuura, S.; Matsui, K.; Shinohara, H.; Segawa, Y.; Itami, K. *Chem. Sci.* **2012**, *3*, 2340.

22. (a) Yamago, S.; Watanabe, Y.; Iwamoto, T. *Angew. Chem., Int. Ed.* **2010**, *49*, 757. (b) Iwamoto, T.; Watanabe, Y.; Sakamoto, Y.; Suzuki, T.; Yamago, S. *J. Am. Chem. Soc.* **2011**, *133*, 8354. (c) Iwamoto, T.; Watanabe, Y.; Sadahiro, T.; Haino, T.; Yamago, S. *Angew. Chem. Int. Ed.* **2011**, 50, 8342. (d) Kayahara, E.; Sakamoto, Y.; Suzuki, T.; Yamago, S. *Org. Lett.* **2012**, *14*, 3284.

23. (a) Fort, E. H.; Donovan, P. M.; Scott, L. T. *J. Am. Chem. Soc.* **2009**, *131*, 16006. (b) Fort, E. H.; Scott, L. T. *Angew. Chem., Int. Ed.* **2010**, *49*, 6626.

24. Yagi, A.; Segawa, Y.; Itami, K. *J. Am. Chem. Soc.* **2012**, *134*, 2962.

25. Omachi, H.; Segawa, Y.; Itami, K. *Org. Lett*. **2011**, 13, 2480.

26. Hitosugi, S.; Nakanishi, W.; Yamasaki, T.; Isobe, H. *Nature. Commun.* **2011**, *2*, 492.

27. Hitosugi, S. Yamasaki, T.; Isobe, H. *J. Am. Chem. Soc.* **2012**, *134*, 12442.

28. Boden, B. N. ; Hui, J. K.-H.; Maclachlan, M. J. *J. Org. Chem.* **2008,** *73*, 8069.

29. Tahara, K.; Furukawa, S.; Uji-i, H.; Uchino, T.; Ichikawa, T.; Zhang, J.; Mamdouh, W.; Sonoda, M.; De Schryver, F. C.; De Feyter, S.; Tobe, Y. *J. Am. Chem. Soc.* **2006**, *128*, 16613.

30. Schwab, M. G.; Qin, T.; Pisula, W.; Mavrinskiy, A.; Feng, X.; Baumgarten, M.; Kim, H.; Laquai, F.; Schuh, S.; Trattnig, R.; List, E. J. W.; Müllen, K. *Chem. Asian J.* **2011**, *6*, 3001.

31. For example of synthesizing non-planar macrocycles from planar conjugated macrocycles by benzannulation, see: (a) Song, Q.; Lebeis, C. W.; Shen, X.; Ho, D. M.; Pascal, R. A. Jr. *J. Am. Chem. Soc.* **2005**, *127*, 13732. (b) Müller, M.; Iyer, V. S.; Kübel, C.; Enkelmann, V.; Müllen, K. *Angew.Chem., Int. Ed.* **1997**, *36*, 1607.

32. Asao, N.; Nogami, T.; Lee, S.; Yamamoto, Y. *J. Am. Chem. Soc.* **2003**, *125*, 10921.

33. As found from the energy minimized model, **5.3** has each phenanthrene unit slightly out of plane and a dihedral angle of 11.6 ° between the neighboring phenaphthrene rings. In contrast, **5.1** and **5.2** are essentially flat as found from the energy minimized models.

34. Shetty, A. S.; Zhang, J.; Moore, J. S. *J. Am. Chem. Soc.* **1996**, *118*, 1019.

35. The association constant of **5.2** estimated with the same model is as small as 6 L $\cdot$mol^{-1}.

36. Schwab, M. G.; Qin, T.; Pisula, W.; Mavrinskiy, A.; Feng, X.; Baumgarten, M.; Kim, H.; Laquai, F.; Schuh, S.; Trattnig, R.; List, E. J. W.; Müllen, K. *Chem. Asian J.* **2011**, *6*, 3001.

37 Ito, Y.; Virkar, A. A.; Mannsfeld, S.; Oh, J. H.; Toney, M.; Locklin, A.; Bao, Z. *J. Am. Chem. Soc.* **2009**, *131*, 9396.

38. Giri, G.; Verploegen, E.; Mannsfeld, S. C. B.; Atahan-Evrenk, S.; Kim, D. H.; Lee, S. Y.; Becerril, H. A.; Aspuru-Guzik, A.; Toney, M. F.; Bao, Z. *Nature* **2011**, *480*, 504.

39. Similar thermal behavior was reported for hexakis(4-decylphenyl)-cyclo-3,6-trisphenanthrylene, see Ref. 12.

40 Boden, B. N.; J. Hui, K.-H.; Maclachlan, M. J. *J. Org. Chem.* **2008,** *73*, 8069.

41 Horman, I.; Dreux, B. *Helv. Chim. Acta.* **1984**, *67*, 754.

42 Zhang, F. J.; Di, C. A.; Berdunov, N.; Hu, Y. Y.; Hu,Y. B.; Gao, X. K.; Meng, Q.; Sirringhaus, H.; Zhu, D. B. *Adv. Mater.* **2013**, 25, 10, 1401.

Appendix

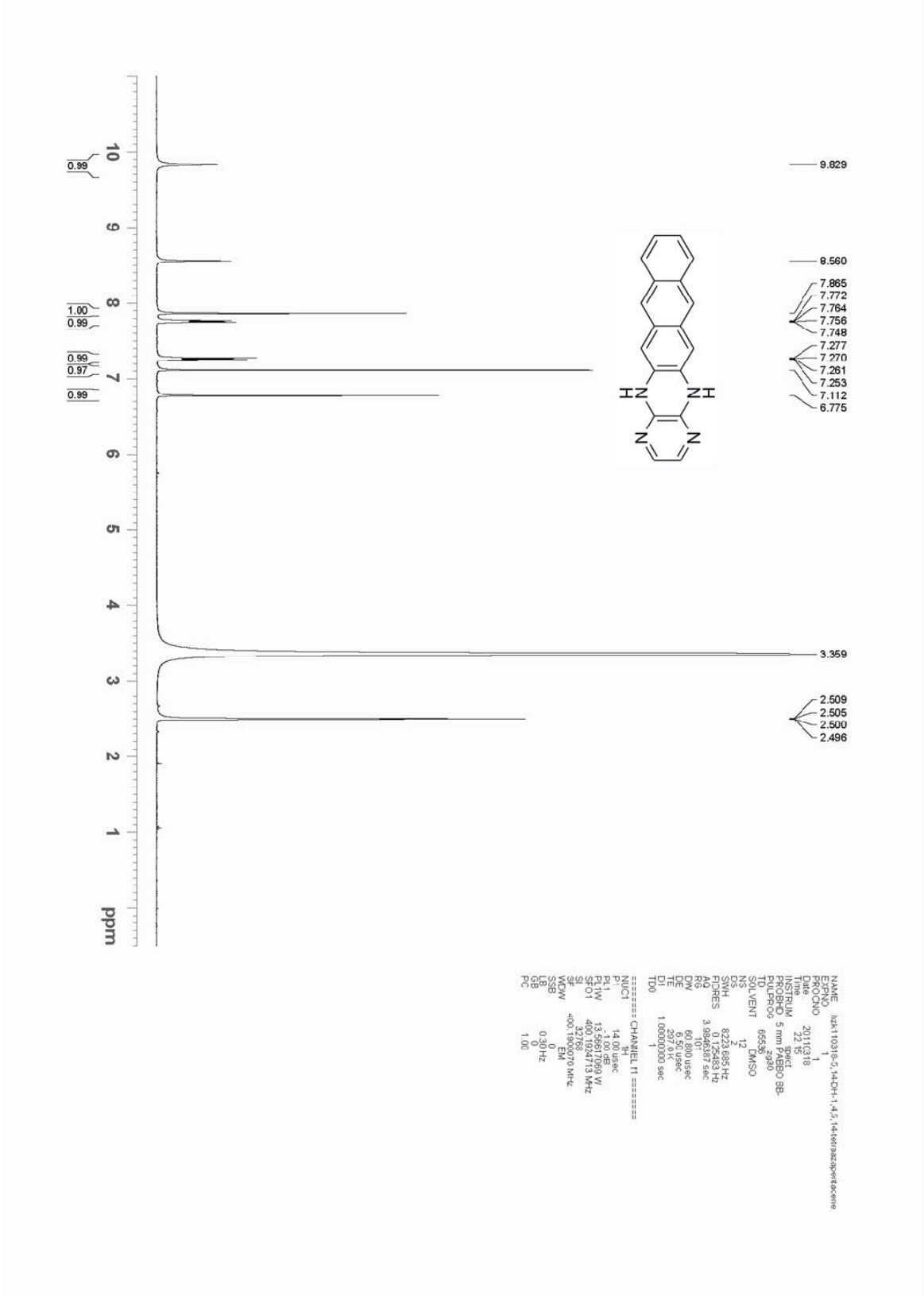

^{1}H-NMR of 5,14-Dihydro-1,4,5,14-tetraazapentacene in DMSO-d_6

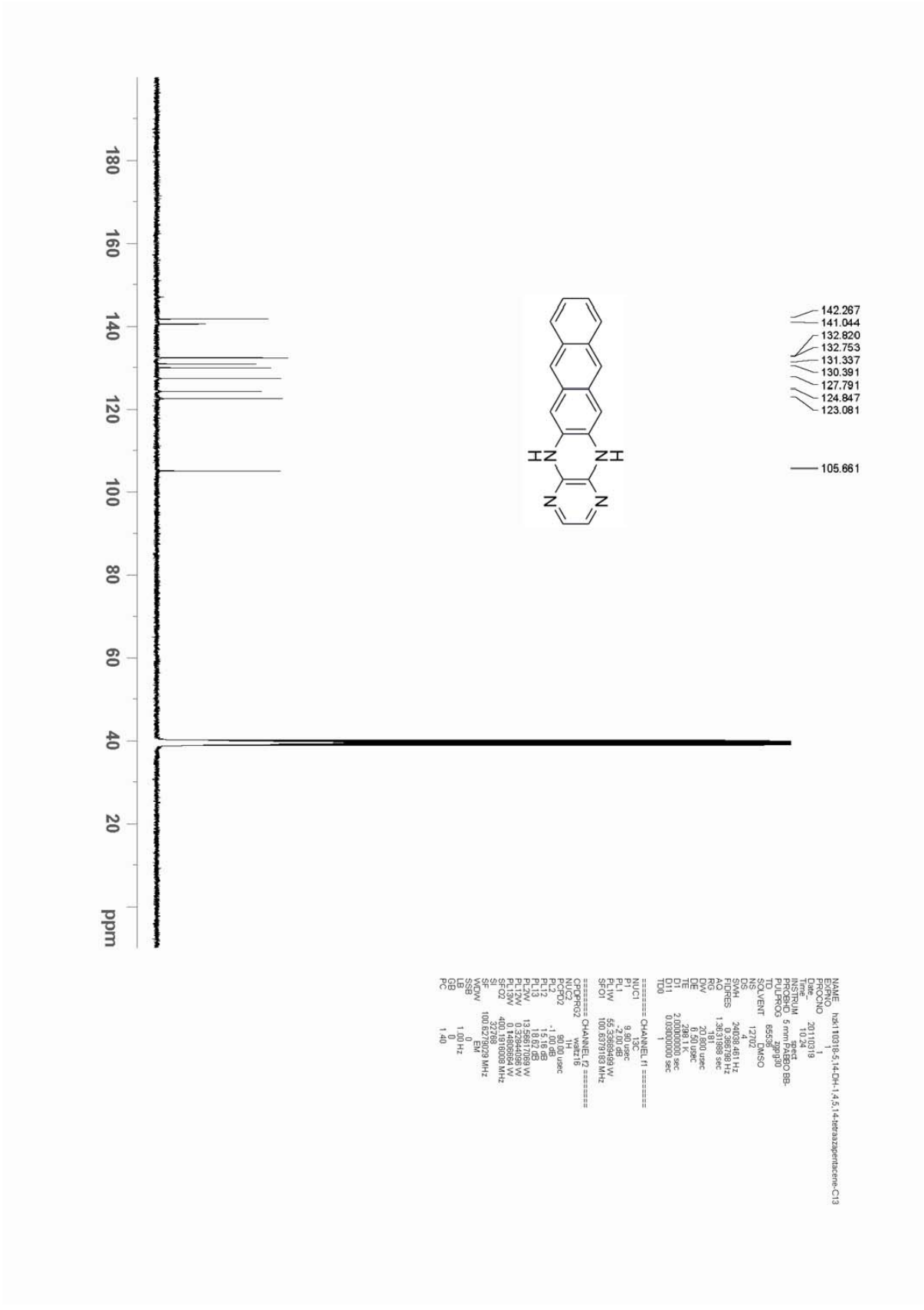

^{13}C-NMR of 5,14-Dihydro-1,4,5,14-tetraazapentacene in DMSO-d_6

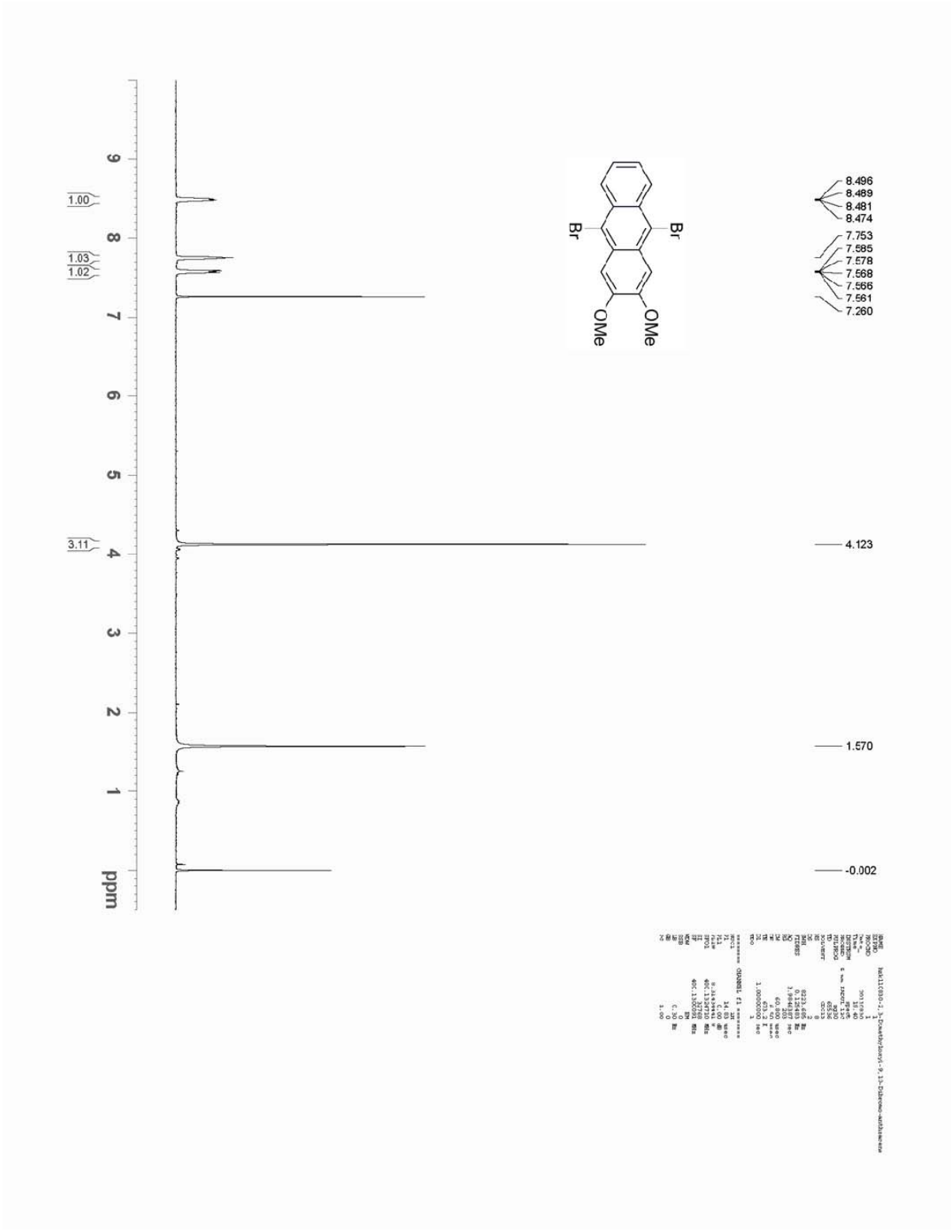

^{1}H-NMR of 9,10-dibromo-2,3-dimethoxyanthracene in $CDCl_3$

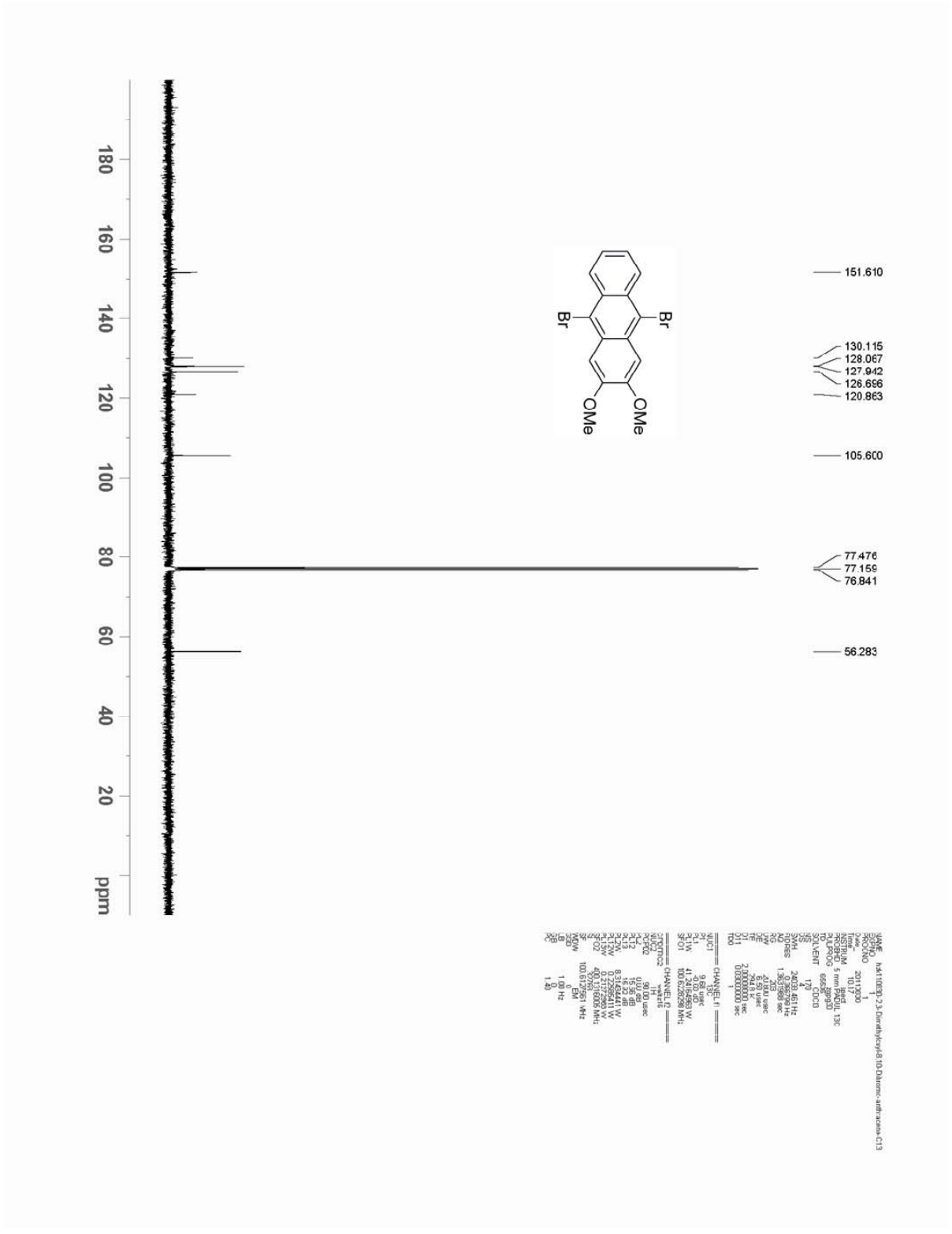

^{13}C-NMR of 9,10-dibromo-2,3-dimethoxyanthracene in $CDCl_3$

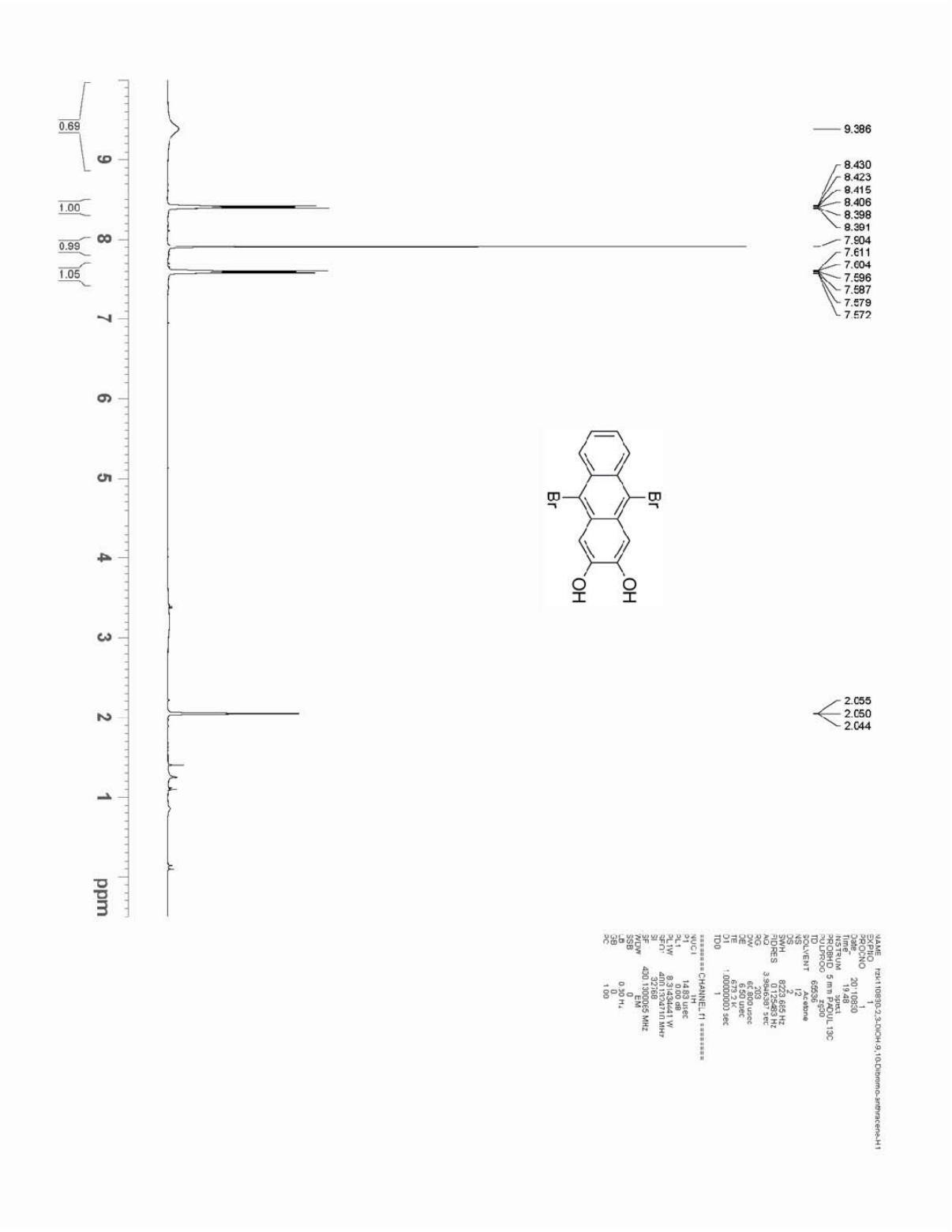

^{1}H-NMR of 9.10-dibromoanthracene-2,3-diol in d_6-acetone

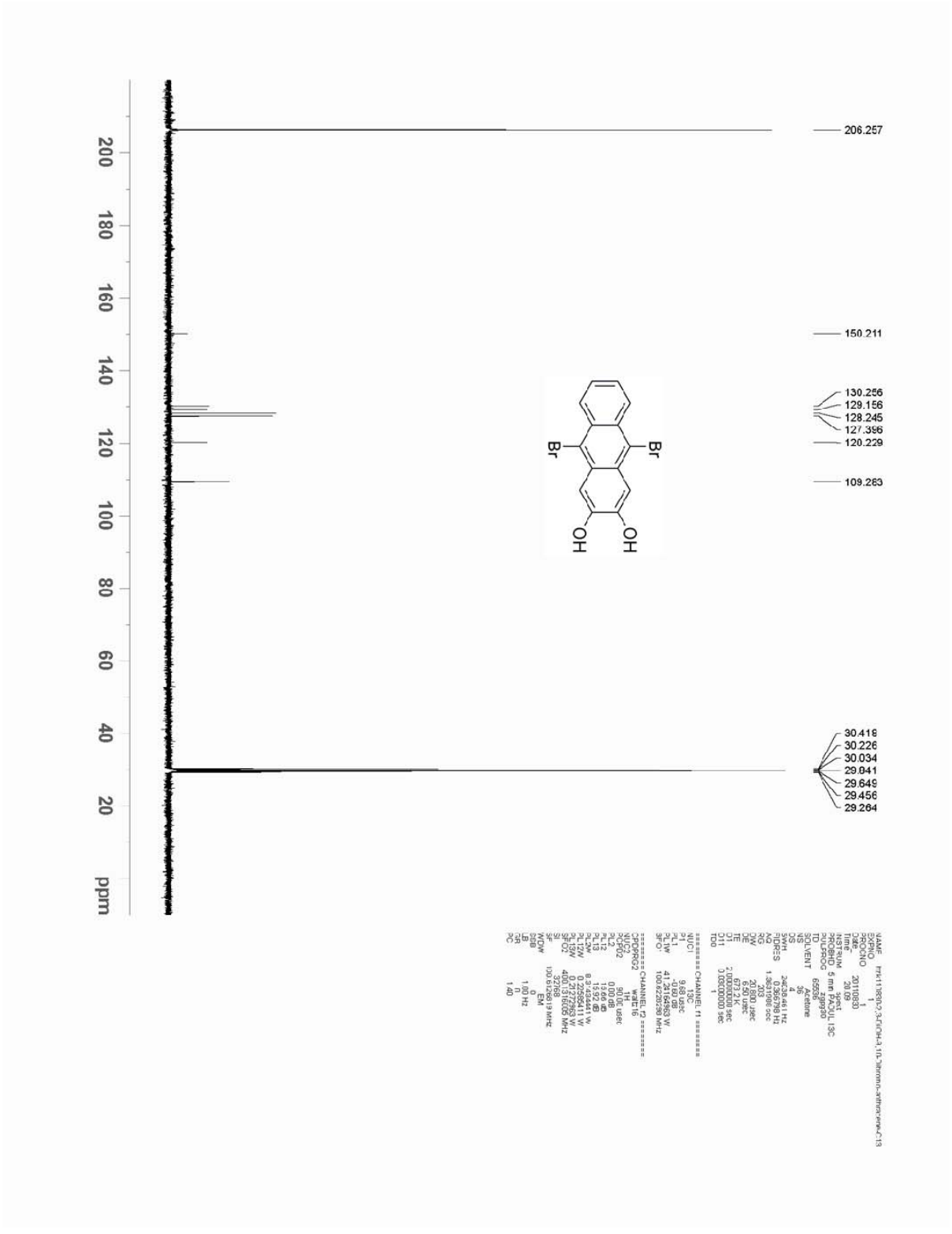

^{13}C-NMR of 9.10-dibromoanthracene-2,3-diol in d_6-acetone

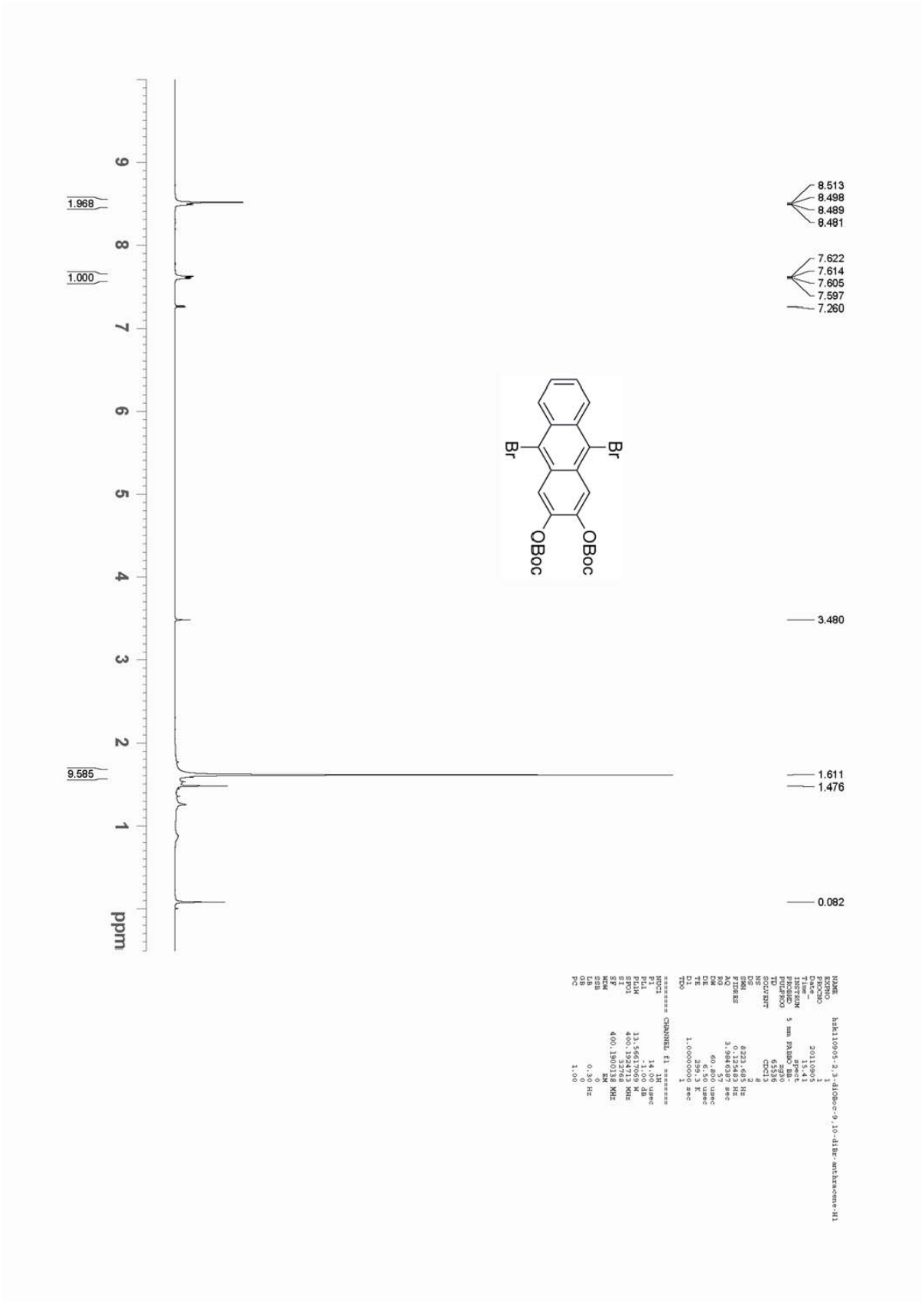

^{1}H-NMR of 9,10-dibromo- 2,3-bis(tert-butyoxycarbonyloxy)-anthracene in $CDCl_3$

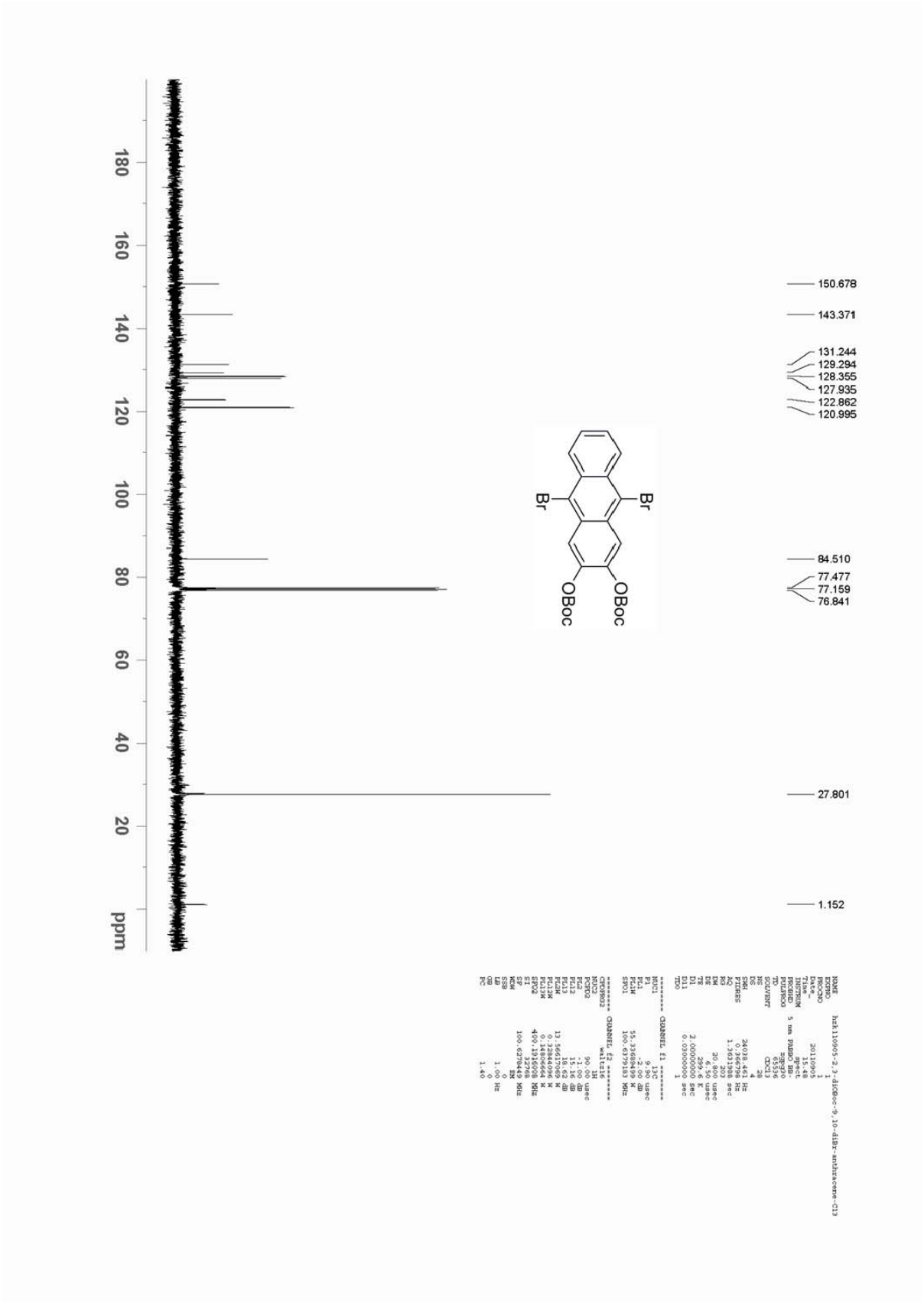

^{13}C-NMR of 9,10-dibromo- 2,3-bis(tert-butyoxycarbonyloxy)-anthracene in $CDCl_3$

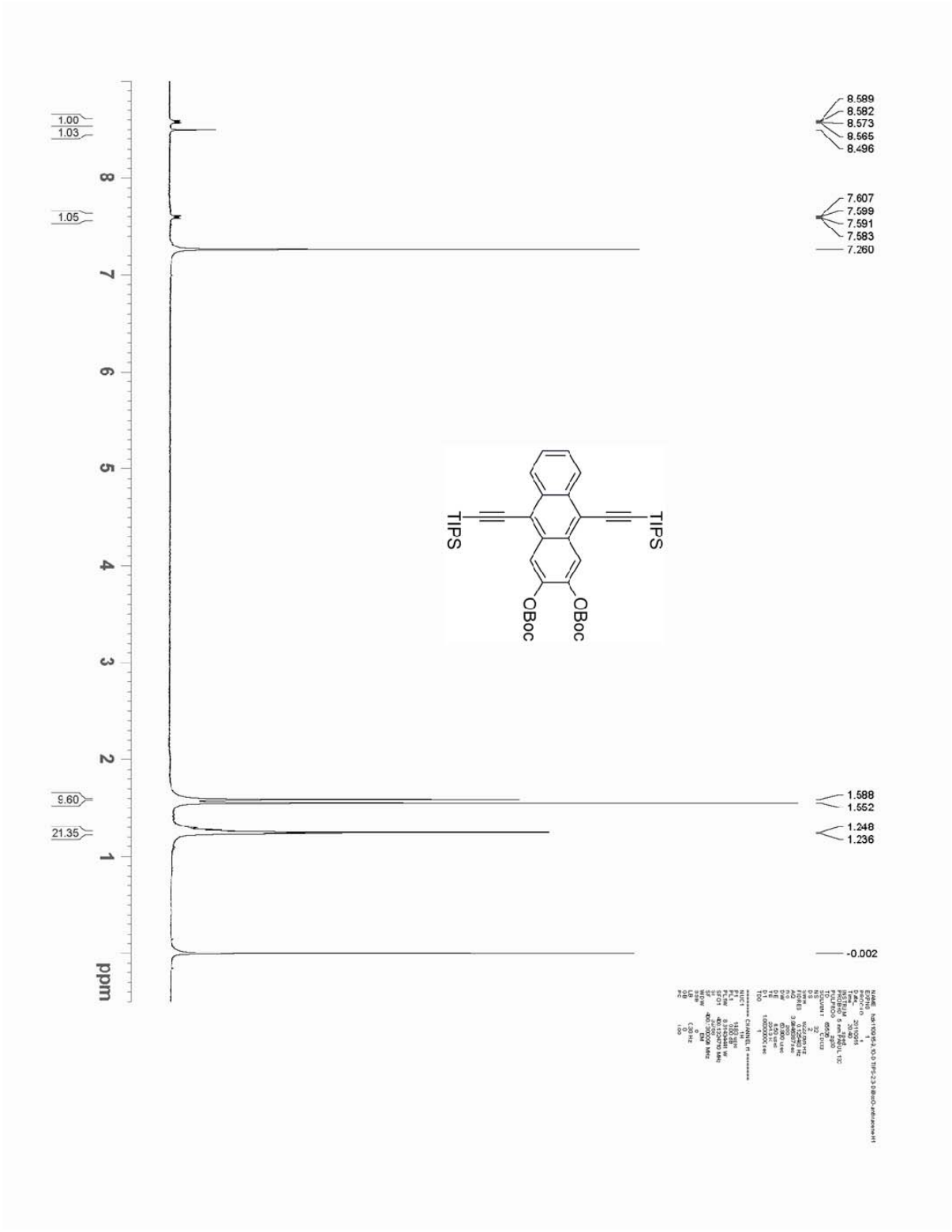

^{1}H-NMR of
9,10-bis((triisopropylsilyl)ethynyl)-2,3-bis(tert-butyoxycarbonyloxy)-anthracene
in $CDCl_3$

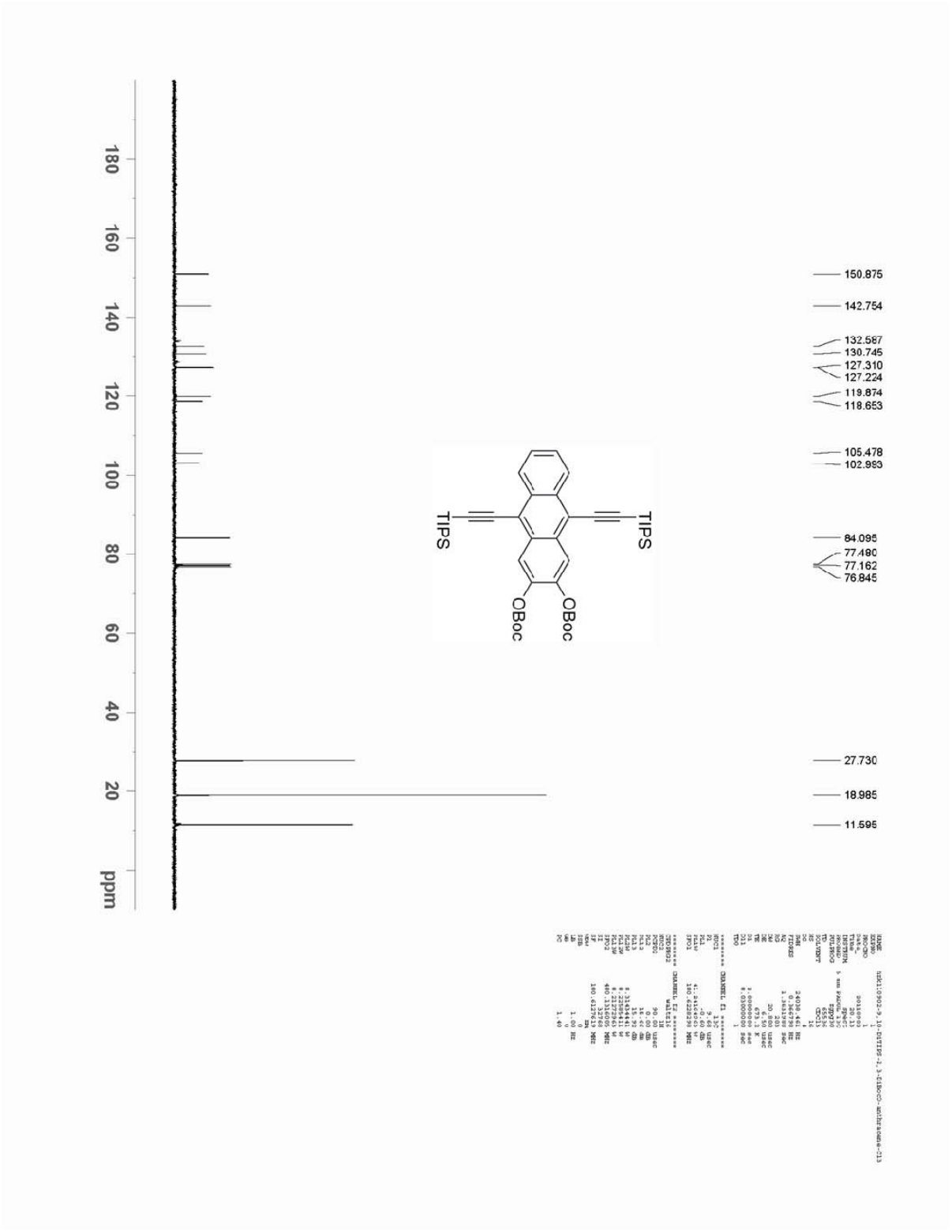

^{13}C-NMR of
9,10-bis((triisopropylsilyl)ethynyl)-2,3-bis(tert-butyoxycarbonyloxy)-anthracene
in $CDCl_3$

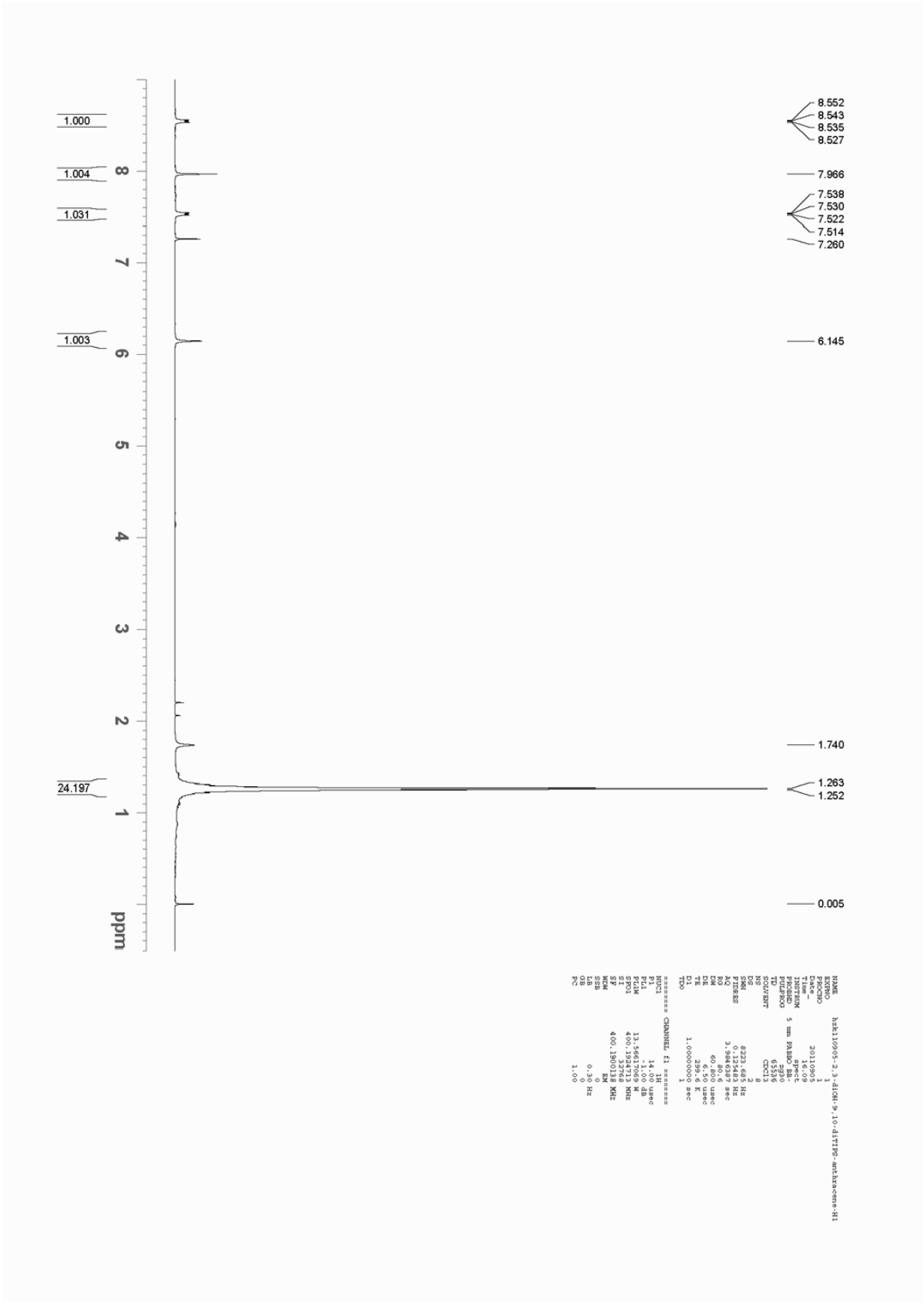

^{1}H-NMR of 9,10-bis((triisopropylsilyl)ethynyl)-anthracene-2,3-diol in $CDCl_3$

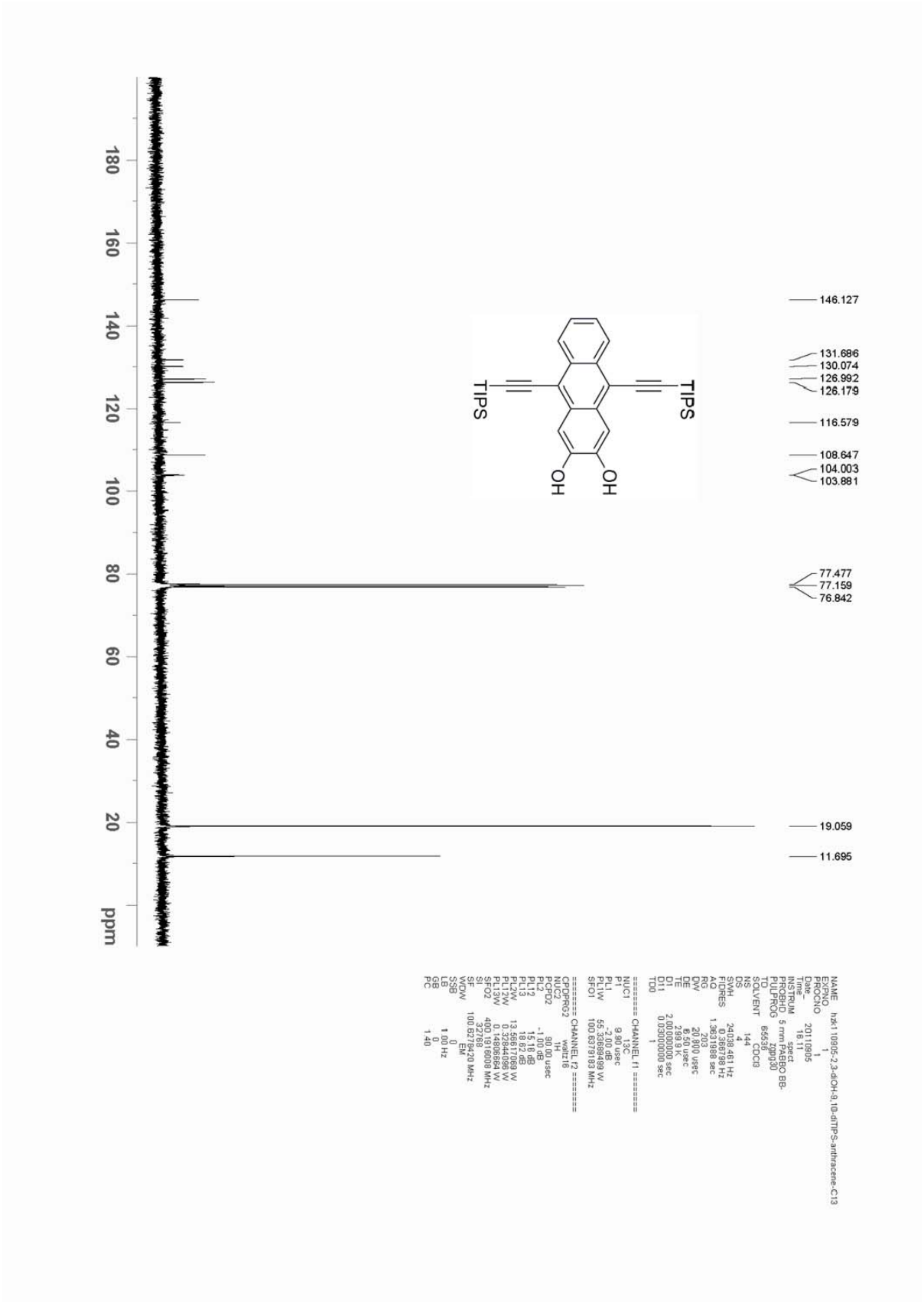

^{13}C-NMR of 9,10-bis((triisopropylsilyl)ethynyl) -anthracene-2,3-diol in $CDCl_3$

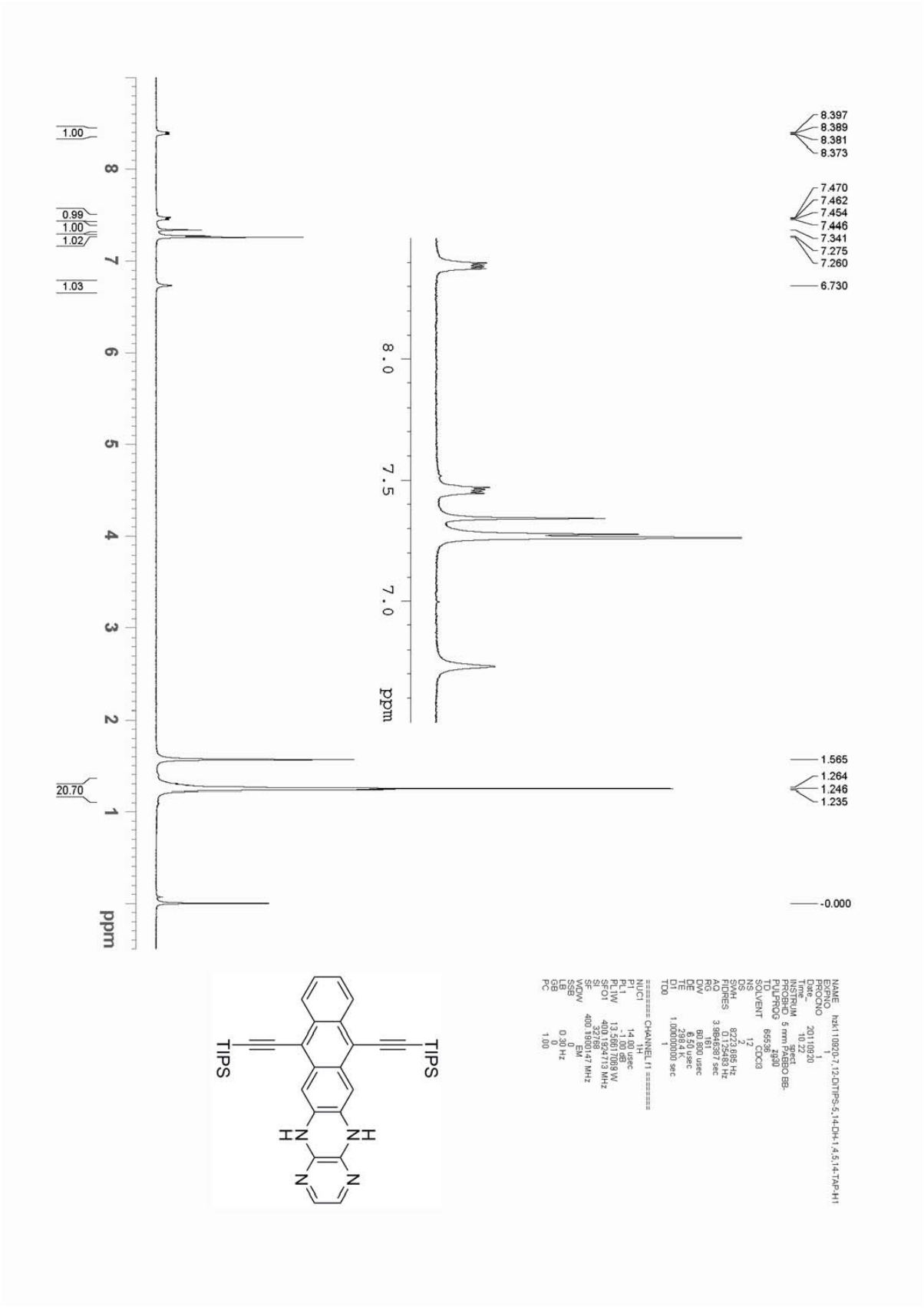

^{1}H-NMR of
7,12-bis((triisopropylsilyl)ethynyl)-5,14-dihydro-1,4,5,14-tetraazapentacene in $CDCl_3$

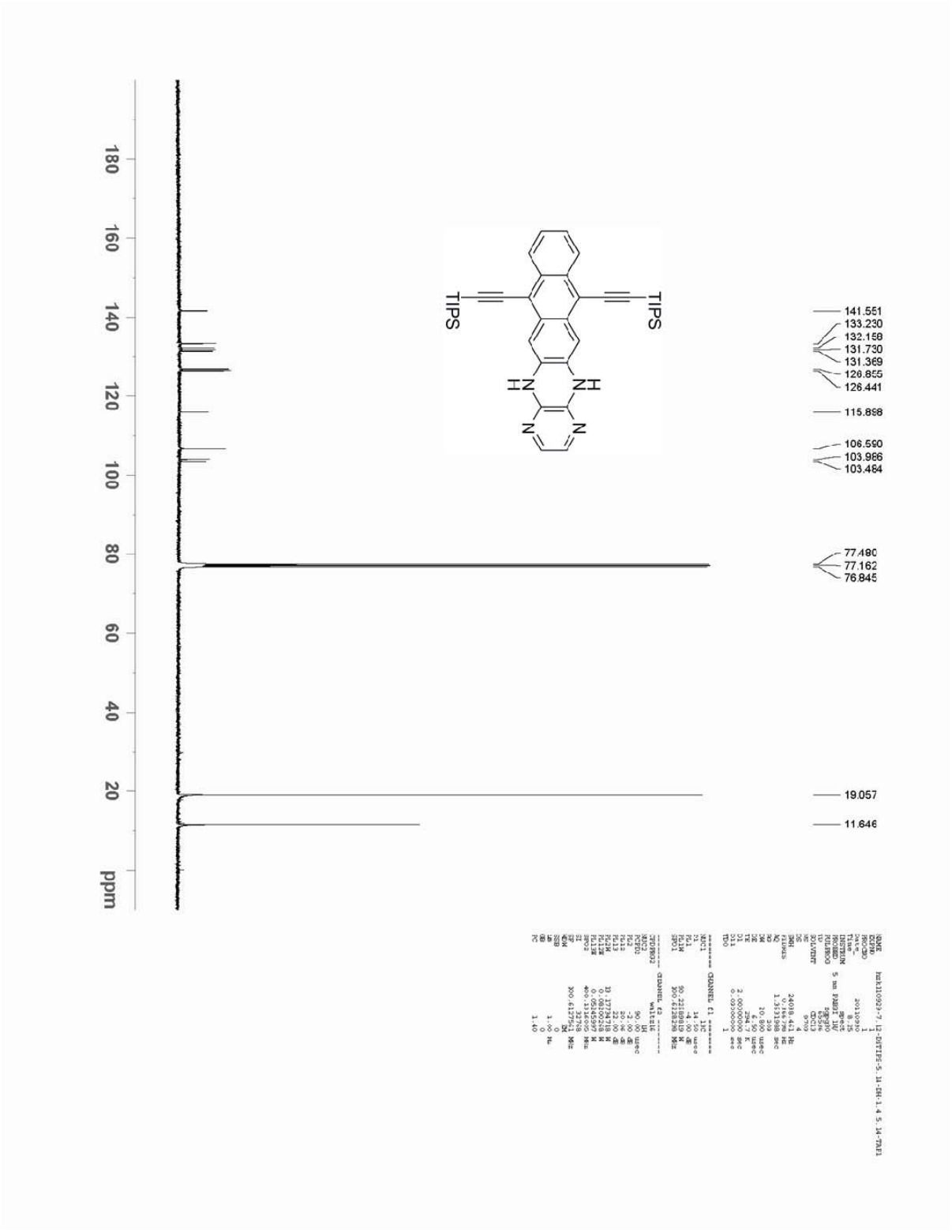

^{13}C-NMR of
7,12-bis((triisopropylsilyl)ethynyl)-5,14-dihydro-1,4,5,14-tetraazapentacene in $CDCl_3$

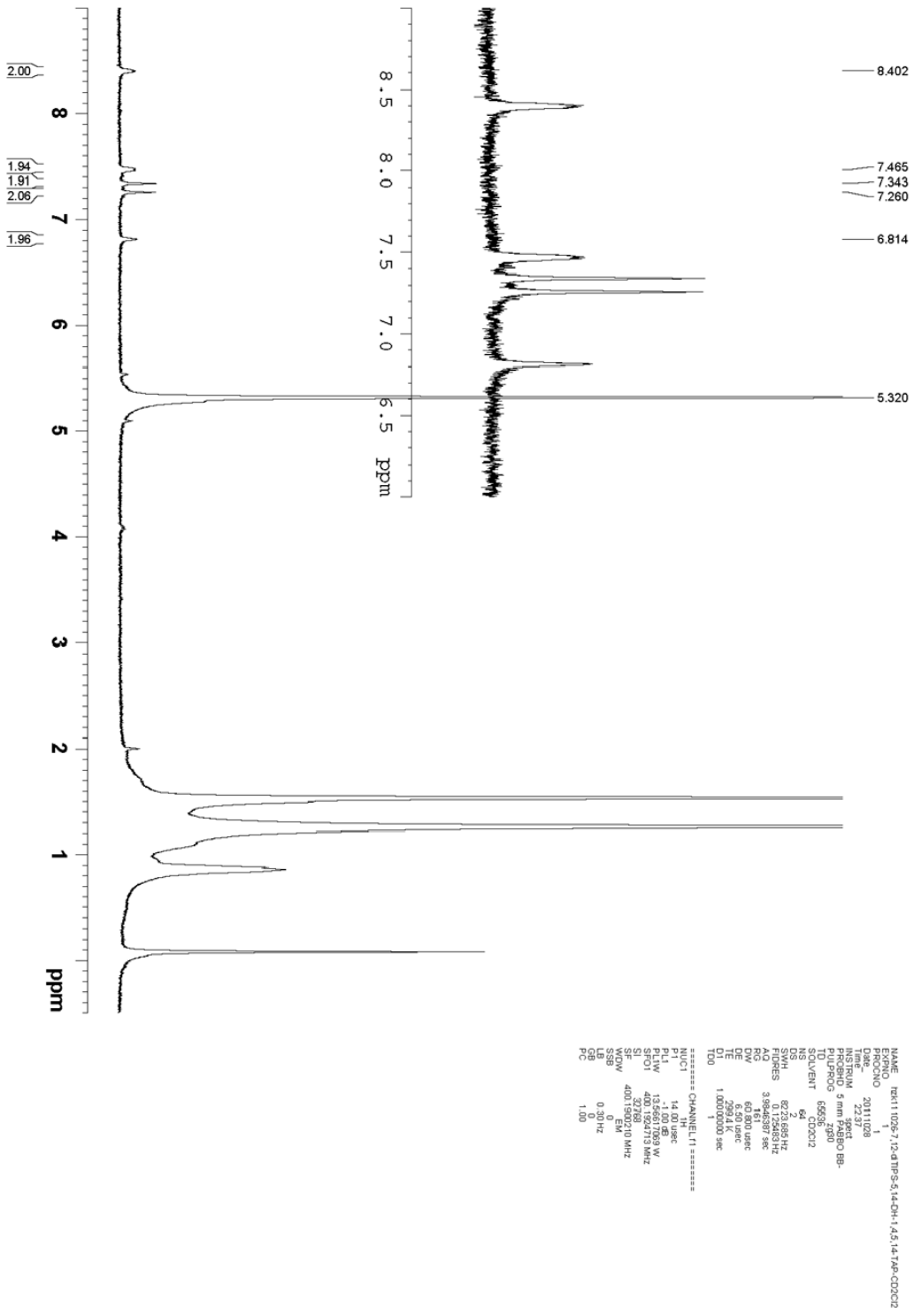

^{1}H-NMR of
7,12-bis((triisopropylsilyl)ethynyl)-5,14-dihydro-1,4,5,14-tetraazapentacene in CD_2Cl_2

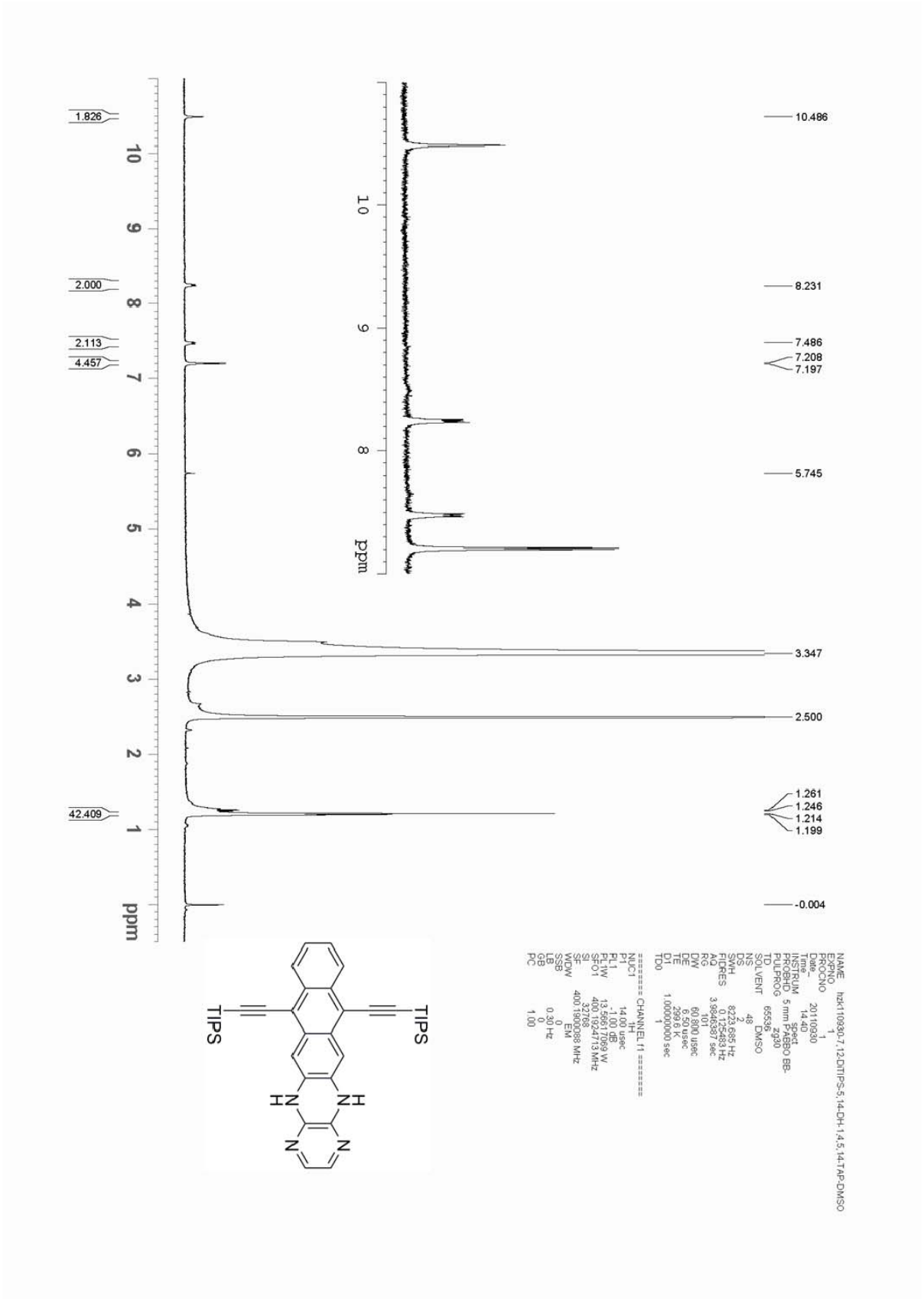

^{1}H-NMR of 7,12-bis((triisopropylsilyl)ethynyl)-5,14-dihydro-1,4,5,14-tetraazapentacene in DMSO-d_6

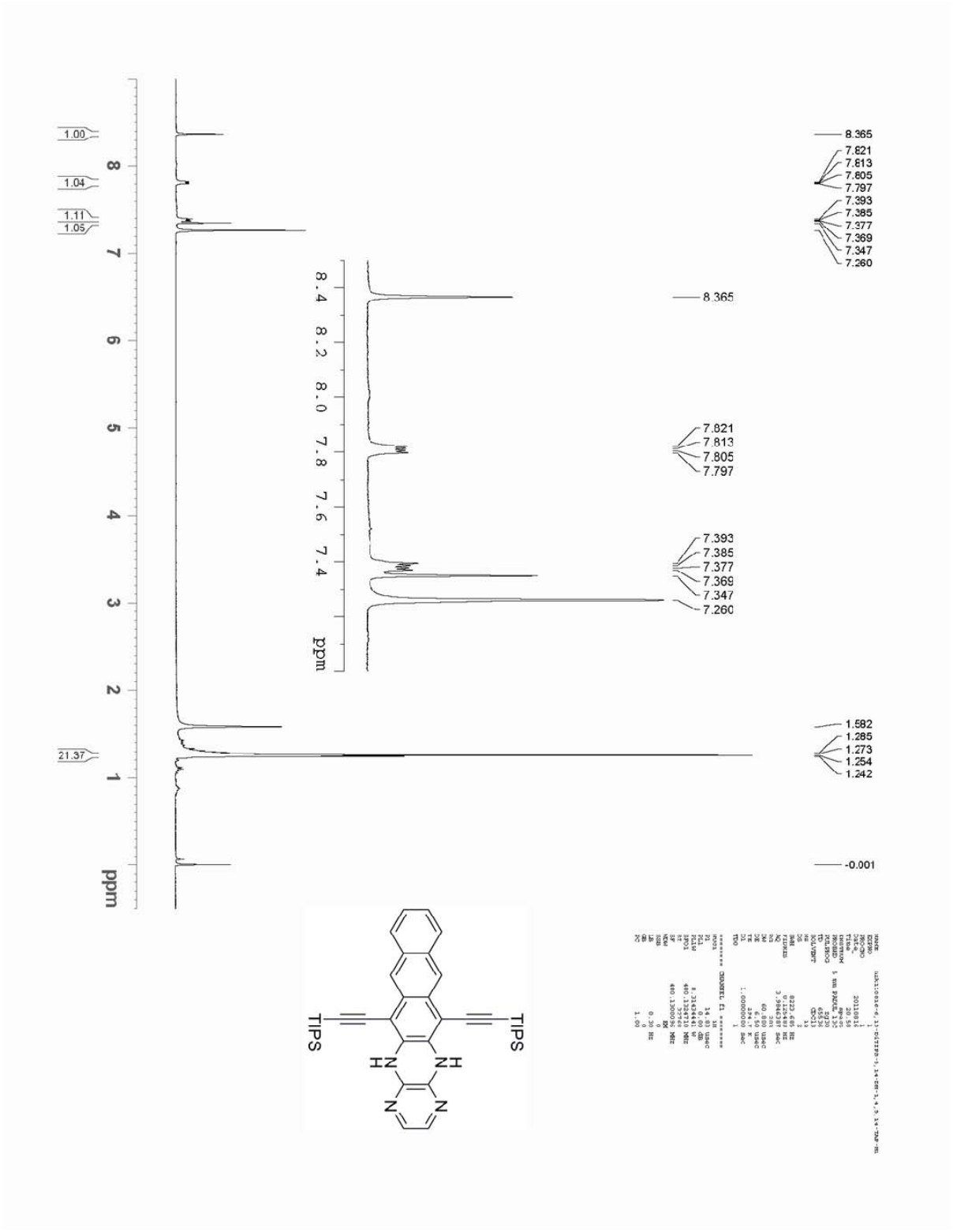

^{1}H-NMR of 6,13-bis((triisopropylsilyl)ethynyl)-5,14-dihydro-1,4,5,14-tetraazapentacene in $CDCl_3$

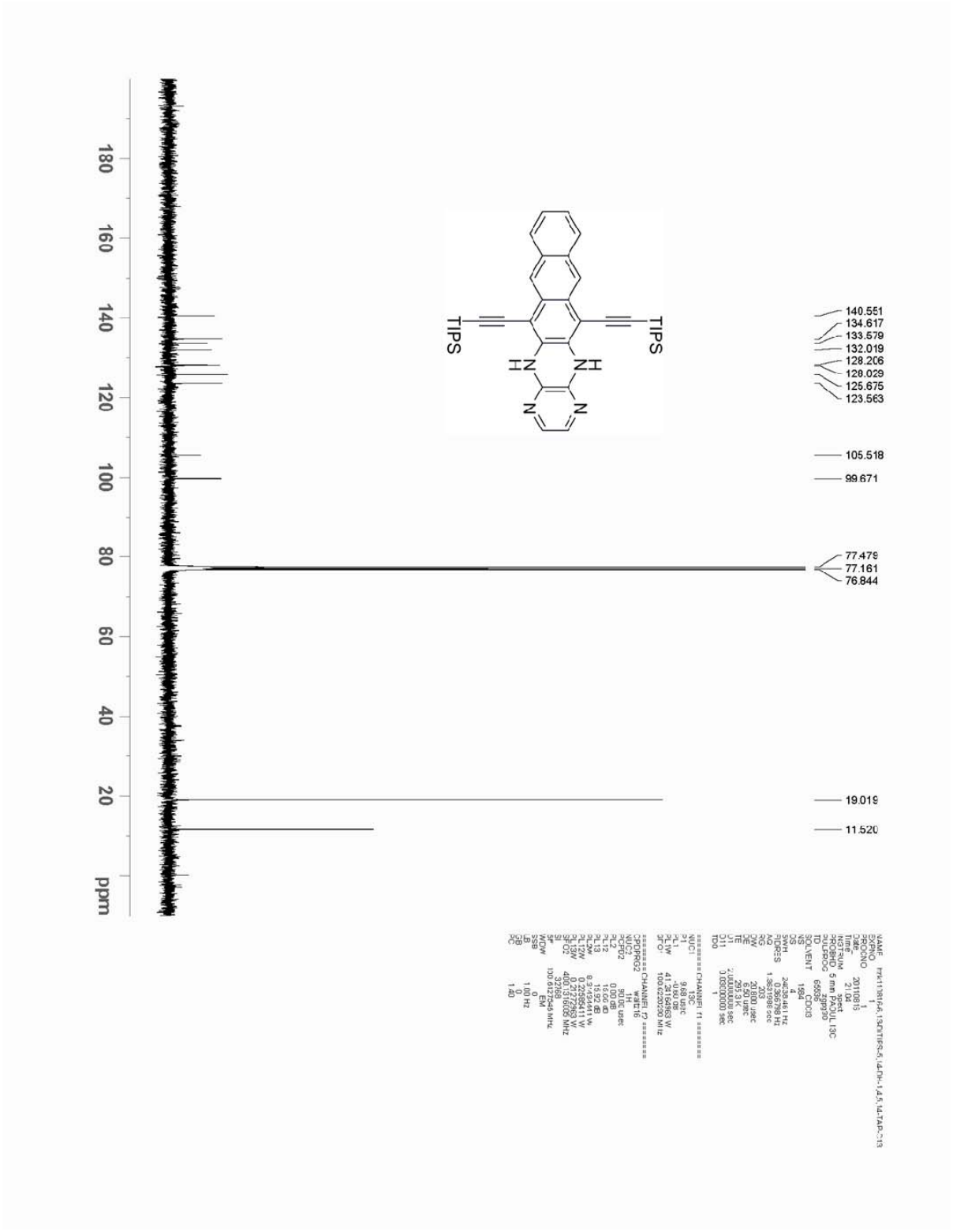

^{13}C-NMR of 6,13-bis(triisopropylsilylethynyl)-5,14-dihydro-1,4,5,14-tetraazapentacene in $CDCl_3$

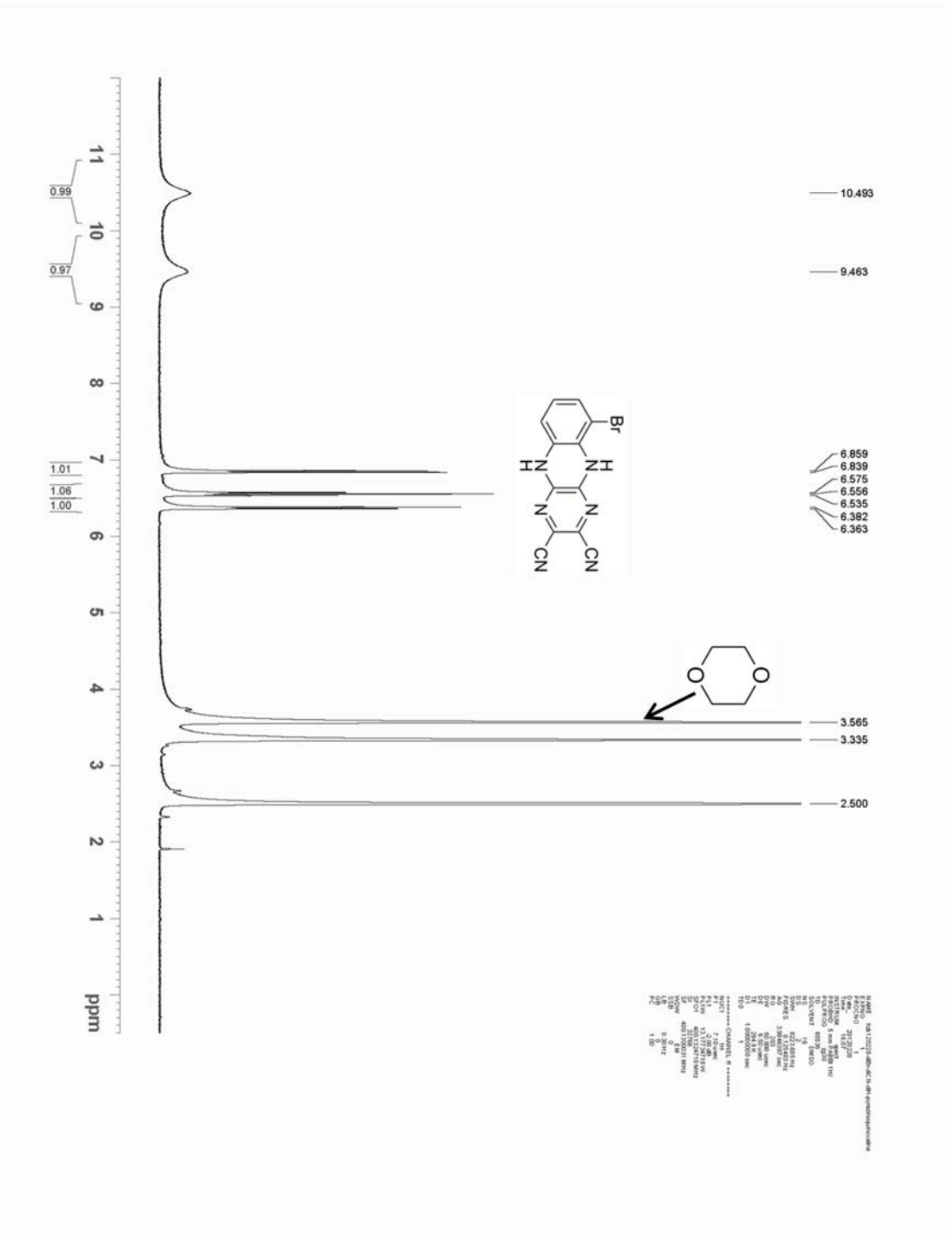

^{1}H-NMR of 6-bromo-5,10-dihydro-2,3-dicyanopyrazinoquinoxaline in DMSO-d_6

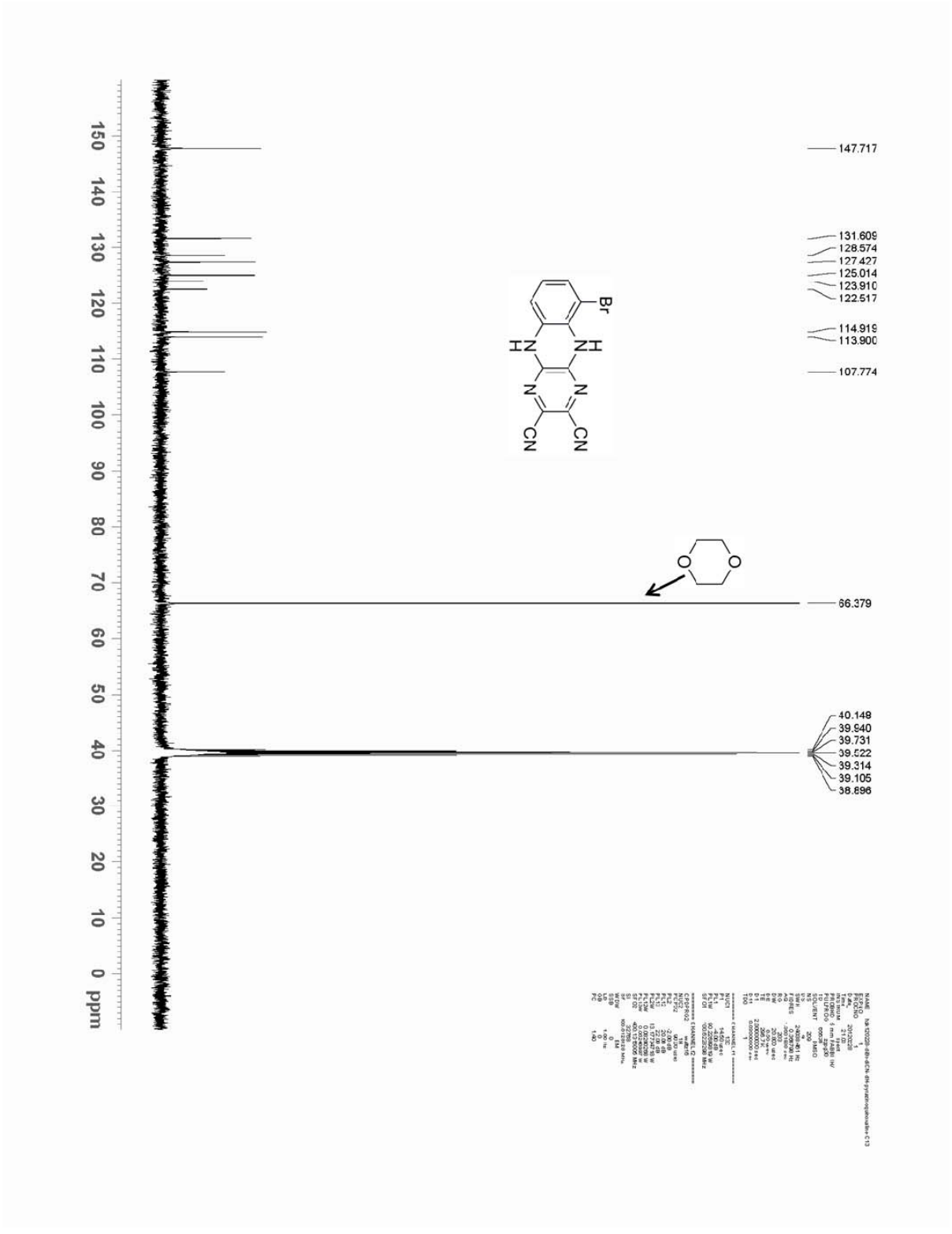

^{13}C-NMR of 6-bromo-5,10-dihydro-2,3-dicyanopyrazinoquinoxaline in DMSO-d_6

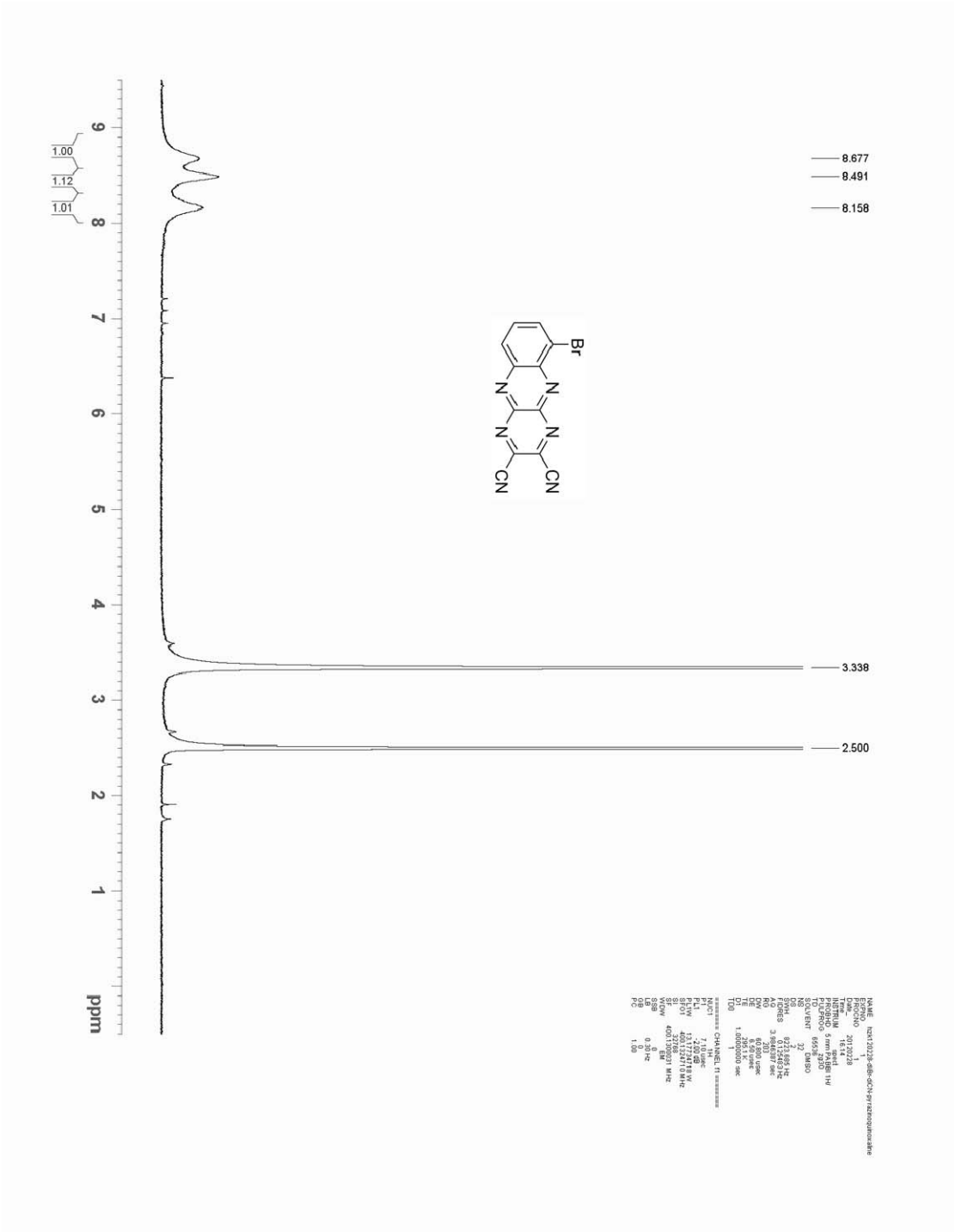

^{1}H-NMR of 6-bromo- -2,3-dicyanopyrazinoquinoxaline in DMSO-d_6

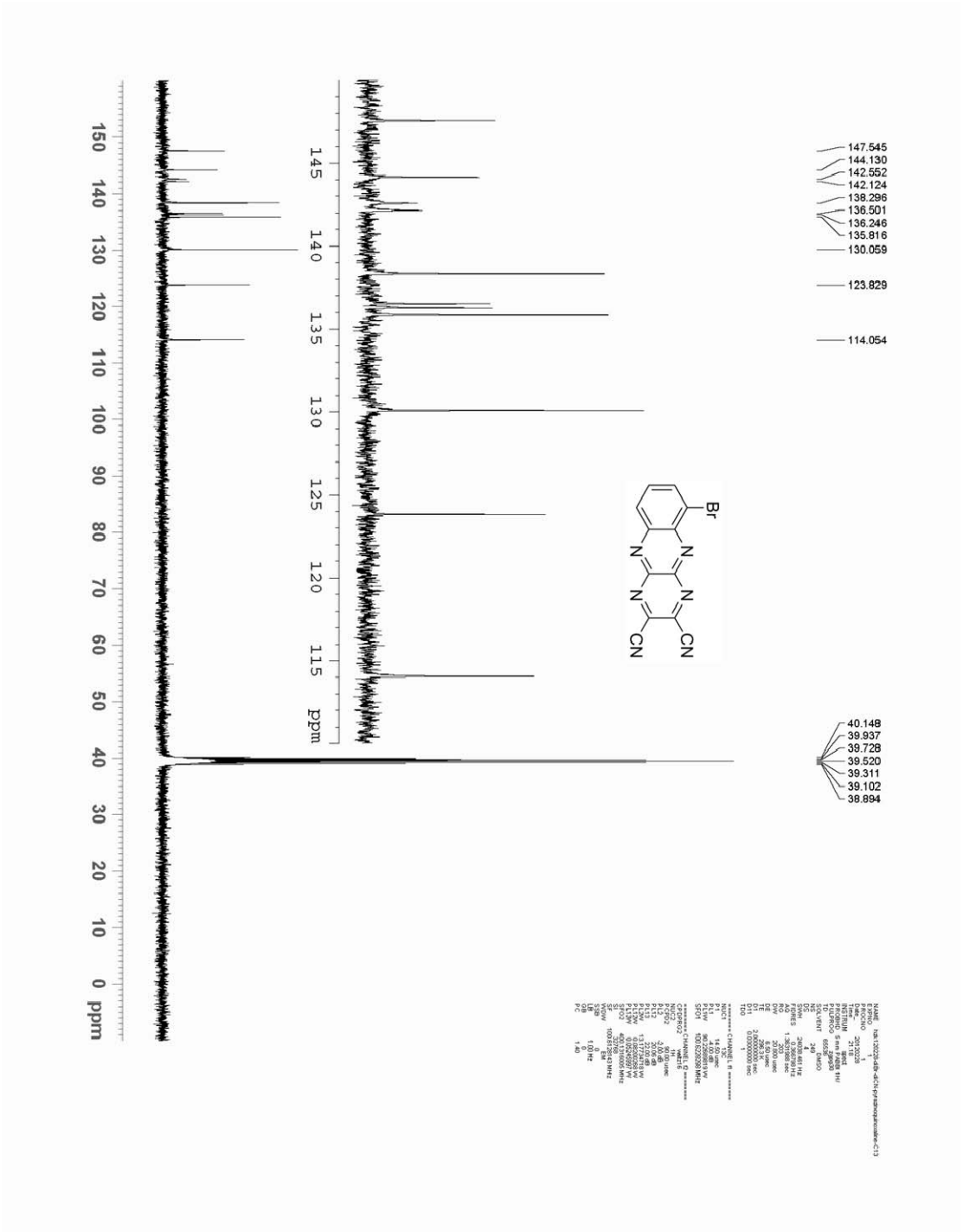

^{13}C-NMR of 6-bromo- -2,3-dicyanopyrazinoquinoxaline in DMSO-d_6

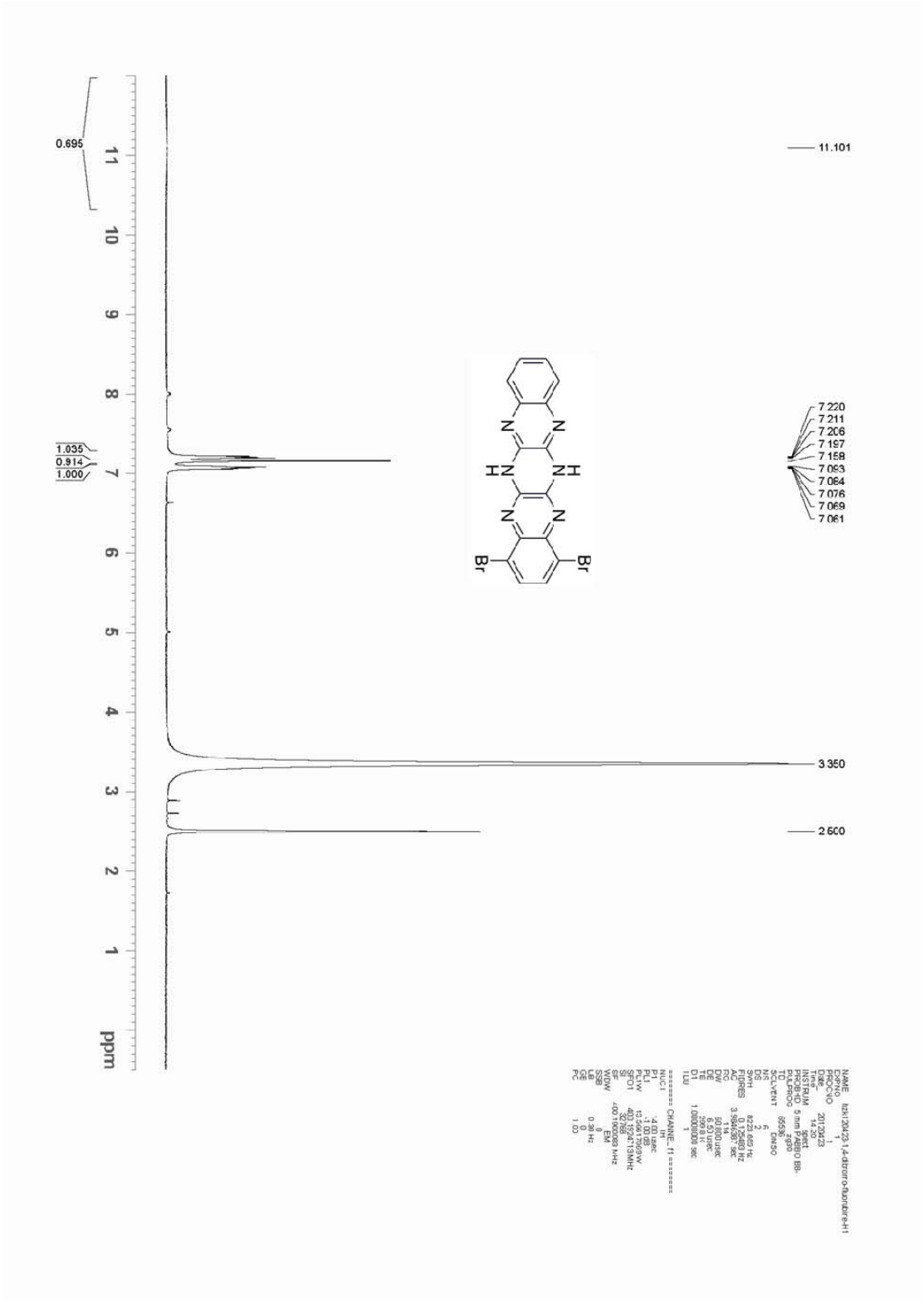

^{1}H-NMR of 1,4-dibromo-6,13-dihydro-5,6,7,12,13,14-hexaazapentacene in DMSO-d_6

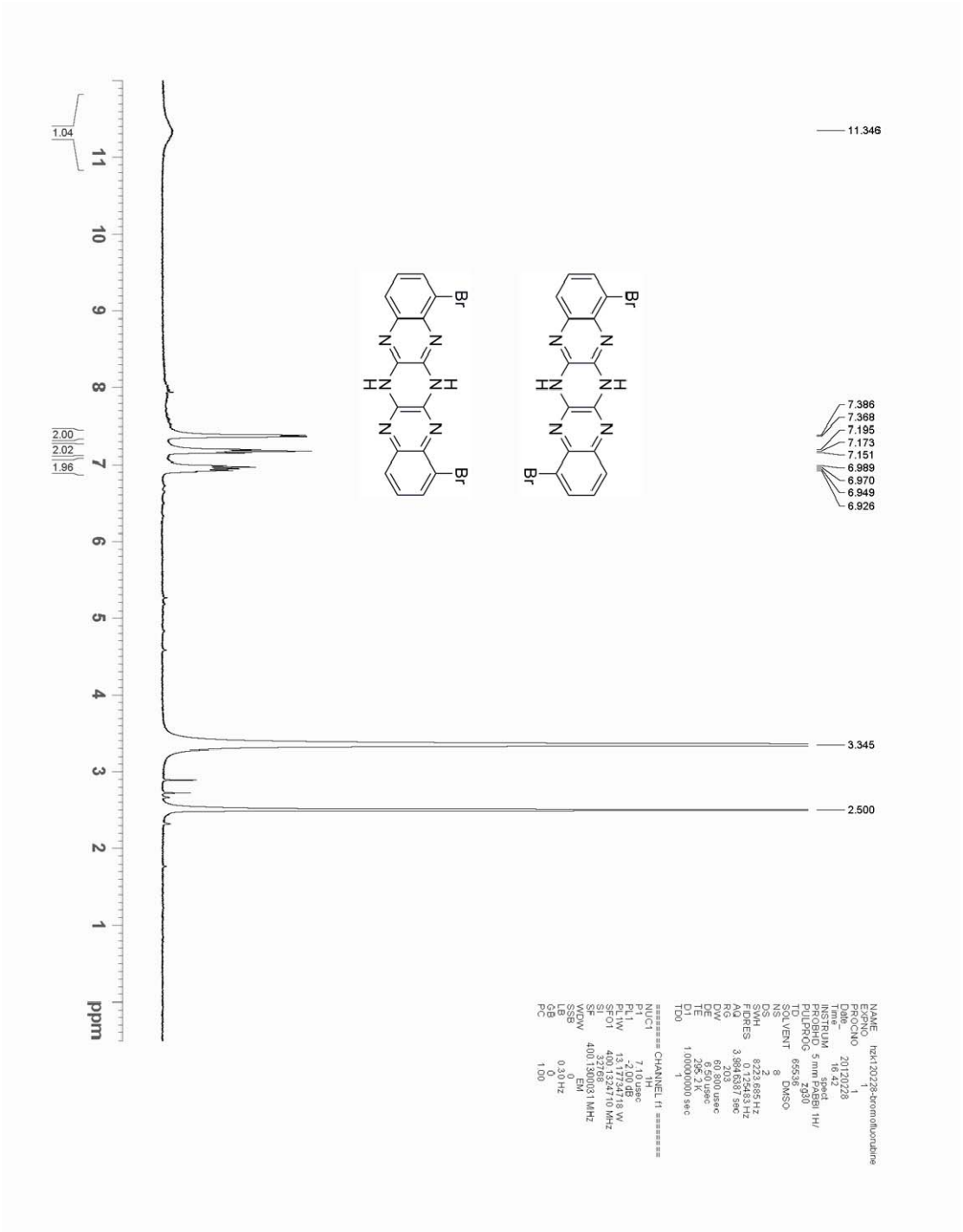

^{1}H-NMR of 1,8-dibromo-6,13-dihydro-5,6,7,12,13,14-hexaazapentacene and 1,11-dibromo-6,13-dihydro-5,6,7,12,13,14-hexaazapentacene in DMSO-d_6

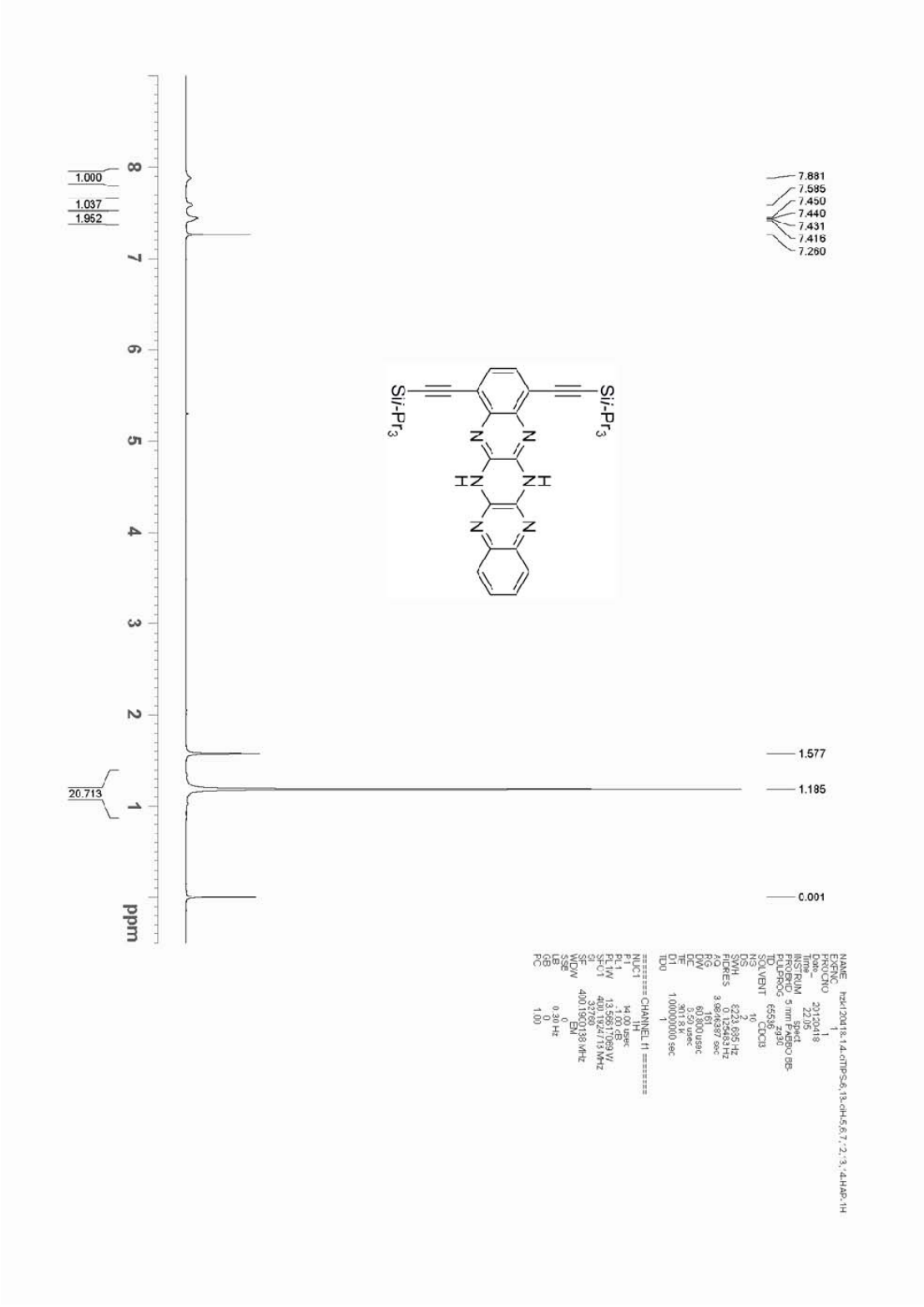

^{1}H-NMR of 1,4-bis((triisopropylsilyl)ethynyl)-6,13-dihydro-5,6,7,12,13,14 -hexaazapentacene in $CDCl_3$

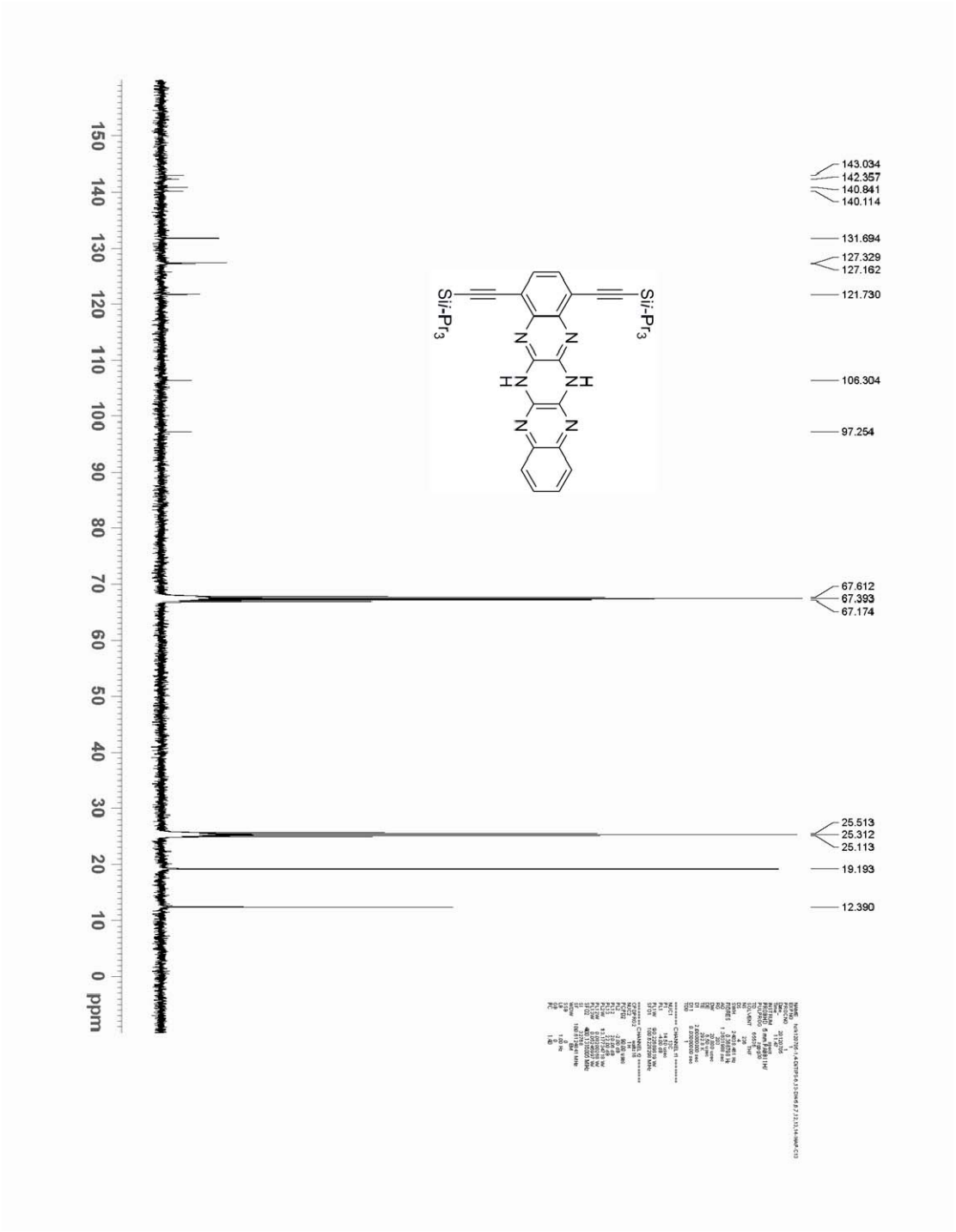

^{13}C-NMR of 1,4-bis((triisopropylsilyl)ethynyl)-6,13-dihydro-5,6,7,12,13,14-hexaazapentacene in THF-d_8.

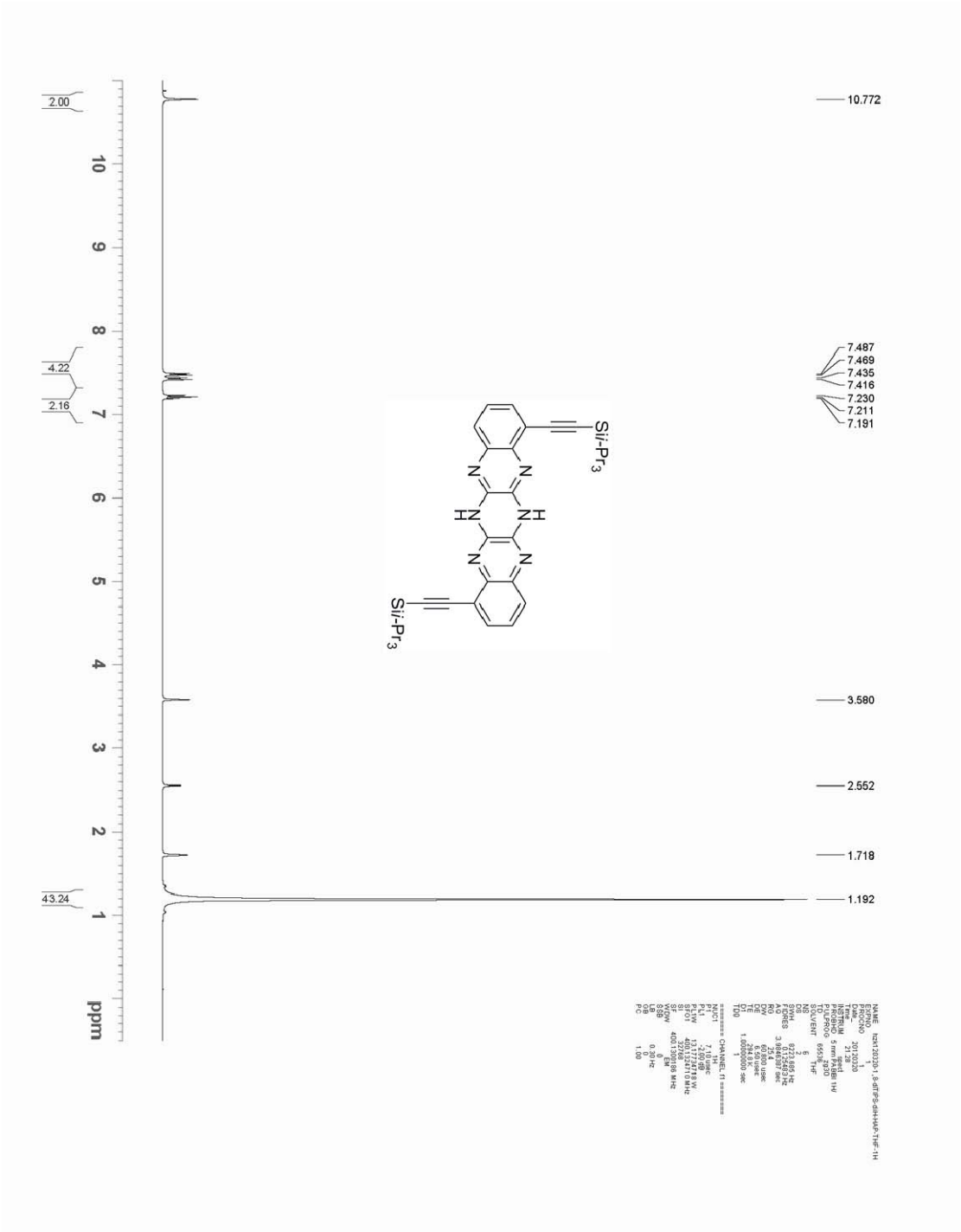

^{1}H-NMR of 1,8-bis((triisopropylsilyl)ethynyl)-6,13-dihydro-5,6,7,12,13,14-hexaazapentacene in THF-d_8.

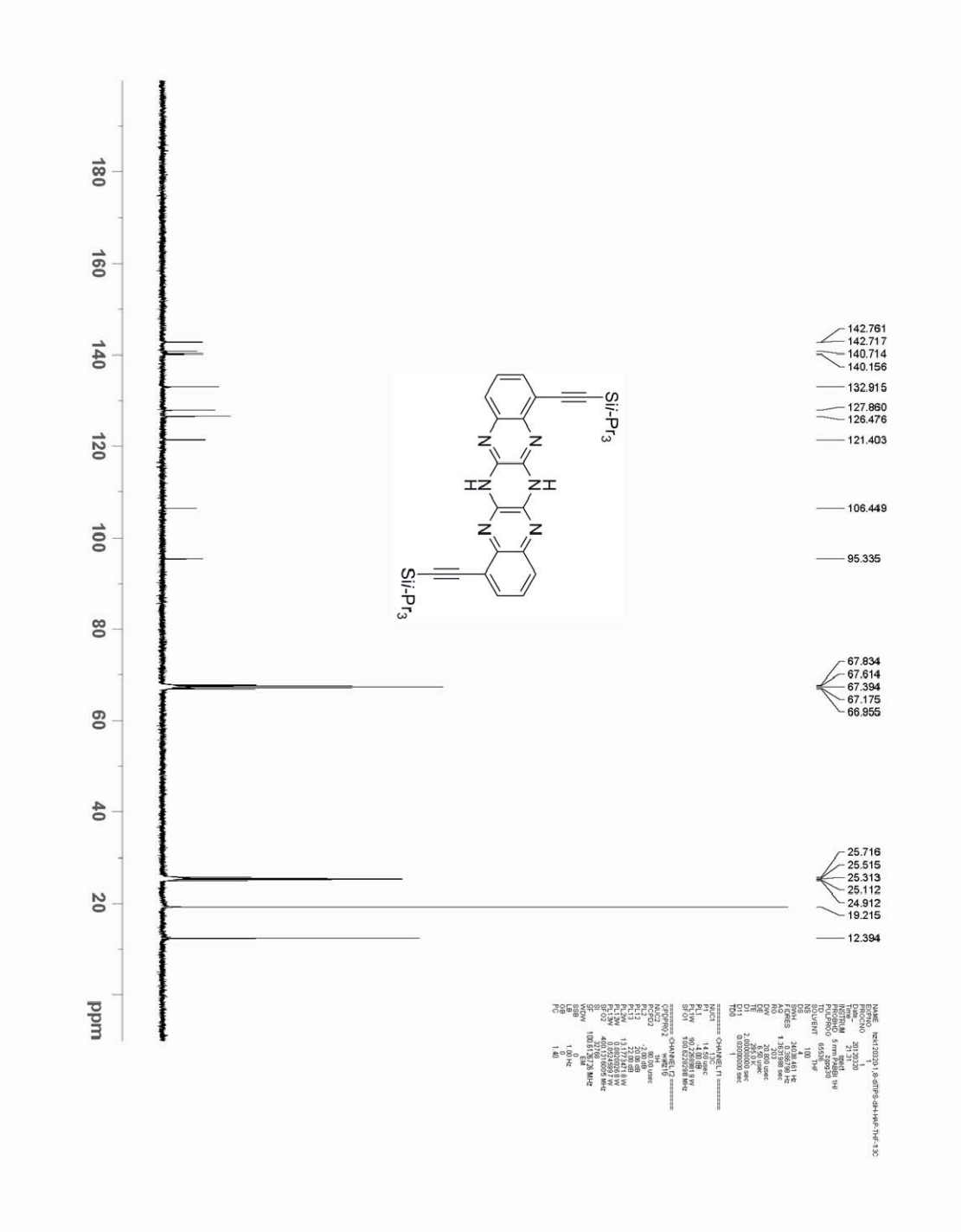

^{13}C-NMR of 1,8-bis((triisopropylsilyl)ethynyl)-6,13-dihydro-5,6,7,12,13,14-hexaazapentacene in THF-d_8.

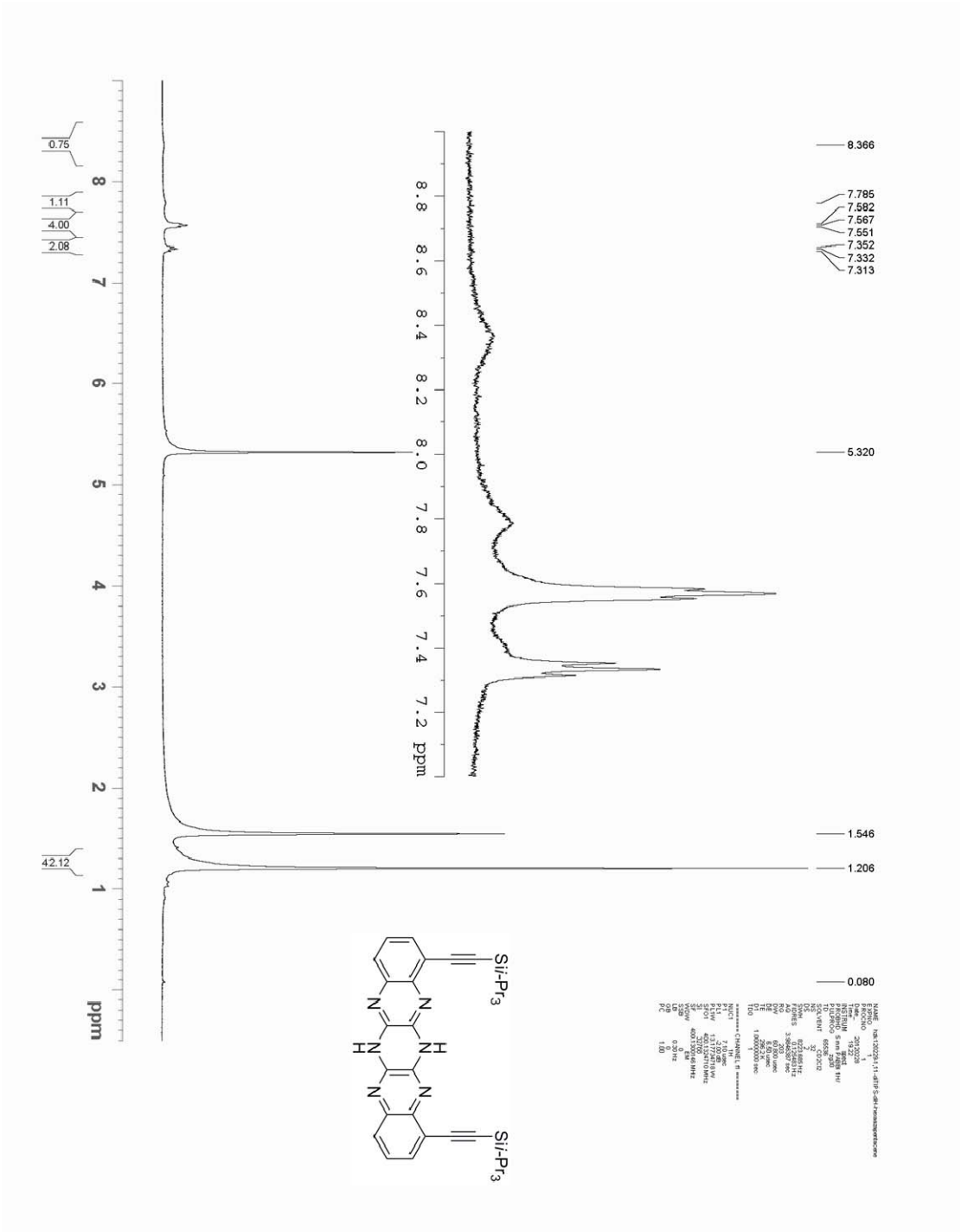

^{1}H-NMR of 1,11-bis((triisopropylsilyl)ethynyl)-6,13-dihydro-5,6,7,12,13,14-hexaazapentacene in $CDCl_3$.

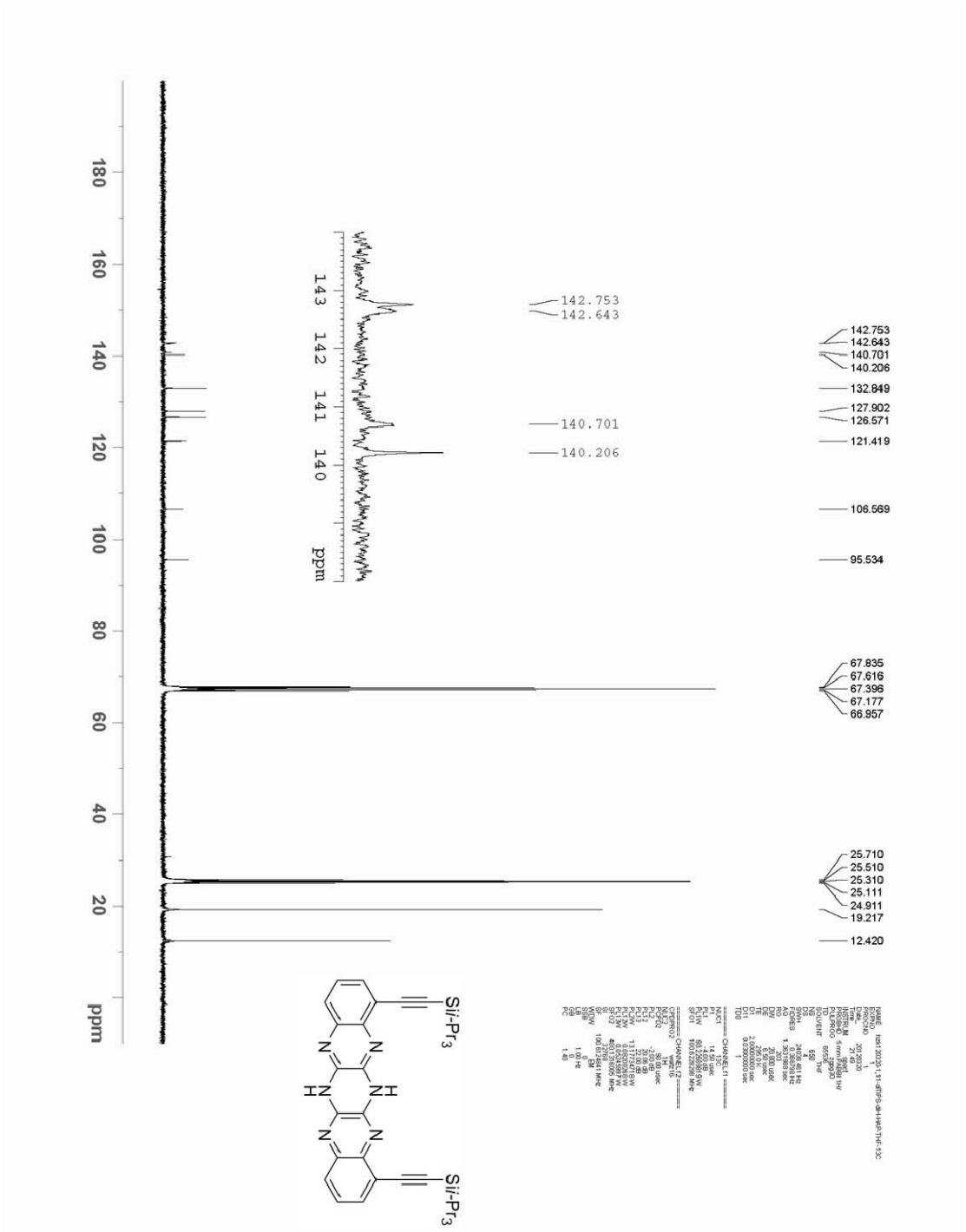

^{13}C-NMR of 1,11-bis((triisopropylsilyl)ethynyl)-6,13-dihydro-5,6,7,12,13,14-hexaazapentacene in THF-d_8.

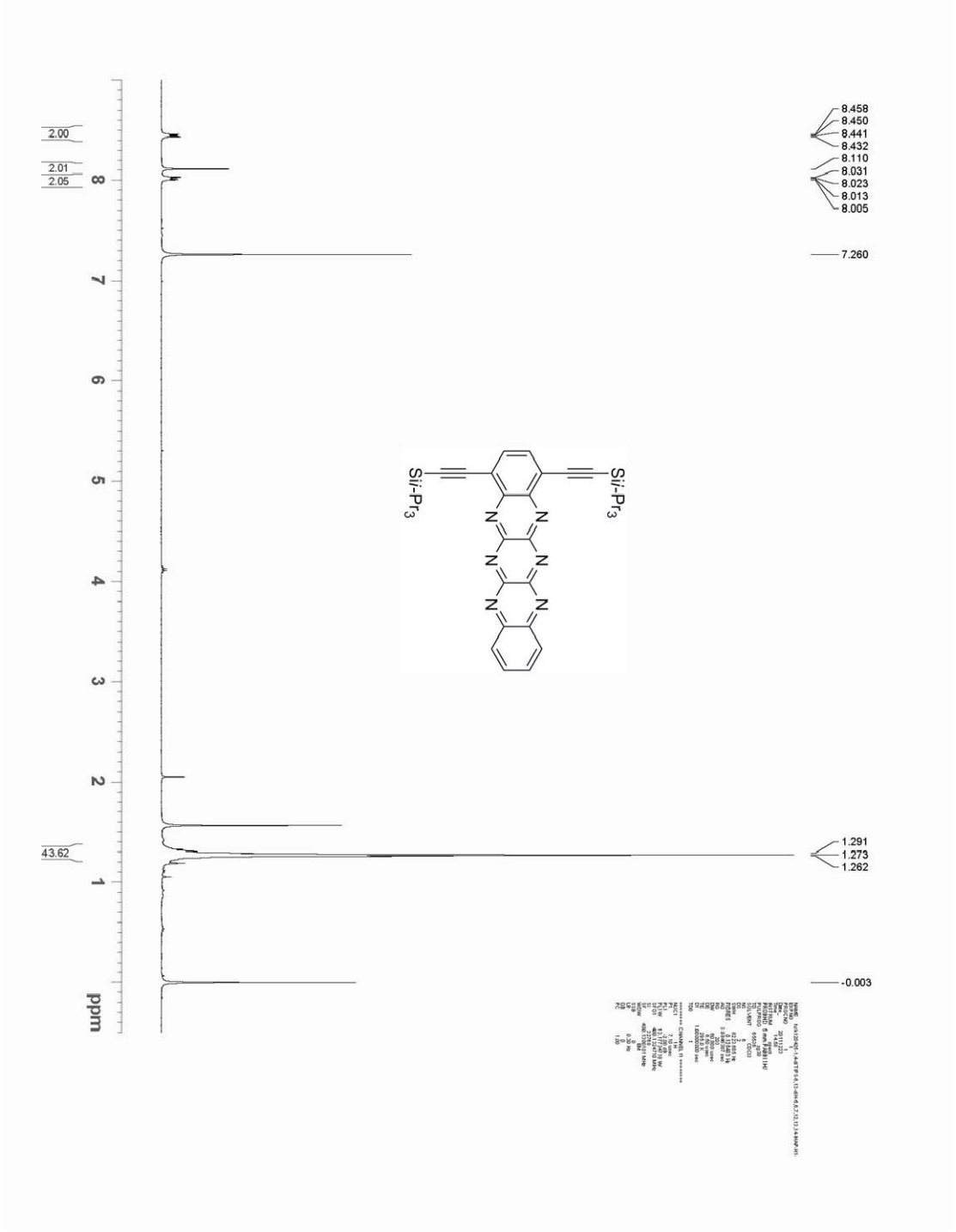

^{1}H-NMR of 1,4-bis((triisopropylsilyl)ethynyl)-5,6,7,12,13,14-hexaazapentacene in $CDCl_3$

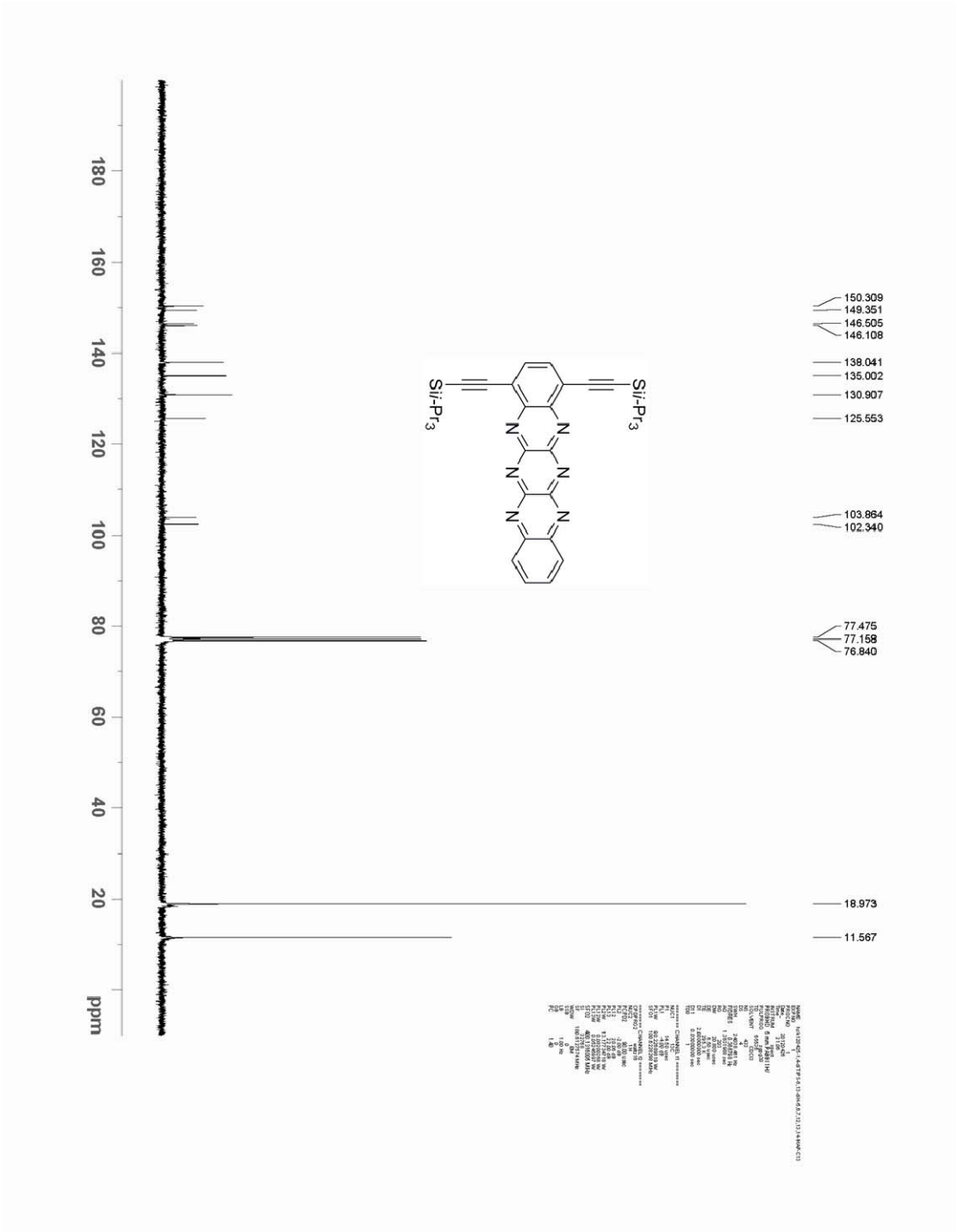

^{13}C-NMR of 1,4-bis((triisopropylsilyl)ethynyl)- 5,6,7,12,13,14-hexaazapentacene in $CDCl_3$

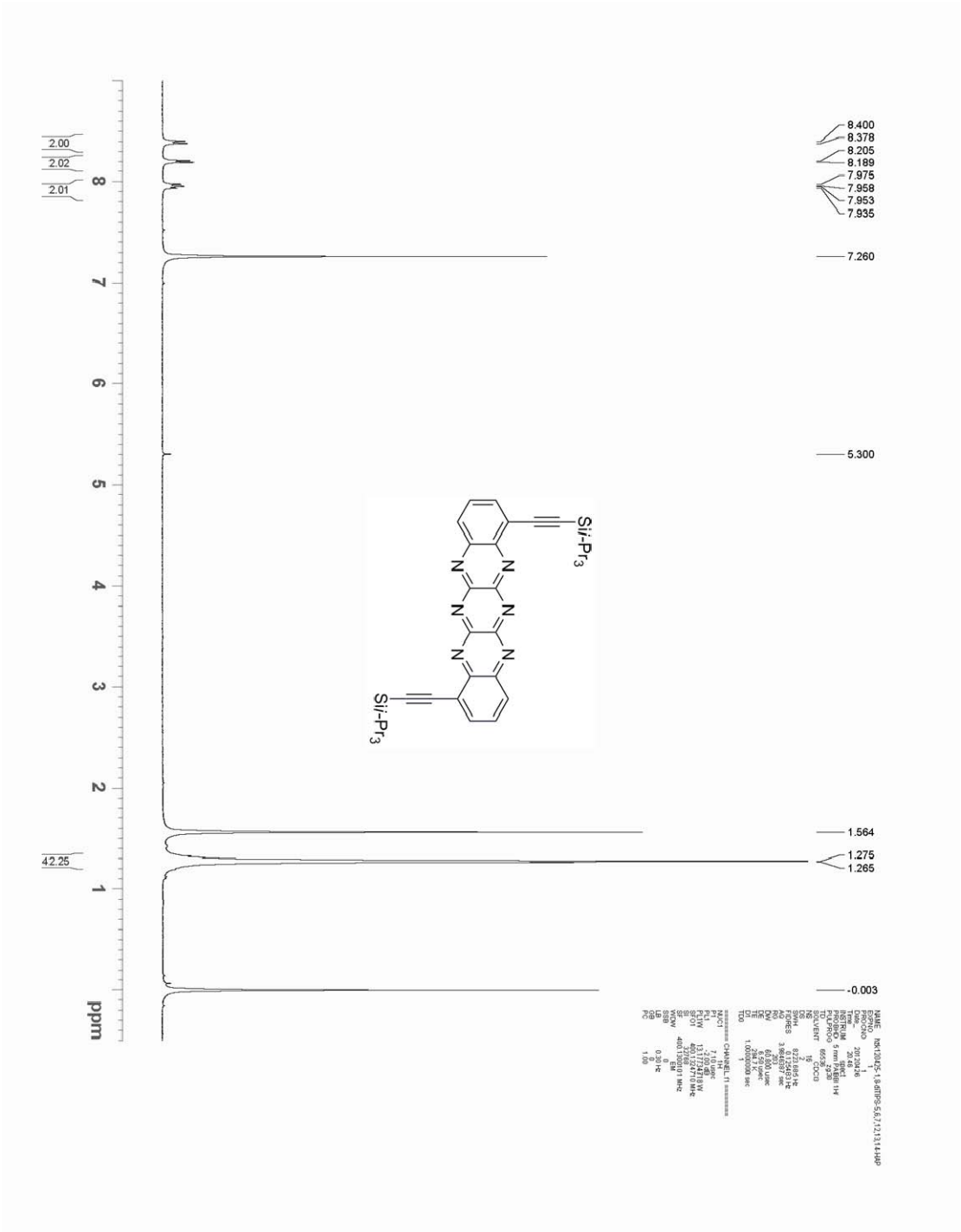

^{1}H-NMR of 1,8-bis((triisopropylsilyl)ethynyl)- 5,6,7,12,13,14-hexaazapentacene in $CDCl_3$

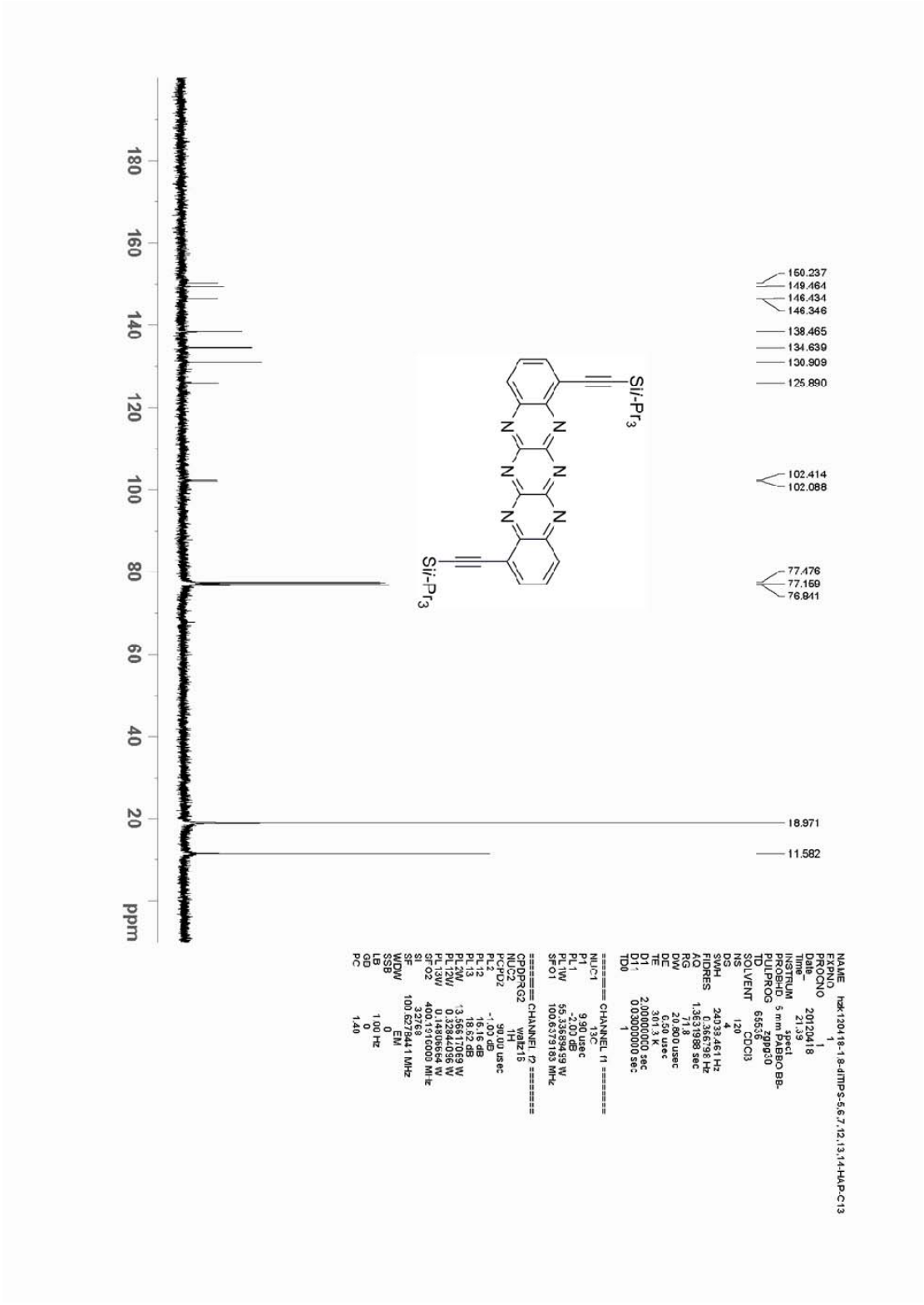

^{13}C-NMR of 1,8-bis((triisopropylsilyl)ethynyl)- 5,6,7,12,13,14-hexaazapentacene in $CDCl_3$

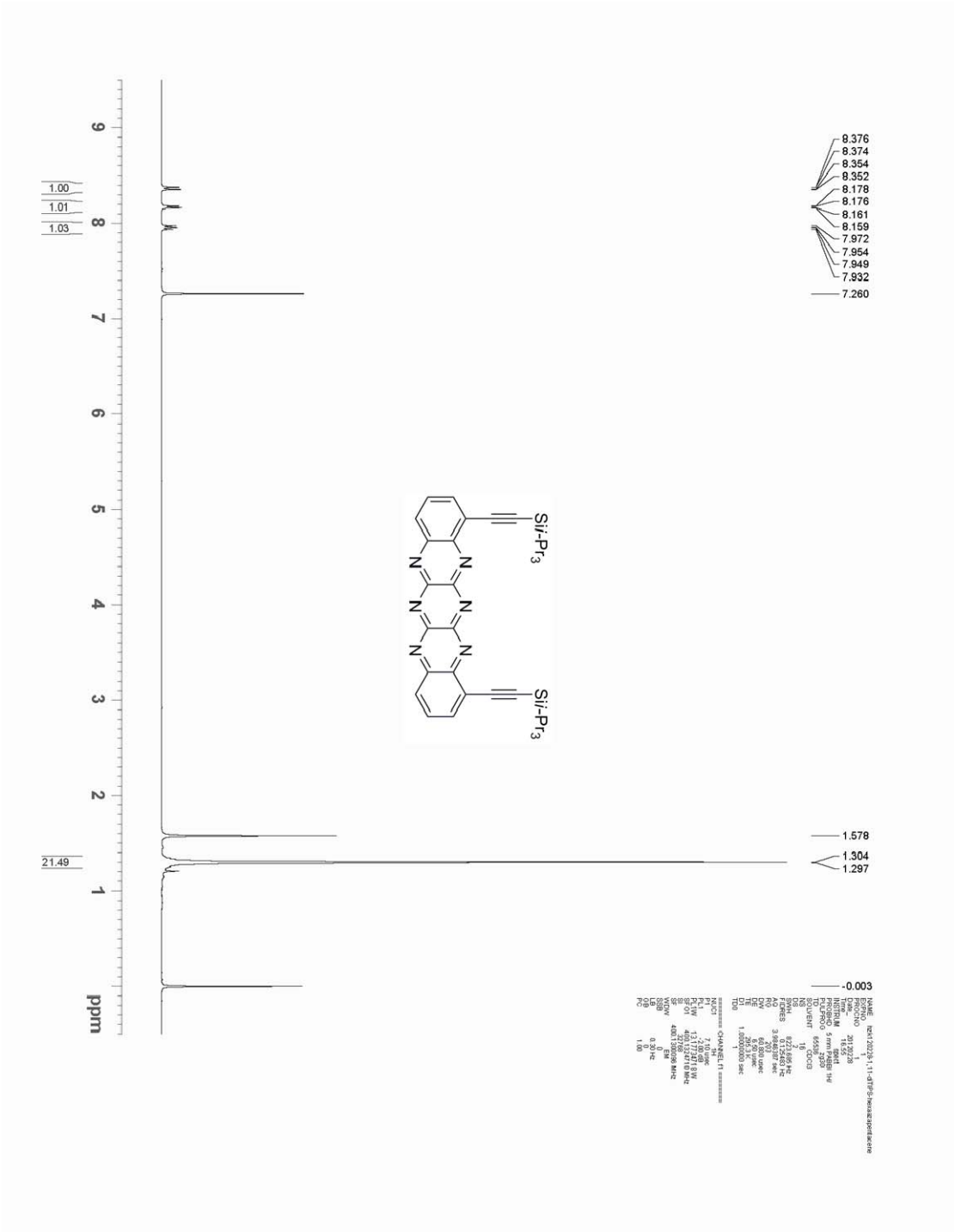

^{1}H-NMR of 1,11-bis((triisopropylsilyl)ethynyl)-5,6,7,12,13,14-hexaazapentacene in $CDCl_3$

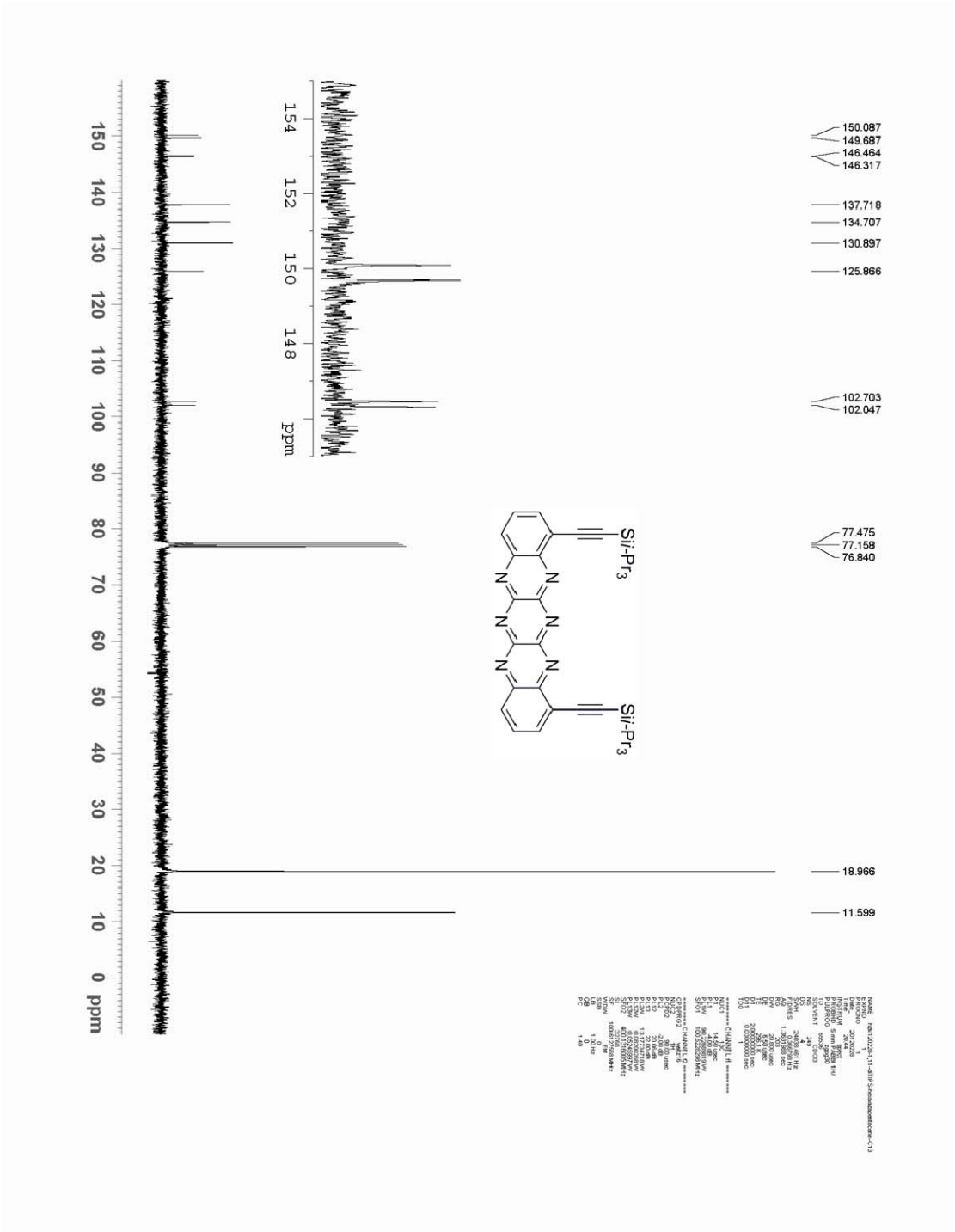

^{13}C-NMR of
1,11-bis((triisopropylsilyl)ethynyl)-5,6,7,12,13,14-hexaazapentacene in $CDCl_3$

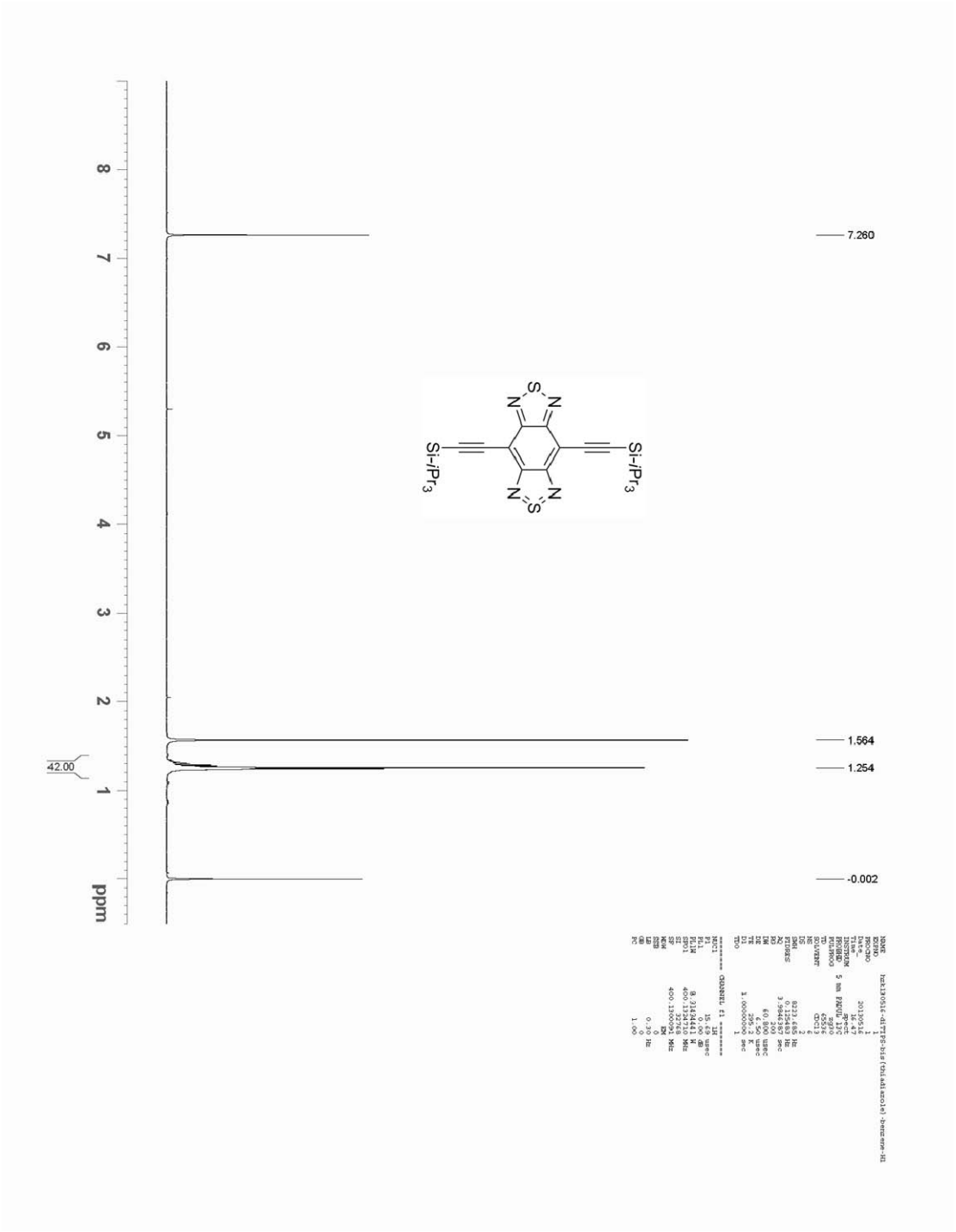

^{1}H NMR of 4,8-bis(triisopropylsilylethynyl)-benzo[1,2-c;4,5-c']bis[2,1,5]thiadiazole in $CDCl_3$.

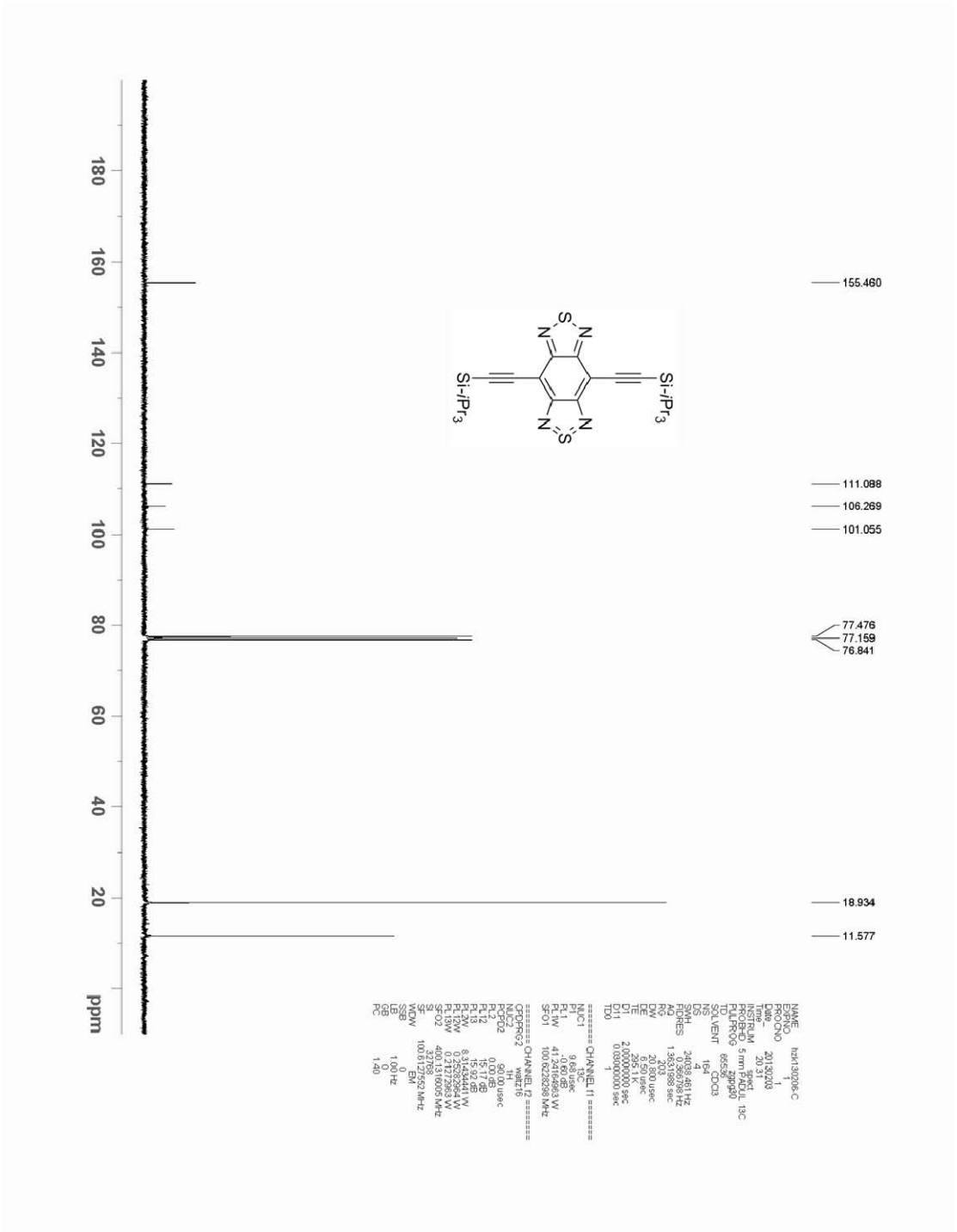

^{13}C NMR of 4,8-bis(triisopropylsilylethynyl)-benzo[1,2-c;4,5-c']bis[2,1,5]thiadiazole in $CDCl_3$.

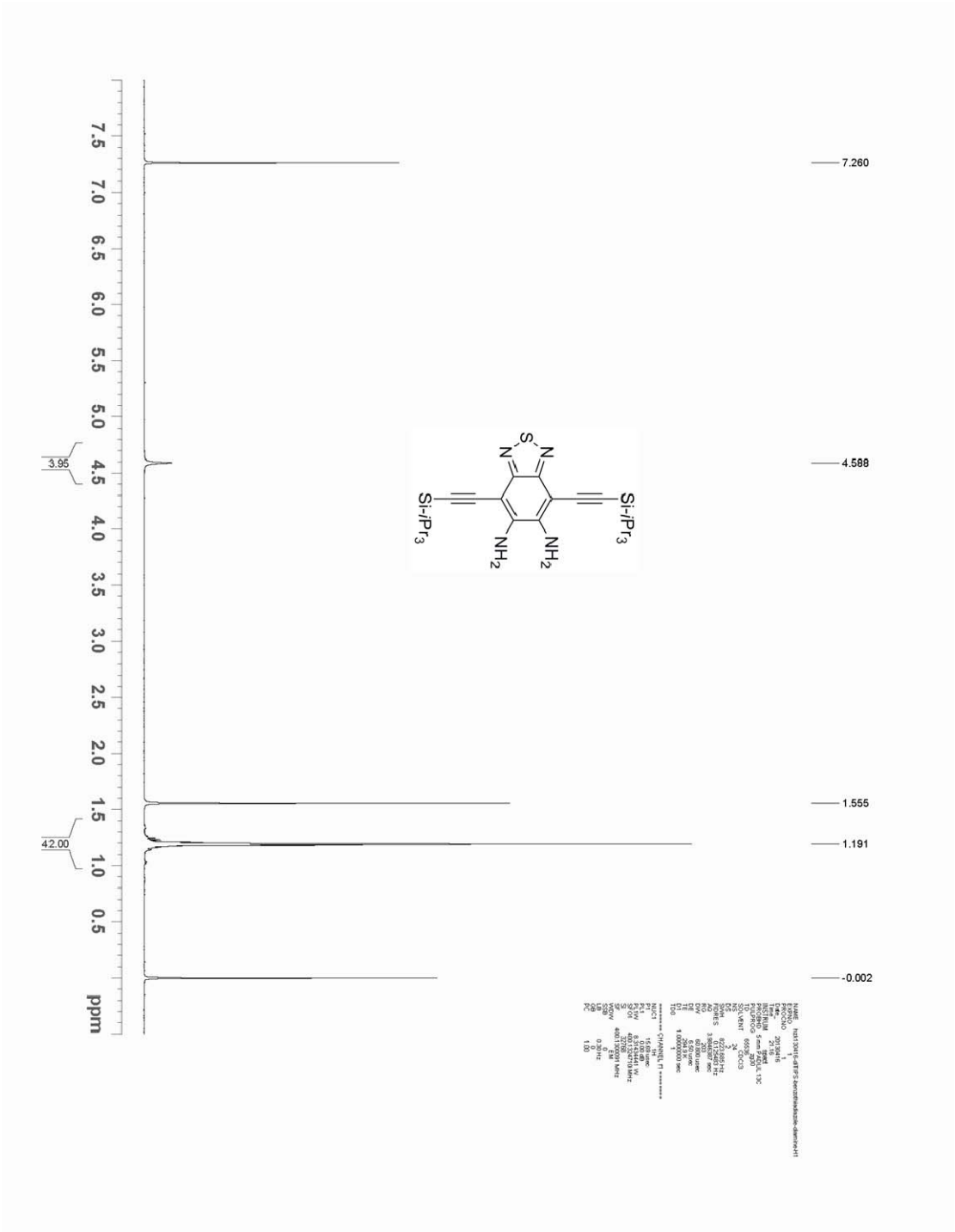

^{1}H NMR of 4,7-bis(triisopropylsilylethynyl)-5,6-diamino-benzo[2,1,3]thiadiazole in $CDCl_3$.

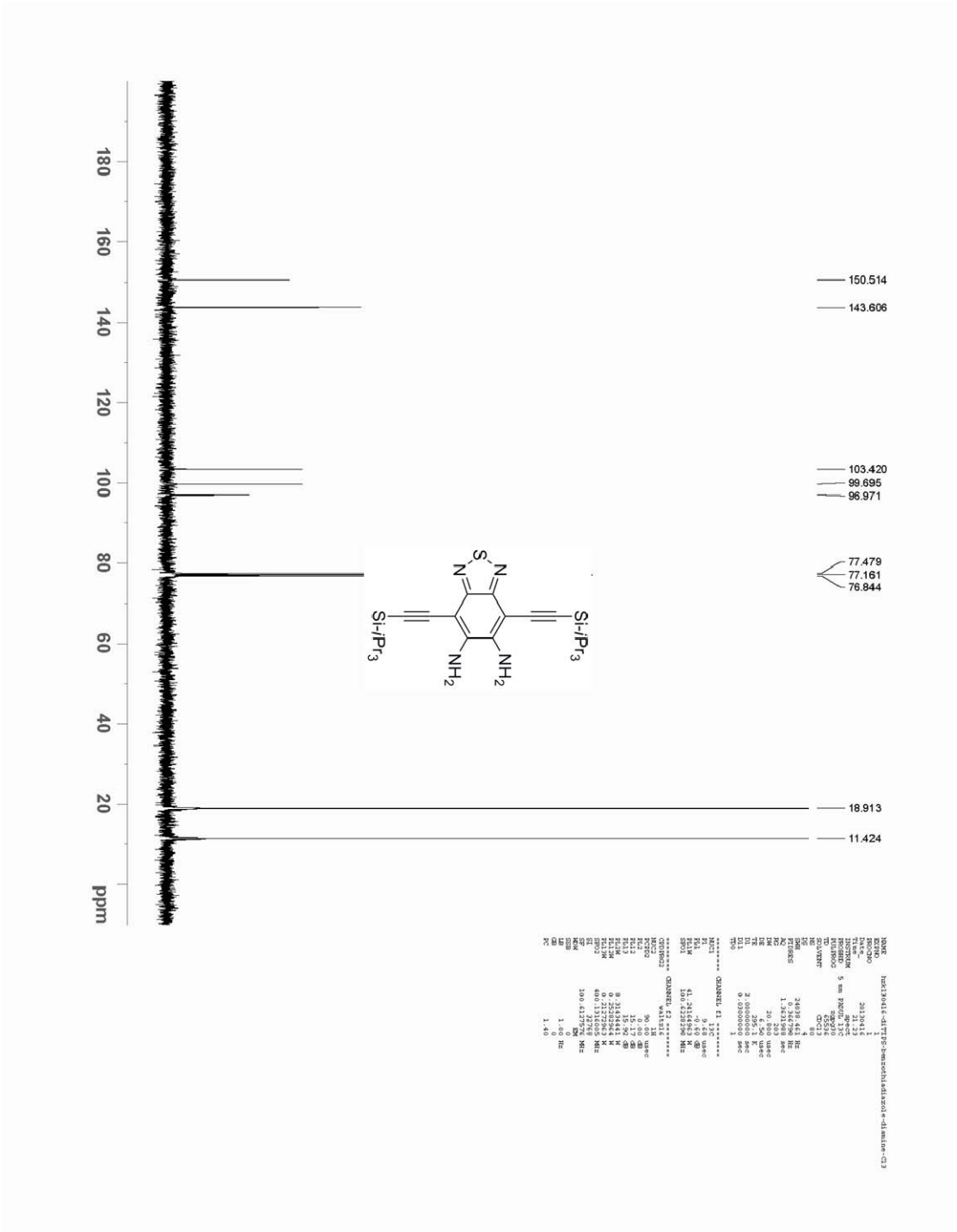

^{13}C NMR of 4,7-bis(triisopropylsilylethynyl)-5,6-diamino-benzo[2,1,3]thiadiazole in $CDCl_3$.

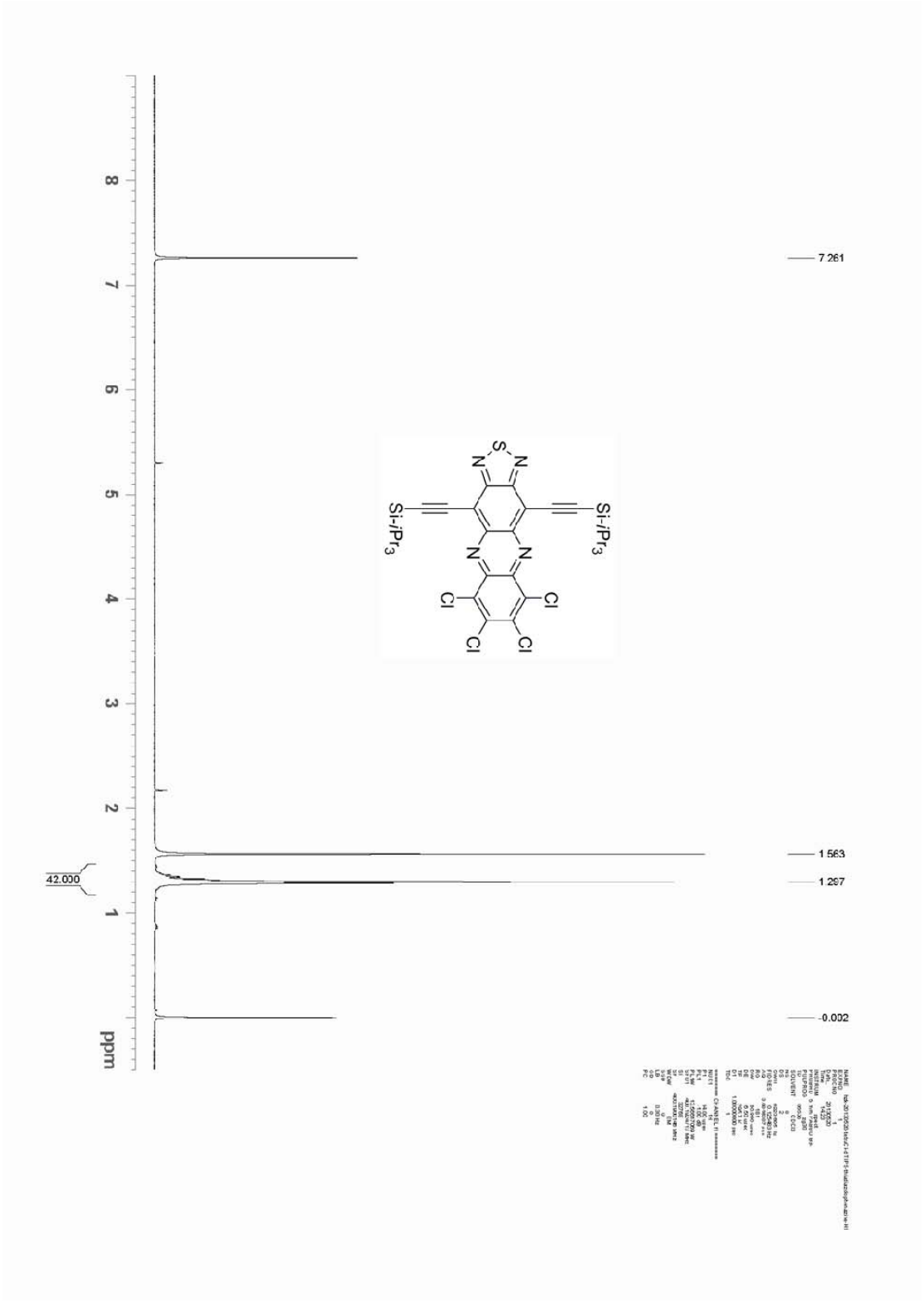

^{1}H NMR of 4,11-bis((triisopropylsilyl)ethynyl)-6,7,8,9-tetrachloro-[1,2,5]thiadiazolo-[3,4-b]phenzino in $CDCl_3$.

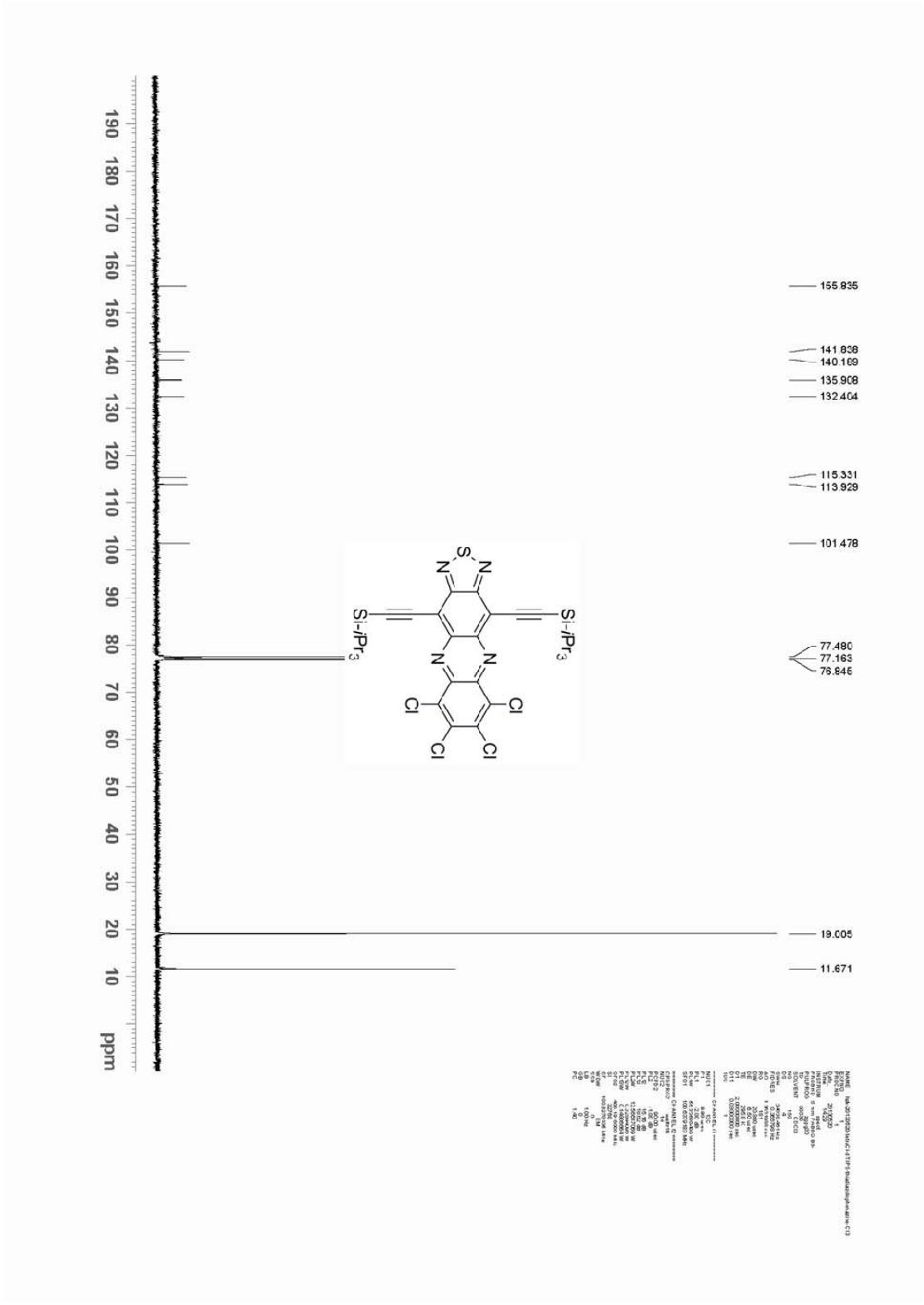

^{13}C NMR of 4,11-bis((triisopropylsilyl)ethynyl)-6,7,8,9-tetrachloro-[1,2,5]thiadiazolo-[3,4-b]phenzino in $CDCl_3$.

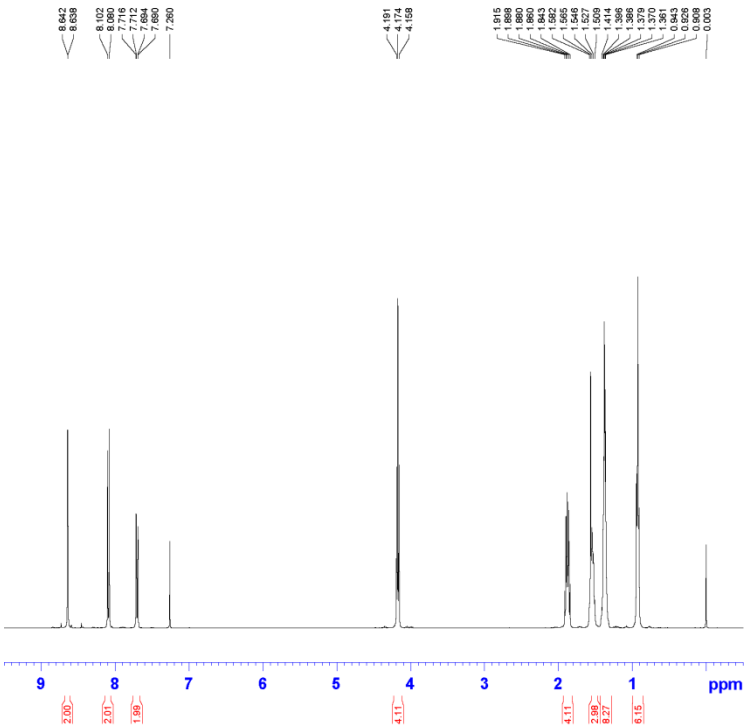

^{1}H-NMR of 3, 6-dibromo-9, 10-bis(hexyloxy)phenanthrene**.**

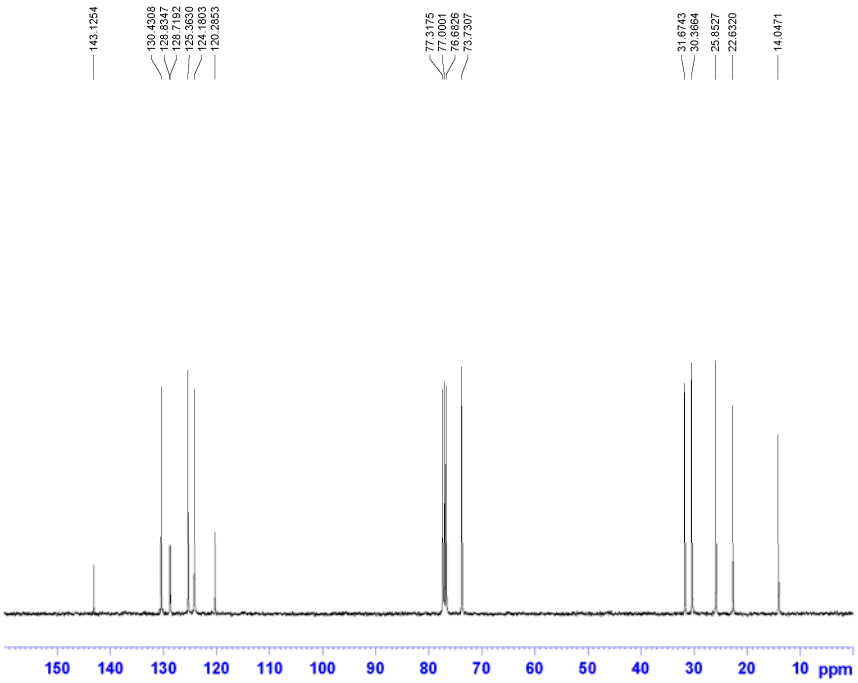

^{13}C-NMR of 3, 6-dibromo-9, 10-bis(hexyloxy)phenanthrene.

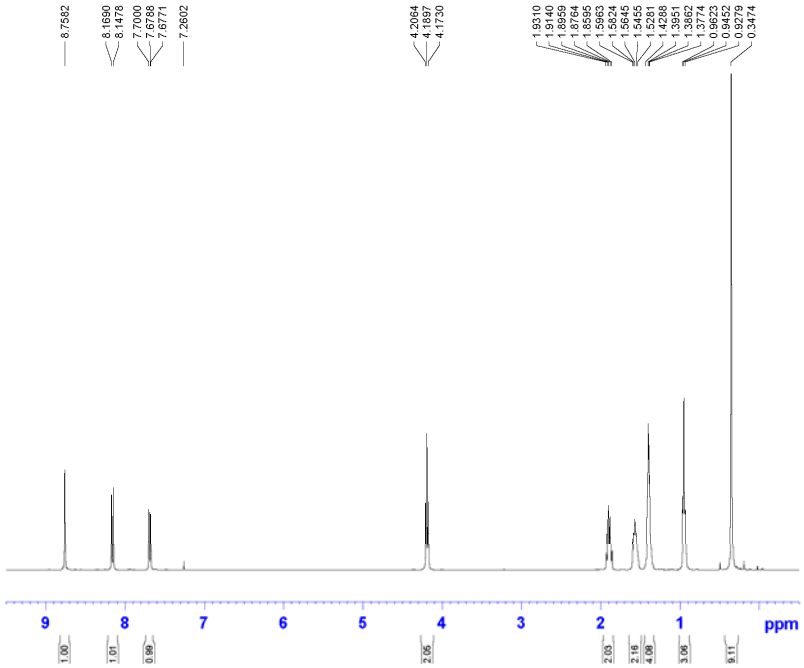

^{1}H-NMR of 3, 6-bis(trimethylsilylethynyl)-9, 10-bis(hexyloxy)-phenanthrene.

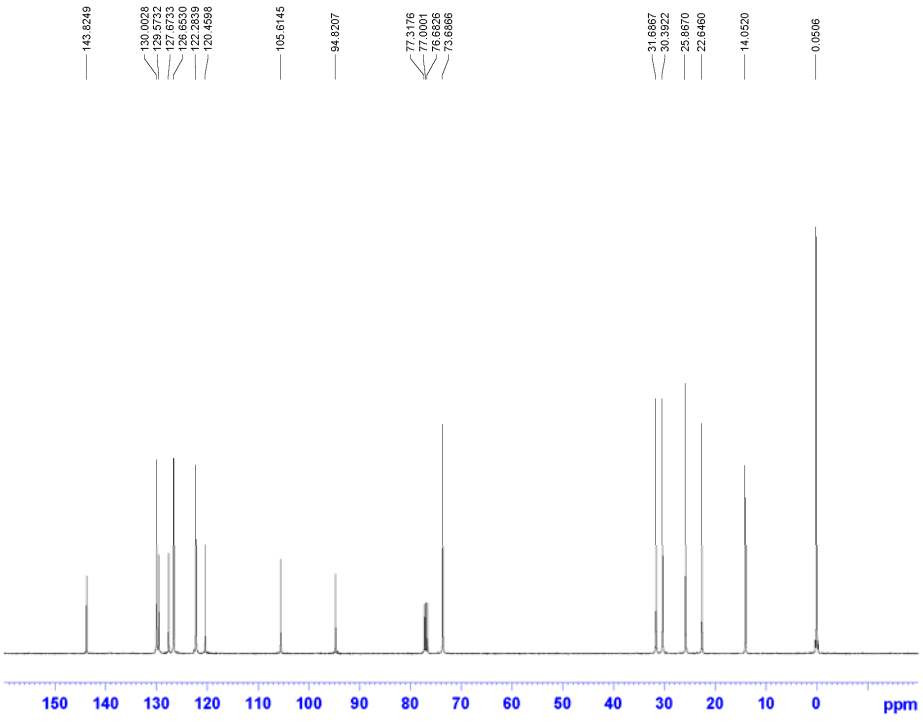

^{13}C-NMR of 3, 6-bis(trimethylsilylethynyl)-9, 10-bis(hexyloxy)-phenanthrene.

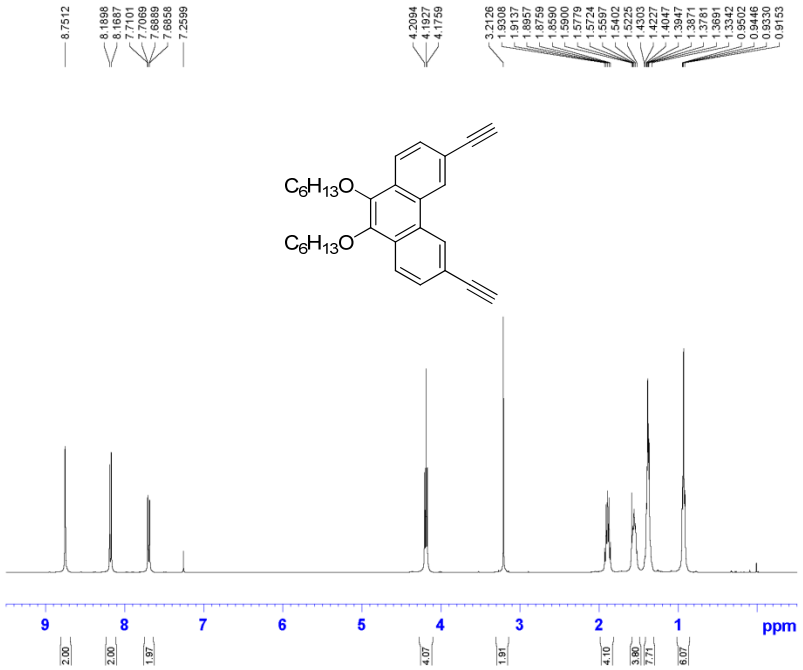

^{1}H-NMR of 3, 6-diethynyl-9, 10-bis(hexyloxy)-phenanthrene.

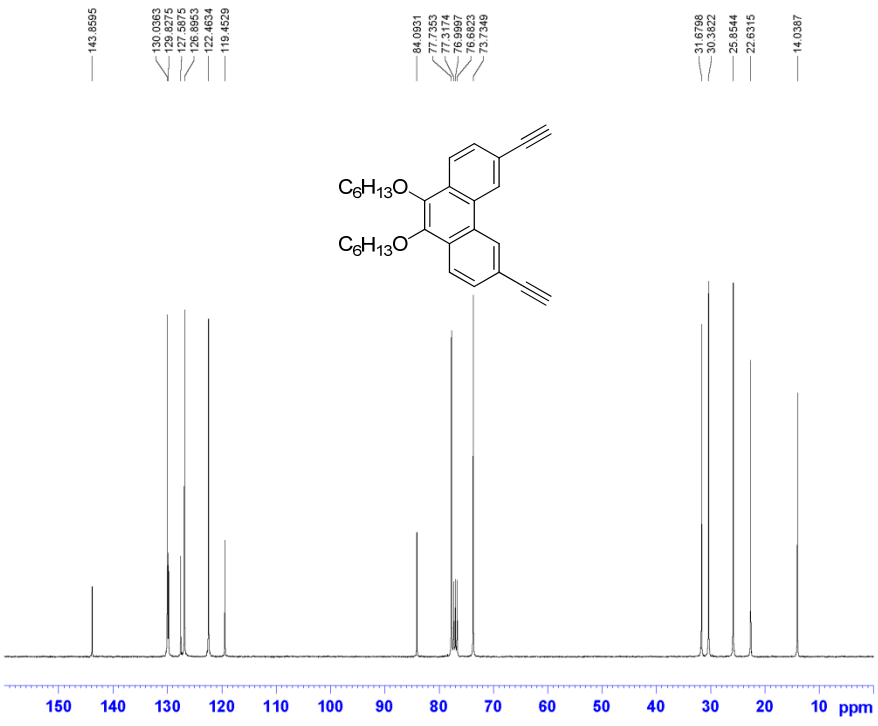

^{13}C-NMR of 3, 6-diethynyl-9, 10-bis(hexyloxy)-phenanthrene.

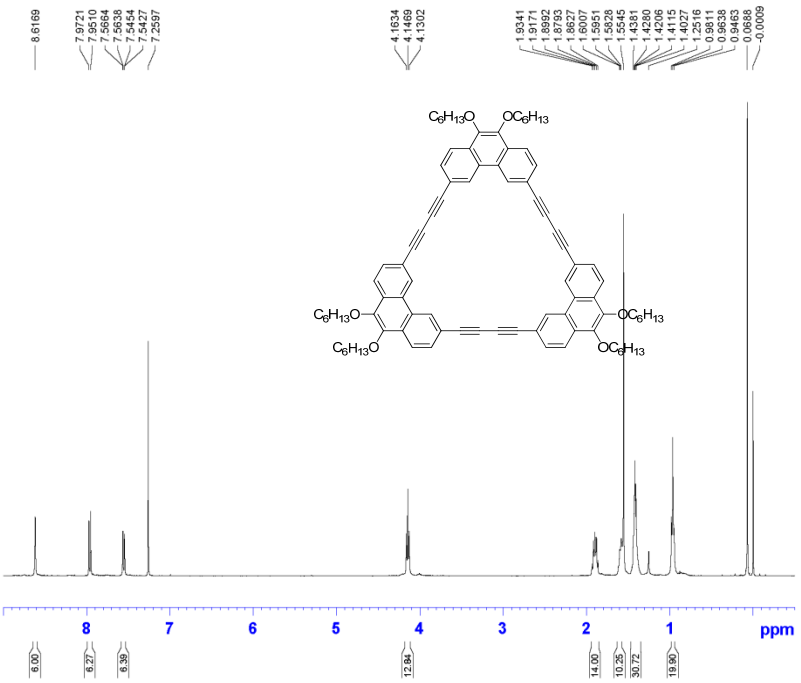

^{1}H-NMR of Cyclic-tri(3, 6-diethynyl-9, 10-bis(hexyloxy)phenanthrene) (4.0 mg/ml in CDCl3)

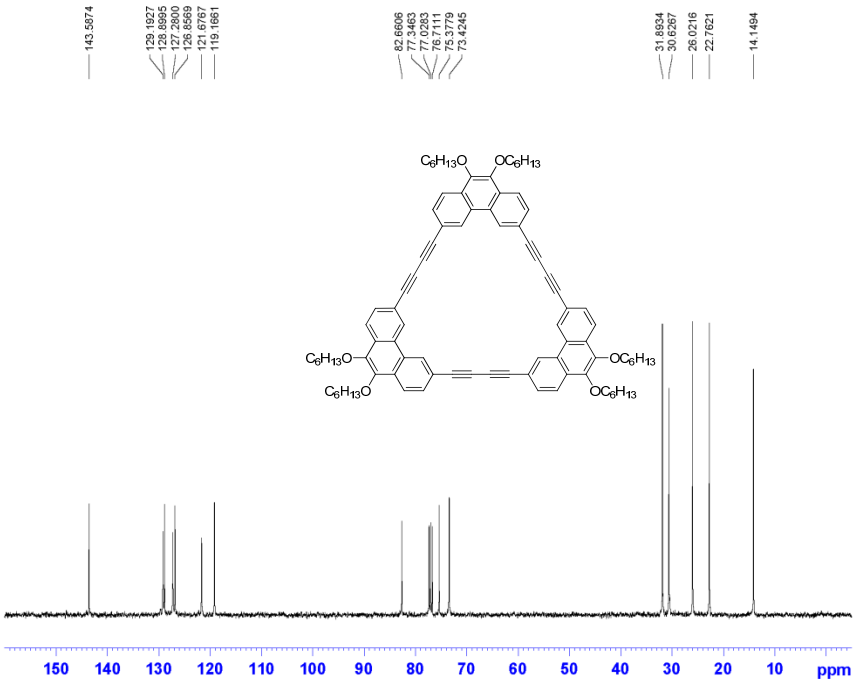

^{13}C-NMR of Cyclic-tri(3, 6-diethynyl-9, 10-bis(hexyloxy)phenanthrene).

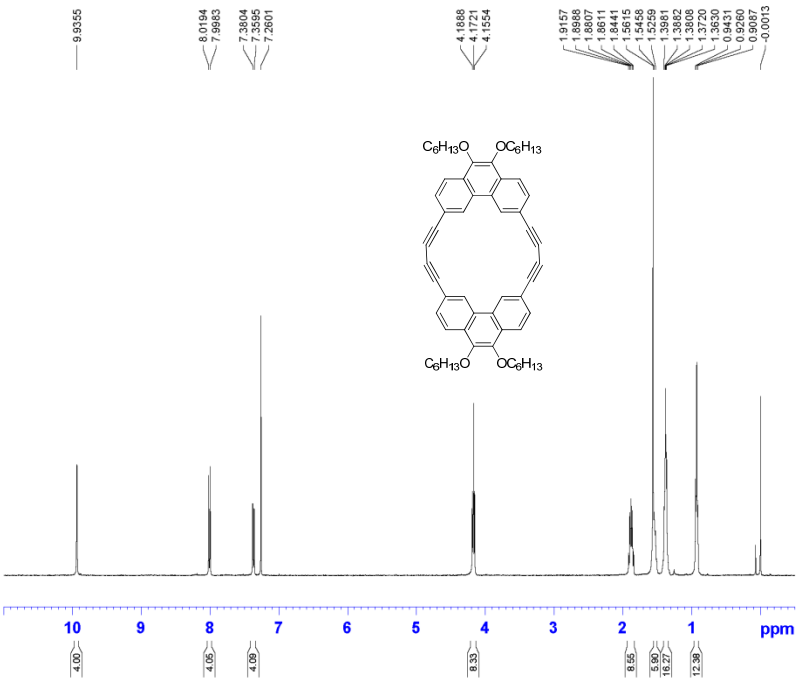

^{1}H-NMR of Cyclic-bis(3, 6-diethynyl-9, 10-bis(hexyloxy)phenanthrene).

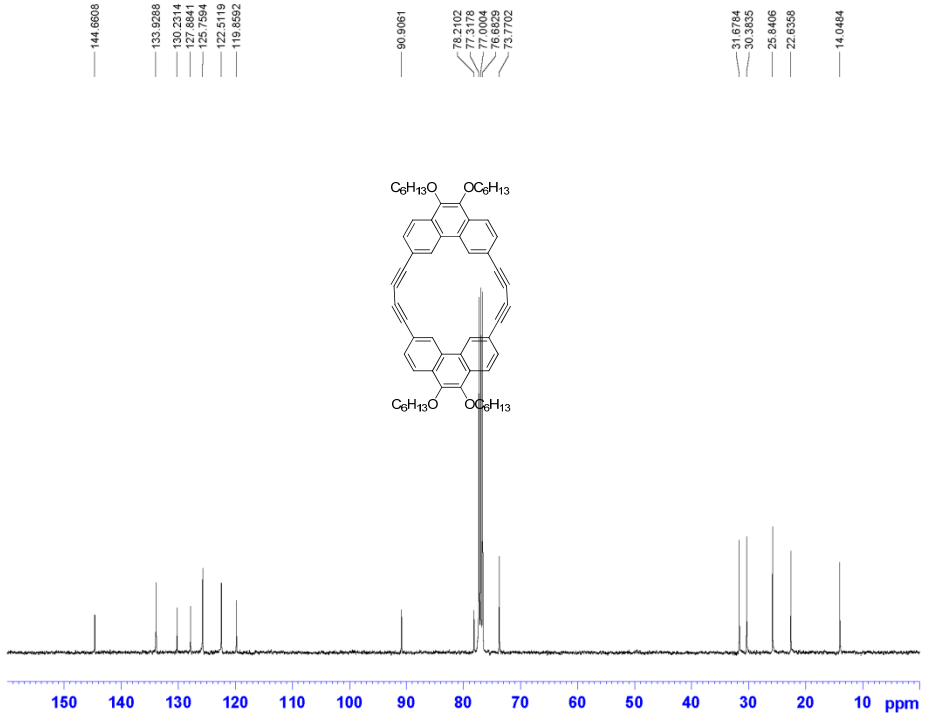

^{13}C-NMR of Cyclic-bis(3, 6-diethynyl-9, 10-bis(hexyloxy)phenanthrene).

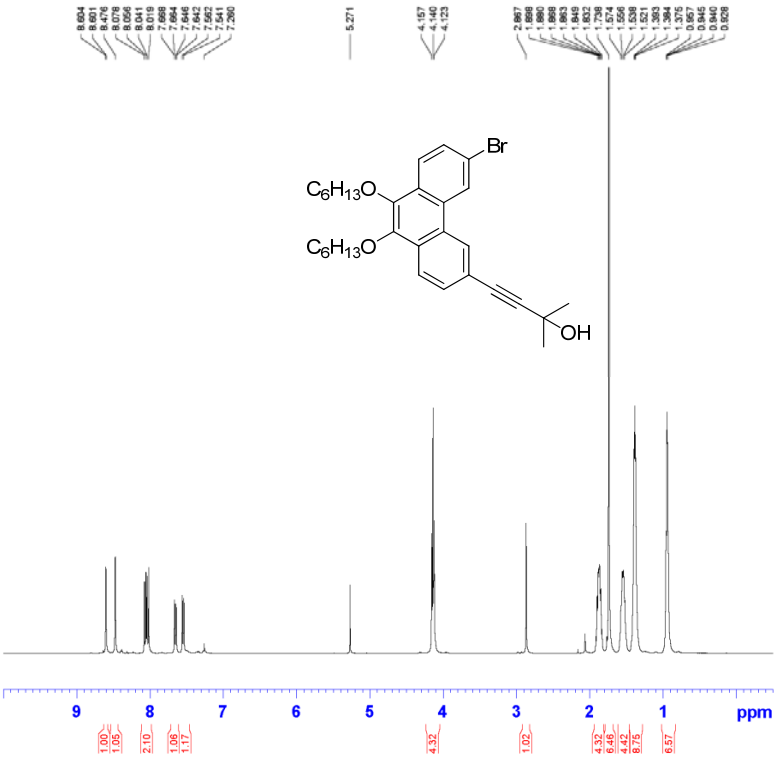

^{1}H-NMR of
3-(2'-methyl-2'-ol-but-3'-ynl)-6-bromo-9,10-bis(hexyloxy)phenanthrene.

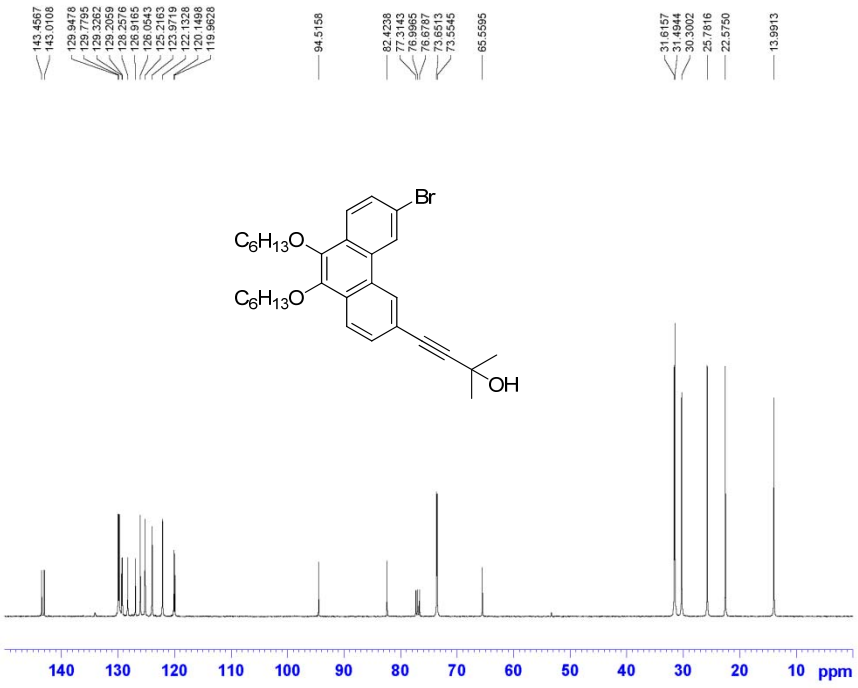

^{13}C-NMR of 3-(2'-methyl-2'-ol-but-3'-ynl)-6-bromo-9, 10-bis(hexyloxy)phenanthrene.

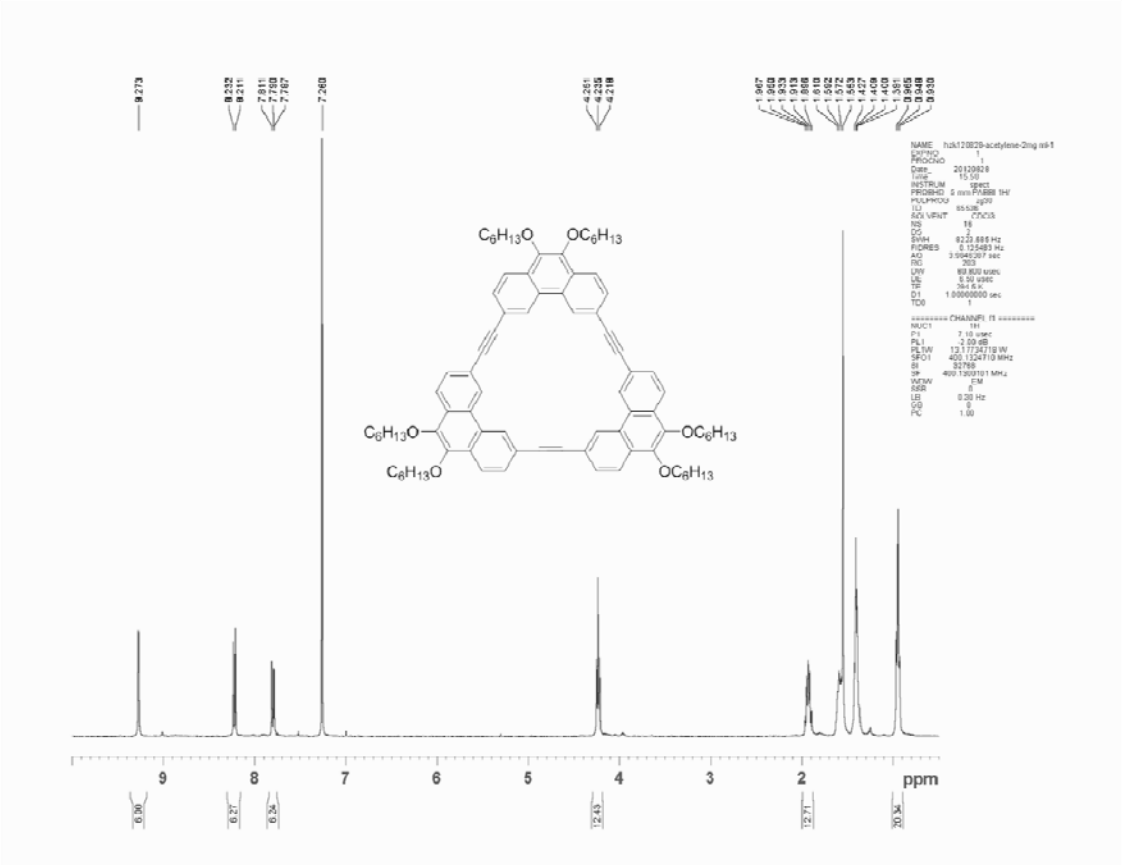

^{1}H-NMR ($CDCl_3$) of Cyclic-tri(3-ethynyl-9, 10-bis(hexyloxy)phenanthrene)

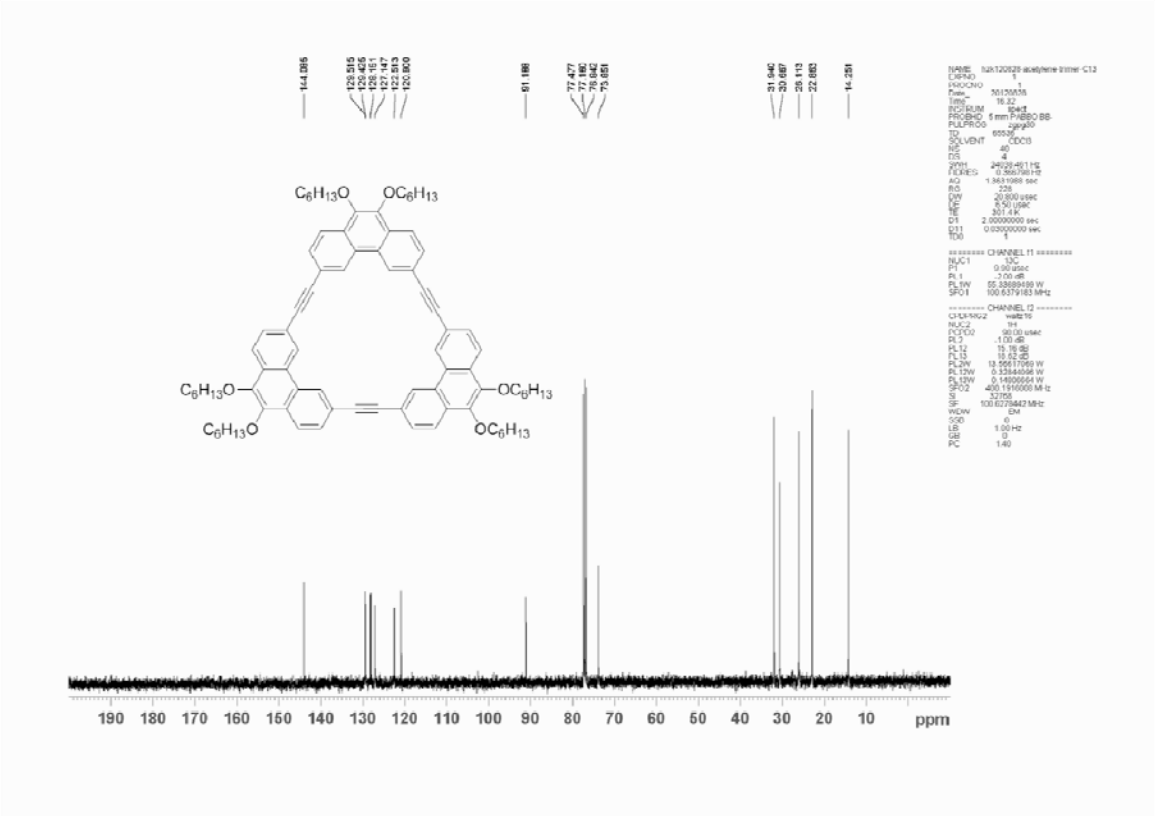

^{13}C-NMR ($CDCl_3$) of Cyclic-tri(3-ethynyl-9, 10-bis(hexyloxy)phenanthrene)

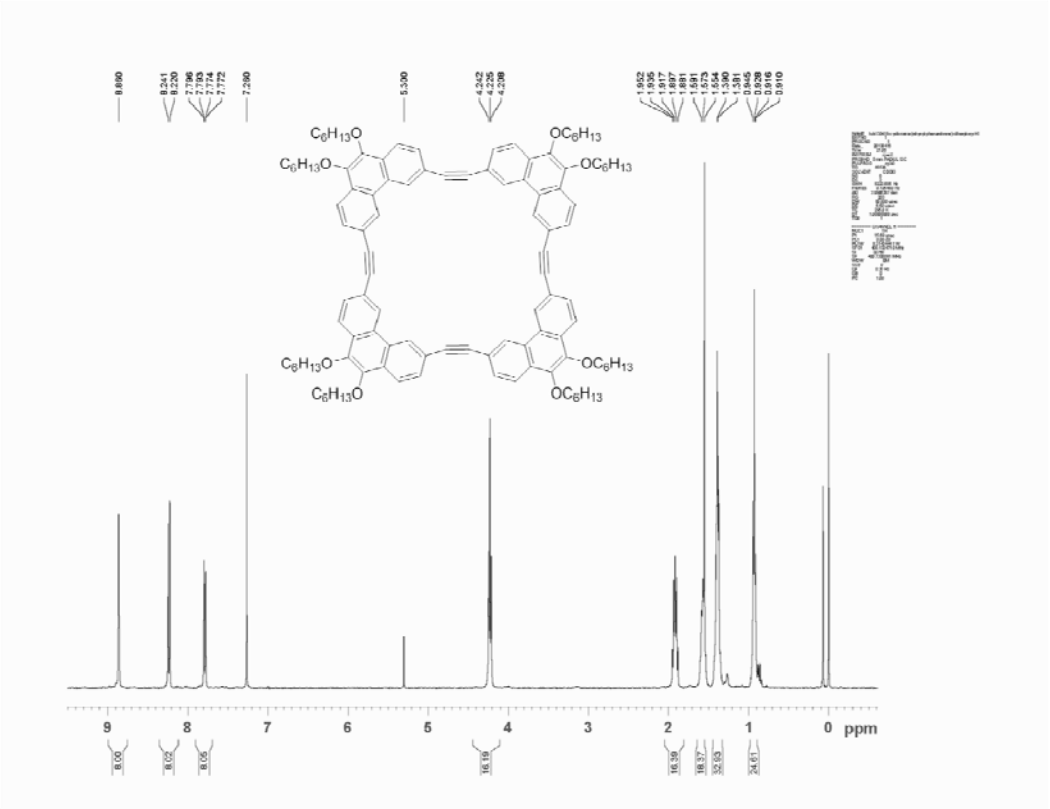

^{1}H-NMR ($CDCl_3$) of Cyclic-tetra(3-ethynyl-9, 10-bis(hexyloxy)phenanthrene)

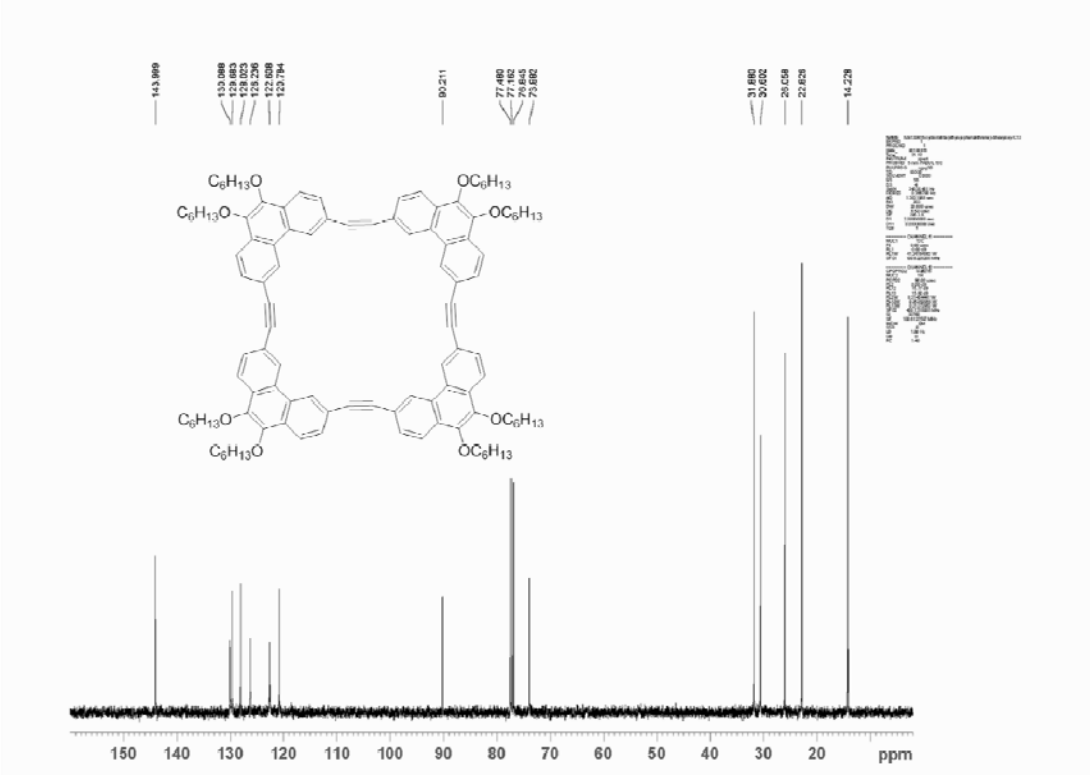

^{13}C-NMR ($CDCl_3$) of Cyclic-tetra(3-ethynyl-9, 10-bis(hexyloxy)phenanthrene)

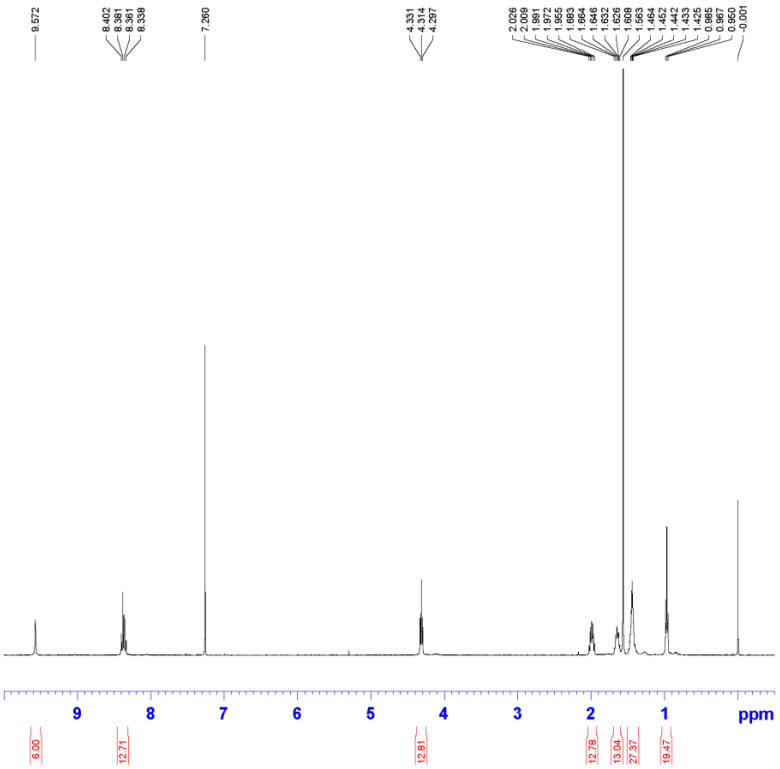

^{1}H-NMR ($CDCl_3$) of Cyclic-tri(9, 10-bis(hexyloxy)phenanthrene)

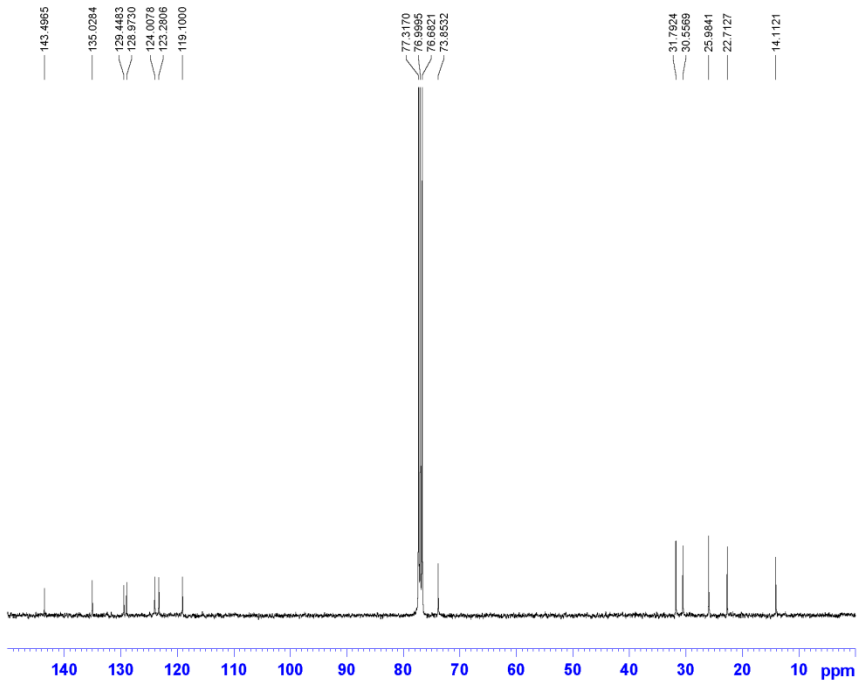

^{13}C-NMR ($CDCl_3$) of Cyclic-tri(9,10-bis(hexyloxy)phenanthrene)

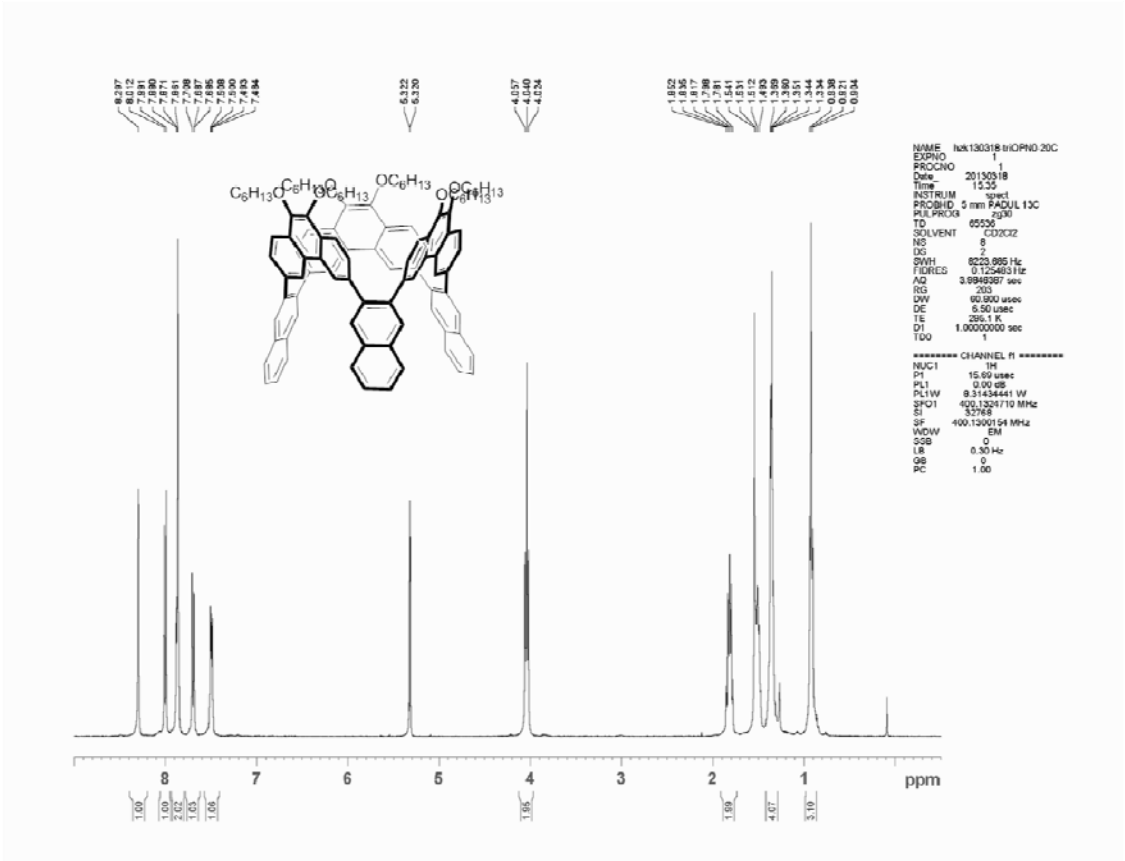

^{1}H-NMR($C_2D_2Cl_2$) of Cyclic-tri(3-(1',2'-naphthyl)-9,10-bis(hexyloxy)phenanthrene)

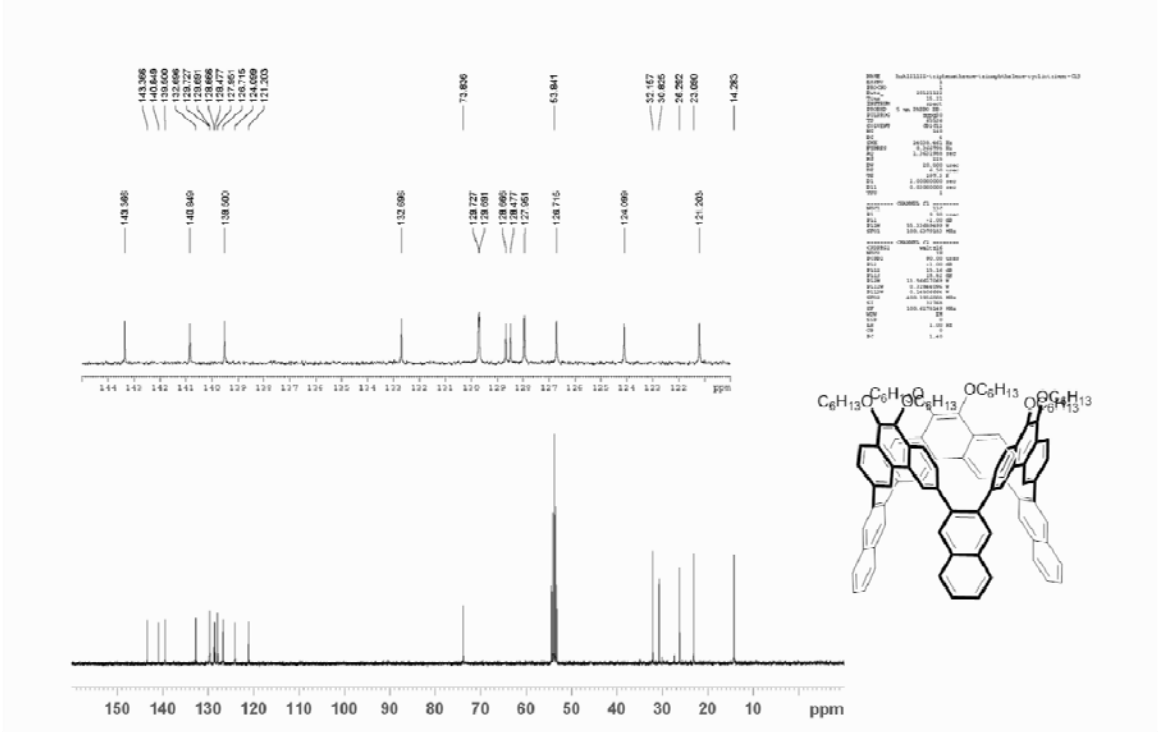

^{13}C-NMR($C_2D_2Cl_2$) of Cyclic-tri(3-(1',2'-naphthyl)-9,10-bis(hexyloxy)phenanthrene)